Controlling Nanoscale Restructuring to Improve Catalyst Activity, Stability, and Material Utilization

by

Alexander J. Hill

A dissertation submitted in partial fulfillment
of the requirements for the degree of
Doctor of Philosophy
(Chemical Engineering)
in the University of Michigan
2022

Doctoral Committee:

Professor Johannes W. Schwank, Co-Chair
Associate Professor Andrej Lenert, Co-Chair
Adjunct Professor Galen, B. Fisher
Assistant Professor Bryan Goldsmith
Associate Professor Charles McCrory

Alexander J. Hill

hillalex@umich.edu

ORCID iD: 0000-0003-0181-7920

Dedication

To my parents, Elizabeth, and Brian.

To my siblings Allyson, Andrew, and Chloe.

To all who accepted me in both good days and bad,

and helped teach me to accept myself during those days.

Acknowledgements

Pursuing a PhD has fundamentally changed me. The work I have done and the people I have met have helped me grow and have provided countless memories that I will cherish forever. I find it difficult to put my gratitude for all the people who have supported me during this time into words. There are far too many. But here is my best attempt.

First, I must acknowledge my advisors, Andrej Lenert, and Johannes Schwank. I was uncertain of my ability to succeed as a Chemical Engineering PhD. You always believed in me, however, and in the process, I learned how to better believe in myself. Your passion for mentoring has been a true inspiration. You both balance sharp, critical attention to detail with a caring and dedicated willingness to provide guidance. There have been times where I have had difficulty, experimentally and personally. And in those times, you were always willing to give good feedback while also acknowledging my humanity. I could not have imagined a better advising scenario. I am not only a better researcher because of your support, I am a better person. I am so proud of you both. May you find continued success and happiness.

To my support group in the Lenert and Schwank labs. Past members of the Schwank lab such as Dr. Xiaoyin Chen, Dr. Lei Ma and Dr. Chang Yup Seo have been instrumental in developing my catalytic synthesis, characterization, and evaluation skills. Thank you, Prof. Galen Fisher, for always providing valuable contributions to research ideas, experiments, and manuscripts. You have a very critical eye, albeit with a dash of cheekiness, which has always made our discussions fruitful and interesting. It has been a pleasure to collaborate with you. I would also like to acknowledge Dr. Adarsh Bhat in particular. Thank you, Adarsh, for always being a reservoir

of encouragement, knowledge, and enjoyment in the lab. What began as a professional working relationship really blossomed into an incredible friendship. My research and practical skills have grown through our collaboration, and it was always a pleasure being able to share the office and lab with you. To the past members of the Lenert lab; Tobias and Hannah. Thank you for inspiring me to join the lab and for taking me in and giving me nothing but encouragement and fun times. Coming to lab was made all the better by the example you set and the environment you created. Sean and Zach, I could not have imagined what this journey would have in store for us as three people living together who joined the same lab. I have seen you become such incredible researchers, mentors and teachers and I am so proud of the both of you. You have become some of my very best friends along the way. And to the future of the Lenert Lab. Bosun, you are an incredible leader, and you have a spark to you that has and will continue to push you to amazing heights. Areefa and Andrés, you have both learned so much and come so far. It has been a pleasure getting to know you both and I know that the lab is in very capable hands. I'm excited to see what the future holds for you. And to Carissa, my fellow Lenert–Schwank co–advisee. The care that you have, not only in the technical aspects of our research, but in ensuring it has a clear and meaningful vision is inspiring. You bring that care to every interaction you have with someone, whether they're your longest friend, or someone you just met. Keep going, you are well on your way. I would also like to acknowledge the undergraduate students who I have worked with during my time here; Tsz Yuet 'Matthew' Chow, Zheweng 'JD' Deng and Anna Klinger. I would like to thank the staff at the Michigan Center for Material Characterization (MC2), specifically Haiping Sun, Tao Ma and Kai Sun for their help with microscopy. It has been a great passion of mine to learn electron microscopy so thank you for making that a reality. Thank you, Prof. Bryan

Goldsmith and Prof. Charles McCrory, for serving on my committee and providing meaningful insights and suggestions throughout my PhD.

Now to my friends. While I have gained many great things during my PhD, the most important will always be the people I've come to know and love along the way. The first day I moved into our house in Ann Arbor one of my roommates Jacques said "My dad told me that his PhD days were some of the best of his life. I bet we're going to have a great time here". I keep pinching myself because I cannot believe how right he was. I have lived with some incredible individuals, Zach, Sean, Jacques, Connor, Patrick, Emily, Marshall, Mackenzie, and Alain. You have seen me at my highs and lows and have loved and encouraged me along the way. Thank you. I have of very large group of friends in addition to these roommates, Rachel, Zixuan, Tobias, Katey, Danielle, Misché, Harrison, Jordyn, Chrissy, my Ann Arbor Hockey teammates (Go Ice Cats, all paws in) and many, many more. And to my partner Anna, we're just getting started, I'm excited to see where things go for us. I am incredibly lucky to have been surrounded by so many work and class mates who have become some of my best friends. You have always been there, from the everyday things like staying up late doing homework or floating on the river, to the big things, like losing a grandparent. Your love has gotten me through some hard times and brought me to greater heights than I thought possible. I will always cherish the connections we have made.

To my family. My parents, Brian and Elizabeth have worked so hard to give me and my siblings everything we needed. No door was closed to us due to their sacrifices. I cannot express my gratitude to you. I have been very privileged to have spent a great deal of time with both during my PhD and it has been wonderful to see my relationship with you get stronger over these past five years. To my siblings, Allyson, Andrew and Chloe. Older or younger, I have always wanted to be like you when I grow up. Thank you for always being great inspirations. I came to the

University of Michigan in part because it was close to my extended family in Canada. Thank you for always welcoming me with open arms on long weekends and holidays. It has been a pleasure to reconnect with you. The importance of family has been very poignant in the last two years of my PhD as I lost my grandmother Josefina and my grandfathers, José and Poppa Bill. Along with my grandmother Momma Joyce, I would like to close my acknowledgments by expressing my gratitude to you.

Table of Contents

Dedication ii

Acknowledgements iii

List of Tables xi

List of Figures xii

Abstract xv

Chapter 1 : Introduction 1

1.1 Material utilization in catalyst systems 1

1.1.1 Definition and relevance 1

1.1.2 Catalyst activity and stability influence material utilization 3

1.2 Unfavorable restructuring impedes material utilization 8

1.2.1 Mechanisms of thermally induced sintering 10

1.2.2 Methods to mitigate unfavorable restructuring 12

1.3 Favorable restructuring as a pathway to improve material utilization 16

1.3.1 Hypothesized ingredients for favorable restructuring 17

1.3.2 Methods to achieve favorable restructuring 18

1.4 Thesis overview 22

1.4.1 Core@shell architectures for directed restructuring 22

1.4.2 Key metrics for evaluating effective material utilization 23

1.5 Thesis outline 24

1.6 References 28

Chapter 2 : Directing Nanoscale Restructuring Through Controlled Core@shell Architectures . 35

2.1 Motivation 35

2.2 Results and Discussion 36
2.2.1 Fresh catalyst synthesis and characterization 36
2.2.2 Fresh catalyst light-off performance 38
2.2.3 Effects of high-temperature aging 41
2.2.4 The role of core@shell encapsulation in restructuring 45
2.2.5 Contribution of reducibility to low-temperature activity gain in aged Pd@CeO_2 46
2.3 Conclusions 50
2.4 Experimental Details 51
2.4.1 Synthesis of conventionally supported Pd/CeO_2 nanospheres 51
2.4.2 Synthesis of core@shell nanoparticles 52
2.4.3 Catalyst aging 53
2.4.4 Catalytic testing parameters 54
2.4.5 Material characterization 56
2.5 References 58
Chapter 3 : Stabilizing Highly Dispersed Active Sites in Favorably Restructured Core@Shell Catalysts 62
3.1 Motivation 62
3.2 Results and Discussion 65
3.2.1 Defining model catalyst systems 65
3.2.2 Identifying activity limits through cycled aging 68
3.2.3 Adverse restructuring in conventionally prepared Pd/CeO_2 70
3.2.4 Metastability of halo sites in Pd@SiO_2 72
3.2.5 Performance and stability of halo sites in Pd@CeO_2 75
3.2.6 Understanding the role of support reducibility on halo site stability 82
3.3 Conclusions 85
3.4 Experimental Details 86
3.4.1 Synthesis of surface-impregnated (conventionally supported) Pd/CeO_2 86
3.4.2 Synthesis of core@shell catalysts 86
3.4.3 Catalyst aging 87

3.4.4 Catalyst testing parameters 88
3.4.5 Material characterization 89
3.5 References 90
Chapter 4 : Regenerating Catalytic Performance and Dispersed Sites Through Favorable Restructuring 95
4.1 Motivation 95
4.2 Results and Discussion 99
4.2.1 The role of 800°C pretreatment on catalyst stability at 1000°C 99
4.2.2 Regenerating activity and dispersed sites through intermediate 800°C aging 103
4.2.3 Ce^{3+} trap site density influences regeneration efficacy 105
4.2.4 General mechanism of agglomeration and regeneration 109
4.2.5 Catalyst performance in the co-oxidation of CO and C_3H_8 112
4.3 Conclusions 117
4.4 Experimental Details 119
4.4.1 Synthesis of model core@shell catalysts 119
4.4.2 Catalyst aging 119
4.4.3 Catalytic testing parameters 120
4.4.4 Material characterization 121
4.5 References 122
Chapter 5 : Favorable Restructuring in Monometallic Au@CeO_2 and Bimetallic AuPd@CeO_2 core@shell catalysts 127
5.1 Motivation 127
5.2 Results and Discussion 129
5.2.1 Defining model nanoparticle systems 129
5.2.2 Absence of redispersion in Au@CeO_2 nanoparticles 132
5.2.3 Co–redispersion of Au and Pd in bimetallic AuPd@CeO_2 nanoparticles 136
5.2.4 Proposing a mechanism for bimetallic restructuring 140
5.3 Conclusions 143
5.4 Experimental details 143

5.4.1 Synthesis of monometallic Au@CeO_2 and bimetallic AuPd@CeO_2 nanoparticles ... 143
5.4.2 Aging parameters ... 144
5.4.3 Material characterization ... 144
5.5 References ... 145
Chapter 6 : Conclusions and Future Work ... 149
6.1 Conclusions ... 149
6.2 Developing a predictive redispersion model ... 150
6.3 Stabilizing the CeO_2 support to retain trap site density ... 155
6.4 Elucidating the mechanisms of bimetallic redispersion ... 156
6.5 Generalizing and scaling the synthesis of core@shell catalysts ... 157
6.6 Applying encapsulation to other catalytic systems ... 160
6.7 References ... 164

List of Tables

Table 2.1. Summary of surface area, average pore size, light-off performance and activity post O_2-cut ($time_{50}$), as fresh and after 800°C O_2-aging. 39

Table 2.2. Surface Pd content and catalyst analysis derived from pulsed CO chemisorption experiments for fresh and aged $Pd@SiO_2$ and $Pd@CeO_2$. 44

Table 2.3. Surface Pd content and catalyst analysis derived from pulsed CO chemisorption experiments for fresh and aged $Pd@SiO_2$ and $Pd@CeO_2$. 45

Table 3.1. Catalytic activity and structural features of samples as a function of aging cycle. 68

Table 3.2. Lattice oxygen release from conventional Pd/CeO_2 and core@shell $Pd@CeO_2$ catalysts. 70

Table 3.3. Oxygen composition for conventional Pd/CeO_2 and core@shell $Pd@CeO_2$ catalysts. 79

Table 4.1. Apparent activation energy (E_a) for CO oxidation. 101

Table 4.2. Summary of average CeO_2 crystallite and sintered Pd nanoparticle size. 103

Table 4.3. Summary of Pd and Ce oxidation states for Pretreated and Control $Pd@CeO_2$ as a function of aging condition. 107

Table 4.4. T_{90} summaries for CO and C_3H_8 oxidation in single and co-fed oxidation conditions. 113

Table 5.1. Oxidation state distribution of Au in fresh and aged $AuPd@CeO_2$ nanoparticles.... 142

Table 6.1. Ce^{3+} abundance and specific surface area for CeO_2 nanospheres aged at a variety of temperatures. 153

List of Figures

Figure 1.1. A top-down view of two configurations of 15 metal (M) atoms on a CeO_2 support. . 2

Figure 1.2. The need for material utilization in automotive emissions control. 3

Figure 1.3. Mars van Krevelen mechanism for CO oxidation on a CeO_2–supported catalyst..... 5

Figure 1.4. Sintering of catalytic nanoparticles. 9

Figure 1.5. Particle migration and Ostwald ripening sintering mechanisms. 11

Figure 1.6. Chemical methods for mitigating unfavorable restructuring. 12

Figure 1.7. Physical methods for mitigating unfavorable restructuring. 14

Figure 1.8. Ingredients for favorable restructuring. 18

Figure 1.9. Transmission electron microscopy (TEM) characterization of Pd/CeO_2 sintering. .. 21

Figure 1.10. Atom trapping Pd at undercoordinated Ce^{3+} sites. 22

Figure 2.1. Graphical overview of core@shell synthesis procedure. 37

Figure 2.2. Microscopy characterization of fresh and aged catalysts. 38

Figure 2.3. Performance of fresh and O_2 aged catalysts. 40

Figure 2.4. Crystallographic characterization of fresh and O_2 aged catalysts. 40

Figure 2.5. Oxidation state characterization of fresh and O_2 aged catalysts. 43

Figure 2.6. Recruitment of lattice oxygen for fresh and O_2 aged catalysts..... 47

Figure 2.7. Contributions of support reducibility to favorable restructuring. 49

Figure 3.1. Graphical overview of cycled aging study. 65

Figure 3.2. Distribution of Pd in initial and cycled catalysts. 67

Figure 3.3. Effects of cycled aging on Pd utilization and T_{90} for CO oxidation..... 69

Figure 3.4. Changes in Pd dispersion, average CeO_2 crystallite size, and BET surface area with cycled aging. 71

Figure 3.5. Characterization of active metal cores in Pd@SiO_2. 74

Figure 3.6. Effects of thermal aging on Pd oxidation state distribution. 78

Figure 3.7. Examining Pd distribution in aged Pd@CeO_2. 80

Figure 3.8. Graphical depiction of the restructuring of Pd@SiO_2 (a) and Pd@CeO_2 (b) catalysts. 82

Figure 3.9. Influence of aging in a reduced environment on Pd@CeO_2 structure and activity... 83

Figure 4.1. Graphical depiction of experimental approach used. 98

Figure 4.2. CO T_{90} (°C) for Control and Pretreated Pd@CeO_2 catalysts as a function of aging condition. 100

Figure 4.3. STEM and EDS characterization of Pretreated and Control Pd@CeO_2 after 1000°C sintering and 800°C regeneration. 101

Figure 4.4. Average Pd nanoparticle and CeO_2 crystallite size for Pd@CeO_2 catalysts with aging condition. 102

Figure 4.5. Additional electron microscopy characterization of Pretreated catalyst post regeneration (R1d-P). 104

Figure 4.6. STEM characterization of changing Ce^{3+} trap site abundance with average crystallite size. 106

Figure 4.7. Changes in oxidation state distribution as a function of aging condition. 108

Figure 4.8. Effect of aging temperature on restructuring outcome. 110

Figure 4.9. Light-off plots for CO and C_3H_8 oxidation in single and co-fed oxidation conditions. 114

Figure 4.10. In situ DRIFTS conducted under CO single fed and CO + C_3H_8 co-fed conditions. 116

Figure 5.1. Thermodynamics of oxidation for Au and Pd. 128

Figure 5.2. Mechanism of core and shell precursor formation. 130

Figure 5.3. STEM, EDS and high-resolution TEM characterization of fresh Au@CeO_2. 131

Figure 5.4. X-ray diffraction characterization of fresh and aged Au@CeO_2 and AuPd@CeO_2. 132

Figure 5.5. STEM and EDS characterization of fresh AuPd@CeO_2. 132

Figure 5.6. STEM and EDS characterization of Au@CeO_2 before and after ex situ aging. 133

Figure 5.7. STEM and EDS characterization of monometallic Au@CeO_2 aged at 800°C and 1000°C. 134

Figure 5.8. Characterization of Au@CeO_2 during in situ aging in the STEM. 135

Figure 5.9. STEM and EDS characterization of Au@CeO_2 before and after ex situ aging. 137

Figure 5.10. Additional STEM and EDS characterization of Au@CeO_2 after ex situ aging. ... 138

Figure 5.11. Characterization of AuPd@CeO_2 during in situ aging in the STEM. 139

Figure 5.12. XPS characterization of fresh and aged AuPd@CeO_2 nanoparticles in the Au4f core scan region. 141

Figure 6.1. Vision for applying a general descriptor to maximize the redispersion of active metal using thermally induced restructuring. 151

Figure 6.2. CeO_2 nanospheres aged at 550°C and 1000°C in air for 2 hours. 152

Figure 6.3. Ce^{3+} abundance as a function of specific surface area. 153

Figure 6.4. Proposed overview of predictive model. 154

Figure 6.5. Synthesized Ag@TiO_2 core@shell nanoparticles done in collaboration with Dr. Adarsh Bhat. 158

Figure 6.6. Au@CeO_2 synthesized according to a standard and 5x volumetrically scaled protocol. 160

Figure 6.7. Summary of Ag–TiO_2 catalyst restructuring. 161

Figure 6.8. Encapsulation promotes Ag stability at 800°C. 162

Abstract

Society relies on catalytic processes for many important chemical transformations, which has contributed to the increasing cost, scarcity, and demand for precious metals. Synthesis techniques can improve the utilization of these metals by controlling the catalyst structure. However, precisely designed structures often degrade during operation, as high-temperature (≥800°C) working conditions agglomerate active metal into large particles, in a process known as sintering. Sintering decreases the dispersion, or fraction of available active sites and, in turn, the activity and material efficiency. Consequently, there is significant interest in delaying or reversing the effects of high-temperature sintering to improve the dispersion and stability of catalytic sites.

This dissertation investigates how nanoscale architecture and aging conditions can direct the restructuring of catalytically active sites away from sintering and towards outcomes that improve metal dispersion, stability, and utilization. This is done through the development of a core@shell architecture, where a sintering–prone active metal core is encapsulated by a porous, metal oxide shell. Palladium (Pd) is used as the model active metal, because of its high cost and widespread use in industrial catalysis. Core@shell catalysts are investigated alongside catalysts prepared through conventional synthesis strategies that create architectures where active metal nanoparticles decorate the external surface of metal oxide supports. This comparison demonstrates that the trajectory of restructuring depends greatly on the initial nanoscale architecture.

Elevated temperature (800°C) aging redisperses active metal within core@shell catalysts. The redispersion is more pronounced, and nearly complete, when palladium is encapsulated by reducible ceria ($Pd@CeO_2$), as opposed to nonreducible silica ($Pd@SiO_2$). This difference in

redispersion is due to the participation of oxygen from the CeO_2 lattice, which promotes redispersion. Aging at 800°C increases dispersion from 33% to 88% in the Pd@CeO_2 system, improving catalytic performance by over two-fold. This result contrasts with the conventionally prepared catalysts, whose dispersion decreases from 31.8% to 10% under identical conditions.

The stability of these redispersed sites is examined through repeated aging at 800°C. Palladium continues to migrate in Pd@SiO_2 because of poor Pd–SiO_2 bonding, which leads to agglomeration. In contrast, redispersed sites formed in aged Pd@CeO_2 remain stable due to the interactions between palladium and the oxygen present in reducible CeO_2. The importance of palladium–oxygen bonding is studied by aging at temperatures (1000°C) that surpass the decomposition temperature of palladium oxide. Although 1000°C aging sinters dispersed palladium sites, these sites can be regenerated by returning to 800°C aging conditions. Consequently, redispersion and sintering can be described by the thermodynamics of palladium–oxygen bond formation and decomposition, respectively. This suggests a generalizable redispersion mechanism that relies on the thermally induced oxidation and disintegration of core metal into highly mobile species. The generalizability of this approach is investigated using a Au@CeO_2 catalyst, as gold exhibits much poorer oxidation thermodynamics when compared to palladium. While metals with unstable oxides, such as gold, do not redisperse at high temperatures, alloying such elements with readily dispersible metals facilitates the redispersion of both species.

Altogether, this dissertation develops the relationship between nanoscale structure, aging conditions, and restructuring outcomes. The findings presented provide guidelines on how controlled thermal energy inputs can create high dispersions of stable, catalytically active sites. These protocols are simple and require little intervention, which makes them attractive as highly scalable synthesis techniques or protocols that can regenerate catalyst performance on-stream.

Chapter 1 : Introduction

1.1 Material utilization in catalyst systems

Small, active metal particles on porous oxide supports are integral to the success of many catalytic processes such as environmental remediation,[1–3] fuel and commodity chemical production,[4–6] and energy generation.[7,8] Precious and platinum group metals (PGMs) have been widely adopted as active metals in industrial catalysis, due to their high activity in the aforementioned applications. Increasing demand for industrial catalysts has contributed to rising cost and scarcity of precious metals and PGMs. As the market share for precious metal and PGM-based catalysts is predicted to grow in the years to come, it is vital that future catalyst designs effectively use the active metal content.

1.1.1 Definition and relevance

Effective material utilization in catalysis is typically described as atom efficiency; the more precious metal atoms that are accessible to reactants (e.g., gas-phase molecules), the more effective the utilization of that costly metal. Figure 1.1 schematically describes this by comparing two configurations of 15 metal (M) atoms supported on a CeO_2 surface. 15 atoms are stacked together as a nanoparticle in Figure 1.1a, whereas the same 15 atoms are spread over the CeO_2 support as an ensemble in Figure1.1b. The ensemble has all 15 atoms accessible to gas phase reactants, while the nanoparticle has metal atoms buried within its structure. Consequently, (a) is not as atomically efficient as the configuration in (b) and can be considered poorer in its material utilization. The ratio of active metal atoms that are accessible to gas-phase reactants compared to the total volume

of metal atoms is defined as the active metal dispersion. Catalysts that contain dispersions closer to 100% are considered better in their material utilization and often exhibit superior catalytic activities.[8,9]

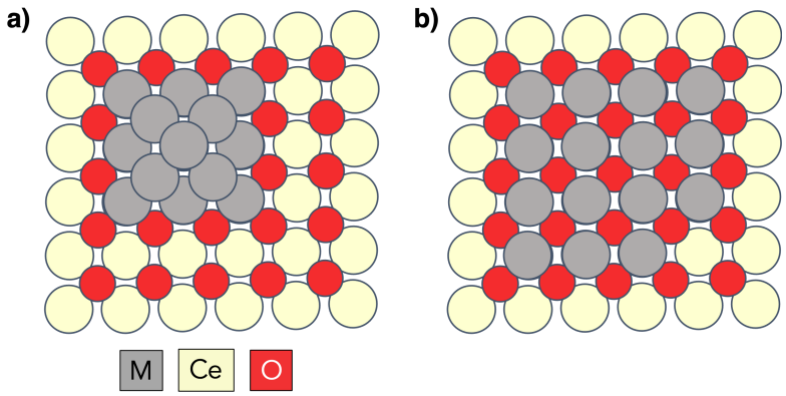

Figure 1.1. A top-down view of two configurations of 15 metal (M) atoms on a CeO_2 support. (a) 15 atoms stacked together as a nanoparticle and (b) 15 atoms spread over CeO_2 as an ensemble.

Current reports estimate a $35 billion USD market size value for industrial catalysts in 2020.[10] As environmental and sustainability standards continue to grow, the demand for high performing environmental remediation and renewable fuel production catalysts will increase. Consequently, the catalyst market size is expected to increase to $48 billion USD by 2027.[10] Given the kiloton quantities of metal used in catalytic processes, designing catalysts that contain high dispersions of active metal has significant industrial relevance.

Such goals are particularly relevant to automotive emissions control applications that must simultaneously manage wide windows of operating temperature, increasing costs of active metals (Pd, Pt and Rh), and regulations controlling emission quality.[2,11] As seen in Figure 1.2, the cost of PGMs used in catalytic converters are particularly volatile. This price volatility makes current practices of loading excess active metal content into catalytic converters undersirable, which are done to offset performance degradation. Although funding is being diverted from emissions control technologies towards electric vehicles, gasoline-powered vehicles are still predicted to

comprise a significant portion of the worldwide vehicular fleet (Figure 1.2).[12] This fact magnifies the need to improve material utilization within automotive emissions control.

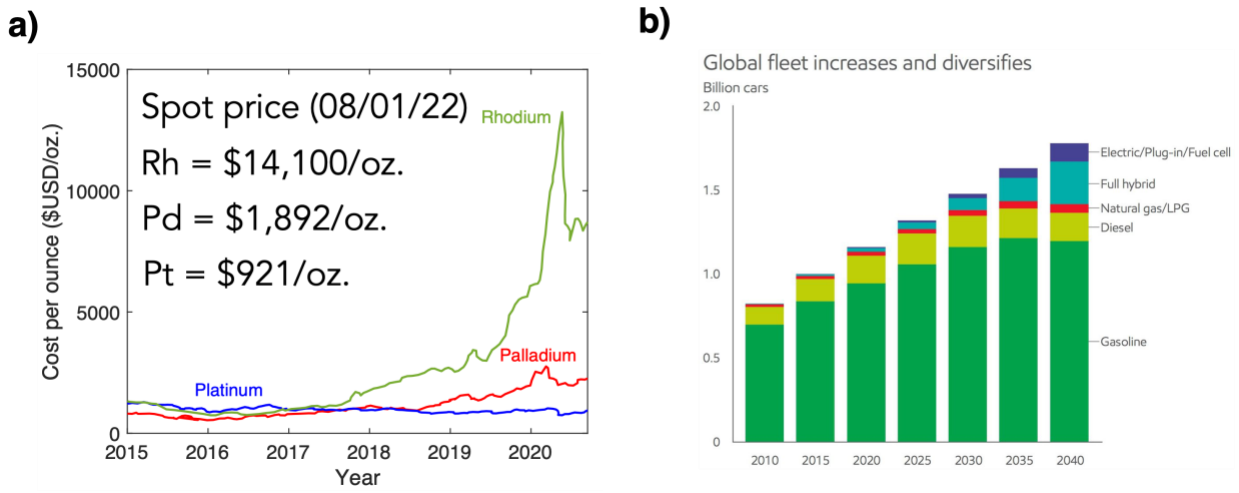

Figure 1.2. The need for material utilization in automotive emissions control.
(a) cost per ounce (in $USD) for Rh, Pd and Pt, the three most common active metals used in emission control technologies, including their spot prize as of 08/01/2022 and (b) the predicted vehicular fleet composition from 2010–2040, adapted from ExxonMobil.

1.1.2 Catalyst activity and stability influence material utilization

Catalyst functionality often depends very strongly on nanoscale morphology. As previously mentioned, dispersion is a key indicator of catalyst performance, with more dispersed active metal sites typically resulting in superior catalytic activity.[13] Maintaining high dispersion is particularly relevant for oxidation catalysts, which are used in many environmental remediation applications such as volatile organic compound and automotive emissions control.[14–16]

Catalytic oxidation activity can be improved when highly dispersed active metal sites are supported on a reducible oxide. The high activity of these materials is derived from mechanisms that use lattice oxygen contained in the support to perform oxidation, due to the ability of the reducible oxide to transition in oxidation state.[17,18] Such mechanisms are referred to as Mars van Krevelen (MvK) oxidation. The participation of lattice oxygen from the reducible oxide support provides a lower energy pathway for oxidation by avoiding the dissociative adsorption of gas-

phase O_2, which is integral in the Langmuir-Hinshelwood mechanisms that occur on non-reducible oxide supports such as SiO_2. Oxygen removed from the support lattice through MvK mechanism leaves an oxygen vacancy (O_{vac}). These vacancies can be replenished from O_2 present in the gas phase with lower energetic penalties.[17,19] A range of studies have emphasized the importance of the active metal–support interface for mediating these MvK oxidation pathways.[20,21] Active metal cluster size has been generally seen to scale inversely with oxidative activity on CeO_2–supported catalysts, because smaller active metal clusters display a higher proportion of interfacial contact sites, with respect to their volume, that can access highly active MvK oxidation pathways.[20] The size of the reducible oxide support domains also affect the ease of abstracting lattice oxygen. Smaller reducible oxide support particles exhibit greater densities of step, edge and defect sites, which can more readily donate oxygen through MvK mechanisms.[22–24] The MvK mechanism, using CO oxidation as a probe reaction, is described in Figure 1.3 and the equation below. The '*' denotes a reactant or product that has been adsorbed to the catalyst surface.

$$CeO_2 \leftrightarrow CeO_{2-x} + O*$$

$$CO_g \leftrightarrow CO*$$

$$CO* + O* \rightarrow CO_2*$$

$$CO_2* \rightarrow CO_{2_g}$$

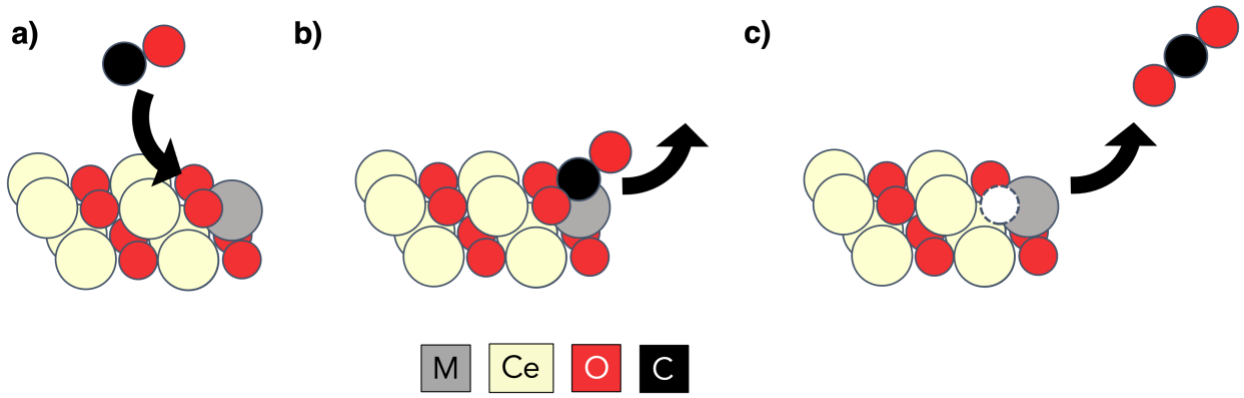

Figure 1.3. Mars van Krevelen mechanism for CO oxidation on a CeO_2–supported catalyst.
(a) A target reactant such as CO adsorbs at the metal–support interface. (b) Oxygen can be provided by the reducible CeO_2 lattice instead of by the gas phase. (c) This lattice oxygen is used to conduct catalytic oxidation, which leaves an oxygen vacancy on the support lattice. Such vacancies are replenished by gas phase O_2 with low energetic requirements.

Reducible oxide supports have been relevant in the automotive industry for a number of decades because of their oxygen storage-release capacity (OSC), which can supplement catalytic activity when the air/fuel ratio in gasoline vehicles oscillates.[25] Early work with CO oxidation over Rh/CeO_2[26] and Pd/CeO_2[27] catalysts in the absence of gas phase oxygen provided evidence that high amounts of CO_2 can be produced by the migration of oxygen from the support to the metal, through MvK oxidation mechanisms. A range of studies of CeO_2-supported catalysts have examined how this leads to high activity and high turnover frequencies.[17,18,20,28,29] CeO_2, owing to its facile transition from a Ce^{4+} to Ce^{3+} oxidation state, has become one of the most widely used reducible oxides in emission control catalysts.[18,28,30] As these mechanisms occur strictly at the active metal–support interface, high dispersions simultaneously increase the fraction of reactant-accessible sites and the use of lattice oxygen through MvK oxidation. This results in high material utilization.

Single atom catalysts (SACs) use single atoms of metal on a supporting material as active sites. SACs, which have emerged over the last decade,[31–33] exhibit a number of properties that make them attractive for addressing material utilization challenges.[32,34] Their 100% dispersion

results in perfect atom efficiency and their isolated nature leads to electronic properties that differ from bulk nanoparticles. This can lead to improved catalytic activity and selectivity to target products.[35,36] In catalytic oxidation, the active sites of SACs directly interact with reducible oxide supports such as CeO_2.[37,38] The electronic nature of a single atom site has also been found to improve the ease of extracting lattice oxygen from a reducible oxide support, which promotes catalytic oxidation activity.[39,40] Conventional SAC preparation strategies are limited to low metal loadings to ensure single atoms do not aggregate into larger nanoparticles during synthesis. Several techniques have emerged to address such challenges. Examples include wet chemistry methods such as strong electrostatic adsorption,[34] dispersing metals with short thermal pulses,[41] and chemical treatments with halogenated compounds.[42] Atom trapping methods, which use thermal aging to redisperse single atoms from larger nanoparticles, are of particular interest and will be discussed in more detail in *Section 1.3*.

It is important to note that although SACs exhibit good material utilization in well-controlled probe reactions such as CO oxidation, their efficacy in application-relevant conditions is often limited. A catalyst must fulfil a series of fundamental steps to complete a catalytic cycle. The cycle can be simplified into the following four steps:

1. Reactants transport, typically through the gas or liquid phase, to active sites where they adsorb through electrostatic attraction.
2. Adsorption perturbs the electronic structure of the reactant, which weakens the strength of its chemical bonds, thereby allowing reactions to proceed with lower energetic requirements.
3. Once a reactant has been converted to a product, it desorbs from the catalyst surface.

4. After desorption, the catalyst restores its active site if has been altered during reaction. One example is replenishing an O_{vac} in the case of MvK oxidation. With a restored active site, the catalytic cycle is complete.

If any of these steps are perturbed, the catalyst will begin to lose its activity. As previously mentioned, SACs exhibit improved activity due to their high dispersion that increases reactant adsorption. SACs also exhibit unique electronic properties in comparison to bulk particles, as there are no neighboring atoms to distribute electron density. The highly localized electron density on single atoms, however, can increase the strength of reactant adsorption. This can cause adsorbates to interact with an active site so strongly that they are essentially blocked from conducting reactions. This process, which is referred to as poisoning, impedes catalytic activity.[43,44]

Poisoning is problematic in applications such as emissions control, which must effectively oxidize both CO and un-combusted hydrocarbons (HCs).[2,45] These two reactants can adsorb on the same active sites, which results in competitive adsorption. Single atom sites exhibit poor adsorption-desorption of HCs such as C_3H_8, due to their highly localized electron density.[46,47] As such, larger HC intermediates can block the availability of active sites for CO oxidation, which impedes catalytic performance.[9,47] Larger metal particles can effectively adsorb and react HCs, despite having lower dispersion than SACs, due to their larger ensembles of atoms that more effectively distribute electron density.[11,47,48] As such, active metal dispersion must be considered alongside other parameters such as reaction composition and reactant adsorption energy to inform the most appropriate catalyst structure. To this end, there has been an extensive body of work done to develop structure–function relationships that can inform how active metal and support material choice, in addition to catalyst morphology, affect performance and material utilization.

The maturation of synthesis strategies and structure–function relationships have informed the design of catalysts that exhibit improved material utilization for many applications.[2,49–51] A catalyst with a desired structure is not valuable however, if it cannot remain stable during extended periods of use. Many working conditions in industrial catalytic applications use elevated pressure, temperature, and adverse reactants, which can degrade the catalyst's structure. As such effective material utilization relies on designing catalysts with high performing and dispersed active sites, that exhibit appreciable structural stability under the adverse conditions they are subjected to in application.

1.2 Unfavorable restructuring impedes material utilization

Although many basic definitions of 'catalyst' often contain a notion of being unchanged or unaltered, very few materials accomplish this in practice. High temperatures are used in many catalytic processes to improve reaction kinetics, which increases both catalytic turnover and product yield. In applications such as emissions control, where heat from the combustion engine is used to provide energy to the catalyst, temperatures can reach upwards of 1000°C.[2,52] This excess thermal energy facilitates catalyst restructuring, whereby the support and active metal components rearrange themselves in order to reach a more energetically favorable state.[53–55]

Dynamic nanoscale restructuring of catalysts is common in many industrial applications which involve high-temperature conditions during synthesis or operation and maintenance such as catalytic converters, fuel cells, and steam reforming.[2,56,57] In addition to its industrial relevance, studying catalyst restructuring at high temperatures also provides insight into long-term stability. Catalyst restructuring as a result of aging or operation at high temperatures (≥800°C) has significant effects on catalytic conversion and selectivity.[43,58–62] Most high-temperature restructuring processes result in unfavorable restructuring through active site agglomeration.[43,53]

This decreases metal dispersion and in cases where reducible oxide supports are used, the accessibility to MvK oxidation mechanisms. This effect is depicted in Figure 1.4 using six metal particles, each comprised of five atoms. Given this arrangement, 80% of the metal atoms (24/30) interface directly with the reducible support. Should these particles agglomerate into a single structure (Figure 1.4b), the number of metal atoms with interfacial contact would be cut in half to 40% (12/30). The loss of interfacial sites and metal dispersion significantly impedes catalytic performance.[43,53] The process of agglomerating dispersed active sites into large particles is referred to as sintering.

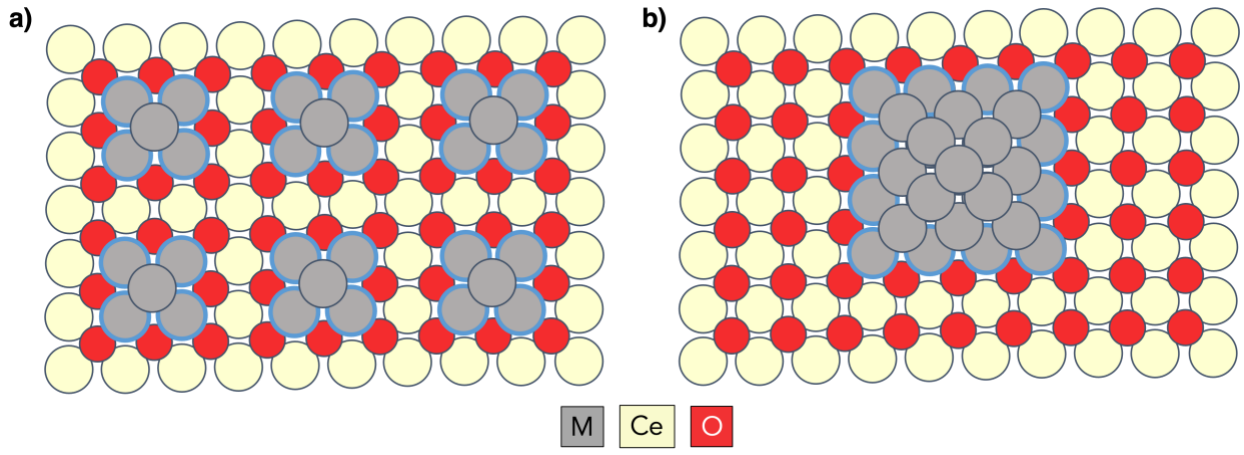

Figure 1.4. Sintering of catalytic nanoparticles.
(a) A highly dispersed catalyst containing small nanoparticles of a metal 'M' on a reducible CeO_2 support, with interfacial sites outlined in blue. Should these highly dispersed particles agglomerate into a single particle as shown in (b), the number of M–CeO_2 interfacial sites and total sites available for reaction would decrease.

Thermally activated sintering[63–65] is a major challenge in the context of automotive emissions control, as catalyst manufacturers typically incorporate higher loadings of PGMs such as Pd, Pt and Rh in order to offset the effects of adverse restructuring processes. PGM overloading practices are quite problematic, however, as discussed above. Deactivation has motivated significant research in understanding the mechanisms of unfavorable restructuring to enhance the thermal stability of catalytic materials, *i.e.*, to make active components less prone to sintering and retain their intended nanoscale structure. Advancements in stabilizing highly active arrangements

of metal would decrease the industrial reliance on methods such as overloading, which would significantly improve material utilization and decrease costs.

1.2.1 Mechanisms of thermally induced sintering

Sintering is a thermodynamically favorable process as small active metal and support domains exert greater surface energy when compared to agglomerated particles.[66,67] Sintering of active metal particles occurs through two widely accepted mechanisms: (1) particle migration and coalescence and (2) Ostwald ripening.[43,53] Particle migration and coalescence is defined by the movement of whole particles towards one another. Once in contact, particles will rearrange their atoms to form a larger cluster, which minimizes their surface energy. Ostwald ripening describes the growth of particles through the emission and transport of atomic species known as adatoms. Adatoms are emitted by particles, transport on the surface or through the gas phase (if their vapor pressure is high enough), and are eventually captured by larger particles, resulting in agglomeration. These two sintering mechanisms are depicted in Figure 1.5.

The likelihood of Ostwald ripening is influenced by the ease of abstracting an adatom from a larger particle. The gases and reactants present during elevated temperature exposure can readily influence adatom emission. Reactants such as CO and NO, which are typically found in emission control applications, can adsorb to the surface of metal particles. This adsorption can destabilize the bonds that anchor the active metal to its neighboring atoms. Combined with the thermal energy provided through high-temperature aging or operation, adatoms can be emitted as mobile metal–adsorbate complexes.[60,61,68] Oxygen can also facilitate adsorbate-induced disintegration of particles.[69–71] It is important to note that emitted adatoms can transport themselves either along the surface of the underlying support, or through the vapor phase, which promotes Ostwald ripening through the evaporation of metal atoms from clusters.[72,73] Oxygen can promote evaporation as

many metal oxide species exhibit higher vapor pressures than their native metal counterparts.[74,75] The mobility of adatom species can be leveraged to redisperse bulk particles into highly dispersed atomic sites, as discussed in Section 1.3.

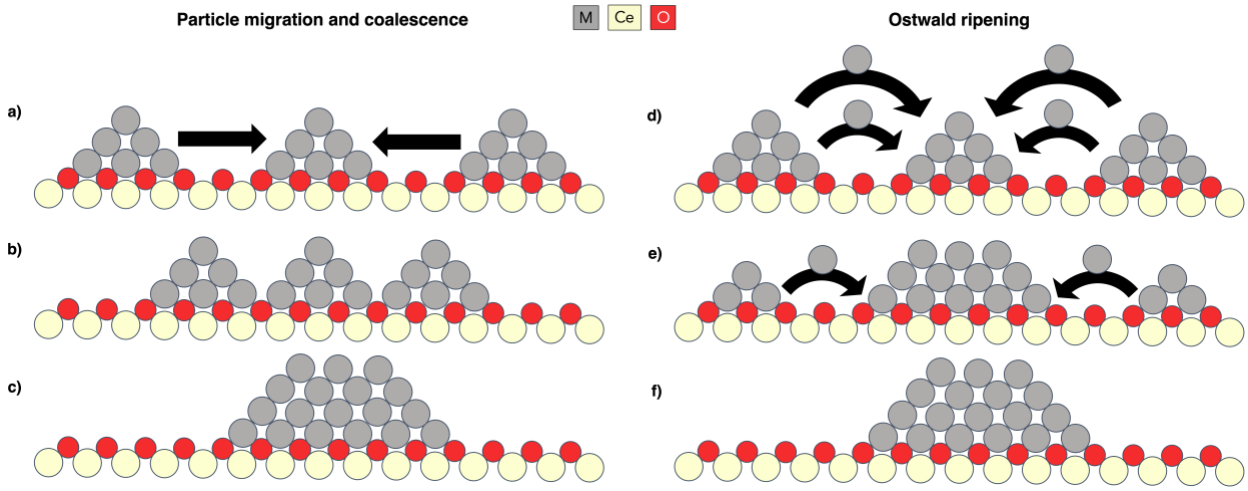

Figure 1.5. Particle migration and Ostwald ripening sintering mechanisms.
A side view of a collection of metal (M) particles undergoing particle migration and coalescence and Ostwald ripening on a reducible CeO_2 support. (a) Excess thermal energy can cause whole particles to move. (b) Once in contact with one another, particles will (c) rearrange their atomic configuration to adopt thermodynamically favorable states with minimized surface energy. (d) Excess thermal energy can also emit mobile adatom species from metal clusters, which causes them to shrink. (e-f) These adatom species can migrate, either through the gas phase or on the surface of the underlying support, and accumulate on the surface of metal particles, which results in agglomeration.

Particle migration mechanisms are mediated by temperature, particle size, adhesion to the support and particle proximity.[76] Elevated temperatures can weaken the cohesive forces that hold particles to support surfaces. This phenomena can be described by the Tamman and Hüttig temperatures, which are defined as the temperatures where bulk or edge atoms in a particle, respectively, start to exhibit mobility.[43,56,77] Once a particle has surpassed its respective Tamman (1/2 of the melting temperature) or Hüttig temperature (1/3 of the melting temperature), its atoms can wet the surface of their supports, which drives migration and diffusion. Larger particles have been shown computationally to exhibit higher detachment energies from their underlying support, which makes their whole migration less likely.[53,61] As such, smaller particles are more likely to become mobile. Small particles are typically deposited with high density on supports in industrial

catalysts to improve yield and overall performance. This can accelerate coalescence however, as particles are more likely to migrate and agglomerate when they are near one another.

1.2.2 Methods to mitigate unfavorable restructuring

Strategies that mitigate unfavorable sintering can be grouped into chemical methods that alter the chemistry of the active materials and physical methods use nanoscale architectures to provide physical barriers that inhibit metal mobility.[78] Chemical methods are summarized in Figure 1.6 and physical methods are summarized in Figure 1.7.

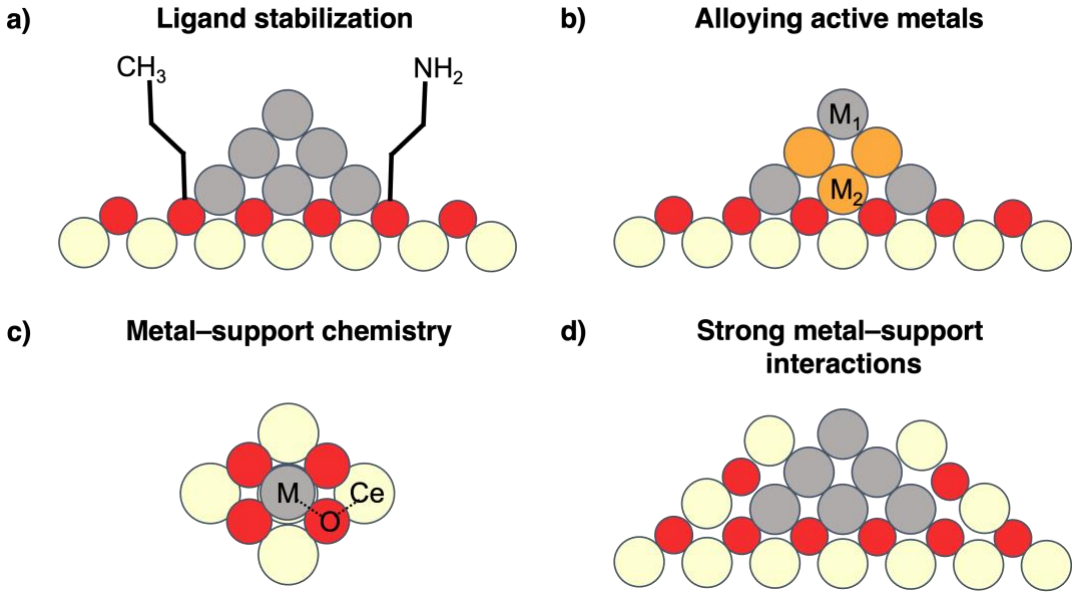

Figure 1.6. Chemical methods for mitigating unfavorable restructuring.

Chemical methods include chemically modifying the support or active particle surface with ligands, which can act as diffusion barriers or anchor metal species.[79,80] These methods can effectively inhibit the mobility of active metal species, however the thermal stability of ligands is relatively low. Once the ligands decompose, particles are free to migrate and can ultimately sinter. As such, ligand stabilization can only be used in catalytic applications that exhibit mild (<500°C) working temperatures.[81]

Alloying active metal species together can significantly change chemical properties. Though alloying can result in improved catalytic performance due to changes in electronic structure,[82] alloys can also exhibit altered thermal stability. Intermixing metals can change metal volatility and Tamman and Hüttig temperature limits. Alloying can also impede the ease of abstracting adatoms through Ostwald ripening processes. Recent work has shown that alloying small Pt nanoparticles with Sn increases the energy required to emit a mobile Pt.[83] This has also been demonstrated for when Pt is alloyed with Pd.[72] Datye *et. al.* have used the alloying of Pt and Pd to anchor rafts of PdO_x between highly dispersed single atoms of Pt that strongly coordinated to CeO_2 supports. The anchored rafts exhibit altered electronic properties, which promoted both stability and activity in CH_4 combustion.[84] Sintering is a thermodynamically favorable outcome due to the decreased system entropy when dispersed metal phases agglomerate into larger particles. Consequently, a chemical method of improving the sintering resistance of active metals is to insert them into a high-entropy alloy. These materials are defined as containing five or more elements that can crystalize into a singular phase.[85] This results in high configurational entropy, which provides intrinsic thermal stability. Pd was recently stabilized in a high entropy single-phase fluorite oxide containing equimolar amounts of Ce, Zr, Hf, Ti and La.[86] This material exhibited thermal stability up to 900°C and appreciable activity in a probe CO oxidation reaction, due to the reducible oxide chemistry conferred by Ce–O and Zr–O coordination.

Electronic interactions between the support and active metal phases can also improve sintering resistance. For example, the strong coordination of active metals (M) to reducible supports such as CeO_2 through M–O–Ce bonding impedes particle detachment and migration.[87] This type of bonding can stabilize both single atoms and whole particles on reducible CeO_2,[88,89] with the latter case occurring through M–O–Ce bonding at metal–support interfacial sites.[90] Metal

oxide supports can be coerced, through chemical treatment, to grow over active metal nanoparticles in what is referred to as a strong metal support interaction (SMSI). These overlayers can be tuned to either partially or completely encapsulate active metal particles, which can alter electronic structure, selectivity, and reactivity, and effectively anchor particles to their underlying support.[91,92]

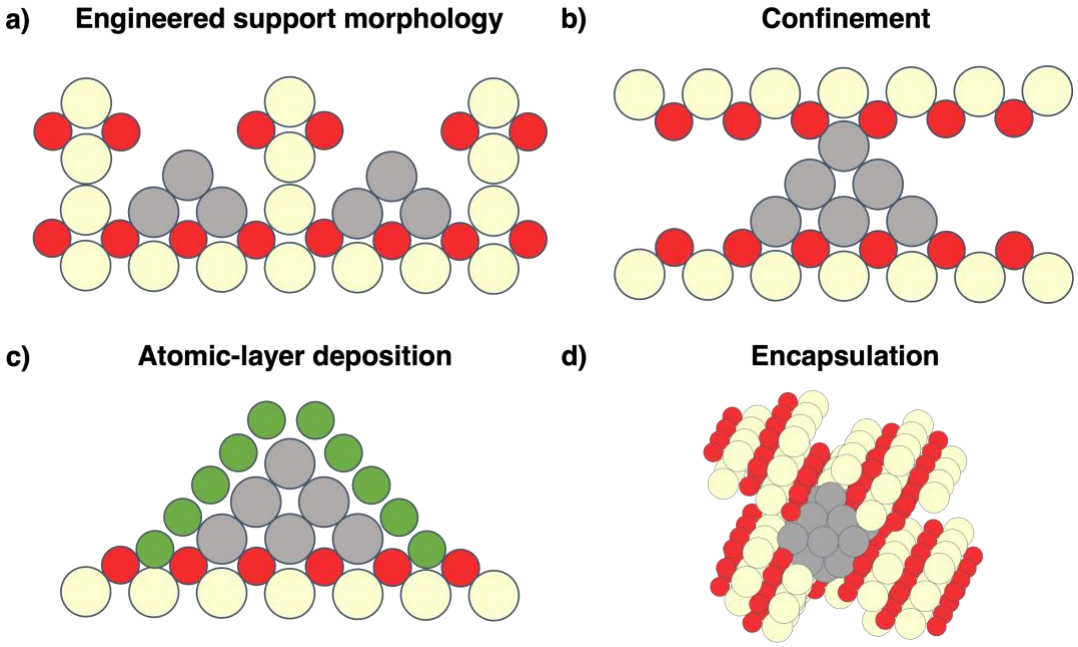

Figure 1.7. Physical methods for mitigating unfavorable restructuring.

Conventional catalyst supports have high surface areas to facilitate gas phase transport to active sites. These supports are typically decorated by active metal species through wet-impregnation techniques, as they volumetrically scale well to produce large quantities of catalyst. Catalysts prepared by these techniques, however, exhibit active particle densities that allow for particle agglomeration. Consequently, physical methods to mitigate sintering typically focus on nanoengineering the structure of the support to impede the accessibility that active metal species have to one another. Recent work by Liu *et. al.* demonstrated this by tuning the nanoscale morphology of SiO_2, which is a commonly used support in heterogeneous catalysis due to its appreciable thermal stability.[93] The use of SiO_2 supports with wide-mouthed pockets effectively

impeded Pt agglomeration in contrast to catalysts prepared by conventional wet-impregnation. The placement of Pt in the pockets effectively separated the particles from being able to interact and sinter. This notion of precisely identifying a critical distance for particle agglomeration has been the subject of recent work. As shown by Liang *et. al.*, the active metal loading, and structure of the support (porosity and surface area) can be tuned to ensure that the average particle-to-particle distance lies above a critical distance, d_c, under which particles can readily agglomerate.[94] Using this method, sintering was mitigated up to 900°C for a Pt/Carbon-black catalyst. The size of active metal particles can be tuned to match the pore size of the support to sterically-hinder active metals from migration. Particle stability at temperatures up to 600°C has been reported by matching pore and particle sizes.[95] It should be noted though, that while particles can remain within these pores, they can grow when exposed to elevated temperatures due to the emission and mobility of adatoms through Ostwald ripening.[96]

Confinement strategies have been further developed to include atomic layer deposition (ALD), which seek to coat active metal particles with conformal thin films. A variety of metal and metal oxide species can be deposited through ALD, which provides a high degree of tunability for creating overlayer structures that can anchor metal particles and in some cases, alter electronic structure (similar to SMSI overlayers) to improve catalytic performance.[97,98]

Encapsulating active metal particles wholly by their porous metal oxide supports, in what is known as a core@shell structure, has emerged as a promising method to mitigate unfavorable restructuring.[99,100] The explicit separation of active metal particles can impede particle accessibility to one another, thereby slowing sintering. This is particularly valuable if the encapsulating shell is a thermally robust support such as SiO_2. For example, Somorjai *et. al.* demonstrated that encapsulating Pt nanoparticles in mesoporous SiO_2 shells inhibited coalescence

and sintering at temperatures up to 750°C.[101] These types of encapsulating architectures also exhibit a variety of additional advantages that arise from careful pore tuning such as size-exclusion of poisoning compounds, and selective reactant orientation to enhance selectivity.[99,102,103] When reducible oxide supports are used, encapsulation has been shown to improve metal–support interfacial contact, which increases the density of perimeter sites that can participate in MvK oxidation.[104–106] This phenomenon is discussed further in Chapter 2. As such, encapsulation appears as a promising physical method for impeding sintering.

1.3 Favorable restructuring as a pathway to improve material utilization

Despite advancements in both physical and chemical methods to impede sintering in catalytic applications, dynamic catalyst restructuring is inevitable, given enough time on stream and/or sufficient operating conditions (e.g., temperature, reactants present, oxygen content). Consequently, there have been several efforts that seek to control or direct restructuring phenomena. As catalytic functionality is strongly dependent on morphology, strategic restructuring can be a promising way of enhancing the performance, stability and PGM utilization of catalysts. Favorable restructuring is defined here as catalyst restructuring that enhances overall activity by improving the dispersion of active metal species on support structures. Changes in morphology that arise from favorable restructuring are typically accompanied with changes to metal coordination and oxidation state chemistry, which can improve the stability of dispersed active sites. Conventional methods of preparing highly dispersed active sites require low metal loadings to minimize agglomeration during synthesis. This can decrease total catalyst activity and turnover when high product yields are required over short operation timeframes. Favorable restructuring, in contrast, focuses on the decomposition and redispersion of metal particles that are derived from catalysts with higher, industrially relevant metal loadings. Consequently, such

strategies are promising methods for synthesizing catalysts with highly dispersed and stable active sites. Favorable restructuring is also attractive for regenerating dispersion and activity once sintering on-stream has occurred, which readily addresses growing concerns over catalyst lifetime and material efficiency.

1.3.1 Hypothesized ingredients for favorable restructuring

Ostwald ripening mechanisms provide a source of highly mobile species through the disintegration and emission of adatoms from larger clusters. Many favorable restructuring methods are designed to take advantage of such mechanisms and interrupt Ostwald ripening processes and stabilize the mobile adatoms before they have an opportunity to agglomerate. Consequently, many favorable restructuring processes can be segmented into three key elements or ingredients, as depicted in Figure 1.8:

1. Driving forces: As in Ostwald ripening, there must be a driving force that facilitates particle disintegration and the emission of mobile adatom species.
2. Separation: Once mobile, adatom–adatom interactions must be minimized such that local agglomeration does not occur and atoms can settle in highly dispersed configurations.
3. Stabilization: Once a highly dispersion of active sites has been obtained, there must be sufficient interactions to minimize continued mobility and sintering during aging or time on stream.

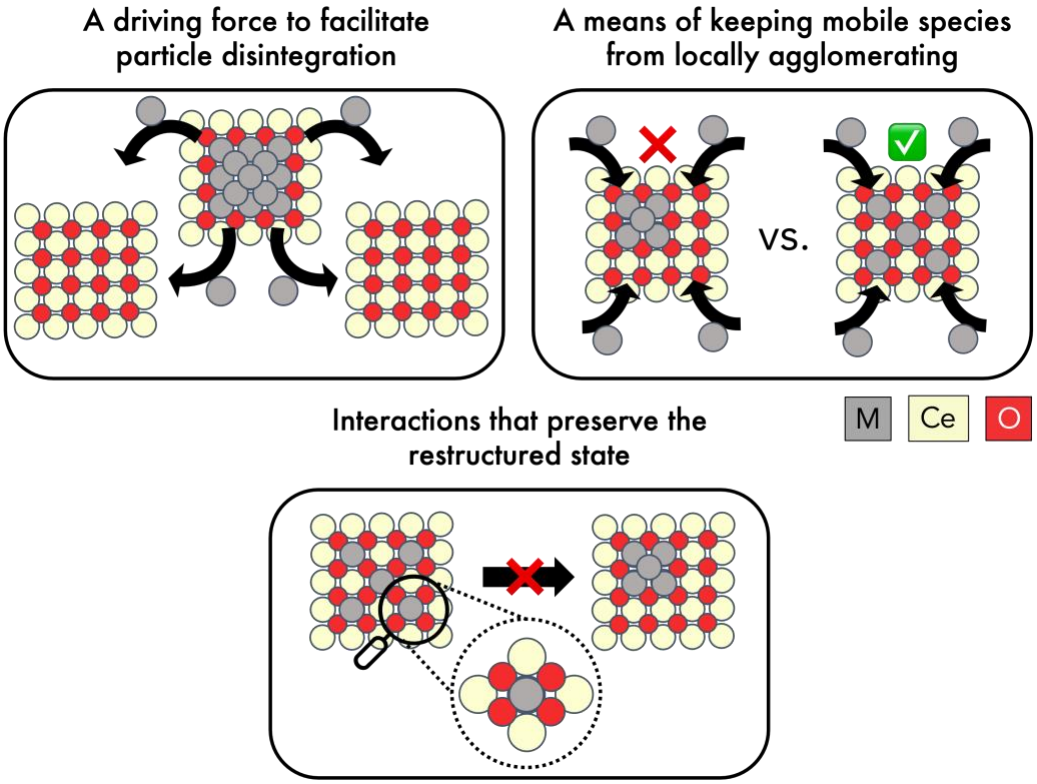

Figure 1.8. Ingredients for favorable restructuring.

1.3.2 Methods to achieve favorable restructuring

As outlined in several computational[107,108] and experimental[55,68,69,71,109] works, elevated temperature conditions can facilitate the disintegration of large active metal clusters into highly mobile adatom species. High temperature exposure is also advantageous, as strong metal–support bonds can be formed at temperatures ≥800°C.[110–112] Given the long times associated with conventional heating and cooling methods, however, elevated temperature exposure during pretreatment, aging, or operation, typically allows mobile adatoms to agglomerate as part of the Ostwald ripening process.[53] Several groups have investigated controlling aging conditions to favor rapid heating and cooling cycles to address such challenges. This can provide the necessary thermal energy to drive metal disintegration and fast migration without the long dwell times that promote agglomeration. As shown by Hu *et. al.*, high temperature pulses of 1500–2000K, held for 55 ms, redispersed Pt, Ru and Co on amorphous carbon, C_3N_4 and TiO_2 supports, which indicates

high generalizability. This group recently demonstrated that the temperature and dwell time can be modified to obtain some control over the redispersed particle size.

As described previously in Section 1.2, adsorbates can destabilize metal–metal bonds, which improves the ease of abstracting adatoms from larger clusters. Halide-based chemicals are particularly effective for adsorbate-induced disintegration, as the electronegative nature of the halide component strongly attracts active metal species.[113,114] For example, Sá *et. al* used a tandem thermal and methyl iodide treatment to redisperse Au supported on Al_2O_3, TiO_2 and SiO_2 to improve ethanol dehydration and benzyl alcohol oxidation.[113] Perez-Ramierez *et. al.* demonstrated that sequential HCl and C_2H_2 exposures could redisperse Ru, Rh and Ir clusters.[115] This occurred through a layer-by-layer method, whereby HCl chlorinates the surface, which perturbed metal–metal bonding such that adatoms could be removed through the formation of M–Cl–C_2H_2 complexes upon C_2H_2 exposure. The degree of redispersion was found to be tunable based on the number of HCl and C_2H_2 cycles deployed.

The dynamics of active metals under high-temperature, oxidizing conditions have been of particular interest, due to the adsorbate-induced disintegration that can occur during the oxidation of an active metal cluster.[53,72,107] Generating mobile adatoms through oxygen adsorption is attractive for driving favorable restructuring *in-operando*, as it relies on parameters which are readily controllable in many catalytic settings such as temperature and oxygen composition. Avoiding the use of halogenated compounds to facilitate adatom formation is also advantageous as such chemicals can carry adverse environmental and human health risks. This strategy particularly applicable to automotive emissions control catalysts as the air-to-fuel ratio can be readily adjusted on board a vehicle to favor oxidizing conditions.[116] This has been shown to recover a portion of sintered Pd species after mild aging at 700°C.[55] It should be noted that the dispersion

recovery was approximately 50% from the as–synthesized or 'fresh' state and that aging temperatures in application can be upwards of 1000°C. Given the growing cost and scarcity of catalytically active metal, it is important to improve the efficacy of active site regeneration through favorable restructuring. Another important factor to consider is that catalytically active metals have very different thermodynamics of oxidation. Pd for example, can be readily oxidized to PdO in the aging temperatures and oxygen partial pressures present in application.[75] Au on the other hand exhibits very poor thermodynamics of oxidation, requiring an oxygen partial pressure upwards of 10^{15} Pa when aged at 800°C. Consequently, the generalizability of this strategy remains to be seen.

Once a driving force has been applied to active metal particles, there must be a means of keeping active metal species from locally agglomerating. As aging temperatures ramp down and cool, the thermal energy for mobility and adatoms can condense on the surface of their support as agglomerates. Consequently, slower cooling rates typically result in more agglomeration. The rapid quenching of high temperature pulses ensure that mobile metal species do not have time to interact and sinter together.[41,117] Regarding adsorbate-induced disintegration methods, the complexation of active metal species with halogenated compounds slows the reformation of metal–metal bonds.[115,118] In oxygen mediated adsorbate-induced disintegration, phase transitions can be particularly helpful. Several works by Datye, Wang *et. al.* report the high temperature redispersion of Pt when aged at 800°C.[89,119,120] In these conditions, Pt readily volatilized into PtO_2, which could redeposit onto CeO_2 supports as single atoms. This process, which is referred to as 'atom-trapping', demonstrates a significant improvement in the degree of redispersion when compared to the previous example that investigated a Pd-based system.[55] Transport in the vapor phase effectively segregated mobile adatom species, which facilitated their redispersion as single atoms. It is important to note, however, that the vapor pressure of PdO (10^{-16} atm) is eight orders

of magnitude lower that PtO_2 (10^{-8} atm) when aged at 800°C in air.[74] As such, adatoms in Pd-based catalysts are unlikely to transport in the gas phase and instead transport via surface diffusion on their underlying supports. In contrast to adatoms transporting in the gas phase, adatoms that transport through surface diffusion can readily interact during high temperature mobility, which results in sintering. This is demonstrated through Figure 1.9, which shows transmission electron microscopy (TEM) characterization on a catalyst prepared through the wet-impregnation of Pd nanoparticles on the surface of CeO_2 nanospheres. The highly dispersed signal of Pd in the fresh state is indicative of small particles on the order of 3–5 nm in diameter. This highly dispersed signal becomes highly concentrated, which suggests agglomeration, despite being aged in identical conditions to the Pt atom-trapping works mentioned above. This suggests that the PdO adatoms in conventional catalyst morphologies have a high degree accessibility to one another and are unable to be readily redispersed. As such, alternative methods are required to facilitate the favorable restructuring of Pd-based catalysts, which are currently the most abundant active metal in emission control systems.

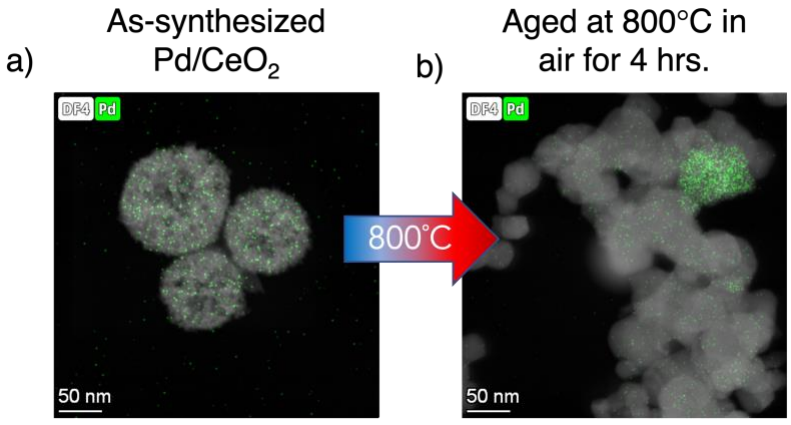

Figure 1.9. Transmission electron microscopy (TEM) characterization of Pd/CeO_2 sintering. A Pd/CeO_2 catalyst (a) prepared by wet-impregnating Pd nanoparticles on the external surface of CeO_2 nanospheres. (b) Upon aging at 800°C, the Pd and CeO_2 domains both agglomerate.

It's important to note that atom-trapping was found to not occur on a non-reducible Al_2O_3 support.[119] Supports with reducible characteristics, such as CeO_2, contain undercoordinated Ce^{3+}

sites, which exist at step, edge and defect sites on polycrystalline CeO_2. The smaller the CeO_2 crystallite, the richer it will be with these undercoordinated sites. These sites can accept oxygen present in a mobile adatom of PtO_2 or PdO, for example, to transition in oxidation state from Ce^{3+} to Ce^{4+}. In doing so, a strong chemical coordination referred to as an M–O–Ce interaction is formed (where M is a metal).[121,122] This process is depicted in Figure 1.10 below. The strong coordination with lattice oxygen results in improved thermal stability and accessibility to MvK mechanisms mediated at the metal–support interface.[89,120,123] This claim is supported by recent computational studies, which show that single atoms anchor themselves to Ce trap cites with high energies of adsorption.[124] As shown in Figure 1.9b, there is some signal of dispersed Pd on the sintered CeO_2 crystallites, however the primary restructuring outcome is sintering, likely due to the accessibility mobile Pd adatoms have to one another.

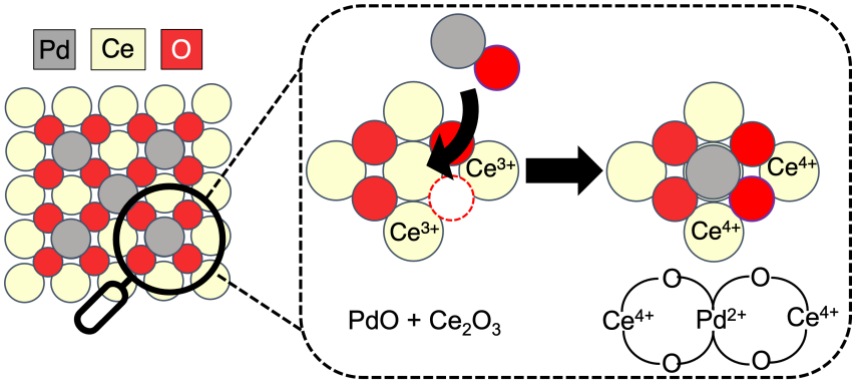

Figure 1.10. Atom trapping Pd at undercoordinated Ce^{3+} sites.

1.4 Thesis overview

1.4.1 Core@shell architectures for directed restructuring

As seen in several experimental works,[43,63] high temperature aging conditions unfavorably affect Pd-based catalysts. If restructuring could be directed towards favorable outcomes, however, the material utilization of this precious metal could be significantly improved. Emissions control catalysts, which rely on CeO_2 supports for promoting activity, are consistently exposed to high temperature and oxygen-rich conditions. As such, favorable restructuring through adsorbate-mediated disintegration and atom-trapping is particularly applicable. It is clear, however, that efforts to more effectively separate active metal domains during thermally induced mobility are required. Kwak *et. al.* used high temperatures to diffuse catalytically active noble metals (including Ni, Co and Cu) along the grain boundaries of host oxide supports.[125] Such reports allude to the role of catalyst morphology in directing thermally-driven active site restructuring. Consequently, this thesis investigates how initial catalyst morphology can be tuned to direct restructuring outcomes towards favorable results that improve activity, durability, and material utilization. Core@shell morphologies are a promising model architecture as their porosity, shell thickness, core size, core and support composition can be readily tuned. Should the distance between active metal cores be sufficiently large, it is expected that redispersion over sintering would occur during high temperature aging. This is especially true given the porous, tortuous nature of the encapsulating shell that adatoms transport through. Core@shell morphologies were demonstrated to be promising structural templates for directed restructuring in previous work from our group using a model $Pd@SiO_2$ catalyst, due to the ease of contrasting Pd against SiO_2 in TEM.[126] The work in this thesis seeks to build upon these findings to examine whether or not similar outcomes can occur in a $Pd@CeO_2$ system.

1.4.2 Key metrics for evaluating effective material utilization

Although the experimental details and key metrics used to draw conclusions are introduced in their respective chapters, this section overviews several key metrics that are used to evaluate effective material utilization throughout this thesis. CO oxidation serves as a probe reaction due to its relevance in industrial catalytic settings, such as vehicle emission control and preferential oxidation for renewable hydrogen production.[127–129] CO oxidation probe reactions can also extract structural information and examine the recruitment of lattice oxygen.[17,20,129] The temperature required for catalyst activation or 'light-off' is used as a standardized metric to evaluate activity. This is defined here as the temperature required for 90% target reactant conversion, or T_{90}. Such metrics are particularly relevant to automotive emissions control catalysts as the Department of Energy's US DRIVE program have aimed to decrease the T_{90} of criteria pollutants, such as un-combusted hydrocarbons (HCs) and carbon monoxide (CO), to below 150°C.[130] As such, lower T_{90} values are more desirable.

As previously described, dispersion is another key metric that defines material utilization. Active metal dispersion, as outlined in Chapter 2, is determined by adsorbate titration, specifically CO chemisorption. The greater the active metal dispersion, the greater the material utilization. Dispersion scales inversely with average Pd particle size, as such smaller Pd particles, as determined through chemisorption of x-ray diffraction experiments, are more desired. Smaller CeO_2 crystallites are similarly targeted as smaller crystals exhibit greater densities of steps, edges, and defects that contain Ce^{3+} trap sites.

1.5 Thesis outline

The research presented in this thesis seeks to understand and systematically direct metal mobility using a model core@shell nanoparticle system. Chapter 2 continues previous work in the group by examining the thermal restructuring behaviors of Pd@CeO_2 alongside Pd@SiO_2

catalysts. This study allows for direct comparison of reducible oxide ($Pd@CeO_2$) and non-reducible oxide ($Pd@SiO_2$) core@shell systems. In addition, comparison with Pd/CeO_2 illustrates the importance of core@shell morphology in separating active metal domains to promote redispersion. Chapter 2 finds that the initial nanoscale morphology influences the restructuring trajectory of a catalyst during high-temperature exposure. Specifically, encapsulating core@shell morphologies can indeed act as structural templates that direct favorable restructuring outcomes in conditions that would typically deactivate a catalyst. 800°C aging redisperses core Pd in as-synthesized $Pd@CeO_2$ and $Pd@SiO_2$ nanoparticles into highly dispersed sites. Chapter 2 quantifies the degree of redispersion and activity gain that arises from this favorable restructuring. This chapter reveals that incorporating a reducible CeO_2 shell dramatically improves the redispersion of highly dispersed Pd species and catalytic turnover by over two-fold. The contents of Chapter 2 have been published elsewhere, and reprinted with permission from ref.[131] Copyright 2020 American Chemical Society.

Favorable catalyst structures are not valuable if they cannot sustain their desired morphology during extended exposure to adverse conditions. As such, Chapter 3 evaluates the stability of favorably restructured $Pd@SiO_2$ and $Pd@CeO_2$. The role of the core@shell morphology as a restructuring template is further investigated. Encapsulation shifts the dominant thermal restructuring pathway away from whole particle migration to the emission-limited transport of smaller, mobile species. This transport process, coupled with the tortuous nature of the shell support, increases the likelihood that mobile species do not locally interact and agglomerate and instead become trapped on the support as sites with high dispersion and catalytic activity. While both SiO_2 and CeO_2 shells facilitate the formation of dispersed metal sites, the stability of these redispersed sites is determined by the underlying support. Only $Pd@CeO_2$ can

retain its favorable catalytic activity after sequential cycles of 800°C aging. Pd@SiO_2 in contrast, exhibits continued mobility of dispersed Pd during repeated aging, which results in agglomeration on the external surface of the SiO_2 shell support. The contents of Chapter 3 have been published elsewhere and reprinted with permission from ref.[123] Copyright 2021 American Chemical Society.

If sintering occurs, catalysts must be regenerated to recover the material. Techniques that can be deployed *in–operando* are particularly valuable as they avoid the cost associated with taking a deactivated catalyst off–stream for regeneration. Many of the strategies used to synthesize highly dispersed sites, however, are not applicable for *in–operando* regeneration as they require wet chemistry, specialized equipment, or halogenated compounds, which can have environmental risks. As such, Chapter 4 demonstrates that the favorable restructuring conditions described in Chapters 2 and 3 can effectively regenerate catalytic performance in sintered Pd-CeO_2 catalysts, through the breakup and partial redispersion of agglomerated Pd. The redispersion of Pd increases the abundance of sites that interface strongly with the CeO_2 support. These findings demonstrate that the thermodynamics of PdO formation and decomposition can effectively describe the conditions that result in sintering, and the conditions that result in redispersion and regeneration. Pretreating the catalyst at 800°C before sintering forms highly dispersed Pd species that slow the sintering of small, polycrystalline CeO_2 domains. This preserves the density of Ce^{3+} sites that trap mobile Pd, thereby improving the efficacy of regeneration. The regenerated catalyst is active in the co-oxidation of CO and C_3H_8, two species which are known to competitively adsorb. The simplicity of this 800°C thermal treatment makes it attractive for on-stream regeneration of catalyst performance.

Chapter 5 investigates the generalizability of favorable restructuring in core@shell morphologies. This is done through a model Au@CeO_2 system. Au@CeO_2 catalysts were found

to not favorably restructure during high temperature exposure. This outcome is expected due to the poor oxidation thermodynamics exhibited by Au nanoparticles, which decreases the likelihood of cluster disintegration redispersion without the use of an adsorbate such as a halogenated compound. Au was found to redisperse after aging however, when Pd was also present as AuPd@CeO_2. This provides an alternative strategy of redispersing noble active metal species that relies solely on temperature instead of temperature combined with chemical adsorbates, which can exhibit toxic or adverse environmental properties.

This thesis closes with Chapter 6, which summarizes key findings and identifies avenues for future work.

1.6 References

(1) Pardiwala, J. M.; Patel, F.; Patel, S. A Review on Catalytic Converter for Automotive Exhaust Emission. **2016**, *7* (2), 927–932.

(2) Datye, A. K.; Votsmeier, M. Opportunities and Challenges in the Development of Advanced Materials for Emission Control Catalysts. *Nat. Mater.* **2020**. https://doi.org/10.1038/s41563-020-00805-3.

(3) Shang, Y.; Xu, X.; Gao, B.; Wang, S.; Duan, X. Single-Atom Catalysis in Advanced Oxidation Processes for Environmental Remediation. *Chem. Soc. Rev.* **2021**, *50* (8), 5281–5322. https://doi.org/10.1039/D0CS01032D.

(4) Schroeder, E.; Christopher, P. Chemical Production Using Light: Are Sustainable Photons Cheap Enough? *ACS Energy Lett.* **2022**, *7* (2), 880–884. https://doi.org/10.1021/acsenergylett.2c00142.

(5) Zhang, F.; Li, Y.-H.; Qi, M.-Y.; Yamada, Y. M. A.; Anpo, M.; Tang, Z.-R.; Xu, Y.-J. Photothermal Catalytic CO2 Reduction over Nanomaterials. *Chem Catal.* **2021**, *1* (2), 272–297. https://doi.org/10.1016/j.checat.2021.01.003.

(6) Nash, C. P.; Dupuis, D. P.; Kumar, A.; Farberow, C. A.; To, A. T.; Yang, C.; Wegener, E. C.; Miller, J. T.; Unocic, K. A.; Christensen, E.; et al. Catalyst Design to Direct High-Octane Gasoline Fuel Properties for Improved Engine Efficiency. *Appl. Catal. B Environ.* **2022**, *301* (September 2021), 120801. https://doi.org/10.1016/j.apcatb.2021.120801.

(7) Wang, C.; Wang, S.; Peng, L.; Zhang, J.; Shao, Z.; Huang, J.; Sun, C.; Ouyang, M.; He, X. Recent Progress on the Key Materials and Components for Proton Exchange Membrane Fuel Cells in Vehicle Applications. **2016**. https://doi.org/10.3390/en9080603.

(8) Zhang, Z.; Li, H.; Wu, D.; Zhang, L.; Li, J.; Xu, J.; Lin, S.; Datye, A. K.; Xiong, H. Coordination Structure at Work: Atomically Dispersed Heterogeneous Catalysts. *Coord. Chem. Rev.* **2022**, *460*, 214469. https://doi.org/10.1016/j.ccr.2022.214469.

(9) Jeong, H.; Shin, S.; Lee, H. Heterogeneous Atomic Catalysts Overcoming the Limitations of Single-Atom Catalysts. *ACS Nano* **2020**, *14* (11), 14355–14374. https://doi.org/10.1021/acsnano.0c06610.

(10) Grand View Research. Catalyst Market Size & Share, Industry Report, 2020-2027; De Gruyter, 2020. https://doi.org/10.1515/9783110668483-202.

(11) Jeong, H.; Kwon, O.; Kim, B.-S.; Bae, J.; Shin, S.; Kim, H.-E.; Kim, J.; Lee, H. Highly Durable Metal Ensemble Catalysts with Full Dispersion for Automotive Applications beyond Single-Atom Catalysts. *Nat. Catal.* **2020**, *3* (4), 368–375. https://doi.org/10.1038/s41929-020-0427-z.

(12) Lambert, C. K. Current State of the Art and Future Needs for Automotive Exhaust Catalysis. *Nat. Catal.* **2019**, *2* (7), 554–557. https://doi.org/10.1038/s41929-019-0303-x.

(13) Wegener, S. L.; Marks, T. J.; Stair, P. C. Design Strategies for the Molecular Level Synthesis of Supported Catalysts. *Acc. Chem. Res.* **2012**, *45* (2), 206–214. https://doi.org/10.1021/ar2001342.

(14) Kamal, M. S.; Razzak, S. A.; Hossain, M. M. Catalytic Oxidation of Volatile Organic Compounds (VOCs) – A Review. *Atmos. Environ.* **2016**, *140*, 117–134. https://doi.org/10.1016/j.atmosenv.2016.05.031.

(15) Royer, S.; Duprez, D. Catalytic Oxidation of Carbon Monoxide over Transition Metal Oxides. *ChemCatChem* **2011**, *3* (1), 24–65. https://doi.org/10.1002/cctc.201000378.

(16) Lambert, C. Next Generation Three-Way Catalysts for Future , Highly Efficient Gasoline Engines. **2016**, 1–38.

(17) Puigdollers, A. R.; Schlexer, P.; Tosoni, S.; Pacchioni, G. Increasing Oxide Reducibility: The Role of Metal/Oxide Interfaces in the Formation of Oxygen Vacancies. *ACS Catal.* **2017**, *7*, 6493–6513. https://doi.org/10.1021/acscatal.7b01913.

(18) Montini, T.; Melchionna, M.; Monai, M.; Fornasiero, P. Fundamentals and Catalytic Applications of CeO_2-Based Materials. *Chem. Rev.* **2016**, *116* (10), 5987–6041. https://doi.org/10.1021/acs.chemrev.5b00603.

(19) Spezzati, G.; Benavidez, A. D.; DeLaRiva, A. T.; Su, Y.; Hofmann, J. P.; Asahina, S.; Olivier, E. J.; Neethling, J. H.; Miller, J. T.; Datye, A. K.; et al. CO Oxidation by Pd Supported on CeO_2 (100) and CeO_2 (111) Facets. *Appl. Catal. B Environ.* **2019**, *243*, 36–46. https://doi.org/10.1016/j.apcatb.2018.10.015.

(20) Cargnello, M.; Doan-Nguyen, V. V. T.; Gordon, T. R.; Diaz, R. E.; Stach, E. A.; Gorte, R. J.; Fornasiero, P.; Murray, C. B. Control of Metal Nanocrystal Size Reveals Metal-Support Interface Role for Ceria Catalysts. *Science (80-.).* **2013**, *341*, 771–773. https://doi.org/10.1126/science.1240148.

(21) Wang, Y. G.; Yoon, Y.; Glezakou, V. A.; Li, J.; Rousseau, R. The Role of Reducible Oxide-Metal Cluster Charge Transfer in Catalytic Processes: New Insights on the Catalytic Mechanism of CO Oxidation on Au/TiO_2 from Ab Initio Molecular Dynamics. *J. Am. Chem. Soc.* **2013**, *135* (29), 10673–10683.

https://doi.org/10.1021/ja402063v.
(22) Dong, C.; Zhou, Y.; Ta, N.; Liu, W.; Li, M.; Shen, W. Shape Impact of Nanostructured Ceria on the Dispersion of Pd Species. *Chinese J. Catal.* **2021**, *42* (12), 2234–2241. https://doi.org/10.1016/S1872-2067(20)63725-1.
(23) Lykaki, M.; Pachatouridou, E.; Carabineiro, S. A. C.; Iliopoulou, E.; Andriopoulou, C.; Kallithrakas-Kontos, N.; Boghosian, S.; Konsolakis, M. Ceria Nanoparticles Shape Effects on the Structural Defects and Surface Chemistry: Implications in CO Oxidation by Cu/CeO_2 Catalysts. *Appl. Catal. B Environ.* **2018**, *230*, 18–28. https://doi.org/10.1016/j.apcatb.2018.02.035.
(24) Paun, C.; Safonova, O. V.; Szlachetko, J.; Abdala, P. M.; Nachtegaal, M.; Sa, J.; Kleymenov, E.; Cervellino, A.; Krumeich, F.; van Bokhoven, J. A. Polyhedral CeO 2 Nanoparticles: Size-Dependent Geometrical and Electronic Structure. *J. Phys. Chem. C* **2012**, *116* (13), 7312–7317. https://doi.org/10.1021/jp300342b.
(25) Gandhi, H. S.; Graham, G. W.; McCabe, R. W. Automotive Exhaust Catalysis. *J. Catal.* **2003**, *216* (1–2), 433–442. https://doi.org/10.1016/S0021-9517(02)00067-2.
(26) Zafiris, G. S.; Gorte, R. J. Evidence for Low-Temperature Oxygen Migration from Ceria to Rh. *J. Catal.* **1993**, *139*, 561–567.
(27) Cordatos, H.; Gorte, R. J. CO, NO, and H_2 Adsorption on Ceria-Supported Pd. *J. Catal.* **1996**, *159* (1), 112–118. https://doi.org/10.1006/JCAT.1996.0070.
(28) Venezia, A. M.; La Parola, V.; Liotta, L. F. Structural and Surface Properties of Heterogeneous Catalysts: Nature of the Oxide Carrier and Supported Particle Size Effects. *Catal. Today* **2017**, *285*, 114–124. https://doi.org/10.1016/j.cattod.2016.11.004.
(29) McFarland, E. W.; Metiu, H. Catalysis by Doped Oxides. *Chem. Rev.* **2013**, *113* (6), 4391–4427. https://doi.org/10.1021/cr300418s.
(30) Li, P.; Chen, X.; Li, Y.; Schwank, J. W. A Review on Oxygen Storage Capacity of CeO_2-Based Materials: Influence Factors, Measurement Techniques, and Applications in Reactions Related to Catalytic Automotive Emissions Control. *Catal. Today* **2019**, *327* (February 2018), 90–115. https://doi.org/10.1016/j.cattod.2018.05.059.
(31) Qiao, B.; Wang, A.; Yang, X.; Allard, L. F.; Jiang, Z.; Cui, Y.; Liu, J.; Li, J.; Zhang, T. Single-Atom Catalysis of CO Oxidation Using Pt_1/FeOx. *Nat. Chem.* **2011**, *3* (8), 634–641. https://doi.org/10.1038/nchem.1095.
(32) Lang, R.; Du, X.; Huang, Y.; Jiang, X.; Zhang, Q.; Guo, Y.; Liu, K.; Qiao, B.; Wang, A.; Zhang, T. Single-Atom Catalysts Based on the Metal–Oxide Interaction. *Chem. Rev.* **2020**, *120* (21), 11986–12043. https://doi.org/10.1021/acs.chemrev.0c00797.
(33) Mitchell, S.; Pérez-Ramírez, J. Single Atom Catalysis: A Decade of Stunning Progress and the Promise for a Bright Future. *Nat. Commun.* **2020**, *11* (1), 4302. https://doi.org/10.1038/s41467-020-18182-5.
(34) Xiong, H.; Datye, A. K.; Wang, Y. Thermally Stable Single-Atom Heterogeneous Catalysts. *Adv. Mater.* **2021**, *2004319*. https://doi.org/10.1002/adma.202004319.
(35) Li, J.; Yang, Z.; Li, Y.; Zhang, G. Advances in Single-Atom Catalysts: Design, Synthesis and Environmental Applications. *J. Hazard. Mater.* **2022**, *429* (January), 128285. https://doi.org/10.1016/j.jhazmat.2022.128285.
(36) Lin, L.; Chen, Z.; Chen, W. Single Atom Catalysts by Atomic Diffusion Strategy. *Nano Res.* **2021**, *12* (1). https://doi.org/10.1007/s12274-021-3412-9.
(37) Zhang, H.; Fang, S.; Hu, Y. H. Recent Advances in Single-Atom Catalysts for CO Oxidation. *Catal. Rev.* **2020**, *00* (00), 1–42. https://doi.org/10.1080/01614940.2020.1821443.
(38) Beniya, A.; Higashi, S. Towards Dense Single-Atom Catalysts for Future Automotive Applications. *Nat. Catal.* **2019**, *2* (7), 590–602. https://doi.org/10.1038/s41929-019-0282-y.
(39) Lu, Y.; Thompson, C.; Kunwar, D.; Datye, A. K.; Karim, A. M. Origin of the High CO Oxidation Activity on CeO_2 Supported Pt Nanoparticles: Weaker Binding of CO or Facile Oxygen Transfer from the Support? *ChemCatChem* **2020**, *12*, 1726–1733. https://doi.org/10.1002/cctc.201901848.
(40) Jiang, D.; Wan, G.; García-Vargas, C. E.; Li, L.; Pereira-Hernández, X. I.; Wang, C.; Wang, Y. Elucidation of the Active Sites in Single-Atom Pd_1/CeO_2 Catalysts for Low-Temperature CO Oxidation. *ACS Catal.* **2020**, *10*, 11356–11364. https://doi.org/10.1021/acscatal.0c02480.
(41) Yao, Y.; Huang, Z.; Xie, P.; Wu, L.; Ma, L.; Li, T.; Pang, Z.; Jiao, M.; Liang, Z.; Gao, J.; et al. High Temperature Shockwave Stabilized Single Atoms. *Nat. Nanotechnol.* **2019**, *14*, 851–857. https://doi.org/10.1038/s41565-019-0518-7.
(42) Giulimondi, V.; Kaiser, S. K.; Agrachev, M.; Krumeich, F.; Clark, A. H.; Mitchell, S.; Jeschke, G.; Pérez-Ramírez, J. Redispersion Strategy for High-Loading Carbon-Supported Metal Catalysts with Controlled Nuclearity. *J. Mater. Chem. A* **2022**, No. ii. https://doi.org/10.1039/d1ta09238c.
(43) Argyle, M. D.; Bartholomew, C. H. Heterogeneous Catalyst Deactivation and Regeneration: A Review. *Catalysts* **2015**, *5*, 145–269. https://doi.org/10.3390/catal5010145.

(44) Wang, L.; Deo, S.; Dooley, K.; Janik, M. J.; Rioux, R. M. Influence of Metal Nuclearity and Physicochemical Properties of Ceria on the Oxidation of Carbon Monoxide. *Chinese J. Catal.* **2020**, *41* (6), 951–962. https://doi.org/10.1016/S1872-2067(20)63557-4.

(45) Zhou, R.; Xing, F.; Wang, S.; Lu, J.; Jin, L.; Luo, M. CO and C_3H_8 Total Oxidation over Pd/La-Al_2O_3 Catalysts: Effect of Calcination Temperature and Hydrothermal Treatment. *J. Rare Earths* **2014**, *32* (7), 621–627. https://doi.org/10.1016/S1002-0721(14)60117-4.

(46) AL-Harbi, M.; Hayes, R.; Votsmeier, M.; Epling, W. S. Competitive No, Co and Hydrocarbon Oxidation Reactions over a Diesel Oxidation Catalyst. *Can. J. Chem. Eng.* **2012**, *90* (6), 1527–1538. https://doi.org/10.1002/cjce.20659.

(47) Jeong, H.; Lee, G.; Kim, B.-S.; Bae, J.; Han, J. W.; Lee, H. Fully Dispersed Rh Ensemble Catalyst To Enhance Low-Temperature Activity. *J. Am. Chem. Soc.* **2018**, *140*, 9558–9565. https://doi.org/10.1021/jacs.8b04613.

(48) Luo, J.-Y.; Meng, M.; Zha, Y.-Q.; Guo, L.-H. Identification of the Active Sites for CO and C_3H_8 Total Oxidation over Nanostructured CuO−CeO_2 and Co_3O_4−CeO_2 Catalysts. *J. Phys. Chem. C* **2008**, *112* (23), 8694–8701. https://doi.org/10.1021/jp800651k.

(49) Abdulrasheed, A.; Jalil, A. A.; Gambo, Y.; Ibrahim, M.; Hambali, H. U.; Shahul Hamid, M. Y. A Review on Catalyst Development for Dry Reforming of Methane to Syngas: Recent Advances. *Renew. Sustain. Energy Rev.* **2019**, *108* (November 2018), 175–193. https://doi.org/10.1016/j.rser.2019.03.054.

(50) Mäki-Arvela, P.; Murzin, D. Y. Effect of Catalyst Synthesis Parameters on the Metal Particle Size. *Appl. Catal. A Gen.* **2013**, *451*, 251–281. https://doi.org/10.1016/j.apcata.2012.10.012.

(51) Munnik, P.; De Jongh, P. E.; De Jong, K. P. Recent Developments in the Synthesis of Supported Catalysts. *Chemical Reviews*. 2015, pp 6687–6718. https://doi.org/10.1021/cr500486u.

(52) Shelef, M.; McCabe, R. . Twenty-Five Years after Introduction of Automotive Catalysts: What Next? *Catal. Today* **2000**, *62* (1), 35–50. https://doi.org/10.1016/S0920-5861(00)00407-7.

(53) Hansen, T. W.; DeLaRiva, A. T.; Challa, S. R.; Datye, A. K. Sintering of Catalytic Nanoparticles: Particle Migration or Ostwald Ripening? *Acc. Chem. Res.* **2013**, *46*, 1720–1730. https://doi.org/10.1021/ar3002427.

(54) Wilson, J.; de Groot, C. Atomic-Scale Restructuring in High-Pressure Catalysis. *J. Phys. Chem.* **1995**, *99* (20), 7860–7866. https://doi.org/10.1021/j100020a005.

(55) Lupescu, J. A.; Schwank, J. W.; Dahlberg, K. A.; Seo, C. Y.; Fisher, G. B.; Peczonczyk, S. L.; Rhodes, K.; Jagner, M. J.; Haack, L. P. Pd Model Catalysts: Effect of Aging Environment and Lean Redispersion. *Appl. Catal. B Environ.* **2016**, *183*, 343–360. https://doi.org/10.1016/j.apcatb.2015.10.018.

(56) He, J.-J.; Wang, C.-X.; Zheng, T.-T.; Zhao, Y.-K. Thermally Induced Deactivation and the Corresponding Strategies for Improving Durability in Automotive Three-Way Catalysts. *Johnson Matthey Technol. Rev.* **2016**, *60*, 196–203. https://doi.org/10.1595/205651316X691960.

(57) Yao, X.; Wei, Y.; Wang, Z.; Gan, L. Revealing the Role of Surface Composition on the Particle Mobility and Coalescence of Carbon-Supported Pt Alloy Fuel Cell Catalysts by In Situ Heating (S)TEM. *ACS Catal.* **2020**, *10*, 7381–7388. https://doi.org/10.1021/acscatal.0c01765.

(58) Yu-Yao, Y. F.; Kummer, J. T. Low-Concentration Supported Precious Metal Catalysts Prepared by Thermal Transport. *J. Catal.* **1987**, *106*, 307–312.

(59) Baker, R. T. K. The Relationship between Particle Motion on a Graphite Surface and Tammann Temperature. *J. Catal.* **1982**, *78* (2), 473–476. https://doi.org/10.1016/0021-9517(82)90332-3.

(60) Goldsmith, B. R.; Sanderson, E. D.; Ouyang, R.; Li, W. X. CO- and NO-Induced Disintegration and Redispersion of Three-Way Catalysts Rhodium, Palladium, and Platinum: An Ab Initio Thermodynamics Study. *J. Phys. Chem. C* **2014**, *118*, 9588–9597. https://doi.org/10.1021/jp502201f.

(61) Ouyang, R.; Liu, J. X.; Li, W. X. Atomistic Theory of Ostwald Ripening and Disintegration of Supported Metal Particles under Reaction Conditions. *J. Am. Chem. Soc.* **2013**, *135* (5), 1760–1771. https://doi.org/10.1021/ja3087054.

(62) Zhang, S.; Chen, C.; Cargnello, M.; Fornasiero, P.; Gorte, R. J.; Graham, G. W.; Pan, X. Dynamic Structural Evolution of Supported Palladium-Ceria Core-Shell Catalysts Revealed by in Situ Electron Microscopy. *Nat. Commun.* **2015**, *6*, 1–6. https://doi.org/10.1038/ncomms8778.

(63) Xu, Q.; Kharas, K. C.; Croley, B. J.; Datye, A. K. The Sintering of Supported Pd Automotive Catalysts. *ChemCatChem* **2011**, *3* (6), 1004–1014. https://doi.org/10.1002/cctc.201000392.

(64) Al Soubaihi, R.; Saoud, K.; Dutta, J. Critical Review of Low-Temperature CO Oxidation and Hysteresis Phenomenon on Heterogeneous Catalysts. *Catalysts* **2018**, *8*, 660. https://doi.org/10.3390/catal8120660.

(65) Yang, J.; Tschamber, V.; Habermacher, D.; Garin, F.; Gilot, P. Effect of Sintering on the Catalytic Activity of a Pt Based Catalyst for CO Oxidation : Experiments and Modeling. *Appl. Catal. B Environ.* **2008**, *83* (3–4), 229–239. https://doi.org/10.1016/j.apcatb.2008.02.018.

(66) German, R. M. Thermodynamics of Sintering. In *Sintering of Advanced Materials*; Elsevier, 2010; pp 3–32. https://doi.org/10.1533/9781845699949.1.110.
(67) Campbell, C. T. The Effect of Size-Dependent Nanoparticle Energetics on Catalyst Sintering. *Science (80-.).* **2002**, *298* (5594), 811–814. https://doi.org/10.1126/science.1075094.
(68) Goodman, E. D.; Johnston-Peck, A. C.; Dietze, E. M.; Wrasman, C. J.; Hoffman, A. S.; Abild-Pedersen, F.; Bare, S. R.; Plessow, P. N.; Cargnello, M. Catalyst Deactivation via Decomposition into Single Atoms and the Role of Metal Loading. *Nat. Catal.* **2019**, *2*, 748–755. https://doi.org/10.1038/s41929-019-0328-1.
(69) Chin, Y. H. C.; García-Diéguez, M.; Iglesia, E. Dynamics and Thermodynamics of Pd-PdO Phase Transitions: Effects of Pd Cluster Size and Kinetic Implications for Catalytic Methane Combustion. *J. Phys. Chem. C* **2016**, *120*, 1446–1460. https://doi.org/10.1021/acs.jpcc.5b06677.
(70) Ruckenstein, E. Spreading and Surface Tension Gradient Driven Phenomena during Heating of Alumina-Supported Palladium Crystallites in Oxygen. *J. Catal.* **1981**, *70*, 233–236. https://doi.org/10.1016/0021-9517(81)90334-1.
(71) Lieske, H.; Voelter, J. Palladium Redispersion by Spreading of Palladium(II) Oxide in Oxygen Treated Palladium/Alumina. *J. Phys. Chem.* **1985**, *89*, 1841–1842. https://doi.org/10.1021/j100256a001.
(72) Johns, T. R.; Goeke, R. S.; Ashbacher, V.; Thüne, P. C.; Niemantsverdriet, J. W.; Kiefer, B.; Kim, C. H.; Balogh, M. P.; Datye, A. K. Relating Adatom Emission to Improved Durability of Pt–Pd Diesel Oxidation Catalysts. *J. Catal.* **2015**, *328*, 151–164. https://doi.org/10.1016/j.jcat.2015.03.016.
(73) Goodman, E. D.; Carlson, E. Z.; Dietze, E. M.; Tahsini, N.; Johnson, A.; Aitbekova, A.; Nguyen Taylor, T.; Plessow, P. N.; Cargnello, M. Size-Controlled Nanocrystals Reveal Spatial Dependence and Severity of Nanoparticle Coalescence and Ostwald Ripening in Sintering Phenomena. *Nanoscale* **2021**, *13*, 930–938. https://doi.org/10.1039/D0NR07960J.
(74) Alcala, R.; DeLaRiva, A.; Peterson, E. J.; Benavidez, A.; Garcia-Vargas, C. E.; Jiang, D.; Pereira-Hernández, X. I.; Brongersma, H. H.; Veen, R. ter; Staněk, J.; et al. Atomically Dispersed Dopants for Stabilizing Ceria Surface Area. *Appl. Catal. B Environ.* **2021**, *284*, 119722. https://doi.org/10.1016/j.apcatb.2020.119722.
(75) Peuckert, M. XPS Study on Surface and Bulk Palladium Oxide, Its Thermal Stability, and a Comparison with Other Noble Metal Oxides. *J. Phys. Chem.* **1985**, *89* (12), 2481–2486. https://doi.org/10.1021/j100258a012.
(76) Dai, Y.; Lu, P.; Cao, Z.; Campbell, C. T.; Xia, Y. The Physical Chemistry and Materials Science behind Sinter-Resistant Catalysts. *Chem. Soc. Rev.* **2018**, *47*, 4314–4331. https://doi.org/10.1039/C7CS00650K.
(77) Baker, R. T. K. The Relationship between Particle Motion on a Graphite Surface and Tammann Temperature. *J. Catal.* **1982**, *78* (2), 473–476. https://doi.org/10.1016/0021-9517(82)90332-3.
(78) Goodman, E. D.; Schwalbe, J. A.; Cargnello, M. Mechanistic Understanding and the Rational Design of Sinter-Resistant Heterogeneous Catalysts. *ACS Catal.* **2017**, *7* (10), 7156–7173. https://doi.org/10.1021/acscatal.7b01975.
(79) Linares, N.; Serrano, E.; Rico, M.; Mariana Balu, A.; Losada, E.; Luque, R.; García-Martínez, J. Incorporation of Chemical Functionalities in the Framework of Mesoporous Silica. *Chem. Commun.* **2011**, *47* (32), 9024. https://doi.org/10.1039/c1cc11016k.
(80) van den Berg, R.; Parmentier, T. E.; Elkjær, C. F.; Gommes, C. J.; Sehested, J.; Helveg, S.; de Jongh, P. E.; de Jong, K. P. Support Functionalization To Retard Ostwald Ripening in Copper Methanol Synthesis Catalysts. *ACS Catal.* **2015**, *5* (7), 4439–4448. https://doi.org/10.1021/acscatal.5b00833.
(81) Bonati, M. L. M.; Douglas, T. M.; Gaemers, S.; Guo, N. Synthesis, Characterization, and Catalytic Properties of Novel Single-Site and Nanosized Platinum Catalysts. *Organometallics* **2012**, *31*, 5243–5251. https://doi.org/10.1021/om200778r.
(82) Schumann, J.; Bao, Y.; Hannagan, R. T.; Sykes, E. C. H.; Stamatakis, M. Periodic Trends in Adsorption Energies Around Single-Atom Alloy Active Sites. 1–25.
(83) Zandkarimi, B.; Gorey, T. J.; Li, G.; Munarriz, J.; Anderson, S. L.; Alexandrova, A. N. Alloying with Sn Suppresses Sintering of Size-Selected Subnano Pt Clusters on SiO 2 with and without Adsorbates. *Chem. Mater.* **2020**, acs.chemmater.0c02926. https://doi.org/10.1021/acs.chemmater.0c02926.
(84) Xiong, H.; Kunwar, D.; Jiang, D.; García-Vargas, C. E.; Li, H.; Du, C.; Canning, G.; Pereira-Hernandez, X. I.; Wan, Q.; Lin, S.; et al. Engineering Catalyst Supports to Stabilize PdOx Two-Dimensional Rafts for Water-Tolerant Methane Oxidation. *Nat. Catal.* **2021**, *4* (10), 830–839. https://doi.org/10.1038/s41929-021-00680-4.
(85) Xin, Y.; Li, S.; Qian, Y.; Zhu, W.; Yuan, H.; Jiang, P.; Guo, R.; Wang, L. High-Entropy Alloys as a Platform for Catalysis: Progress, Challenges, and Opportunities. *ACS Catal.* **2020**, *10* (19), 11280–11306. https://doi.org/10.1021/acscatal.0c03617.
(86) Xu, H.; Zhang, Z.; Liu, J.; Do-Thanh, C.-L.; Chen, H.; Xu, S.; Lin, Q.; Jiao, Y.; Wang, J.; Wang, Y.; et al.

Entropy-Stabilized Single-Atom Pd Catalysts via High-Entropy Fluorite Oxide Supports. *Nat. Commun.* **2020**, *11* (1), 3908. https://doi.org/10.1038/s41467-020-17738-9.

(87) Figueroba, A.; Kovács, G.; Bruix, A.; Neyman, K. M. Towards Stable Single-Atom Catalysts: Strong Binding of Atomically Dispersed Transition Metals on the Surface of Nanostructured Ceria. *Catal. Sci. Technol.* **2016**, *6* (18), 6806–6813. https://doi.org/10.1039/C6CY00294C.

(88) Spezzati, G.; Su, Y.; Hofmann, J. P.; Benavidez, A. D.; DeLaRiva, A. T.; McCabe, J.; Datye, A. K.; Hensen, E. J. M. Atomically Dispersed Pd–O Species on CeO_2 (111) as Highly Active Sites for Low-Temperature CO Oxidation. *ACS Catal.* **2017**, *7*, 6887–6891. https://doi.org/10.1021/acscatal.7b02001.

(89) Kunwar, D.; Zhou, S.; Delariva, A.; Peterson, E. J.; Xiong, H.; Pereira-Hernández, X. I.; Purdy, S. C.; Ter Veen, R.; Brongersma, H. H.; Miller, J. T.; et al. Stabilizing High Metal Loadings of Thermally Stable Platinum Single Atoms on an Industrial Catalyst Support. *ACS Catal.* **2019**, *9*, 3978–3990. https://doi.org/10.1021/acscatal.8b04885.

(90) Ta, N.; Liu, J. (Jimmy); Chenna, S.; Crozier, P. A.; Li, Y.; Chen, A.; Shen, W. Stabilized Gold Nanoparticles on Ceria Nanorods by Strong Interfacial Anchoring. *J. Am. Chem. Soc.* **2012**, *134* (51), 20585–20588. https://doi.org/10.1021/ja310341j.

(91) Matsubu, J. C.; Zhang, S.; DeRita, L.; Marinkovic, N. S.; Chen, J. G.; Graham, G. W.; Pan, X.; Christopher, P. Adsorbate-Mediated Strong Metal-Support Interactions in Oxide-Supported Rh Catalysts. *Nat. Chem.* **2017**, *9* (2), 120–127. https://doi.org/10.1038/NCHEM.2607.

(92) Zhang, Y.; Yang, X.; Yang, X.; Duan, H.; Qi, H.; Su, Y.; Liang, B.; Tao, H.; Liu, B.; Chen, D.; et al. Tuning Reactivity of Fischer–Tropsch Synthesis by Regulating TiOx Overlayer over Ru/TiO2 Nanocatalysts. *Nat. Commun.* **2020**, *11* (1), 3185. https://doi.org/10.1038/s41467-020-17044-4.

(93) Liu, J.; Ji, Q.; Imai, T.; Ariga, K.; Abe, H. Sintering-Resistant Nanoparticles in Wide-Mouthed Compartments for Sustained Catalytic Performance. *Sci. Rep.* **2017**, *7* (1), 41773. https://doi.org/10.1038/srep41773.

(94) Yin, P.; Hu, S.; Qian, K.; Wei, Z.; Zhang, L.-L.; Lin, Y.; Huang, W.; Xiong, H.; Li, W.-X.; Liang, H.-W. Quantification of Critical Particle Distance for Mitigating Catalyst Sintering. *Nat. Commun.* **2021**, *12* (1), 4865. https://doi.org/10.1038/s41467-021-25116-2.

(95) Zhang, J.; Wang, L.; Zhang, B.; Zhao, H.; Kolb, U.; Zhu, Y.; Liu, L.; Han, Y.; Wang, G.; Wang, C.; et al. Sinter-Resistant Metal Nanoparticle Catalysts Achieved by Immobilization within Zeolite Crystals via Seed-Directed Growth. *Nat. Catal.* **2018**, *1* (7), 540–546. https://doi.org/10.1038/s41929-018-0098-1.

(96) Tavasoli, A.; Trépanier, M.; Dalai, A. K.; Abatzoglou, N. Effects of Confinement in Carbon Nanotubes on the Activity, Selectivity, and Lifetime of Fischer−Tropsch Co/Carbon Nanotube Catalysts. *J. Chem. Eng. Data* **2010**, *55* (8), 2757–2763. https://doi.org/10.1021/je900984c.

(97) Neill, B. J. O.; Jackson, D. H. K.; Lee, J.; Canlas, C.; Stair, P. C.; Marshall, C. L.; Elam, W.; Kuech, T. F.; Dumesic, J. A.; Huber, G. W. Catalyst Design with Atomic Layer Deposition. *ACS Catal.* **2015**, *5* (3), 1804–1825. https://doi.org/10.1021/cs501862h.

(98) McNeary, W. W.; Tacey, S. A.; Lahti, G. D.; Conklin, D. R.; Unocic, K. A.; Tan, E. C. D.; Wegener, E. C.; Erden, T. E.; Moulton, S.; Gump, C.; et al. Atomic Layer Deposition with TiO 2 for Enhanced Reactivity and Stability of Aromatic Hydrogenation Catalysts. *ACS Catal.* **2021**, *11* (14), 8538–8549. https://doi.org/10.1021/acscatal.1c02101.

(99) Zhang, Q.; Lee, I.; Joo, J. B.; Zaera, F.; Yin, Y. Core-Shell Nanostructured Catalysts. *Acc. Chem. Res.* **2013**, *46* (8), 1816–1824. https://doi.org/10.1021/ar300230s.

(100) Gao, C.; Lyu, F.; Yin, Y. Encapsulated Metal Nanoparticles for Catalysis. *Chem. Rev.* **2021**, *121*, 834–881. https://doi.org/10.1021/acs.chemrev.0c00237.

(101) Joo, S. H.; Park, J. Y.; Tsung, C.-K.; Yamada, Y.; Yang, P.; Somorjai, G. A. Thermally Stable Pt/Mesoporous Silica Core–Shell Nanocatalysts for High-Temperature Reactions. *Nat. Mater.* **2009**, *8* (2), 126–131. https://doi.org/10.1038/nmat2329.

(102) Gawande, M. B.; Goswami, A.; Asefa, T.; Guo, H.; Biradar, A. V; Peng, D.-L.; Zboril, R.; Varma, R. S. Core-Shell Nanoparticles: Synthesis and Applications in Catalysis and Electrocatalysis. *Chem. Soc. Rev.* **2015**, *44*, 7540–7590. https://doi.org/10.1039/c5cs00343a.

(103) Zhang, J.; Wang, B.; Nikolla, E.; Medlin, J. W. Directing Reaction Pathways through Controlled Reactant Binding at Pd–TiO_2 Interfaces. *Angew. Chem. Int. Ed* **2017**, *56* (23), 6594–6598. https://doi.org/10.1002/anie.201703669.

(104) Ye, J.; Cheng, D.; Chen, F.; Zhan, X. Controlled Synthesis of Sintering-Resistant Pd@CeO_2 Core–Shell Nanotube Catalysts for CO Oxidation. *Ind. Eng. Chem. Res.* **2019**, *58*, 21972–21982. https://doi.org/10.1021/acs.iecr.9b04697.

(105) Cargnello, M.; Jaen, J. J. D.; Garrido, J. C. H.; Bakhmutsky, K.; Montini, T.; Gamez, J. J. C.; Gorte, R. J.;

Fornasiero, P. Exceptional Activity for Methane Combustion over Modular Pd@CeO2 Subunits on Functionalized Al2O3. *Science (80-.).* **2012**, *337* (6095), 713–717. https://doi.org/10.1126/science.1222887.

(106) Adijanto, L.; Sampath, A.; Yu, A. S.; Cargnello, M.; Fornasiero, P.; Gorte, R. J.; Vohs, J. M. Synthesis and Stability of Pd@CeO_2 Core-Shell Catalyst Films in Solid Oxide Fuel Cell Anodes. *ACS Catal.* **2013**, *3* (8), 1801–1809. https://doi.org/10.1021/cs4004112.

(107) Su, Y.-Q.; Liu, J.-X.; Filot, I. A. W.; Hensen, E. J. M. Theoretical Study of Ripening Mechanisms of Pd Clusters on Ceria. *Chem. Mater.* **2017**, *29*, 9456–9462. https://doi.org/10.1021/acs.chemmater.7b03555.

(108) Wan, Q.; Hu, S.; Dai, J.; Chen, C.; Li, W.-X. First-Principles Kinetic Study for Ostwald Ripening of Late Transition Metals on TiO_2 (110). *J. Phys. Chem. C* **2019**, *123*, 1160–1169. https://doi.org/10.1021/acs.jpcc.8b08530.

(109) Chen, X.; Schwank, J. W.; Fisher, G. B.; Cheng, Y.; Jagner, M.; McCabe, R. W.; Katz, M. B.; Graham, G. W.; Pan, X. Nature of the Two-Step Temperature-Programmed Decomposition of PdO Supported on Alumina. *Appl. Catal. A Gen.* **2014**, *475*, 420–426. https://doi.org/10.1016/j.apcata.2014.01.056.

(110) Wei, S.; Li, A.; Liu, J.-C.; Li, Z.; Chen, W.; Gong, Y.; Zhang, Q.; Cheong, W.-C.; Wang, Y.; Zheng, L.; et al. Direct Observation of Noble Metal Nanoparticles Transforming to Thermally Stable Single Atoms. *Nat. Nanotechnol.* **2018**, *13* (9), 856–861. https://doi.org/10.1038/s41565-018-0197-9.

(111) Fei, H.; Dong, J.; Feng, Y.; Allen, C. S.; Wan, C.; Volosskiy, B.; Li, M.; Zhao, Z.; Wang, Y.; Sun, H.; et al. General Synthesis and Definitive Structural Identification of MN4C4 Single-Atom Catalysts with Tunable Electrocatalytic Activities. *Nat. Catal.* **2018**, *1* (1), 63–72. https://doi.org/10.1038/s41929-017-0008-y.

(112) Yin, P.; Yao, T.; Wu, Y.; Zheng, L.; Lin, Y.; Liu, W.; Ju, H.; Zhu, J.; Hong, X.; Deng, Z.; et al. Single Cobalt Atoms with Precise N-Coordination as Superior Oxygen Reduction Reaction Catalysts. *Angew. Chemie Int. Ed.* **2016**, *55* (36), 10800–10805. https://doi.org/10.1002/anie.201604802.

(113) Sá, J.; Taylor, S. F. R.; Daly, H.; Goguet, A.; Tiruvalam, R.; He, Q.; Kiely, C. J.; Hutchings, G. J.; Hardacre, C. Redispersion of Gold Supported on Oxides. *ACS Catal.* **2012**, *2*, 552–560. https://doi.org/10.1021/cs300074g.

(114) Zhou, X.; Zhang, Y.; Wang, J. DFT Study on the Regeneration of Pt/γ-Al_2O_3 Catalyst: The Effect of Chlorine on the Redispersion of Metal Species. *Appl. Surf. Sci.* **2021**, *545*, 148988. https://doi.org/10.1016/j.apsusc.2021.148988.

(115) Giulimondi, V.; Kaiser, S. K.; Agrachev, M.; Krumeich, F.; Clark, A. H.; Mitchell, S.; Jeschke, G.; Pérez-Ramírez, J. Redispersion Strategy for High-Loading Carbon-Supported Metal Catalysts with Controlled Nuclearity. *J. Mater. Chem. A* **2022**, No. ii. https://doi.org/10.1039/D1TA09238C.

(116) Munahar, S.; Purnomo, B. C.; Setiyo, M.; Triwiyatno, A.; Setiawan, J. D. Design and Application of Air to Fuel Ratio Controller for LPG Fueled Vehicles at Typical Down-Way. *SN Appl. Sci.* **2020**, *2* (1), 37. https://doi.org/10.1007/s42452-019-1839-8.

(117) Xie, H.; Hong, M.; Hitz, E. M.; Wang, X.; Cui, M.; Kline, D. J.; Zachariah, M. R.; Hu, L. High-Temperature Pulse Method for Nanoparticle Redispersion. *J. Am. Chem. Soc.* **2020**, *142*, 17364–17371. https://doi.org/10.1021/jacs.0c04887.

(118) Duan, X.; Tian, X.; Ke, J.; Yin, Y.; Zheng, J.; Chen, J.; Cao, Z.; Xie, Z.; Yuan, Y. Size Controllable Redispersion of Sintered Au Nanoparticles by Using Iodohydrocarbon and Its Implications. *Chem. Sci.* **2016**, *7*, 3181–3187. https://doi.org/10.1039/C5SC04283F.

(119) Jones, J.; Xiong, H.; DeLaRiva, A. T.; Peterson, E. J.; Pham, H.; Challa, S. R.; Qi, G.; Oh, S.; Wiebenga, M. H.; Hernández, X. I. P.; et al. Thermally Stable Single-Atom Platinum-on-Ceria Catalysts via Atom Trapping. *Science (80-.).* **2016**, *353* (6295), 150–154. https://doi.org/10.1126/science.aaf8800.

(120) Pereira-Hernández, X. I.; DeLaRiva, A.; Muravev, V.; Kunwar, D.; Xiong, H.; Sudduth, B.; Engelhard, M.; Kovarik, L.; Hensen, E. J. M.; Wang, Y.; et al. Tuning Pt-CeO_2 Interactions by High-Temperature Vapor-Phase Synthesis for Improved Reducibility of Lattice Oxygen. *Nat. Commun.* **2019**, *10*, 1358. https://doi.org/10.1038/s41467-019-09308-5.

(121) Dvořák, F.; Camellone, M. F.; Tovt, A.; Tran, N. D.; Negreiros, F. R.; Vorokhta, M.; Skála, T.; Matolínová, I.; Mysliveček, J.; Matolín, V.; et al. Creating Single-Atom Pt-Ceria Catalysts by Surface Step Decoration. *Nat. Commun.* **2016**, *7*. https://doi.org/10.1038/ncomms10801.

(122) Wu, Z.; Hwang, I.; Cha, G.; Qin, S.; Tomanec, O.; Badura, Z.; Kment, S.; Zboril, R.; Schmuki, P. Optimized Pt Single Atom Harvesting on TiO_2 Nanotubes—Towards a Most Efficient Photocatalyst. *Small* **2022**, *18* (2), 2104892. https://doi.org/10.1002/smll.202104892.

(123) Hill, A. J.; Bhat, A.; Berquist, Z. J.; Fisher, G. B.; Lenert, A.; Schwank, J. W. Stabilizing Highly Dispersed Halo Sites in Thermally Restructured Palladium Core@Shell Nanoparticles for Improved Catalyst Activity and Durability. *ACS Appl. Nano Mater.* **2021**, *4* (10), 10985–10998. https://doi.org/10.1021/acsanm.1c02436.

(124) Neitzel, A.; Figueroba, A.; Lykhach, Y.; Skála, T.; Vorokhta, M.; Tsud, N.; Mehl, S.; Ševčíková, K.; Prince, K. C.; Neyman, K. M.; et al. Atomically Dispersed Pd, Ni, and Pt Species in Ceria-Based Catalysts: Principal Differences in Stability and Reactivity. *J. Phys. Chem. C* **2016**, *120* (18), 9852–9862. https://doi.org/10.1021/acs.jpcc.6b02264.

(125) Kwak, N. W.; Jeong, S. J.; Seo, H. G.; Lee, S.; Kim, Y.; Kim, J. K.; Byeon, P.; Chung, S.; Jung, W. In Situ Synthesis of Supported Metal Nanocatalysts through Heterogeneous Doping. *Nat. Commun.* **2013**, *12*. https://doi.org/10.1038/s41467-018-07050-y.

(126) Seo, C. Y.; Chen, X.; Sun, K.; Allard, L. F.; Fisher, G. B.; Schwank, J. W. Palladium Redispersion at High Temperature within the Pd@SiO_2 Core@shell Structure. *Catal. Commun.* **2018**, *108*, 73–76. https://doi.org/10.1016/j.catcom.2018.01.027.

(127) Lee, J.; Theis, J. R.; Kyriakidou, E. A. Vehicle Emissions Trapping Materials: Successes, Challenges, and the Path Forward. *Appl. Catal. B Environ.* **2019**, *243*, 397–414. https://doi.org/10.1016/j.apcatb.2018.10.069.

(128) Trovarelli, A.; de Leitenburg, C.; Boaro, M.; Dolcetti, G. The Utilization of Ceria in Industrial Catalysis. *Catal. Today* **1999**, *50*, 353–367. https://doi.org/10.1016/S0920-5861(98)00515-X.

(129) Freund, H.-J.; Meijer, G.; Scheffler, M.; Schlögl, R.; Wolf, M. CO Oxidation as a Prototypical Reaction for Heterogeneous Processes. *Angew. Chemie Int. Ed.* **2011**, *50*, 10064–10094. https://doi.org/10.1002/anie.201101378.

(130) Zammit, M.; Dimaggio, C.; Kim, C.; Lambert, C.; Muntean, G.; Peden, C.; Parks, J.; Howden, K. Future Automotive Aftertreatment Solutions : The 150 °C Challenge Workshop Report. *US DRIVE* **2012**.

(131) Hill, A. J.; Seo, C. Y.; Chen, X.; Bhat, A.; Fisher, G. B.; Lenert, A.; Schwank, J. W. Thermally Induced Restructuring of Pd@CeO_2 and Pd@SiO_2 Nanoparticles as a Strategy for Enhancing Low-Temperature Catalytic Activity. *ACS Catal.* **2020**, *10*, 1731 – 1741. https://doi.org/10.1021/acscatal.9b05224.

Chapter 2 : Directing Nanoscale Restructuring Through Controlled Core@shell Architectures

2.1 Motivation

As previously discussed, catalyst restructuring as a result of aging or operation at high temperatures (≥800°C) typically causes severe catalyst deactivation through active site agglomeration.[1,2] This thermally induced deactivitation[3–5] is a major challenge in the context of automotive emissions control, where recent efforts (e.g., Department of Energy's US DRIVE program) have aimed to decrease the required temperature for 90% conversion (i.e., light-off temperature or T_{90}) of criteria pollutants, such as un-combusted hydrocarbons (HCs) and carbon monoxide (CO), to below 150°C.[6]

Here, we report on a catalyst design strategy that leverages 800°C aging of a well-controlled Pd@CeO_2 core@shell morphology to induce favorable restructuring. The resulting catalyst is stable and achieves a repeatable light-off temperature (T_{90}) below 90°C for CO oxidation. Our results on Pd@CeO_2 are compared with a catalyst prepared by Pd surface-impregnation on CeO_2 nanospheres (Pd/CeO_2) and a catalyst encapsulated in a non-reducible, SiO_2 shell (Pd@SiO_2). In doing so, we provide insight into the role of support morphology and reducibility on the redispersion of Pd and the restructuring of Pd@CeO_2, complementing recent works that have investigated the effects of aging core@shell catalysts at high temperatures.[7–10] It should be noted that the term redispersion, here, encompasses both the physical breakup of the active metal core into smaller, dispersed clusters, and the accompanying changes in metal coordination and oxidation state.[11–13]

Our experiments allow for direct comparison of reducible oxide ($Pd@CeO_2$) and non-reducible oxide ($Pd@SiO_2$) core@shell systems. Aging in 2.5% oxygen at 800°C resulted in redispersion of active Pd throughout the shells of both structures, which is consistent with our previous work on thermally induced restructuring in $Pd@SiO_2$ core@shell catalysts.[14] However, $Pd@CeO_2$, after aging, exhibits a markedly lower light-off temperature than $Pd@SiO_2$. Studies of aging under inert gas environments emphasize the role of reducibility in contributing to Pd redispersion and thereby, to the light-off decrease seen in aged $Pd@CeO_2$. In addition, comparison with Pd/CeO_2 illustrates the importance of core@shell morphology in separating active metal domains to promote redispersion. Serendipitously, redispersion of Pd in a core@shell morphology also inhibits the growth of ceria crystallites, preserving active lattice configurations such as steps and edges. A set of comprehensive material characterization techniques (electron microscopy, x-ray energy dispersive and photoelectron spectroscopy, physisorption and chemisorption) provides a holistic analysis of the catalysts at the focus of this study.

Collectively, these results demonstrate how thermally induced catalyst restructuring can be facilitated by the core@shell configuration to promote low-temperature catalytic activity. Our redispersed catalysts do not require a regeneration or pretreatment step in order to function, which also emphasizes the simplicity of our strategy.

2.2 Results and Discussion

2.2.1 Fresh catalyst synthesis and characterization

Three catalyst systems were prepared to compare the effects of support morphology and composition on restructuring. It should be noted that the term ‘fresh’ is used here to describe catalysts that have been synthesized and subsequently treated in air at 500°C for 1 hour (see *Sections 2.4.1* and *2.4.2* for complete synthesis and treatment details).

The two core@shell catalyst systems ($Pd@CeO_2$, $Pd@SiO_2$) were prepared using a scalable synthesis protocol that we have previously reported.[15] As outlined in Figure 2.1 and *Sections 2.4.1*, the synthesis can be discretized into a two–step process. Stable, dispersed nanoparticle core seeds are first formed through the ionic dissolution of a metal precursor. These core seeds interact through a surfactant with a shell precursor, which polymerizes around the cores through a base–catalyzed hydrolysis.

Figure 2.2 provides representative transmission electron microscopy (TEM) and x-ray energy dispersive spectroscopy (XEDS) characterization of fresh and aged catalysts. Fresh core@shell samples consist of Pd cores, ranging from 3 – 5 nm in diameter, that are encapsulated by shells ranging from 7 – 10 nm in thickness. While both CeO_2 and SiO_2 completely encapsulate Pd cores, the nanoscale structure of the shells is noticeably different. SiO_2 exhibits a porous, amorphous shell structure, in comparison with the CeO_2 shell, which appears polycrystalline. The CeO_2 shell is made up of randomly oriented crystallites, ranging in length from 2 – 5 nm, which are packed together to form a total $Pd@CeO_2$ nanoparticle diameter of 20 – 25 nm.

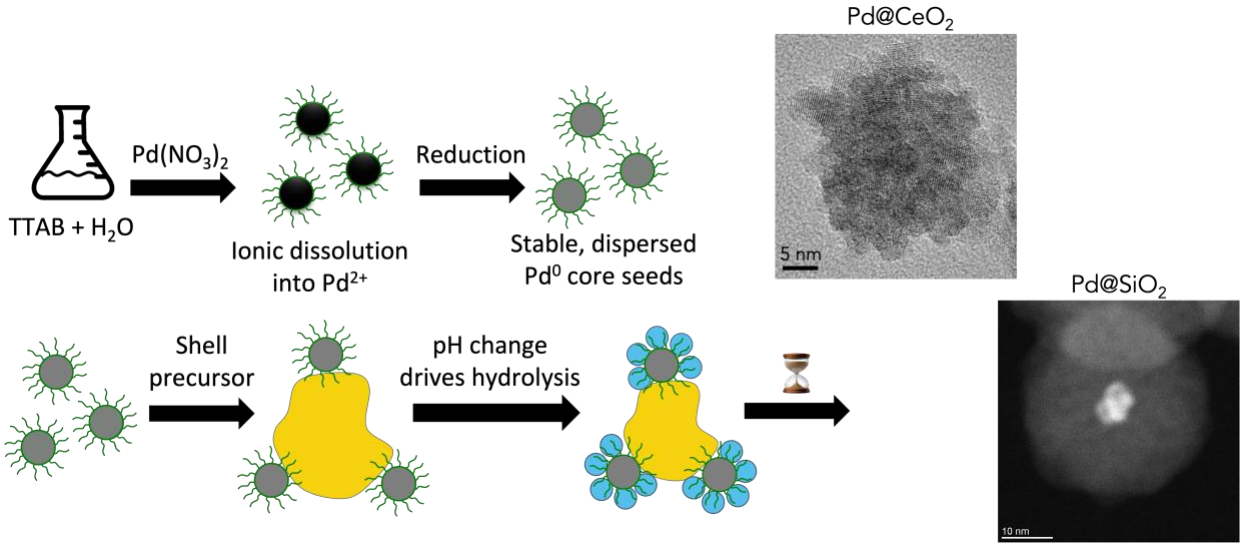

Figure 2.1. Graphical overview of core@shell synthesis procedure.

The Pd/CeO_2 catalyst was prepared through incipient wetness impregnation, which is often used to synthesize conventional, surface-impregnated catalysts.[16,17] The Pd/CeO_2 catalyst is made up of 2 – 5 nm Pd nanoparticles distributed along the surface of CeO_2 nanospheres. Similar to the $Pd@CeO_2$ shell, the CeO_2 nanospheres are made up of numerous, packed crystallites that form a structure on the order of 50 nm in diameter. The similarity between the CeO_2 shells and CeO_2 nanospheres allows us to compare how restructuring events differ more readily because of encapsulation versus surface-impregnation.

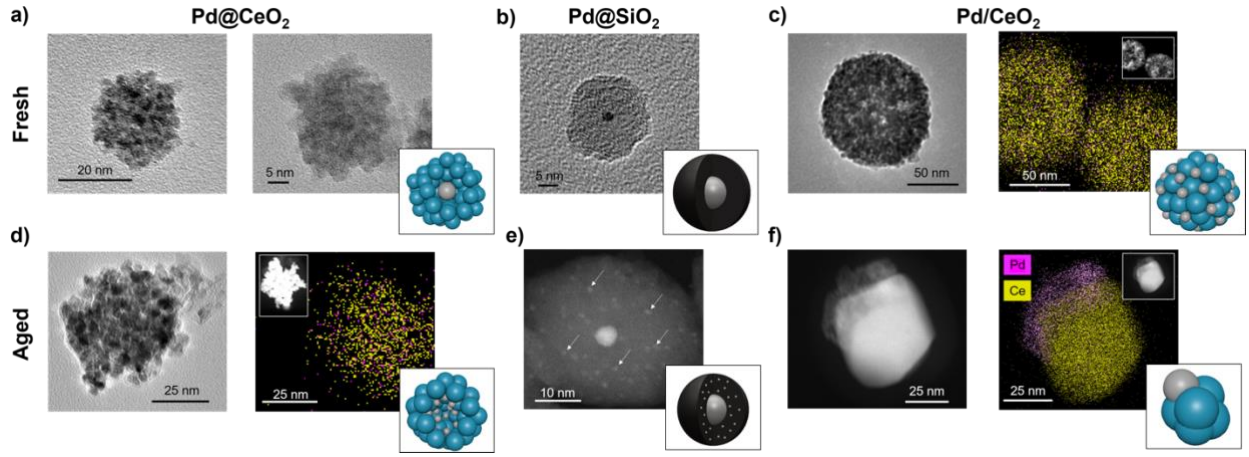

Figure 2.2. Microscopy characterization of fresh and aged catalysts.
TEM and XEDS images of (a – c) fresh and (d – f) O_2-aged 2 wt. % $Pd@CeO_2$, $Pd@SiO_2$ and Pd/CeO_2 catalysts. XEDS images (c, d, f) have been included to account for limited Z-contrast when imaging small Pd clusters supported on CeO_2. Dark-field images of the areas used for XEDS mapping have been included as insets. XEDS images are color-coordinated, with embedded legend (Pd – magenta, Ce – yellow) on aged Pd/CeO_2. Bright-field TEM of fresh $Pd@CeO_2$ shows the polycrystalline nature of the CeO_2 shell. After O_2-aging, several Pd clusters in $Pd@SiO_2$ shell are highlighted by arrows. Graphical schematics of fresh and aged catalysts are included to illustrate morphological changes (Pd – silver, CeO_2 – blue, SiO_2 – black). Core@shell schematics (b, e) have been cut through to provide cross-sectional comparisons.

2.2.2 Fresh catalyst light-off performance

CO oxidation was chosen as a probe reaction to evaluate catalyst performance due to its well-established scaling with the number of available active sites[18] and relevance to automotive emissions control. T_{90} values for all tested catalysts, in addition to surface area and porosity characteristics, are summarized in Table 2.1.

Table 2.1. Summary of surface area, average pore size, light-off performance and activity post O_2-cut ($time_{50}$), as fresh and after 800°C O_2-aging.

Sample	BET Surface Area		Avg. Pore Size		Light-off			$Time_{50}$	
	Fresh (m^2/g)	Aged (m^2/g)	Fresh (nm)	Aged (nm)	Fresh T_{90} (°C)	Aged T_{90} (°C)	ΔT_{90} (%)	Fresh (s)	Aged (s)
$Pd@CeO_2$	137.5	39.2	2.0	1.7	133	88	- 34	80	140
$Pd@SiO_2$	290.4	124.9	1.5	1.3	186	177	- 5	48	48
Pd/CeO_2	76.4	19.2	1.8	1.2	148	177	+ 20	73	61

The $Pd@SiO_2$ catalyst, as seen in Figure 2.3, shows the highest fresh light-off temperature (186°C). In comparison, the fresh Pd/CeO_2 and $Pd@CeO_2$ catalysts exhibited T_{90} values of 148°C and 133°C, respectively. The difference in light-off temperature between the silica and ceria encapsulated catalysts can be attributed to the lack of MvK oxidation pathways for silica. One possible explanation for the light-off difference between the CeO_2-based catalysts is that encapsulation increases the number of sites that form Pd-CeO_2 interfaces. As there is a lower activation energy on a per site basis for interfacial vs. bulk Pd (due to the oxygen storage-release capacity of the CeO_2 support),[19] more interfacial sites in $Pd@CeO_2$ could explain the differences in fresh light-off. Although the activity of MvK oxidation mechanisms is known to be facet dependent, with (111) facets of CeO_2 reported as being most active,[20] it is unlikely that crystallographic variability can explain the observed differences in fresh light-off behavior here; x-ray diffraction (XRD) patterns of both Pd/CeO_2 and $Pd@CeO_2$ (Figure 2.4) match standard XRD patterns[21,22] for bare CeO_2.

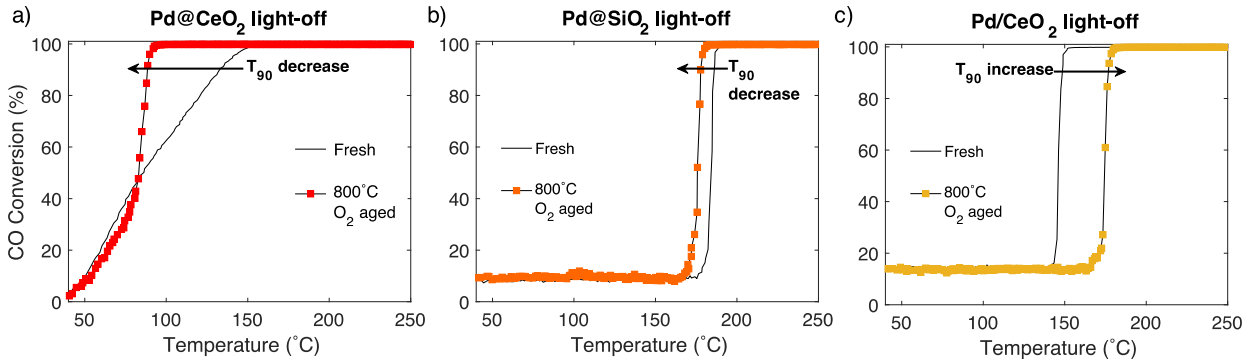

Figure 2.3. Performance of fresh and O_2 aged catalysts.
CO oxidation light-off profiles for fresh (solid line) and 800°C O_2-aged (square markers) (a) Pd@CeO_2, (b) Pd@SiO_2 and (c) Pd/CeO_2 catalysts.

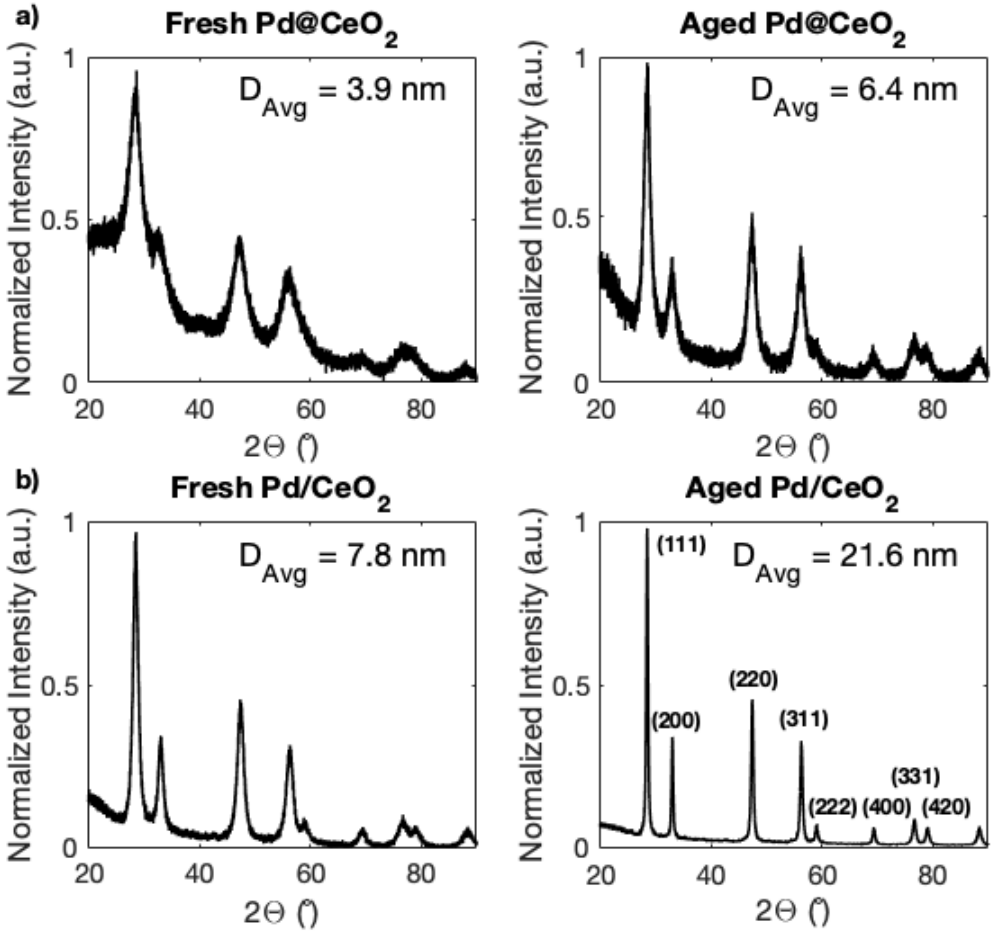

Figure 2.4. Crystallographic characterization of fresh and O_2 aged catalysts.
XRD patterns for fresh and O_2-aged (a) Pd@CeO_2 and (b) Pd/CeO_2. Patterns have been normalized to their respective background signals. Characteristic peaks for CeO_2 nanoparticles have been identified on the aged Pd/CeO_2 patterns. Average CeO_2 crystallite size values (D_{Avg}), as calculated by the Debye–Scherrer equation, are inset.

2.2.3 Effects of high-temperature aging

Aging at 800°C in O_2 (2.5%), with N_2 balance (referred to here as 'O_2-aging'), was chosen to be consistent with previous studies investigating Pd restructuring.[7,14] Upon aging, appreciable changes in active site morphology (Figure 2.2, 2.4) and catalytic behavior (Figure 2.3) were observed, albeit with diverging trends depending on the support material and initial morphology. It should be noted that all catalyst samples exhibited a degree of pore closure and loss of surface area upon O_2–aging. These observations are consistent with similar studies that have investigated thermally induced catalyst restructuring.[9,13,23] As outlined in published work, transport limitations were not significant in any of the catalytic systems studied here.[24]

For the surface-impregnated catalyst, Pd/CeO_2, aging resulted in a substantial agglomeration of the initially dispersed Pd clusters (Figure 2.2f). Consequently, the Pd/CeO_2 light-off profile shifted to higher temperatures, accompanied by a T_{90} that increased by 29°C to 177°C (a $\triangle T_{90}$ of + 20%). In this case, sintering of the active Pd most likely caused the T_{90} increase, which is in agreement with previous observations where sintering was the dominant active site restructuring mechanism.[2,5]

When an oxide shell encapsulated Pd, noticeably different light-off behavior was observed. Aging the $Pd@SiO_2$ catalyst at 800°C resulted in redispersion, not sintering, of Pd throughout the shell (Figure 2.2e). This redispersion is accompanied by a T_{90} that has decreased by 9°C from 186°C to 177°C (a $\triangle T_{90}$ of -5%), in agreement with our previous work.[14] As the $Pd@SiO_2$ system exhibits negligible reducibility, it is likely that the change in T_{90} observed is primarily caused by the physical breakup of the core increasing the number of exposed Pd sites capable of CO oxidation (see chemisorption discussion below).

After O_2-aging, the T_{90} for Pd@CeO_2 decreased by 45°C from 133°C to a remarkably low value of 88°C (a $\triangle T_{90}$ of -34%). This low temperature light–off was found to be repeatable and was maintained after an additional O_2–aging cycle, suggesting the catalyst had reached a stable structural state after the initial aging and is stable under the CO oxidation conditions used here. In contrast to the observations on the Pd@SiO_2 catalyst, TEM and XEDS imaging indicates that the O_2-aging process appears to have completely redispersed the core Pd throughout the CeO_2 shell (see Figure 2.2d).

Although electron microscopy techniques work well for the Pd@SiO_2 system, the poor contrast between Pd and Ce makes it difficult to resolve sub-nanometer clusters of Pd in the O_2–aged Pd@CeO_2. Hence, to confirm and analyze the redispersion in our catalysts, we performed XPS analysis and pulsed CO chemisorption studies. XPS analysis of the O_2-aged Pd@CeO_2 catalyst is shown in Figure 2.5. The low Pd signal of the fresh Pd@CeO_2 spectra, with respect to the background, confirms complete encapsulation by CeO_2 shells. This contrasts with the fresh Pd/CeO_2, which exhibits much more intense characteristic Pd peaks. After aging Pd@CeO_2, photoelectrons with characteristic Pd_{3d} binding energies were detected with appreciable intensity. The growth of the Pd_{3d} peak suggests that Pd has migrated closer toward the outer perimeter of the shell so that more Pd species exist within the pertinent photoelectron escape depth for the XPS experiment. Although further study is warranted, based on previous literature[25–29] and the aging conditions used in this work, an Ostwald Ripening mechanism is most likely responsible for Pd mobility, as opposed to transport in the vapor phase.

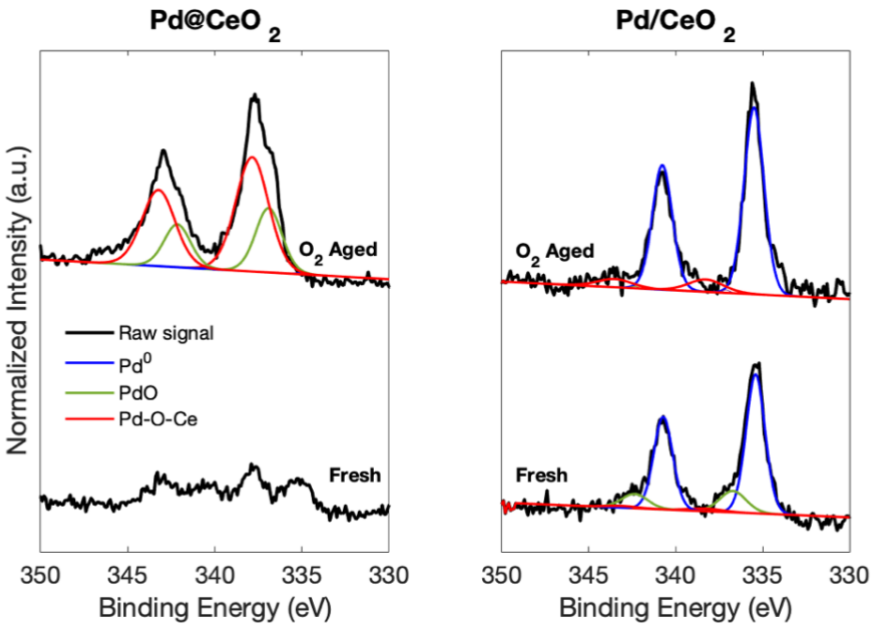

Figure 2.5. Oxidation state characterization of fresh and O_2 aged catalysts.
XPS spectra in the Pd_{3d} scan region for fresh and O_2-aged (a) $Pd@CeO_2$ catalysts and (b) Pd/CeO_2 catalysts.

Pulsed CO chemisorption similar to that used by Takeguchi *et. al.*[30] and Lee *et. al.*[31] was used to quantify how active metal surface area for the $Pd@CeO_2$ and $Pd@SiO_2$ catalysts changed after high-temperature aging. CO chemisorption results and calculated values of Pd dispersion and approximate particle size are summarized in Table 2.2. CO chemisorption results agree well with electron microscopy observations of Pd core size in the fresh $Pd@SiO_2$ and $Pd@CeO_2$ samples, which suggests the chemisorption experiment was not convoluted by CO sorption on the CeO_2 support. The amount of accessible Pd increased approximately 1.8 times, from 6.3×10^{-2} mmol/g_{cat} to 1.2×10^{-1} mmol/g_{cat} in $Pd@SiO_2$, and approximately 2.7 times from 6.2×10^{-2} mmol/g_{cat} to 1.6×10^{-1} mmol/g_{cat} in $Pd@CeO_2$. Such an increase in the number of sites capable of adsorbing CO would contribute to the light–off temperature decrease observed in both catalysts after O_2–aging. The dispersion in the $Pd@CeO_2$ catalyst increased from 33% to 88% after O_2–aging, which surpasses the dispersion increase seen in the $Pd@SiO_2$ catalyst (which increased from 36% to 61%). The average Pd particle size of the $Pd@CeO_2$ catalyst decreased from 3.4 nm to 1.3 nm

after O_2–aging (62% decrease in average size), while the Pd@SiO_2 average Pd particle size decreased from 3.2 nm to 1.8 nm (41% decrease). These observations are consistent with the notion that the Pd@CeO_2 catalyst experienced a more extensive disintegration and redispersion of core Pd during aging than the Pd@SiO_2 catalyst.

Table 2.2. Surface Pd content and catalyst analysis derived from pulsed CO chemisorption experiments for fresh and aged Pd@SiO_2 and Pd@CeO_2.

	Pd@SiO_2		**Pd@CeO_2**	
	Fresh	Aged	Fresh	Aged
Amount of accessible Pd (mmol/g_{cat})	6.3×10^{-2}	1.2×10^{-1}	6.2×10^{-2}	1.6×10^{-1}
Dispersion (%)	36	61	33	88
Average Pd particle size (nm)	3.1	1.8	3.4	1.3

Arrhenius experiments and turnover frequency calculations were conducted on the fresh and O_2–aged Pd@CeO_2 to investigate if changes in the dispersion, average particle size and amount of accessible Pd were accompanied by changes in intrinsic catalytic activity (see Table 2.3). The apparent activation energy for CO oxidation decreased from 42 kJ/mol to 33 kJ/mol after aging. The TOF increased from 0.20 s^{-1} when fresh, to 0.39 s^{-1} after O_2–aging. These changes in intrinsic activity suggest that the enhanced low temperature activity of the Pd@CeO_2 catalyst seen after O_2–aging is not solely caused by an increased number of accessible sites for CO oxidation.

XPS deconvolution performed on the O_2–aged Pd@CeO_2 catalyst provides evidence that the physical redispersion of Pd sites is accompanied with oxidation state and coordination changes. The catalyst shows a strong abundance of Pd^{2+} species that are associated with highly dispersed PdO (335.8–336.3 eV) and Pd-O-Ce species (338.0–338.1 eV).[32–36] Such structures have been previously identified as particularly active at low temperatures for CO oxidation.[12,35,37,38] This is in contrast to the XPS spectra of the aged Pd/CeO_2, which exhibits significant peak growth in regions characteristic for Pd^0 (335.2 – 335.3 eV).[39–41] While these structures exhibit high thermal stability, they have been identified as less active for low temperature oxidation.[13,42]

Table 2.3. Surface Pd content and catalyst analysis derived from pulsed CO chemisorption experiments for fresh and aged Pd@SiO_2 and Pd@CeO_2.

	Pd@CeO_2	
	Fresh	Aged
Activation energy, E_a (kJ/mol)	42	33
Turnover frequency at 40°C (s^{-1})	0.20	0.39

Overall, the above analysis provides evidence that high-temperature exposure restructures the Pd@CeO_2 catalysts, resulting in the formation of an abundance of metal species that can better utilize the reducibility of the CeO_2 shell support. This observation is consistent with previous work by Datye et. al.[43] In the following sections, we investigate how the morphology of the shell and its composition can influence the restructuring observed after aging.

2.2.4 The role of core@shell encapsulation in restructuring

The appreciable T_{90} and Pd dispersion changes seen after O_2-aging indicate that the core@shell morphology influences the formation of redispersed Pd active sites. The tortuous pore structure in the shell is most likely providing sufficient separation of active metal to decrease the likelihood that mobile species locally sinter. This could explain why redispersion was observed on a support material such as SiO_2, which does not typically exhibit substantial metal trapping capability.

The polycrystalline nature of the CeO_2 shell may also contribute to enhanced redispersion of Pd. Existing as an amalgam of packed crystallites, the CeO_2 shell has both mesopores and grain boundaries to facilitate transport (Figure 2.2). The more uniform SiO_2 shells, in contrast, have only mesopores to mediate transport. BET analysis confirms that some of these mesopores and grain boundaries in the CeO_2 remain after O_2-aging. As grain boundaries can act as transport pathways for mobile metal species,[44] it is possible that the CeO_2 shell provides additional routes for metal

movement, which would promote redispersion. In addition, CeO_2 supports (e.g., step sites on CeO_2 (111) facets) are known to exhibit affinity for trapping PGMs.[45,46] As the CeO_2 crystallites in $Pd@CeO_2$ show a high occurrence of the (111) facet (Figure 2.4), it is possible that such a phenomenon is also occurring during O_2-aging here.

As seen in Figure 2.2, both $Pd@CeO_2$ and Pd/CeO_2 are comprised of CeO_2 crystallites that are packed together. In the case of Pd/CeO_2, 800°C O_2-aging results in large CeO_2 crystals with sharp XRD peaks. In contrast, line broadening is preserved in the XRD patterns of O_2-aged $Pd@CeO_2$, indicating that the CeO_2 crystallites in the shell do not undergo substantial agglomeration and growth (see Figure 2.4). Changes in average CeO_2 crystallite size was investigated further by the Debye–Scherrer equation. The average crystallite size increased 1.6 times in $Pd@CeO_2$, 2.8 times in Pd/CeO_2 and 5.3 times in a control sample of bare CeO_2 nanospheres. The persistence of smaller CeO_2 grains and abundance of Pd coordinated with oxygen and cerium in the O_2–aged $Pd@CeO_2$ suggests that redispersed Pd intercalates between crystallites of CeO_2. The retention of these small crystallites with many step and edge sites, which are known to enhance oxygen mobility and promote CO oxidation at low temperatures,[20,37] is likely a major contributor to the enhanced low-temperature activity that we observe in aged $Pd@CeO_2$.

2.2.5 Contribution of reducibility to low-temperature activity gain in aged $Pd@CeO_2$

To investigate how changes in Pd dispersion affected oxygen recruitment from the CeO_2 support, the O_2 gas flow was cut abruptly while the reactor maintained a temperature of 250°C (a temperature sufficient for complete CO conversion in all samples). The drop-off in CO conversion as a function of time after cutting O_2 flow is depicted in Figure 2.6. The term '$time_{50}$' is defined

as the time required for CO conversion to drop to 50% after cutting the O_2 flow (see Table 2.1). It is used to provide a comparative metric between the catalysts tested.

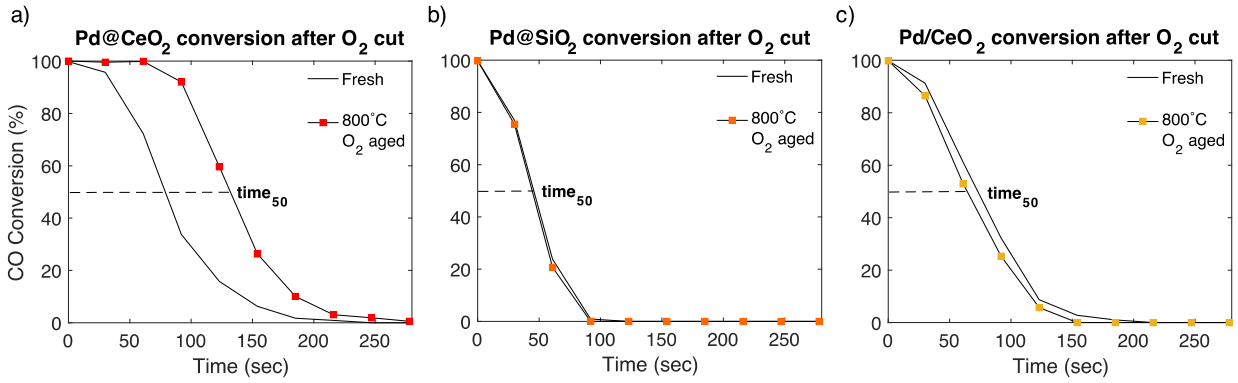

Figure 2.6. Recruitment of lattice oxygen for fresh and O_2 aged catalysts.
Percent conversion of CO as a function of time after cutting O_2 gas flow at 250°C for fresh and O_2-aged (a) $Pd@CeO_2$, (b) $Pd@SiO_2$ and (c) Pd/CeO_2. The dashed line indicates the time at which conversion falls to 50% ($time_{50}$).

Removing the gaseous oxygen supply forces the catalysts to utilize residual oxygen in the system to maintain CO conversion. This residual oxygen could be in three forms; (1) as residual gaseous O_2 in the feed lines and dead volume of the reactor, (2) absorbed/trapped O_2 in the pores of the catalyst, or (3) solid-phase oxygen in the case of a reducible oxide support. The same reactor preparation and packing procedures were used for all three samples. Consequently, any dead volume effects are assumed to be uniform between catalysts. As the $Pd@SiO_2$ system does not exhibit OSC, residual gaseous oxygen in the feed lines and dead volume of the reactor and trapped in the pores provide the only two sources of oxygen that can prolong conversion. $Pd@SiO_2$ had the shortest $time_{50}$ among all samples tested, regardless of whether the catalyst was fresh or aged. This indicates that changes in pore size, pore volume, and consequently the content of residual gas-phase O_2 are not significant descriptors of CO conversion after cutting the O_2 flow. Thus, the $Pd@SiO_2$ data provide us with the best measure of the system response associated with purging the feed lines and reactor dead volume. In comparison, the fresh Pd/CeO_2 maintained a longer

time$_{50}$. A longer time$_{50}$ is expected as the reducible oxide provides a source of atomic oxygen in the absence of gas-phase O_2. Interestingly, once aged, the Pd/CeO_2 time$_{50}$ dropped slightly. This faster downturn for aged Pd/CeO_2 is consistent with sintering processes that produce larger Pd macroparticles with a lower number of sites capable of accessing lattice oxygen, and the light-off behavior discussed above.

Pd@CeO_2 exhibited the longest time$_{50}$ among fresh samples. Similar to its light-off performance, this observation is attributed to enhanced interfacial contact by encapsulation of Pd. 800°C O_2-aging of the Pd@CeO_2 catalyst extended the time$_{50}$ by 75%. These experimental findings support the notion that thermally induced active site restructuring in Pd@CeO_2 enhances access to solid-phase oxygen in the CeO_2 support. With a greater proportion of the restructured active sites capable of accessing MvK oxidation pathways, the thermal barriers for catalyst light-off can be considerably decreased.

To probe how oxygen storage-release capacity influences redispersion during aging, catalysts with reducible (Pd@CeO_2) and non-reducible (Pd@SiO_2) oxide shells were aged at 800°C in a pure nitrogen environment termed 'N_2-aging'. Light-off plots for CO oxidation before and after two sequential 4-hour N_2-aging cycles are displayed in Figure 2.7. The light-off profile for the Pd@SiO_2 catalyst did not significantly change following N_2 aging (Figure 2.7a). This observation persisted after a second aging under the same conditions. The absence of a T_{90} change implies that redispersion of the core Pd does not occur in the absence of oxygen, which is consistent with previously proposed mechanisms of PdO mobility.[14,47,48]

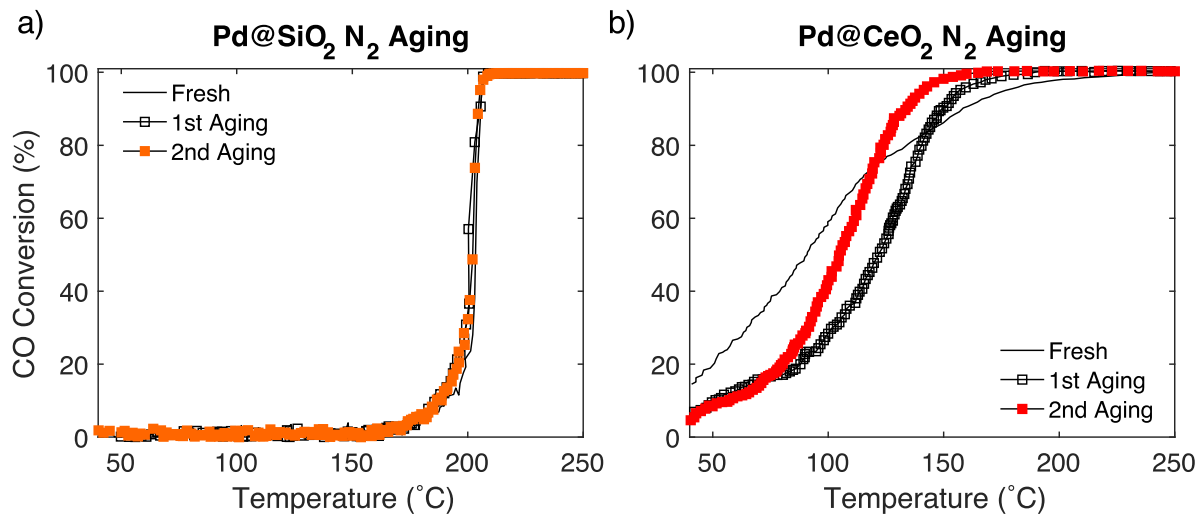

Figure 2.7. Contributions of support reducibility to favorable restructuring.
CO oxidation light-off profiles for fresh and 800°C N_2-aged (a) $Pd@SiO_2$ and (b) $Pd@CeO_2$ catalysts. The T_{90} profile for $Pd@SiO_2$ does not change after N_2-aging.

We see a correlation between the availability of oxygen during aging and the extent of light-off decrease, which ranges from 0% ΔT_{90} when no oxygen source is available ($Pd@SiO_2$ N_2-aging), to -34% when oxygen is supplied in the gas phase and solid phase through a reducible oxide ($Pd@CeO_2$, O_2-aging). N_2-aging of $Pd@CeO_2$ produced both a change in T_{90} and light-off profile in line with this correlation, where the T_{90} decreased over two aging cycles, from a $\triangle T_{90}$ of -5% to -15%. Our O_2-cutoff experiments (Figure 2.6) and literature[49] indicate that the aging temperature used here is within the range for observable oxygen donation from CeO_2. In addition, XEDS analysis of the $Pd@CeO_2$ catalyst subjected to one cycle of N_2–aging illustrates that redispersion of Pd had occurred. Consequently, the nitrogen aging experiments are entirely consistent with the notion that the accessibility of lattice oxygen plays an important role in the redispersion and restructuring of core@shell catalysts. Although there are small, but noticeable, T_{90} differences between this batch of "fresh" catalysts and the one used in the earlier figures, the main point of this experiment is to demonstrate that, in the absence of gas-phase oxygen, the lattice oxygen can participate in the restructuring process.

In summary, the participation of lattice oxygen during high temperature restructuring, as suggested by the N_2–aging studies, may act synergistically with the abundant pathways for Pd mobility, conferred by the CeO_2 shell crystallites, to produce the extensive redispersion observed in the O_2–aged Pd@CeO_2. Altogether, it appears that thermally induced redistribution of core Pd, which is facilitated by the core@shell morphology, combines synergistically with accompanying changes in metal coordination and oxidation state to enhance low temperature activity.

2.3 Conclusions

The work in this chapter has delineated a promising strategy of using thermally induced restructuring in well-controlled core@shell morphologies to enhance low-temperature activity. Thermally induced catalyst restructuring has a strong dependence on both support morphology and composition. Unlike aging of Pd/CeO_2 catalysts, that resulted in Pd agglomeration and a T_{90} increase in line with typical sintering behavior, Pd encapsulated with mesoporous oxide shells responds with active site redispersion, which significantly decreases the light-off temperature. In summary, these results exemplify that active-site restructuring in core@shell nanoparticles can be used to improve low-temperature activity in the following ways:

- Encapsulation facilitates separation of active metal domains, increasing the likelihood that mobile metal species will redisperse rather than locally agglomerate. Thus, encapsulation allows for extended utilization of the active metal in the catalyst.

- When a CeO_2 shell is used, high-temperature restructuring produces an abundance of Pd species that can readily access highly active mechanisms for oxidation.

- The inhibition of CeO_2 shell crystallite growth, with sites that are highly active for CO oxidation, is attributed to the presence of redispersed Pd.

- The reducibility of CeO_2 appears to contribute towards favorable restructuring processes.

Using a probe CO oxidation reaction, these factors combine to produce a substantial T_{90} decrease for an aged Pd@CeO_2 system without the need for additional treatment or reactivation steps. The stark contrast of these observations with conventional sintering suggests that core@shell morphologies can be promising for catalyst design in applications, such as automotive emissions catalysis, where high-temperature degradation is a significant challenge. In addition, the simplicity of our aging protocol illustrates the possibility of using temperature inputs as an inexpensive and scalable post-synthesis method to significantly enhance, instead of hinder, low-temperature activity.

2.4 Experimental Details

2.4.1 Synthesis of conventionally supported Pd/CeO_2 nanospheres

Cerium nitrate hexahydrate (99%, Sigma Aldrich, $Ce(NO_3)_3 \cdot 6H_2O$) was made into a 2.30 M solution with deionized water and left to stir. A 0.564 mM solution of acetic acid (99.7%, Sigma Aldrich, CH_3COOH) in ethylene glycol (99.8%, Sigma Aldrich, anhydrous, $(CH_2OH)_2$) was added under stirring to the $Ce(NO_3)_3 \cdot 6H_2O$ solution. The solution was heated at 180°C for 4 hours. The resulting solid nanosphere particles were centrifuged and washed three times with deionized water and three times with ethanol prior to 3 hours of 550°C calcination.

Pd/CeO_2 catalysts were prepared from the previously made CeO_2 nanospheres by wet impregnation. A 7.51 mM solution of palladium nitrate dihydrate (99%, Sigma Aldrich, $Pd(NO_3)_2 \cdot 2H_2O$) in deionized water was added to a 64.6 mM dispersion of the CeO_2 nanospheres in deionized water under vigorous stirring. The solution was dried in an oven at 110°C for 6 hours after 12 hours of vigorous stirring, followed by treatment in a muffle furnace at 500°C for 1 hour.

At this stage, catalysts were considered fresh. Once treated, all catalysts were subjected to TEM and XEDS characterization (see Section 2.4.5 for more details on characterization techniques).

2.4.2 Synthesis of core@shell nanoparticles

Core@shell nanoparticles were prepared using a one-pot methodology of base-catalyzed polymerization of a shell precursor around fully formed palladium core seeds.

Upon synthesis completion, the core@shell catalysts were collected by centrifugation and washed three times with water and three times with ethanol. All catalysts were treated in a muffle furnace at 500°C in air for 1 hour. At this stage, catalysts were considered fresh. Once treated, all catalysts were subjected to TEM and XEDS characterization (see Section 2.4.5).

Synthesis of Pd@SiO_2 core@shell catalyst: Tetraethylorthosilicate (99%, Sigma Aldrich, TEOS) was made into a 572 mM solution with ethanol. A 10 mM solution of trimethyl tetradecyl ammonium bromide (99% Sigma Aldrich, TTAB) in deionized water was prepared and left under vigorous stirring.

Pd nanoparticles were synthesized from a 30 mM solution of $Pd(NO_3)_2 \cdot 2H_2O$ in deionized water. This solution was added to the TTAB solution. A solution of 36 mM hydrazine hydrate (99%, Sigma Aldrich, $N_2H_4 \cdot H_2O$) in deionized water was added to reduce the Pd^{2+} into Pd core seeds. The pH of the solution was adjusted to 10.7 with sodium hydroxide (99%, Sigma Aldrich, NaOH) in deionized water and left under vigorous stirring for 30 minutes to ensure excess N_2H_4 decomposition. The solution's pH was re-adjusted to 10.7 after the 30 minutes, and the TEOS solution was added dropwise. After 24 hours, the solution was transferred to an oven for hydrothermal aging at 80°C for 4 hours.

Synthesis of Pd@CeO_2 core@shell catalyst: Cerium-isobutyrate (Ce-Iso) was made into a 52.2 mM solution with ethanol. 13.6 mmol of triethanolamine (99%, Sigma Aldrich, TEA) was

used as a chelating agent to form cerium-atrane. A separate solution of 5.95 mM TTAB in water was made and left under vigorous stirring.

Pd nanoparticles were made from a 15.8 mM solution of $Pd(NO_3)_2 \cdot 2H_2O$ in deionized water. This solution was added to the TTAB solution. A 1.02 M $N_2H_4 \cdot H_2O$ solution in deionized water was added to reduce the ionic dissolution of Pd^{2+} into Pd core seeds.

Once reduced, a 5.20 mM TTAB solution was added to further disperse the Pd core seeds and promote discretized encapsulation. The pH of the solution was adjusted to 10.7 with NaOH and left uncovered for 30 minutes to ensure decomposition of excess N_2H_4.

After the 30 minutes, the pH of the system was readjusted to 10.7 and the cerium-atrane solution was added dropwise. After 24 hours, the solution was transferred to an oven for hydrothermal aging at 80°C for 4 hours.

2.4.3 Catalyst aging

For the purposes of this study, *in situ* aging refers to aging in the catalytic test bed for analyzing the effects of aging on catalytic performance. *Ex situ* aging refers to aging in a tube-furnace system for morphology characterization as a function of aging. All gas flow rates were set to 200 mL/min total.

In situ air aging of core@shell catalysts*:* Samples were transferred to a quartz reactor and placed inside a tube furnace for catalytic activity testing once post-synthesis treatment was completed (see Section 4). Prior to initial testing, catalysts were exposed to 2.5% O_2 with N_2 balance (aging gas), flowing at 200 mL/min at 500°C for 1 hour to ensure a clean catalytic surface. After initial treatment, the sample was cooled down to 35°C and stabilized for 1 hour in the aging gas mixture. Initial catalytic testing was then undertaken. Once complete, the sample was purged in aging gas conditions at a temperature of 100°C for 1 hour. The temperature was raised to 800°C

at a rate of 2°C/min and held for 4 hours. Samples were left to ambiently cool after aging. Once aged and cooled, an additional catalytic test was undertaken.

In situ N_2 aging of core@shell catalysts: To examine the role of the reducible oxide in the redispersion process, *in situ* aging of both Pd@CeO_2 and Pd@SiO_2 catalysts were performed in a pure nitrogen gas environment. The procedure was similar to that in Section 3.1, however after sample purging in aging gas conditions at 100°C for 1 hour, the inlet gas was changed to pure nitrogen and the system was left to purge any excess oxygen for an additional hour. After purging, the catalyst was aged for 4 hours in pure nitrogen at 800°C and left to ambiently cool. Once cooled, the inlet gas was changed from nitrogen to the aging gas and left to stabilize for 1 hour. An additional catalytic test was undertaken once stabilization was complete.

Ex situ air aging of core@shell catalysts: Once post-synthesis treatment was complete, samples were subjected to initial characterization (see Section 2.4.5). Samples were then placed in a tube furnace and under aging gas flow, subjected to 800°C aging for 4 hours. Samples were left to cool in ambient conditions prior to additional characterization.

2.4.4 Catalytic testing parameters

***CO oxidation light-off tests*:** Catalytic measurements were carried out using a 4.00 mm ID quartz reactor subjected to continuous flow. Test gas was comprised of 1% CO and 2.5% O_2 (with N_2 gas balance) set to 200 mL/min total flow. 60 mg of catalyst (60-80 mesh) diluted with 100 mg of SiO_2 (60-80 mesh) was used to obtain CO oxidation light-off curves. The reactor system was encased in a muffle furnace, and the temperature was raised from 35°C to 250°C by a 2°C/min ramp to ensure good linear temperature control and proper heat transfer. The reactor was connected to a downstream FTIR to quantify effluent gas components.

Cutting O_2 supply to examine oxygen recruitment from CeO_2: The supply of gaseous O_2 was cut once the light-off test (see Section 4.1) had concluded and the temperature had stabilized at 250°C. The percent CO conversion was then monitored as a function of time since the cutting of the O_2 gas supply.

Arrhenius plotting to estimate apparent activation energy for Pd@CeO_2: Arrhenius experiments were carried out using a 4.00 mm ID quartz reactor subjected to continuous flow. Test gas was comprised of 1% CO and 2.5% O_2 (with N_2 gas balance) set to 200 mL/min total flow. 20 mg of fresh Pd@CeO_2 was used to obtain apparent activation energy. The reactor system was encased in a muffle furnace, and temperatures points used for Arrhenius plotting were kept under 60°C to ensure that CO conversion was under 20%. Each temperature point was stabilized for 45 minutes, with constant effluent gas analysis by downstream FTIR. Upon completion of the Arrhenius experiment, the fresh Pd@CeO2 catalyst was subjected to *in–situ* O_2 aging (see Experimental section 3.2), followed by an additional Arrhenius experiment.

The rate of CO_2 production at a given temperature (r_{CO_2}) was calculated as follows:

$$r_{CO_2} = \frac{[CO_0] \cdot X_{CO,T} \cdot V_f}{m_{cat}}$$

where $[CO_0]$ is the inlet concentration of CO, $X_{CO,T}$ is the CO conversion at the given temperature, V_f is the test gas flow rate and m_{cat} is the mass of catalyst used in the experiment.

Calculation of turnover frequency: Turnover frequency (TOF) for the fresh and post O_2–aged Pd@CeO_2 catalysts was determined by the following equation:

$$TOF\ (s^{-1}) = \left. CO\ conversion \cdot [inlet\ CO]\left(\frac{mmol}{sec}\right) \right/ catalyst\ mass\ (g) \cdot accessible\ Pd\ \left(\frac{mmol}{g\ cat}\right)$$

where $CO\ conversion$ is the fractional conversion of CO at 40°C, $[inlet\ CO]$ is the molar flow rate of CO into the reactor system (1% CO at a total flow of 200 mL/min = 0.0814 mmol/sec), the $catalyst\ mass$ is 20 mg and the amount of $accessible\ Pd$ is taken from pulsed CO chemisorption experiments (see below).

2.4.5 Material characterization

Characterization of samples was done using six techniques: transmission electron microscopy (TEM), x-ray energy dispersive spectroscopy (XEDS), x-ray photoelectron spectroscopy (XPS), x-ray powder diffraction (XRD), Brunauer–Emmett–Teller derived N_2 physisorption surface analysis (BET) and pulsed CO chemisorption.

A JEOL 3011 HREM was used to obtain standard bright-field TEM characterizations. A JEOL 2100F Probe-Corrected Electron Microscope with a zirconated tungsten thermal field emission tip was used for high-angle annular dark-field scanning transmission electron microscopy characterization and XEDS mapping/line scans of samples. Line scans were conducted with a line ~3 nm in diameter.

XPS measurements used a Kratos Axis Ultra XPS with a monochromatic Al x-ray source operating at 10 mA and 15 kV. XPS spectra were normalized relative to the adventitious C_{1S} peak at 284.5 eV. Deconvolution in the Pd3d scan region was done according to three characteristic peaks, each with a spin-doublet at +5.26 eV: zero-valent Pd^0 (335.2–335.3 eV [39–41]), bulk PdO existing as Pd^{2+} (335.8–336.5 eV [32,35]) and electron-deficient Pd interacting strongly with the CeO_2 support, denoted as $Pd^{\delta+}$ or Pd–O–Ce (338.0–338.1 eV [32–34]). Deconvolution in the Ce3d scan region was done according to two different oxidation states. Ce^{4+} peaks were centered at 882.3, 889.0, 898.3, 900.8, 907.5 and 916.7 eV and Ce^{3+} peaks were centered at 885.7 and 903.6 eV.

A Rigaku 600 Miniflex with a step size of 0.01 was used for XRD measurements A Micromeritics ASAP 2020 was used for BET surface area and pore distribution characterization.

Pulsed CO chemisorption similar to that described by was performed by Takeguchi *et. al.*[30] and Lee *et. al.*[31] was performed with a Quantachrome ChemBET 3000. All gas flows were kept at 70 mL/min. The sample was pretreated in 3% O_2 (with N_2 gas balance) for 1.5 hours at 300°C, achieved with a ramp rate of 10°C/min. After a system purge with pure He, 5% H_2 (with Ar gas balance) was flown over the sample at 300°C for 1.5 hours to ensure complete reduction of the catalyst surface. Pure He was used again to purge the system once the temperature had cooled to 50°C. 3% O_2 (with N_2 gas balance) was then flown over the sample for 5 minutes. 1% CO_2 (with N_2 gas balance) was subsequently flown over the sample for 5 minutes. 5% H_2 (with Ar gas balance) was then flown over the sample for 10 minutes, prior to a final He purge. The pulse CO chemisorption test was then conducted.

The number of molecules adsorbed per mass of catalyst, N_m [mol/g] was calculated by:

$$N_m = \frac{V_T \times \rho_{CO} \times M_{CO}^{-1} \times N_A}{m_{cat}}$$

Where V_T is the total volume of chemisorbed CO, ρ_{CO} is the density of CO at the temperature used for the experiment, M_{CO} is the molar mass of CO, N_A is Avogadro's constant and m_{cat} is the mass of catalyst used in the experiment.

Metal dispersion, γ [%], was calculated by:

$$\gamma = \frac{(F_S \times M_{Pd} \times N_m)}{100 \times W_{Pd}}$$

Where F_s is a stoichiometric fitting number (1 in this case), M_{Pd} is the molar mass of Pd and W_{Pd} is the weight percent of Pd in the catalyst sample.

The average Pd nanoparticle size, d_P was calculated by the following relationship defined by Baylet *et. al.*[50]:

$$d_P = \frac{(6 \times 10^5) \times M_{Pd}}{\rho_{Pd} \times \gamma \times S_{Pd}}$$

Where ρ_{Pd} is the density of Pd and S_{Pd} is the metal molar surface area of Pd, assuming an equidistribution of low index faces.

The turnover frequency, TOF [s^{-1}], at a given temperature, T, was calculated by:

$$TOF = \frac{F_{CO,0} \times X_{CO,T}}{m_{cat} \times N_m \times F_S}$$

Where $F_{CO,0}$ is the molar flowrate of CO at the inlet of the reactor and $X_{CO,T}$ is the conversion at a temperature, T (which was taken to be 40°C in this case).

2.5 References

(1) Hansen, T. W.; DeLaRiva, A. T.; Challa, S. R.; Datye, A. K. Sintering of Catalytic Nanoparticles: Particle Migration or Ostwald Ripening? *Acc. Chem. Res.* **2013**, *46*, 1720–1730. https://doi.org/10.1021/ar3002427.

(2) Argyle, M. D.; Bartholomew, C. H. Heterogeneous Catalyst Deactivation and Regeneration: A Review. *Catalysts* **2015**, *5*, 145–269. https://doi.org/10.3390/catal5010145.

(3) Xu, Q.; Kharas, K. C.; Croley, B. J.; Datye, A. K. The Sintering of Supported Pd Automotive Catalysts. *ChemCatChem* **2011**, *3* (6), 1004–1014. https://doi.org/10.1002/cctc.201000392.

(4) Al Soubaihi, R.; Saoud, K.; Dutta, J. Critical Review of Low-Temperature CO Oxidation and Hysteresis Phenomenon on Heterogeneous Catalysts. *Catalysts* **2018**, *8*, 660. https://doi.org/10.3390/catal8120660.

(5) Yang, J.; Tschamber, V.; Habermacher, D.; Garin, F.; Gilot, P. Effect of Sintering on the Catalytic Activity of a Pt Based Catalyst for CO Oxidation : Experiments and Modeling. *Appl. Catal. B Environ.* **2008**, *83* (3–4), 229–239. https://doi.org/10.1016/j.apcatb.2008.02.018.

(6) Zammit, M.; Dimaggio, C.; Kim, C.; Lambert, C.; Muntean, G.; Peden, C.; Parks, J.; Howden, K. Future Automotive Aftertreatment Solutions : The 150 °C Challenge Workshop Report. *US DRIVE* **2012**.

(7) Zhang, S.; Chen, C.; Cargnello, M.; Fornasiero, P.; Gorte, R. J.; Graham, G. W.; Pan, X. Dynamic Structural Evolution of Supported Palladium-Ceria Core-Shell Catalysts Revealed by in Situ Electron Microscopy. *Nat. Commun.* **2015**, *6*, 1–6. https://doi.org/10.1038/ncomms8778.

(8) Chen, C.; Cao, J.; Cargnello, M.; Fornasiero, P.; Gorte, R. J. High-Temperature Calcination Improves the Catalytic Properties of Alumina-Supported Pd@ceria Prepared by Self Assembly. *J. Catal.* **2013**, *306*, 109–115. https://doi.org/10.1016/j.jcat.2013.06.013.

(9) Li, L.; Zhang, N.; Huang, X.; Liu, Y.; Li, Y.; Zhang, G. Hydrothermal Stability of Core − Shell Pd @ $Ce_{0.5}Zr_{0.5}O_2$ / Al_2O_3 Catalyst for Automobile Three-Way Reaction. *ACS Catal.* **2018**, *8*, 3222–3231. https://doi.org/10.1021/acscatal.8b00358.

(10) Adijanto, L.; Bennett, D. A.; Chen, C.; Yu, A. S.; Cargnello, M.; Fornasiero, P.; Gorte, R. J.; Vohs, J. M. Exceptional Thermal Stability of Pd@CeO2core-Shell Catalyst Nanostructures Grafted onto an Oxide Surface. *Nano Lett.* **2013**, *13* (5), 2252–2257. https://doi.org/10.1021/nl4008216.

(11) Goodman, E. D.; Johnston-Peck, A. C.; Dietze, E. M.; Wrasman, C. J.; Hoffman, A. S.; Abild-Pedersen, F.; Bare, S. R.; Plessow, P. N.; Cargnello, M. Catalyst Deactivation via Decomposition into Single Atoms and the Role of Metal Loading. *Nat. Catal.* **2019**, *2*, 748–755. https://doi.org/10.1038/s41929-019-0328-1.

(12) Slavinskaya, E. M.; Gulyaev, R. V.; Zadesenets, A. V.; Stonkus, O. A.; Zaikovskii, V. I.; Shubin, Y. V.; Korenev, S. V.; Boronin, A. I. Low-Temperature CO Oxidation by Pd/CeO_2 Catalysts Synthesized Using the Coprecipitation Method. *Appl. Catal. B Environ.* **2015**, *166–167*, 91–103. https://doi.org/10.1016/j.apcatb.2014.11.015.

(13) Stonkus, O. A.; Kardash, T. Y.; Slavinskaya, E. M.; Zaikovskii, V. I.; Boronin, A. I. Thermally Induced Structural Evolution of Palladium-Ceria Catalysts. Implication for CO Oxidation. *ChemCatChem* **2019**, *11*, 3505–3521. https://doi.org/10.1002/cctc.201900752.

(14) Seo, C. Y.; Chen, X.; Sun, K.; Allard, L. F.; Fisher, G. B.; Schwank, J. W. Palladium Redispersion at High Temperature within the $Pd@SiO_2$ Core@shell Structure. *Catal. Commun.* **2018**, *108*, 73–76. https://doi.org/10.1016/j.catcom.2018.01.027.

(15) Seo, C.; Yi, E.; Nahata, M.; Laine, R. M.; Schwank, J. W. Facile, One-Pot Synthesis of $Pd@CeO_2$ Core@shell Nanoparticles in Aqueous Environment by Controlled Hydrolysis of Metalloorganic Cerium Precursor. *Mater. Lett.* **2017**, *206*, 105–108. https://doi.org/10.1016/j.matlet.2017.06.114.

(16) Cooper, B. J.; Evans, W. D. J.; Harrison, B. *Aspects of Automotive Catalyst Preparation, Performance and Durability*; 1987; Vol. 30. https://doi.org/10.1016/S0167-2991(09)60417-1.

(17) Wang, J.; Chen, H.; Hu, Z.; Yao, M.; Li, Y. A Review on the Pd-Based Three-Way Catalyst. *Catal. Rev. Sci. Eng.* **2015**, *57*, 79–144. https://doi.org/10.1080/01614940.2014.977059.

(18) Soliman, N. K. Factors Affecting CO Oxidation Reaction over Nanosized Materials: A Review. *J. Mater. Res. Technol.* **2019**, *8* (2), 2395–2407. https://doi.org/10.1016/j.jmrt.2018.12.012.

(19) Cargnello, M.; Doan-Nguyen, V. V. T.; Gordon, T. R.; Diaz, R. E.; Stach, E. A.; Gorte, R. J.; Fornasiero, P.; Murray, C. B. Control of Metal Nanocrystal Size Reveals Metal-Support Interface Role for Ceria Catalysts. *Science.* **2013**, *341*, 771–773. https://doi.org/10.1126/science.1240148.

(20) Spezzati, G.; Benavidez, A. D.; DeLaRiva, A. T.; Su, Y.; Hofmann, J. P.; Asahina, S.; Olivier, E. J.; Neethling, J. H.; Miller, J. T.; Datye, A. K.; et al. CO Oxidation by Pd Supported on CeO_2 (100) and CeO_2 (111) Facets. *Appl. Catal. B Environ.* **2019**, *243*, 36–46. https://doi.org/10.1016/j.apcatb.2018.10.015.

(21) Jayakumar, G.; Irudayaraj, A. A.; Raj, A. D. Particle Size Effect on the Properties of Cerium Oxide (CeO_2) Nanoparticles Synthesized by Hydrothermal Method. *Mech. Mater. Sci. Eng. J.* **2017**, *9*, 2–7. https://doi.org/10.2412/mmse.3.4.481.

(22) Babitha, K. K.; Sreedevi, A.; Priyanka, K. P.; Sabu, B.; Varghese, T. Structural Characterization and Optical Studies of CeO_2 Nanoparticles Synthesized by Chemical Precipitation. *Indian J. Pure Appl. Phys.* **2015**, *53*, 596–603.

(23) Jones, J.; Xiong, H.; DeLaRiva, A. T.; Peterson, E. J.; Pham, H.; Challa, S. R.; Qi, G.; Oh, S.; Wiebenga, M. H.; Hernández, X. I. P.; et al. Thermally Stable Single-Atom Platinum-on-Ceria Catalysts via Atom Trapping. *Science.* **2016**, *353* (6295), 150–154. https://doi.org/10.1126/science.aaf8800.

(24) Hill, A. J.; Seo, C. Y.; Chen, X.; Bhat, A.; Fisher, G. B.; Lenert, A.; Schwank, J. W. Thermally Induced Restructuring of $Pd@CeO_2$ and $Pd@SiO_2$ Nanoparticles as a Strategy for Enhancing Low-Temperature Catalytic Activity. *ACS Catal.* **2020**, *10*, 1731 – 1741. https://doi.org/10.1021/acscatal.9b05224.

(25) Lupescu, J. A.; Schwank, J. W.; Fisher, G. B.; Chen, X.; Peczonczyk, S. L.; Drews, A. R. Pd Model Catalysts: Effect of Aging Duration on Lean Redispersion. *Appl. Catal. B Environ.* **2016**, *185*, 189–202. https://doi.org/10.1016/j.apcatb.2015.12.012.

(26) Zavitsanos, P. D. The Vapor Pressure of Palladium. *J. Phys. Chem.* **1964**, *68* (10), 2899–2901. https://doi.org/10.1021/j100792a026.

(27) Norman, J. H.; Staley, H. G.; Bell, W. E. Mass Spectrometric Knudsen Cell Measurements of the Vapor Pressure of Palladium and the Partial Pressure of Palladium Oxide. *J. Phys. Chem.* **1985**, *69* (4), 1373–1376. https://doi.org/10.1021/j100888a046.

(28) Peuckert, M. XPS Study on Surface and Bulk Palladium Oxide, Its Thermal Stability, and a Comparison with Other Noble Metal Oxides. *J. Phys. Chem.* **1985**, *89* (12), 2481–2486. https://doi.org/10.1021/j100258a012.

(29) Brewer, L. Thermodynamic Properties of the Oxides and Their Vaporization Processes. *Chem. Rev.* **1953**, *52* (1), 1–75. https://doi.org/10.1021/cr60161a001.
(30) Takeguchi, T.; Manabe, S.; Kikuchi, R.; Eguchi, K.; Kanazawa, T.; Matsumoto, S.; Ueda, W. Determination of Dispersion of Precious Metals on CeO_2-Containing Supports. *Appl. Catal. A Gen.* **2005**, *293*, 91–96. https://doi.org/10.1016/j.apcata.2005.07.013.
(31) Jeong, H.; Bae, J.; Han, J. W.; Lee, H. Promoting Effects of Hydrothermal Treatment on the Activity and Durability of Pd/CeO2 Catalysts for CO Oxidation. *ACS Catal.* **2017**, *7* (10), 7097–7105. https://doi.org/10.1021/acscatal.7b01810.
(32) Gulyaev, R. V.; Osadchii, D. Y.; Koscheev, S. V.; Boronin, A. I. Films of the Pd $_xCe_{1-x}O_2$ Solid Solution as a Model Object for the XPS Study of the Surface Chemistry of Pd/CeO_2 Catalysts. *J. Struct. Chem.* **2015**, *56* (3), 566–575. https://doi.org/10.1134/S0022476615030257.
(33) Priolkar, K. R.; Bera, P.; Sarode, P. R.; Hegde, M. S.; Emura, S.; Kumashiro, R.; Lalla, N. P. Formation of $Ce_{1-x}PdO_{2-\delta}$ Solid Solution in Combustion-Synthesized Pd/CeO_2 Catalyst: XRD, XPS, and EXAFS Investigation. *Chem. Mater.* **2002**, *14* (5), 2120–2128. https://doi.org/10.1021/cm0103895.
(34) Bera, P.; Patil, K. C.; Jayaram, V.; Subbanna, G. N.; Hegde, M. S. Ionic Dispersion of Pt and Pd on CeO_2 by Combustion Method: Effect of Metal-Ceria Interaction on Catalytic Activities for NO Reduction and CO and Hydrocarbon Oxidation. *J. Catal.* **2000**, *196* (2), 293–301. https://doi.org/10.1006/jcat.2000.3048.
(35) Slavinskaya, E. M.; Kardash, T. Y.; Stonkus, O. A.; Gulyaev, R. V.; Lapin, I. N.; Svetlichnyi, V. A.; Boronin, A. I. Metal-Support Interaction in Pd/CeO_2 Model Catalysts for CO Oxidation: From Pulsed Laser-Ablated Nanoparticles to Highly Active State of the Catalyst. *Catal. Sci. Technol.* **2016**, *6* (17), 6650–6666. https://doi.org/10.1039/c6cy00319b.
(36) Gulyaev, R. V.; Kardash, T. Y.; Malykhin, S. E.; Stonkus, O. A.; Ivanova, A. S.; Boronin, A. I. The Local Structure of $Pd_xCe_{1-x}O_{2-x-\delta}$ Solid Solutions. *Phys. Chem. Chem. Phys.* **2014**, *16* (26), 13523–13539. https://doi.org/10.1039/c4cp01033g.
(37) Spezzati, G.; Su, Y.; Hofmann, J. P.; Benavidez, A. D.; DeLaRiva, A. T.; McCabe, J.; Datye, A. K.; Hensen, E. J. M. Atomically Dispersed Pd–O Species on CeO_2 (111) as Highly Active Sites for Low-Temperature CO Oxidation. *ACS Catal.* **2017**, *7*, 6887–6891. https://doi.org/10.1021/acscatal.7b02001.
(38) Wang, X.; Chen, J.; Zeng, J.; Wang, Q.; Li, Z.; Qin, R.; Wu, C.; Xie, Z.; Zheng, L. The Synergy between Atomically Dispersed Pd and Cerium Oxide for Enhanced Catalytic Properties. *Nanoscale* **2017**, *9* (20), 6643–6648. https://doi.org/10.1039/c6nr09707c.
(39) Schmitz, P. J.; Otto, K.; de Vries, J. E. An X-Ray Photoelectron Spectroscopy Investigation of Palladium in Automotive Catalysts. Binding Energies and Reduction Characteristics. *Appl. Catal. A, Gen.* **1992**, *92* (1), 59–72. https://doi.org/10.1016/0926-860X(92)80279-L.
(40) Fleisch, T. H.; Mains, G. J. Photoreduction and Reoxidation of Platinum Oxide and Palladium Oxide Surfaces. *J. Phys. Chem.* **1986**, *90* (21), 5317–5320. https://doi.org/10.1021/j100412a082.
(41) Pillo, T.; Zimmermann, R.; Steiner, P.; Hüfner, S. The Electronic Structure of PdO Found by Photoemission (UPS and XPS) and Inverse Photoemission (BIS). *J. Phys. Condens. Matter* **1997**, *9* (19), 3987–3999. https://doi.org/10.1088/0953-8984/9/19/018.
(42) Contreras, J. L.; Fuentes, G. A. Sintering of Supported Metal Catalysts. *Sinter. - Methods Prod.* **2012**, 91–126.
(43) Pereira-hernández, X. I.; Sudduth, B.; Engelhard, M.; Datye, A. K.; Delariva, A.; Muravev, V.; Kunwar, D.; Xiong, H.; Kovarik, L.; Hensen, E. J. M.; et al. Tuning $Pt\text{-}CeO_2$ Interactions by High-Temperature Vapor-Phase Synthesis for Improved Reducibility of Lattice Oxygen. *Nat. Commun.* **2019**, *10*, 1358. https://doi.org/10.1038/s41467-019-09308-5.
(44) Kwak, N. W.; Jeong, S. J.; Seo, H. G.; Lee, S.; Kim, Y.; Kim, J. K.; Byeon, P.; Chung, S.; Jung, W. In Situ Synthesis of Supported Metal Nanocatalysts through Heterogeneous Doping. *Nat. Commun.* **2013**, *12*. https://doi.org/10.1038/s41467-018-07050-y.
(45) Dvořák, F.; Camellone, M. F.; Tovt, A.; Tran, N. D.; Negreiros, F. R.; Vorokhta, M.; Skála, T.; Matolínová, I.; Mysliveček, J.; Matolín, V.; et al. Creating Single-Atom Pt-Ceria Catalysts by Surface Step Decoration. *Nat. Commun.* **2016**, *7*. https://doi.org/10.1038/ncomms10801.
(46) Su, Y.-Q.; Liu, J.-X.; Filot, I. A. W.; Hensen, E. J. M. Theoretical Study of Ripening Mechanisms of Pd Clusters on Ceria. *Chem. Mater.* **2017**, *29*, 9456–9462. https://doi.org/10.1021/acs.chemmater.7b03555.

(47) Baaziz, W.; Bahri, M.; Gay, A. S.; Chaumonnot, A.; Uzio, D.; Valette, S.; Hirlimann, C.; Ersen, O. Thermal Behavior of Pd@SiO_2 Nanostructures in Various Gas Environments: A Combined 3D and in Situ TEM Approach. *Nanoscale* **2018**, *10* (43), 20178–20188. https://doi.org/10.1039/c8nr06951d.

(48) Lupescu, J. A.; Schwank, J. W.; Fisher, G. B.; Hangas, J.; Peczonczyk, S. L.; Paxton, W. A. Pd Model Catalysts: Effect of Air Pulse Length during Redox Aging on Pd Redispersion. *Appl. Catal. B Environ.* **2018**, *223*, 76–90. https://doi.org/10.1016/j.apcatb.2017.07.055.

(49) Li, P.; Chen, X.; Li, Y.; Schwank, J. W. A Review on Oxygen Storage Capacity of CeO_2-Based Materials: Influence Factors, Measurement Techniques, and Applications in Reactions Related to Catalytic Automotive Emissions Control. *Catal. Today* **2019**, *327* (February 2018), 90–115. https://doi.org/10.1016/j.cattod.2018.05.059.

(50) Baylet, A.; Royer, S.; Marécot, P.; Tatibouët, J. M.; Duprez, D. Effect of Pd Precursor Salt on the Activity and Stability of Pd-Doped Hexaaluminate Catalysts for the CH_4 Catalytic Combustion. *Appl. Catal. B Environ.* **2008**, *81* (1–2), 88–96. https://doi.org/10.1016/j.apcatb.2007.12.004.

Chapter 3 : Stabilizing Highly Dispersed Active Sites in Favorably Restructured Core@Shell Catalysts

3.1 Motivation

As described in Chapter 2, core@shell architectures can facilitate favorable and counter-intuitive restructuring when exposed to the high-temperature (800°C) conditions common to many catalytic applications.[1,2] Specifically, we discovered that core Pd disintegrated and migrated outward into the encapsulating shell, nearly doubling the number of available sites for reaction. The resulting highly dispersed Pd species formed an arrangement that resembled a "halo" around the original location of the core. The formation of these halo sites, which occurred within reducible CeO_2 and nonreducible SiO_2 shells, significantly improved active metal utilization and low-temperature activity in a probe CO oxidation reaction. The divergent restructuring behaviors exhibited by core@shell and surface-decorated structures emphasized that the initial nanoscale morphology influences the restructuring trajectory of a catalyst during high-temperature exposure. Specifically, it appears that encapsulating core@shell morphologies can act as a structural template that directs favorable restructuring outcomes in conditions that would typically deactivate a catalyst.

Such favorable outcomes are for naught if they cannot be sustained during extended periods at elevated temperature. Catalyst deactivation on-stream due to thermal degradation tends to be unidirectional, and methods that reverse such processes have remained elusive. As such, it is important to continue developing methods that can achieve favorable nanoscale restructuring by

directly using conditions that are intrinsic to and compatible with industrial applications. While some work has been done to achieve such outcomes,[3–5] the challenge remains to achieve long term stability of favorably restructured catalysts under the transient gas compositions and temperature profiles encountered in industrially-relevant applications.

As such, the long-term stability of halo sites in favorably restructured core@shell systems remains uncertain. To address this question, here, we study the formation, activity, and structural stability of Pd halo sites in core@shell configurations over successive high-temperature aging cycles. Specifically, we examine the morphology and catalytic performance of three catalyst systems with comparable initial Pd dispersion, in between sequential 4-hour cycles of 800°C aging in air as summarized in Figure 3.1. Pd@CeO_2 catalysts are compared to (1) Pd surface decorated on CeO_2 (Pd/CeO_2) to understand the role of active metal placement, specifically encapsulation, and (2) Pd@SiO_2 to understand the role of encapsulating shell chemistry and morphology, as polycrystalline CeO_2 and amorphous SiO_2 exhibit significant differences in their reducibility and porous nanoscale structure. We use a suite of analysis techniques that includes scanning and conventional transmission electron microscopy (STEM, TEM), x-ray energy dispersive spectroscopy (EDS), N_2 physisorption for surface area analysis, CO chemisorption, thermogravimetric analysis (TGA), x-ray photoelectron spectroscopy (XPS) and x-ray powder diffraction (XRD) to obtain structural and morphological insights. CO oxidation serves as a probe reaction due to its relevance in industrial catalytic settings, such as vehicle emission control and preferential oxidation for renewable hydrogen production.[6–8] CO oxidation probe reactions can also extract structural information and examine the recruitment of lattice oxygen.[8–10]

Our investigation into the nanoscale structure of the aged catalysts identifies that encapsulation and support chemistry are key to mediating the formation and trapping of Pd halo

sites. Encapsulation appears to shift the dominant thermal restructuring pathway away from whole particle migration to the emission-limited transport of smaller, mobile species. This transport process, coupled with the tortuous nature of the shell support, increases the likelihood that mobile species do not locally interact and agglomerate and instead become trapped on the support as halo sites with high dispersion and catalytic activity. While both SiO_2 and CeO_2 shells facilitate the formation of dispersed metal sites,[4,11–13] we show here that only Pd@CeO_2 can retain its favorable catalytic activity after sequential cycles of 800°C aging. Pd@SiO_2 in contrast, exhibits continued mobility of dispersed Pd during repeated aging, which results in agglomeration on the external surface of the SiO_2 shell support. The improved stability and retention of activity in Pd@CeO_2 is due to the strong anchoring of Pd halo sites on the CeO_2 support, which synergistically stabilizes the CeO_2 domains. We subsequently age the restructured Pd@CeO_2 catalyst in pure N_2 after it has been reduced under the flow of excess CO to further probe the stability limits of halo sites. These conditions result in some agglomeration of Pd halo sites and loss of catalytic activity, which emphasizes the importance of support chemistry for forming and stabilizing highly dispersed active sites. We demonstrate, however, that returning to 800°C air aging conditions can recover halo sites and low-temperature activity. Thus, in addition to probing the applicability of core@shell architectures in catalytic settings that require exposure to high-temperature conditions, this work offers insights into how core@shell nanostructures can be more generally designed and aged to facilitate favorable restructuring that improves both material utilization and robustness.

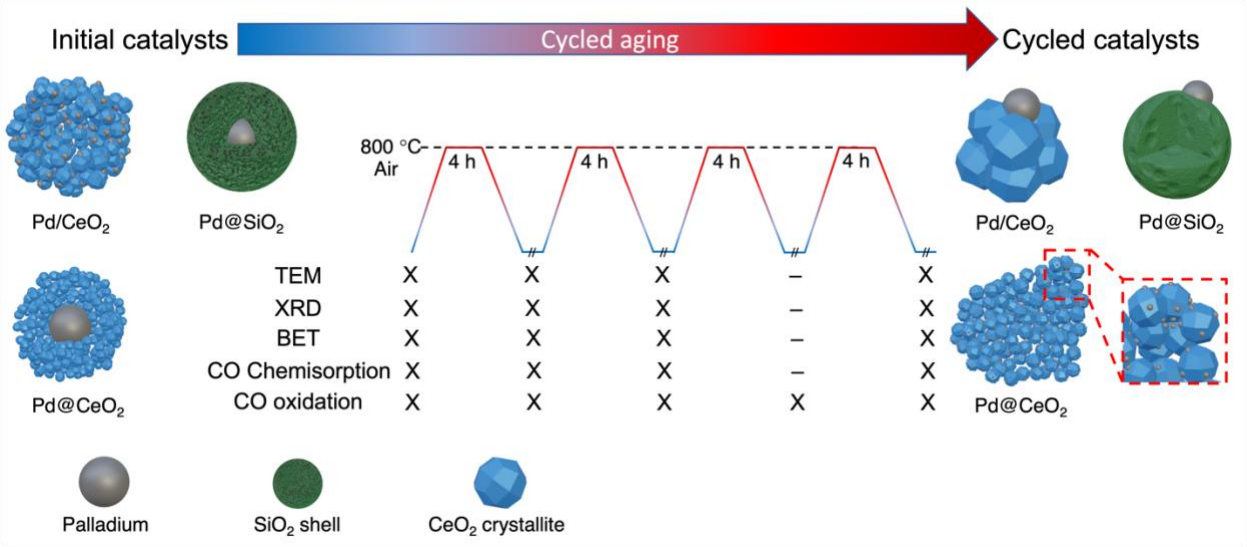

Figure 3.1. Graphical overview of cycled aging study.
$Pd@CeO_2$, $Pd@SiO_2$, and Pd/CeO_2 catalysts are subjected to four sequential cycles aging at 800°C in air for 4 hours to examine Pd transport and trapping in various catalytic architectures. A suite of structural analysis techniques complements CO oxidation activity measurements prior to each aging cycle to understand better how morphology can be used to direct catalyst restructuring and improve material utilization.

3.2 Results and Discussion

3.2.1 Defining model catalyst systems

The three model catalyst systems prior to cycled aging (referred to as initial catalysts) are shown in the first column of Figure 3.2. We note that these catalysts were prepared following previously described methods[1,2,14] and have been exposed to 500°C in air for 2 hours (see *Section 3.4* for more information). The $Pd@SiO_2$ and $Pd@CeO_2$ have comparable Pd core size on the order of 3 – 5 nm in diameter and similar oxide shell thickness of approximately 10 – 12 nm. The overall core@shell structures have total diameters on the order of 20 – 25 nm. CO chemisorption confirms that all catalysts exhibit similar initial Pd dispersion values between 32 and 36%. Meanwhile, XRD analysis of the initial $Pd@CeO_2$ and Pd/CeO_2 demonstrates a slight difference in the CeO_2 crystallite size as calculated by the Debye–Scherrer Equation. The crystallites in the encapsulated catalyst are smaller (~4 nm) than those in the conventionally

prepared system (~8 nm). This data is summarized in Table 3.1. See published work for additional microscopy characterization of the model catalysts before and after aging.[15]

The comparable size of the core and shell domains in Pd@SiO_2 and Pd@CeO_2 are contrasted by differences in the morphology of the encapsulating shells. SiO_2 shells exist as single, porous encapsulating envelopes. The formation of these envelopes is due to the way that silicate–based precursors, such as tetraethyl orthosilicate (TEOS, which is used here), undergo polymerization into a unified structure around a surfactant micelle as they proceed through stages of homogeneous and heterogeneous nucleation.[16] In contrast, CeO_2 shells form through the stacking of smaller CeO_2 crystallites, which are approximately 3 – 5 nm in size (Figure 3.2). Precursors that strongly coordinate Ce^{4+} ions,[17] such as cerium–atrane (used here), provide a degree of steric hindrance to mitigate agglomeration into larger crystals and facilitate slow hydrolysis. This process increases the likelihood that CeO_2 crystallites form around Pd core seeds through surfactant–mediated interactions instead of quickly hydrolyzing into larger CeO_2 structures that do not adequately encapsulate Pd. The packing of these smaller CeO_2 grains creates void spaces that provide the shell with its porosity and facilitates reactant accessibility to the active metal. These differences in shell morphology appear responsible for the different BET surface areas of the initial Pd@CeO_2 and Pd@SiO_2, which are 131 and 296 m^2/g, respectively. Pd/CeO_2, whose support also consists of stacks of smaller CeO_2 crystallites, has a surface area of 150 m^2/g. This surface area is comparable to Pd@CeO_2 (see Table 3.1).

Overall, these well-defined structures facilitate a direct comparison of how active metal placement, support shell morphology, and the chemical differences between nonreducible SiO_2 and reducible CeO_2 affect the formation and stability of Pd halo sites during high-temperature exposure.

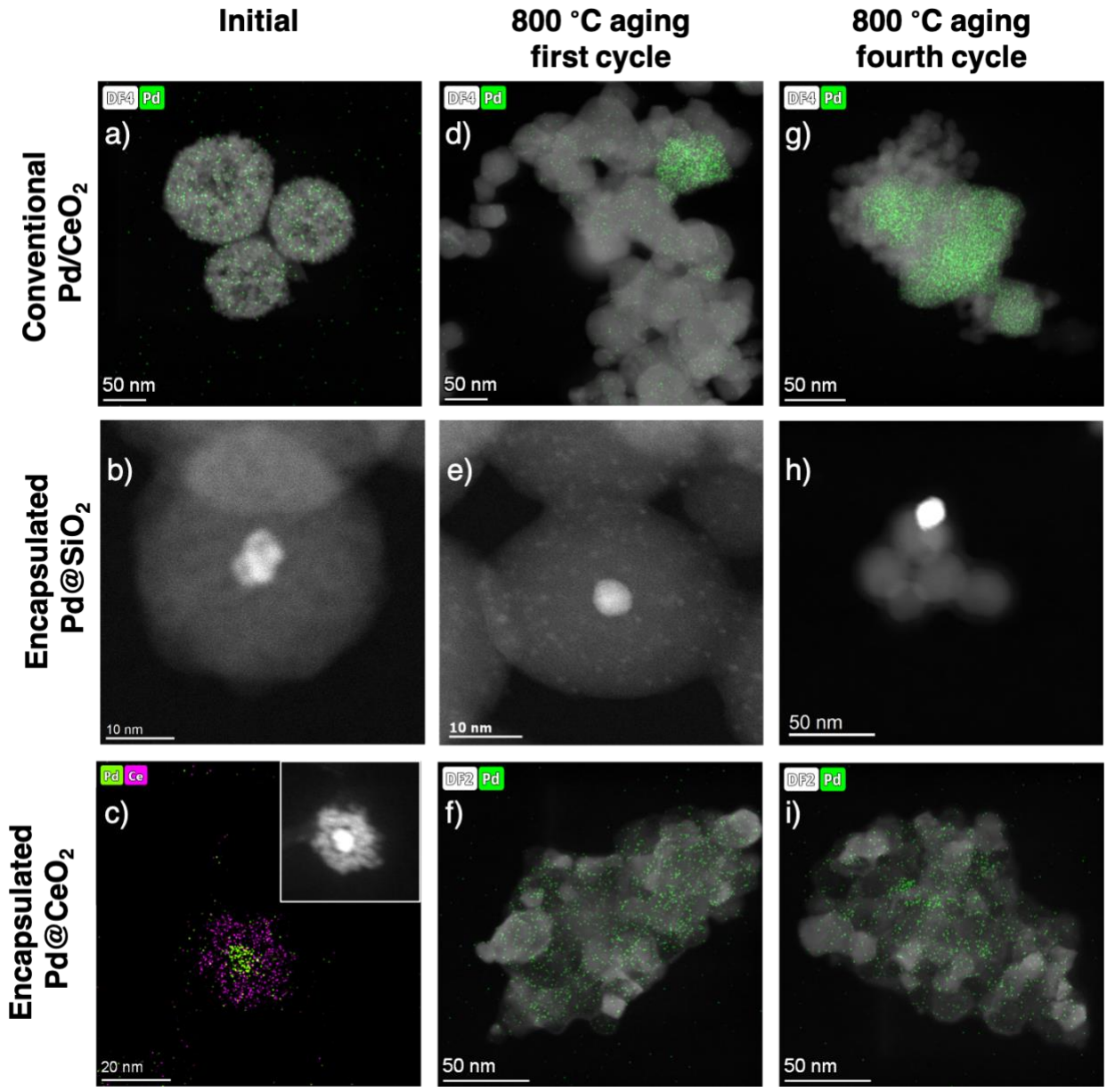

Figure 3.2. Distribution of Pd in initial and cycled catalysts.
Electron microscopy characterization of encapsulated Pd/CeO_2, $Pd@SiO_2$, and $Pd@CeO_2$ as synthesized (a–c), and after one (d–f) and four (g–i) repeated cycles of 4-hour aging at 800°C in air. EDS elemental mapping has been included for Pd/CeO_2 and $Pd@CeO_2$ due to poor Z-contrast between Pd and Ce. Embedded legends on each Figure indicate the corresponding colors for the elemental maps (Pd: Green, Ce: Pink) and the detector used to collect the STEM image (DF: Dark-field). The overlay elemental map of Pd and Ce has been included for initial $Pd@CeO_2$ to demonstrate the relative placement of active metal and support domains as synthesized. The dark-field image that corresponds to the elemental map of the initial $Pd@CeO_2$ is inset.

Table 3.1. Catalytic activity and structural features of samples as a function of aging cycle.

Sample		No. of 4-hour 800°C aging cycles			
		0 (Initial)	**1**	**2**	**4**
Bare CeO_2	CeO_2 crystallite size (nm)	6.4	30.4	32.8	34.2
	BET surface area (m^2/g)	164	18	8	5
Pd/CeO_2	T_{90} (°C)	150	177	199	210
	Pd dispersion (%)	31.8	10.0	8.6	5.9
	CeO_2 crystallite size (nm)	7.8	21.6	25.3	26.6
	BET surface area (m^2/g)	150	33	17	11
$Pd@SiO_2$	T_{90} (°C)	186	177	193	197
	Pd dispersion (%)	35.9	61.9	25.3	11.1
	BET surface area (m^2/g)	296	117	50	32
$Pd@CeO_2$	T_{90} (°C)	153	103	102	103
	Pd dispersion (%)	32.8	88.4	85.7	83.7
	CeO_2 crystallite size (nm)	3.9	6.4	6.5	8.2
	BET surface area (m^2/g)	131	72	63	40

3.2.2 Identifying activity limits through cycled aging

CO oxidation was used as a probe reaction to monitor how nanoscale restructuring affected catalytic performance, as it is particularly sensitive to active site abundance and active site recruitment of lattice oxygen at the metal-support interface when reducible oxide supports, such as CeO_2, are present.[9,10] The rate of CO oxidation at 40°C, as displayed in Figure 3.3a, was normalized by the total mass of Pd present in the catalyst and examined before and after the first cycle of 800°C aging to probe how thermally induced restructuring affected Pd utilization. As a commonly used measure of catalytic activity,[18] the temperature required for 90% conversion of CO, also known as the light-off temperature, or T_{90}, was used to examine structural and functional

stability over the four sequential 800°C aging cycles (Figure 3.3b). See *Section 3.4* for more detail on catalytic testing. As seen in Figure 3.3, Pd@SiO_2 exhibited the poorest utilization of Pd among the initial catalysts, which coincided with the highest T_{90} (186°C). This high T_{90} is attributed to the fact that Pd@SiO_2 does not contain a reducible oxide component, thereby impeding the possibility of high-activity MvK oxidation mechanisms.[10] Instead, CO oxidation on Pd@SiO_2 occurs via Langmuir-Hinshelwood kinetics, which requires the dissociative adsorption of gas-phase O_2. The CeO_2-containing Pd/CeO_2 exhibited a lower T_{90} (150°C) and a higher rate of CO_2 production, normalized by its Pd content, which suggests a greater utilization of the active metal present. Pd@CeO_2 exhibited the greatest Pd utilization among the initial catalysts, with a mass-normalized CO_2 production rate almost one and a half times greater than that observed on conventional Pd/CeO_2. It is possible that CeO_2 encapsulation, which has been shown to enhance interfacial contact,[19] improved the recruitment of lattice oxygen and consequently, the rate of oxidation at low temperatures. However, the T_{90} for the initial Pd@CeO_2 (153°C) was similar to Pd/CeO_2 (150°C). This is likely due to the autocatalytic nature of exothermic CO oxidation as the reaction temperature increases.[20]

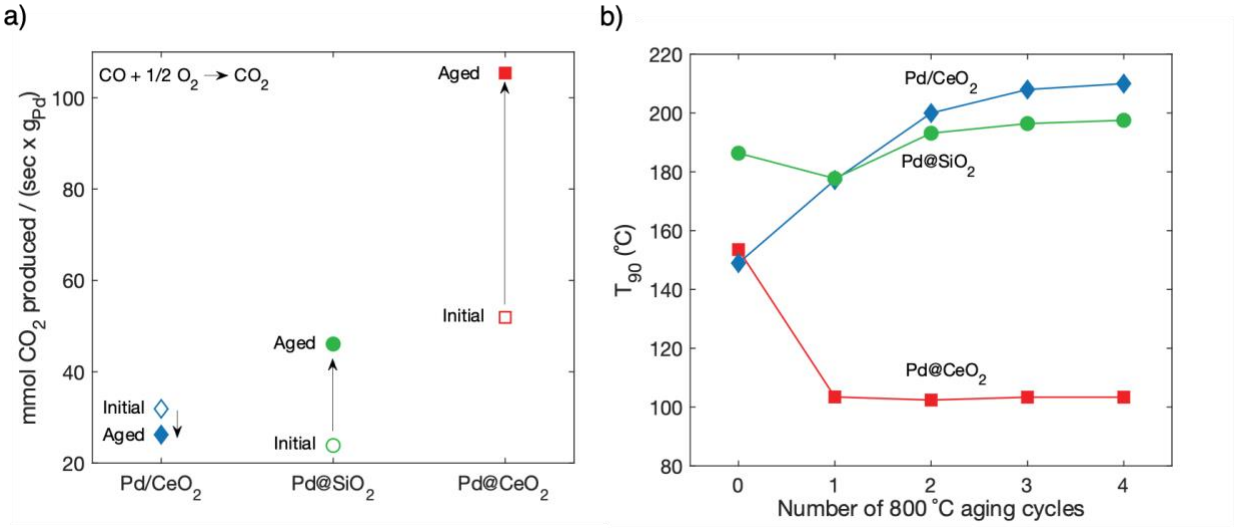

Figure 3.3. Effects of cycled aging on Pd utilization and T_{90} for CO oxidation.

Rate of CO_2 production at 40°C, normalized by the mass content of Pd, for Pd/CeO_2 and encapsulated $Pd@SiO_2$ and $Pd@CeO_2$ as-synthesized and after one cycle of aging (a). Temperature for 90% conversion of CO (T_{90}) for conventional Pd/CeO_2 and encapsulated $Pd@SiO_2$ and $Pd@CeO_2$ as a function of the number of 4-hour 800°C aging cycles in air (b).

3.2.3 Adverse restructuring in conventionally prepared Pd/CeO_2

As demonstrated in Figure 3.4, cycled aging at 800°C revealed diverging trends in the relative stability of the three restructured catalysts. Pd in the conventionally prepared, surface-impregnated Pd/CeO_2 underwent significant sintering, consistent with our previous observations.[1,2] Pd dispersion in Pd/CeO_2 decreased from 31.8 to 10.0%, and average CeO_2 crystallite size increased over two and a half times, from 7.8 to 21.6 nm. The release of atomic oxygen from the lattice of reducible CeO_2, which dramatically affects catalytic performance, is particularly sensitive to changes in active metal dispersion and CeO_2 crystallite size.[21] As such, we used TGA experiments to probe how thermal restructuring affected the ease of oxygen release from the CeO_2 lattice. This data is shown in Table 3.2. Pd/CeO_2 and $Pd@CeO_2$ initially have comparable amounts of lattice oxygen released per mass of catalyst. This agrees well with the similar T_{90} values of the initial Pd/CeO_2 and $Pd@CeO_2$ catalysts as shown in Figure 3.3b. The total oxygen released from Pd/CeO_2 however, decreased over three and a half times from 0.696 to 0.198 mmol O released/g_{cat} after the first cycle of 800°C aging in air. This suggests that the adverse sintering of Pd and CeO_2 in the conventionally-prepared catalyst has impeded the recruitment of lattice oxygen. This loss in utilization coincided with a T_{90} that increased from 150 to 177°C.

Table 3.2. Lattice oxygen release from conventional Pd/CeO_2 and core@shell $Pd@CeO_2$ catalysts.

	Total mmol O released/g_{cat}	
	Initial	Aged
Conventional Pd/CeO_2	0.696	0.198
$Pd@CeO_2$ core@shell	0.536	1.634

It should be noted that the crystallite growth of Pd/CeO_2 was less than that exhibited by a control sample of bare CeO_2, whose domains grew from 6.4 to 30.4 nm after 800°C aging. There was also better retention of porosity in Pd/CeO_2 (33 m^2/g) compared to bare CeO_2 (18 m^2/g) after aging (Table 3.1). This suggests that the presence of active metal can impede support sintering at elevated temperatures. It is possible that the stabilization of CeO_2 in the conventional catalyst was conferred by some Pd species that remained dispersed, as seen in EDS analysis (Figure 3.2). Such observations have been corroborated in recent work by Datye *et al.*, which demonstrated that atomically dispersed metal dopants can stabilize the surface area of CeO_2 amidst high-temperature aging.[22] As demonstrated in recent experimental and computational work, metal species can become stabilized or trapped on the surface of CeO_2 supports in high dispersions during periods of thermally induced mobility. The reducibility of CeO_2 facilitates this trapping, as dispersed active metal species can form strong chemical bonds with undercoordinated Ce^{3+}.[4,23–25] While Pd species trapped on CeO_2 exhibit high energetic barriers for mobility, the observation of sintered Pd by EDS, and increased T_{90} after aging support that placing Pd active sites in close proximity through surface decoration promotes sintering over redispersion and trapping at high temperatures. This is consistent with other works which have shown that the initial placement of active metal readily implicates thermal stability.[26,27]

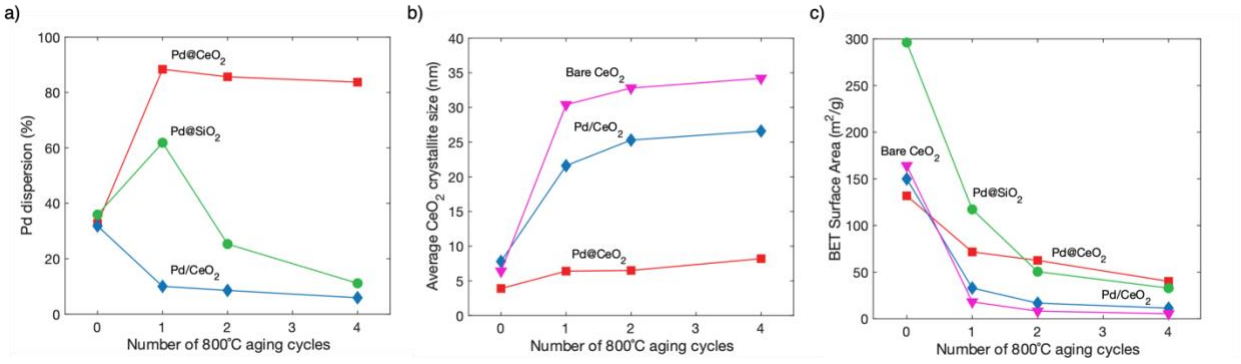

Figure 3.4. Changes in Pd dispersion, average CeO_2 crystallite size, and BET surface area with cycled aging.

Pd dispersion as calculated from CO chemisorption for Pd/CeO_2, $Pd@SiO_2$, and $Pd@CeO_2$ catalysts as a function of the number of 4-hour 800°C aging cycles in air (a). Average CeO_2 crystallite size as calculated by the Debye-Scherrer equation applied to XRD patterns of Pd/CeO_2, $Pd@CeO_2$ and bare CeO_2 nanospheres (b). BET surface area as determined by N_2 physisorption (c).

Pd and CeO_2 continued to agglomerate with successive aging cycles. By the end of the fourth 800°C aging cycle, the Pd dispersion dropped over five times to 5.9%. This sintering is supported by XRD analysis, which shows a sharp peak corresponding to the (111) plane of bulk Pd.[15] The CeO_2 crystallite size increased over three times to 26.6 nm, and the BET surface area had dropped around ten times to 11 m^2/g. Thus, the initial 800°C aging caused the most profound restructuring, with the relative magnitude of sintering dropping with each successive aging cycle. The continued sintering of Pd/CeO_2 resulted in a gradual increase in T_{90}. Similar to the Pd dispersion loss and CeO_2 domain growth trends, the T_{90} increase was more severe after the first aging cycle and plateaued over sequential cycles to a value of 210°C. By the fourth exposure to 800°C aging conditions, Pd/CeO_2 had achieved a stable, albeit catalytically less active, structural state.

3.2.4 Metastability of halo sites in $Pd@SiO_2$

In contrast to the surface-impregnated Pd/CeO_2, the encapsulated $Pd@SiO_2$ catalyst exhibited the formation of Pd halo sites, which increased dispersion from 35.9 to 61.9%, after an initial 800°C aging (Figure 3.4, Table 3.1). Coinciding with the appearance of these sites was an increase in active metal utilization and a concurrent decrease in T_{90}. The $Pd@SiO_2$ catalyst exhibited a T_{90} that decreased from 186 to 177°C, corresponding to a decrease of ~5%. Due to the non-reducible nature of the supporting SiO_2 shell, the improvements in Pd utilization and low-temperature activity are attributed solely to redispersion increasing the availability of active metal sites for reaction. Recent work by Cargnello *et al.* demonstrated that whole particle migration and coalescence could exist as the dominant restructuring mechanism in Pd/SiO_2 catalysts during

800°C aging.[27] In the core@shell system, however, we observe the coexistence of Pd cores alongside dispersed halo sites after the first cycle of aging. This suggests that total particle migration and coalescence is not the dominant restructuring mechanism in core@shell architectures. Several computational[23,28] and experimental[29–33] works suggest that the decomposition or disintegration of larger clusters into smaller mobile species can also occur in 800°C aging conditions. As such, it appears that encapsulation promotes active metal disintegration and transport, which is a process that is limited by the emission of mobile species. This may be due to steric effects imposed by the average pore size of the shell (1.7 nm) being twice as narrow as the initial core size (3 – 5 nm). To this end, we observed an aged Pd@SiO_2 nanoparticle that contained redispersed Pd along with two Pd cores that had not sintered together Figure 3.5. If particle migration was dominant in encapsulated morphologies, these two Pd cores would not exist as separate entities after high temperature aging. As such, this observation is consistent with the notion that encapsulation promotes active metal disintegration and redispersion, instead of total particle migration and coalescence, during high-temperature exposure. TEM investigation also identified some aged Pd cores that do not appear as unified nanoparticles as seen in the initial structures. Instead, these cores appear to have fragmented into many smaller Pd clusters, as seen in Figure 3.5. This observation also supports that Pd cores in encapsulated architectures do not migrate as single entities during high-temperature aging, but instead restructure through disintegration and emission. Consequently, it appears that encapsulation facilitates favorable restructuring by providing a physical barrier that promotes the emission-limited mobility of small metal species and inhibits local agglomeration through its porous, tortuous structure.

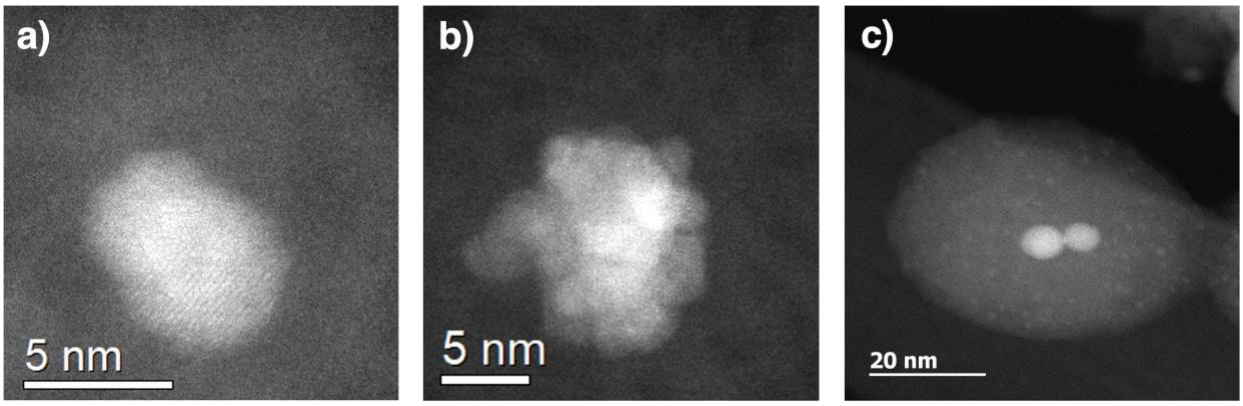

Figure 3.5. Characterization of active metal cores in Pd@SiO_2.
Core regions of Pd@SiO_2 (a) as synthesized and (b) after the first 800°C aging cycle. (c) A serendipitous finding of a Pd@SiO_2 particle after the first 800°C aging cycle with two Pd cores.

The existence of halo sites in Pd@SiO_2 is short-lived, however. Cycled aging led to the eventual sintering of Pd in the Pd@SiO_2 system after subsequent aging cycles. Pd dispersion dropped from 61.9% to 25.3% between the first and second 800°C aging cycle and proceeded to drop over five times to 11.1% by the fourth aging cycle. STEM analysis identified that the Pd did not remain within the encapsulating SiO_2 envelope but had moved to the external surface of the supporting shell where it was locally sintered. The Pd@SiO_2 catalyst also exhibited a significant loss in porosity over the four sequential aging cycles, as the surface area dropped from 296 to 32 m^2/g (Figure 3.4, Table 3.1). These adverse morphological changes are reflected in the loss of catalytic activity. The T_{90} increased to 193°C and 197°C after the second and fourth cycles, respectively.

Our observation of initial dispersion and formation of halo sites, followed by sintering, suggests that the chemical interactions between the Pd metal and SiO_2 support are insufficient to prevent mobile species from eventually agglomerating at high temperatures. On SiO_2 supports, active metals are known to coordinate with silanol groups through dehydrogenation.[34,35] As demonstrated in work by Guo *et al.*, the interaction between dispersed metal and the SiO_2 support is relatively weak, as even mild temperature (500°C) conditions can dislocate PGM from these

isolated sites and induce local agglomeration into small, nanosized clusters.[34] It appears that such a phenomenon occurs in Pd@SiO_2 (Figure 3.2). As the concentration of silanol groups is strongly temperature-dependent,[12] it is likely that repeated aging would decrease the number of trapping sites on the SiO_2 support, which would increase the likelihood of sintering.

3.2.5 Performance and stability of halo sites in Pd@CeO_2

Unlike the two catalysts discussed above, which exhibit degradation during high-temperature cycling, the catalytic performance of Pd@CeO_2 obtained after the first aging was retained over four aging cycles (Figure 3.3, Table 3.1). EDS characterization confirmed that the first 800°C aging cycle redistributed core Pd into halo sites. These halo sites appear highly dispersed, as confirmed by electron microscopy and EDS analysis conducted at high magnification and resolution (Figure 3.7). These results are corroborated by CO chemisorption, which shows that dispersion increased by over two and a half times, from 32.8 to 88.4% (Figure 3.4, Table 3.1). Accompanying the improved utilization was a T_{90} that decreased from 153 to 103°C. corresponding to a T_{90} decrease of ~33%, which is greater than that of aged Pd@SiO_2.

The more uniform and complete redispersion of Pd observed after aging Pd@CeO_2, compared to Pd@SiO_2, suggests that the encapsulating CeO_2 environment promotes the formation of highly dispersed halo sites. As both encapsulated catalysts have comparable initial core size and shell thickness, causes for the difference in redispersion appear to be related to the chemistry of the supporting material and the morphology of the encapsulating structure. Concerning chemical differences, Pd species have been shown to be trapped preferentially as single atoms on Ce^{3+} step-edges.[23] Pd cannot be stabilized in this highly dispersed fashion on SiO_2 due to the weaker bonding between metal species and the SiO_2 support. In addition, we previously demonstrated the reducibility of the CeO_2 support was able to facilitate the oxidation and subsequent disintegration

of core Pd to promote redispersion.[2] Regarding morphological differences, the stacked crystallites of the CeO_2 shell, which undergo dynamic restructuring simultaneously with the redispersing Pd, may offer a larger resistance to outward transport of active metal. This would increase the likelihood of trapping on the CeO_2 surface. Furthermore, the theoretical mean free path of gaseous PdO at 800°C, which is on the order of 116 nm, is significantly larger than the average pore diameter of the CeO_2 shell, which is 1.5 nm (see published work[15] for mean free path calculation details). Such considerations emphasize that encapsulation increases the likelihood that Pd species remain separated from one another and readily collide with the CeO_2 surface to become trapped in highly dispersed arrangements during periods of thermally induced transport.

Although the greater redispersion plays a role in promoting activity and utilization, the reducible CeO_2 environment should also be considered because catalytic turnover on reducible oxide supports is strongly dependent on the degree of interfacial contact between the active metal and the support.[9] XPS analysis of the aged Pd@CeO_2 catalyst conducted in our previous work identified that these halo sites exhibit Pd–O–Ce bonding.[2] This is characteristic of dispersed Pd that bonds through an oxygen atom to undercoordinated Ce^{3+}, which are typically located at step and edge sites on CeO_2 crystals.[23,36,37] As demonstrated in recent work by Wang *et al.*, these Pd species adopt a coordination-unsaturated, square-planar structure.[24] The formation of coordination-undersaturated Pd–O–Ce bonds perturb the local electronic environment of the CeO_2, which improves lattice oxygen mobility and, subsequently, oxidative activity at low temperatures.[24,38,39] XPS measurements in the Pd3d scan region of Pd@CeO_2 and Pd/CeO_2 in their initial state, and after the first and fourth cycles of 800°C aging in air, were used to track the abundance of Pd–O–Ce during cycled aging. As shown in Figure 3.6, deconvolution of the XPS spectra showed a distribution of metallic Pd^0, Pd^{2+} as PdO and Pd–O–Ce in the initial Pd/CeO_2

catalyst. The abundance of Pd–O–Ce increased slightly after the first aging cycle, which is consistent with notion that some Pd was redispersed on the surface of the CeO_2 nanospheres during elevated temperature aging. The abundance of Pd–O–Ce appreciably decreased by the fourth aging cycle, however, giving rise to peak growth in regions characteristic of Pd^0. This loss in Pd–O–Ce species likely contributes to the activity loss observed in aged Pd/CeO_2. The initial Pd@CeO_2 sample was not subjected to deconvolution due to the low relative Pd signal obtained. This is likely due to screening from the encapsulating CeO_2 shell. As Pd redisperses throughout the CeO_2 shell during elevated temperature aging, the population of metal that exists within the photoelectron escape depth of the XPS instrument increases.[2] This improves signal collection and permits deconvolution. Deconvolution identified Pd–O–Ce as the most abundant form of Pd on the aged Pd@CeO_2 catalyst. The abundance of this type of oxidized Pd, which is known to promote facile oxygen transfer on CeO_2 supports and oxidative activity, likely contributes to the superior performance of the catalyst.

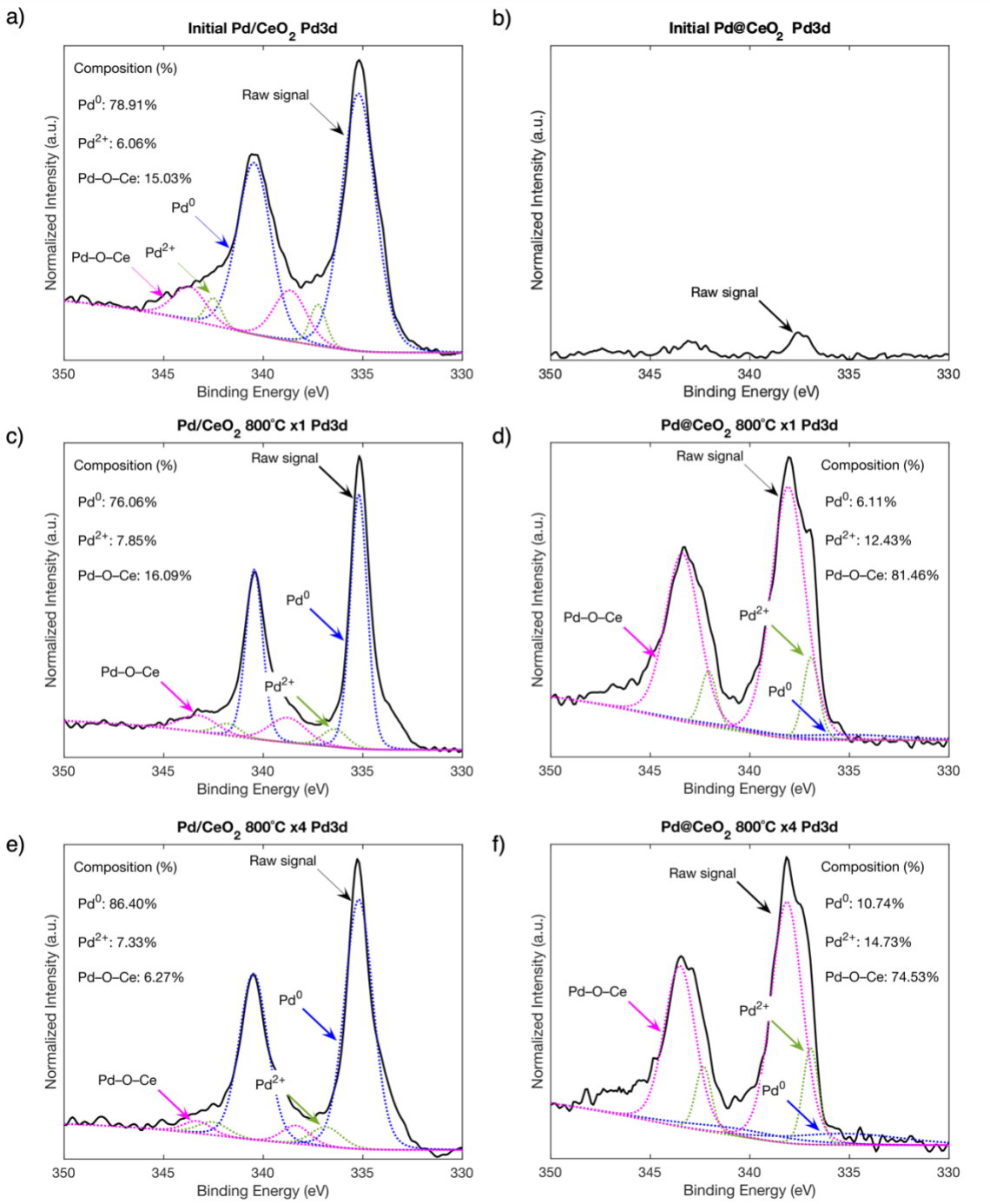

Figure 3.6. Effects of thermal aging on Pd oxidation state distribution.
Effects of thermal aging on Pd oxidation state distribution. XPS spectra of the Pd3d scan region of Pd/CeO_2 and $Pd@CeO_2$ in their initial state (a, b) and after one '×1' (c, d) and four '×4' (e, f) repeated cycles of 4-hour 800°C aging in air. The relative percentage of each type of Pd, obtained through spectra deconvolution, have been inset.

TGA experiments confirmed that the formation of halo sites improved the ease of abstracting oxygen from the CeO_2 lattice, particularly at the low temperatures (≤150°C) where aged $Pd@CeO_2$ exhibits its superior catalytic performance. The total amount of oxygen released

in Pd@CeO_2 increased from 0.536 to 1.634 mmol O released/g_{cat} after aging. XPS analysis in the O1s scan region for Pd/CeO_2 and Pd@CeO_2 after the first cycle of 800°C air aging was also conducted to examine how thermally induced restructuring affected the distribution of oxygen species on the catalyst. Deconvolution on the obtained spectra indicated that both catalysts exhibit varying abundances of three types of oxygen: O_I, which is associated with bulk oxygen in the CeO_2 lattice,[40,41] O_{II}, which is associated with surface bound oxygen species and/or oxygen vacancies,[41,42] and O_{III}, which is associated with hydroxyl groups or H_2O bound to the surface of CeO_2.[43] O_{II}, which has been discussed in literature as being particularly mobile on CeO_2 supports and thus contributing to improved oxidative activity, is over 1.5 times more abundant in Pd@CeO_2 than Pd/CeO_2 after the first cycle of aging (Table 3.3). As such, it is likely that the superior Pd redispersion and greater access to lattice oxygen are working synergistically here to improve catalytic performance. It should be noted that this type of bonding has been leveraged to improve activity on metal oxide supports beyond CeO_2, such as TiO_2.[44]

Table 3.3. Oxygen composition for conventional Pd/CeO_2 and core@shell Pd@CeO_2 catalysts.

	O_I / O_{II} / O_{III} composition (%)	
	800°C ×1	800°C ×4
Conventional Pd/CeO_2	61.36 / 18.62 / 20.02	58.07 / 9.73 / 32.2
Pd@CeO_2 core@shell	42.95 / 30.37 / 26.68	40.8 / 17.29 / 41.91

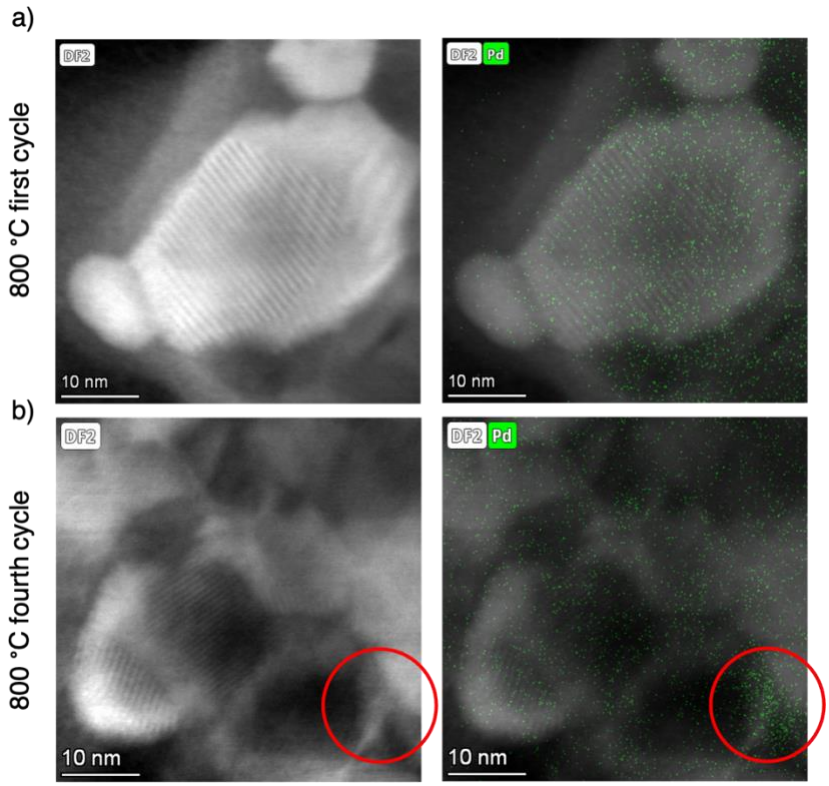

Figure 3.7. Examining Pd distribution in aged Pd@CeO_2.
High-resolution TEM and overlaid EDS elemental mapping of Pd@CeO_2 catalysts after one (a) and four (b) repeated cycles of 4-hour 800°C aging in air. Embedded legends on each Figure indicate the corresponding colors for the elemental maps (Pd: Green) and the detector used to collect the STEM image (DF: Dark-field). Red circles highlight grain boundaries between multiple restructured CeO_2 crystallites, where Pd appears to have localized after sequential aging.

Cycled aging of Pd@CeO_2 resulted in slight CeO_2 support growth and Pd dispersion loss. The slight loss of Pd dispersion was reflected in XPS experiments as the abundance of Pd–O–Ce was seen to drop from 81.46 to 74.53% between the first and fourth cycles of 800°C aging. However, these effects were significantly smaller than in the other catalysts and did not readily affect catalytic performance as the low T_{90} obtained after the first aging was retained after four aging cycles (Figure 3.7, Table 3.1). Pd@CeO_2 also exhibited the greatest surface area (40 m^2/g) among all catalysts subjected to the four aging cycles, which further demonstrates the relative stability of the structure. The most apparent structural change as result of cycled aging is the that the supporting domains between Pd@CeO_2 particles had grown together during high-temperature aging. XRD analysis shows that the CeO_2 domains grow, albeit slightly, from ~4 nm to ~8 nm by

the fourth aging cycle. This slight rearrangement and growth may be responsible for the observed localizing of halo sites at CeO_2 grain boundaries, as shown in Figure 3.7. This localizing, however, did not significantly impact the Pd dispersion, as it dropped only slightly from 88.4 to 83.7%. CO chemisorption and light-off experiments also confirm that the crystallite growth did not adversely affect gas-phase accessibility to active sites.

Overall, the robust catalytic performance of Pd@CeO_2 can be attributed to the ability of the support to effectively trap Pd and the synergistic slowing down of CeO_2 grain growth. The CeO_2 crystallites that form the encapsulating shell are favorable for facilitating active metal trapping. They exhibit a high abundance of step and edge sites relative to their volume (Figure 2.2), containing undercoordinated Ce^{3+} that can readily form strong chemical bonds with mobile PGM species.[4,45] Furthermore, comparison with the adverse growth of both Pd and CeO_2 domains on conventional Pd/CeO_2 demonstrates that the stabilization of supporting crystallites scales with the degree of metal redispersion. This demonstrates the importance of encapsulated morphologies for directing the formation of abundant and highly dispersed halo sites that can effectively stabilize support morphology. Such observations are consistent with previous works, which show that M–O–Ce bonding (where M is a PGM) on CeO_2 slows sintering and support collapse.[22,24,46] A number of computational studies demonstrate the stability of Pd trapped on CeO_2 surfaces.[36,47–49] It is the strength of these interactions and the physical intercalation of metal species that likely stabilizes the Pd halo sites, as well as the supporting CeO_2 domains. A schematic interpretation of the formation and stability of Pd halo sites in Pd@SiO_2 and Pd@CeO_2 is presented in Figure 3.8 to summarize these findings. The consistent performance and structural stability of aged Pd@CeO_2 experimentally validate how precise tuning of support morphology and chemistry can improve material utilization and robustness in high-temperature conditions.

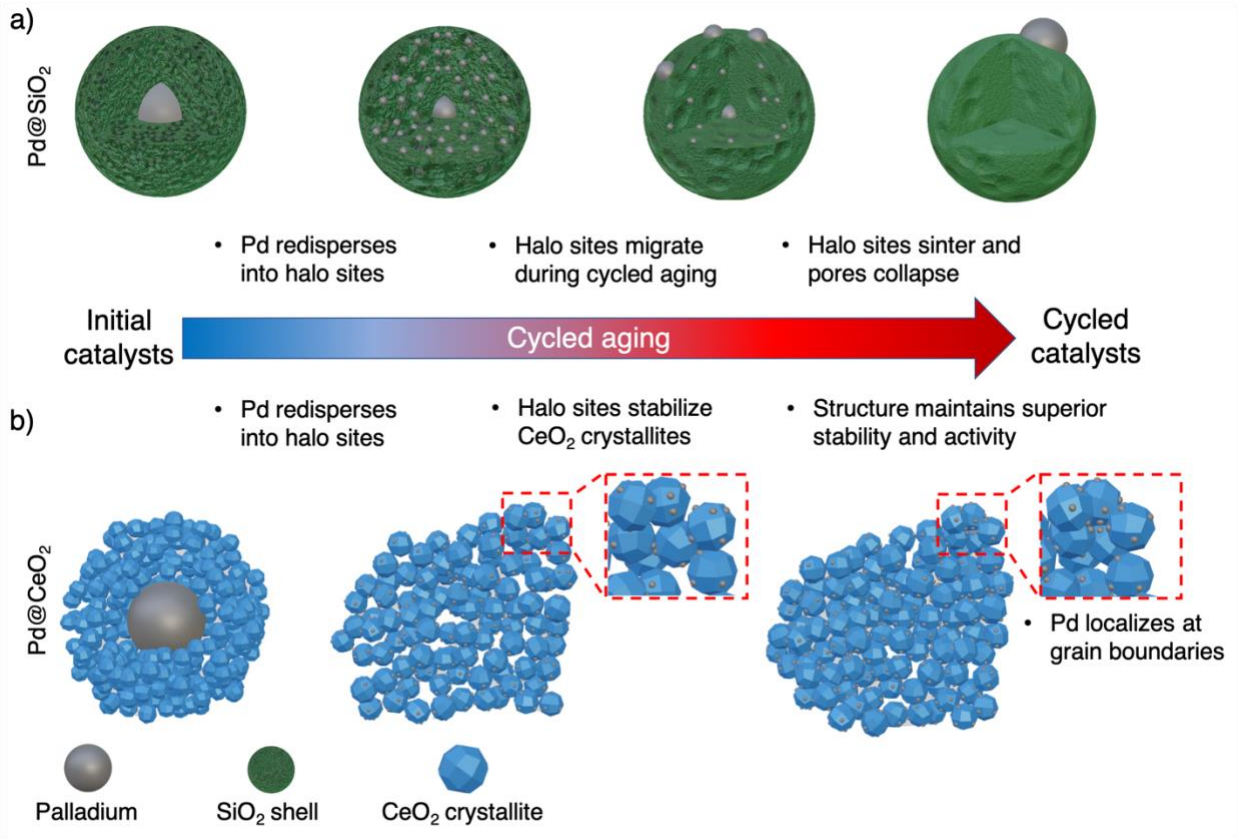

Figure 3.8. Graphical depiction of the restructuring of $Pd@SiO_2$ (a) and $Pd@CeO_2$ (b) catalysts.

3.2.6 Understanding the role of support reducibility on halo site stability

The reducibility of the CeO_2 shell support dramatically improves both catalytic performance and stability through the formation of strong metal-support interactions.[13,39,50] As such, we sought to better understand the role of support reducibility in promoting the stability of dispersed Pd species. To achieve this, we aged the $Pd@CeO_2$ catalyst, after forming halo sites through 800°C air aging, in a completely reduced state, as shown in Figure 3.9. Complete reduction of the catalyst was performed by cutting the flow of gaseous O_2 in the presence of 1% CO and N_2, as demonstrated in previous work.[2] For conciseness, we refer to this aging protocol as 'reduced' aging (see *Section 3.4* for reduced aging protocols and published work for additional characterization).[15]

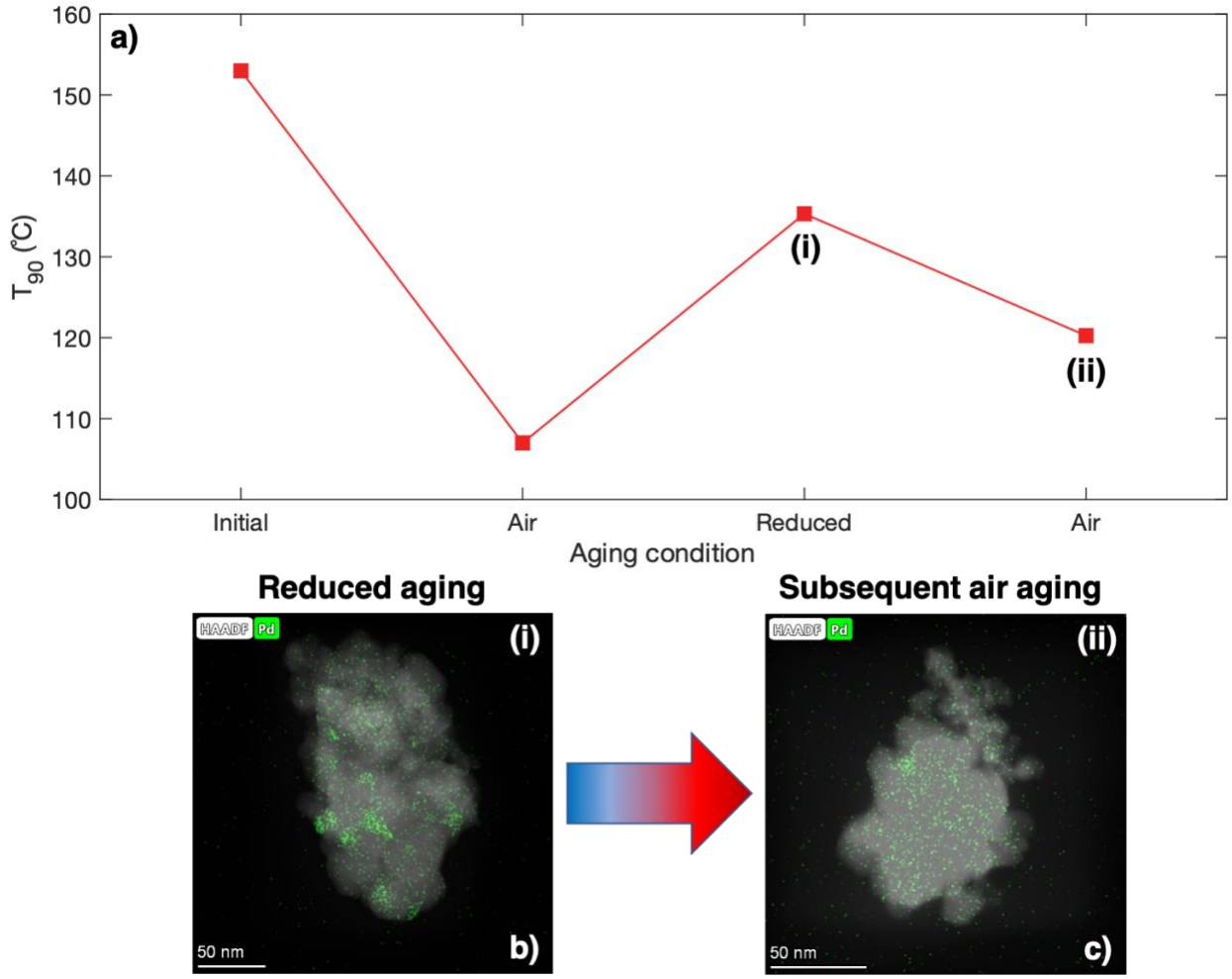

Figure 3.9. Influence of aging in a reduced environment on Pd@CeO_2 structure and activity.
T_{90} for CO oxidation for Pd@CeO_2, which has been subsequently aged in air (Air aging), then reduced under the flow of excess CO and aged at 800°C in pure N_2 (Reduced aging), and then subsequently aged again in air at 800°C (a). STEM analysis with overlaid EDS elemental mapping of the latter two aging cycles have been included to elucidate trends in Pd dispersion (b, c). These microscopy images have been labelled as (i) and (ii) respectively, to indicate which data points they correspond to in Figure 3.9a.

The bonding of dispersed active metal species that exhibit M–O–Ce coordination is mediated through atomic oxygen.[51–53] As such, it is expected that conditions which perturb the stability of that oxygen species would dislocate trapped active metal. Consistent with this expectation, reduced aging at 800°C appeared to affect halo site stability adversely. EDS analysis identified some Pd species that seemed to remain dispersed. However, several Pd agglomerates, some on the order of ~25 nm in diameter, were also observed. The loss of some halo sites also

appeared to affect the stability of polycrystalline CeO_2, as grains larger than those obtained after four cycles of 800°C aging in air were seen under STEM inspection. Coinciding with this adverse restructuring was a T_{90} for CO oxidation that increased from 103 to 135°C. This finding builds upon our previous work, which showed that the reducibility of CeO_2 could promote Pd redispersion,[2] by demonstrating that the oxidation state of CeO_2 helps stabilize halo sites during high-temperature exposure. Kim *et al.* showed that subjecting catalysts with appreciable Pt–O–Ce sites to reducing conditions can remove some of the oxygen species that promote anchoring, adversely affecting the structural stability.[46] Our findings from the reduced aging of Pd@CeO_2, which are consistent with this past literature, support the conclusion that the stability of atomic oxygen, which mediates the interaction between dispersed active metal and metal oxide supports, directly affects the overall stability of Pd halo sites.

The T_{90} value of the reduced aged Pd@CeO_2 (135°C) is lower than that of the initial Pd@CeO_2, likely due to the partial retention of highly dispersed halo sites as confirmed by EDS analysis. This T_{90} value is also lower than that of a Pd@CeO_2 catalyst that has been subjected to reduced aging prior to the 800°C air aging protocol that forms halo sites (186°C). These observations suggest that Pd halo sites exhibit greater resistance to adverse restructuring under highly reducing, elevated temperature conditions than as-prepared Pd species. The Pt species in the study conducted by Kim *et al.* exhibited improved stability to the adverse reduction that promotes metal dislocation and sintering due to the strong Pt–O–Ce bonding that forms after 800°C exposure.[46] As such, the abundance of Pd–O–Ce bonding likely contributes to the improved stability of halo sites under high-temperature reducing conditions.

To examine the role of catalyst oxidation for promoting favorable restructuring, we aged the partially deactivated, reduced Pd@CeO_2 back in air at 800°C for 4 hours. As shown in

Figure 3.9, returning to these aging conditions recovered a portion of the low-temperature catalytic performance as the T_{90} decreased from 135 to 120°C. EDS analysis identified a greater abundance of dispersed Pd halo sites, which is likely the cause for the improved T_{90}. Although some larger Pd agglomerates persisted, our observations demonstrate that aging at 800°C in air can regenerate a portion of the Pd halo sites that have sintered. Our findings agree with other works that have emphasized the importance of controlling redox conditions for directing the restructuring behavior of Pd.[31,54]

3.3 Conclusions

In this work, we sought to understand the formation, activity, and structural stability of nanoscale Pd halo sites formed by exposing core@shell catalysts repeatedly to the high-temperature conditions commonly encountered in industrial applications. While encapsulation improves metal utilization and activity through the formation of halo sites, our cycled aging experiments indicate that these sites cannot be maintained in all catalysts. The weak bonding between Pd and SiO_2 makes halo sites in Pd@SiO_2 susceptible to continued Pd transport and ultimately sintering. In contrast, the formation of halo sites improves structural stability in Pd@CeO_2, likely due to the Pd–O–Ce bonding that forms between the CeO_2 support and dispersed Pd. In stabilizing step and edge sites on the CeO_2 lattice, halo sites were found to mitigate the adverse sintering and structural collapse of support domains during cycled high-temperature aging. The retention of the Pd@CeO_2 catalyst's superior low-temperature performance between the first and fourth aging cycles emphasizes that favorable restructuring in core@shell architectures can significantly improve catalytic lifetime. By subjecting the Pd@CeO_2 catalyst to reduced aging, we further demonstrate that the oxidation state of the support is integral to stabilizing high dispersions of the active metal. Returning to air aging conditions can regenerate a portion of highly dispersed

species from larger agglomerates, which delineates a simple methodology for recovering dispersion and activity on-stream. By examining the stability of highly active halo sites in core@shell architectures, we demonstrate how the initial catalyst can be designed to promote favorable high-temperature nanoscale restructuring that improves catalytic performance, stability, and material utilization.

3.4 Experimental Details

3.4.1 *Synthesis of surface-impregnated (conventionally supported) Pd/CeO_2*

Surface-impregnated Pd/CeO_2 catalysts were prepared by wet impregnating Pd onto already synthesized CeO_2 nanospheres (NS) outlined in *Section 2.4.1*. All initial catalysts were subjected to characterization by transmission electron microscopy and x-ray energy dispersive spectroscopy prior to catalytic testing. After initial characterization to confirm morphology, synthesized samples were split into two batches: one set to be used for catalytic testing and subjected to *in situ* aging and another set for *ex situ* aging and material characterization.

3.4.2 Synthesis of core@shell catalysts

$Pd@CeO_2$ and $Pd@SiO_2$ catalysts were prepared by methods outlined in *Section 2.4.2*. It should be noted that the method of preparing $Pd@CeO_2$ was improved upon by periodically adjusting the pH during the synthesis to maintain alkaline conditions. This was inspired by recent work, which demonstrated that the synthesis pH plays a critical role in mediating the crystallinity and stability of encapsulating metal oxide structures.[55,56]

All initial catalysts were subjected to characterization by transmission electron microscopy and x-ray energy dispersive spectroscopy prior to catalytic testing. Similar to the surface-impregnated Pd/CeO_2, synthesized samples were then split into two batches: one set to be used for

catalytic testing and subjected to *in situ* aging and another set for *ex situ* aging and material characterization.

3.4.3 Catalyst aging

In situ and *ex situ* aging, as outlined in *Section 2.4.3*, was conducted to examine how cycled aging affected catalyst structure and activity.

In situ Aging to Examine Changes in Catalytic Activity: Upon completing an initial light-off test (see below for light-off test reaction conditions), catalysts were left to cool to ambient conditions under the flow of dry air at 200 mL/min. Once cooled, the catalysts were heated to 800°C with a ramp of 5°C/min under flowing air at 200 mL/min. Finally, the catalysts were held at 800°C for 4 hours. This defined one cycle of 800°C aging. Once the 4-hour aging period had finished, the catalysts were cooled to 35°C, and the flowing gas was changed from air to the test gas (see below for test gas information). This cycled aging and light-off testing was repeated until four cycles of 800°C aging had been conducted.

Ex situ Aging to Examine Changes in Catalyst Structure and Morphology: Catalyst samples were placed in a tube furnace and heated to 800°C with a ramp of 5°C/min under flowing air at 200 mL/min. The catalysts were held at 800°C for 4 hours. This process defined one cycle of 800°C aging. Once the 4-hour aging period had finished, the catalysts were cooled to ambient temperature, removed from the tube furnace, and subjected to characterization (see below for more information). This cycled aging and characterization was repeated until four cycles of 800°C aging had been conducted.

In situ Reduced Aging of Pd@CeO_2: Two sets of initial Pd@CeO_2 catalyst were subjected to aging while the supporting ceria was reduced to examine the role of support reducibility in facilitating Pd mobility and trapping. Reduction of the Pd@CeO_2 catalyst was conducted at 300°C

after the conclusion of a light-off test to maintain 100% conversion of CO. The flow of gas-phase O_2 was cut, and the catalyst was exposed to flowing 1% CO in an N_2 gas balance for 15 minutes. The CO conversion, which was monitored by downstream FTIR, was confirmed to drop to zero over this timeframe, which indicated the complete reduction of the ceria support. This O_2-cut approach was described in our previous work.[2] Once the support was reduced, the flow of CO was cut, and the Pd@CeO_2 was aged at 800°C for 4 hours in pure N_2 flowing at 200 mL/min to ensure the support would not re-oxidize. Once the 4-hour aging period had finished, the catalysts were cooled to ambient temperature and exposed to 2.5% O_2 with an N_2 gas balance, flowing at 200 mL/min for 2 hours prior to light-off testing to ensure re-oxidation of the support. One set of Pd@CeO_2 was subjected to this N_2 aging after an initial light-off test, and another set of Pd@CeO_2 was subjected to N_2 aging after being aged *in situ* under the flow of air at 800°C for 4 hours.

3.4.4 Catalyst testing parameters

CO oxidation light-off tests were used to examine catalytic activity. Catalyst preparation, reactor set up and analysis was identical to that outlined *Section 2.4.4*. A notable difference is the temperature range used to conduct the light-off experiments. The encapsulating furnace temperature was raised from 50°C to 300°C, achieved by a 2°C/min ramp. Catalysts were subjected to a variety of *in situ* aging in the testbed after initial testing.

Rate of CO Conversion to Probe Pd Utilization: The rate of CO_2 production at 40°C, normalized by the mass content of Pd within each catalyst, was used to probe active metal utilization prior to and post 800°C aging. 40°C was used for the experiment to ensure a completely kinetic regime. During each experiment, the conversion of CO was monitored at 40°C for 30 minutes and averaged. The rate was calculated as follows:

$$r_{CO2}\left[\frac{mmol}{\text{sec} \times g_{Pd}}\right] = \frac{\dot{N}_{CO,in} \times X_{CO,40\,^{\circ}C}}{m_{Pd}}$$

where r_{CO2} is the rate of CO_2 conversion, $\dot{N}_{CO,in}$ is the inlet molar flow rate of CO, $X_{CO,40\,^{\circ}C}$ is the conversion of CO at 40°C and m_{Pd} is the mass of Pd present in the catalyst.

3.4.5 Material characterization

Sample characterization was done using seven techniques: transmission electron microscopy (TEM), X-ray energy dispersive spectroscopy (EDS), thermogravimetric analysis (TGA), X-ray photoelectron spectroscopy (XPS), X-ray powder diffraction (XRD), Brunauer−Emmett−Teller-derived N_2 physisorption surface analysis (BET), and CO chemisorption. Refer to *Section 2.4.5* for details pertaining to that latter four techniques, as characterization and acquisition methods were identical. XPS data analysis differed in that the integrated intensity of the deconvoluted peaks were used to calculate the composition [%] of various oxidation states with the samples.

A Thermo Fisher Talos F200X G2 S/TEM was used for simultaneous conventional bright-field, dark-field and scanning transmission electron microscopy (STEM) imaging and EDS elemental mapping. The electron source was an X-FEG high-brightness Schottky-type emission gun. A Super-X windowless EDS detector was used to conduct EDS mapping. A JEOL 3100R05 double Cs corrected S/TEM was used for high-resolution aberration-corrected bright-field and high-angle annular dark-field imaging (HAADF). The electron source was a tungsten cold field emission tip.

Thermogravimetric analysis of the Pd/CeO_2 and $Pd@CeO_2$ catalysts was conducted before and after the first cycle of 800°C aging to quantitatively examine how thermally induced restructuring affected the release of oxygen from the CeO_2 lattice, which plays a role in mediating

catalytic performance in oxidation reactions. A TA Q500 thermogravimetric analyser (TA Instruments) was used to perform the TGA experiments. According to previous work by Schwank *et al.*,[57] initial catalyst samples were loaded onto the TGA sample pan and pretreated under pure N_2 gas flowing at 100 mL/min for 1 hour at 300°C, achieved with a ramp of 5°C/min. This was done to remove any adsorbed water from the catalyst. The catalyst was then cooled to 50°C. Once the weight was stable at 50°C, the gas flow was switched to a 4% H_2/ N_2 mixture (also at 100 mL/min) and the sample was kept at 50°C for 4 hours. The sample was then heated by 50°C with a ramp of 5°C/min, and left at 100°C for 4 hours. This process of ramping to the next temperature, point at intervals of 50°C and holding at each temperature point for 4 hours, was repeated until the temperature reached 600°C. The amount of oxygen released at each temperature, normalized by the mass of catalyst, was calculated as follows:

$$n_{O,c}\left[\frac{\text{mmol}}{g_{cat}}\right] = \left(\frac{\bar{m}_{T,p} - \bar{m}_{T,c}\,[\text{mg}]}{16\left[\frac{g}{\text{mol}}\right]}\right) \times \frac{1000\left[\frac{\text{mg}}{g}\right]}{m_{cat}\,[\text{mg}]}$$

where n_O is the mmol amount of oxygen released at the current temperature point, $\bar{m}_{T,p}$ is the mass of the sample at the preceding temperature point averaged over its respective 4-hour dwelling period, $\bar{m}_{T,c}$ is the mass of the sample at the current temperature point averaged over its respective 4-hour dwelling period and m_{cat} is the mass of the catalyst used in the experiment, after the 1-hour pre-treatment at 300°C in pure N_2.

3.5 References

(1) Seo, C. Y.; Chen, X.; Sun, K.; Allard, L. F.; Fisher, G. B.; Schwank, J. W. Palladium Redispersion at High Temperature within the Pd@SiO_2 Core@shell Structure. *Catal. Commun.* **2018**, *108*, 73–76. https://doi.org/10.1016/j.catcom.2018.01.027.

(2) Hill, A. J.; Seo, C. Y.; Chen, X.; Bhat, A.; Fisher, G. B.; Lenert, A.; Schwank, J. W. Thermally Induced Restructuring of Pd@CeO_2 and Pd@SiO_2 Nanoparticles as a Strategy for Enhancing Low-Temperature Catalytic Activity. *ACS Catal.* **2020**, *10*, 1731 – 1741. https://doi.org/10.1021/acscatal.9b05224.

(3) Jeong, H.; Lee, G.; Kim, B.-S.; Bae, J.; Han, J. W.; Lee, H. Fully Dispersed Rh Ensemble Catalyst To

Enhance Low-Temperature Activity. *J. Am. Chem. Soc.* **2018**, *140*, 9558–9565. https://doi.org/10.1021/jacs.8b04613.

(4) Kunwar, D.; Zhou, S.; Delariva, A.; Peterson, E. J.; Xiong, H.; Pereira-Hernández, X. I.; Purdy, S. C.; Ter Veen, R.; Brongersma, H. H.; Miller, J. T.; et al. Stabilizing High Metal Loadings of Thermally Stable Platinum Single Atoms on an Industrial Catalyst Support. *ACS Catal.* **2019**, *9*, 3978–3990. https://doi.org/10.1021/acscatal.8b04885.

(5) Choi, M. S.; Jeong, H.; Lee, H. Re-Dispersion of Pd-Based Bimetallic Catalysts by Hydrothermal Treatment for CO Oxidation. *RSC Adv.* **2021**, *11*, 3104–3109. https://doi.org/10.1039/D0RA09912K.

(6) Lee, J.; Theis, J. R.; Kyriakidou, E. A. Vehicle Emissions Trapping Materials: Successes, Challenges, and the Path Forward. *Appl. Catal. B Environ.* **2019**, *243*, 397–414. https://doi.org/10.1016/j.apcatb.2018.10.069.

(7) Trovarelli, A.; de Leitenburg, C.; Boaro, M.; Dolcetti, G. The Utilization of Ceria in Industrial Catalysis. *Catal. Today* **1999**, *50*, 353–367. https://doi.org/10.1016/S0920-5861(98)00515-X.

(8) Freund, H.-J.; Meijer, G.; Scheffler, M.; Schlögl, R.; Wolf, M. CO Oxidation as a Prototypical Reaction for Heterogeneous Processes. *Angew. Chemie Int. Ed.* **2011**, *50*, 10064–10094. https://doi.org/10.1002/anie.201101378.

(9) Cargnello, M.; Doan-Nguyen, V. V. T.; Gordon, T. R.; Diaz, R. E.; Stach, E. A.; Gorte, R. J.; Fornasiero, P.; Murray, C. B. Control of Metal Nanocrystal Size Reveals Metal-Support Interface Role for Ceria Catalysts. *Science.* **2013**, *341*, 771–773. https://doi.org/10.1126/science.1240148.

(10) Puigdollers, A. R.; Schlexer, P.; Tosoni, S.; Pacchioni, G. Increasing Oxide Reducibility: The Role of Metal/Oxide Interfaces in the Formation of Oxygen Vacancies. *ACS Catal.* **2017**, *7*, 6493–6513. https://doi.org/10.1021/acscatal.7b01913.

(11) Choi, Y. S.; Moschetta, E. G.; Miller, J. T.; Fasulo, M.; McMurdo, M. J.; Rioux, R. M.; Tilley, T. D. Highly Dispersed Pd-SBA15 Materials from Tris(Tert-Butoxy)Siloxy Complexes of Pd(II). *ACS Catal.* **2011**, *1*, 1166–1177. https://doi.org/10.1021/cs2002719.

(12) Goldsmith, B. R.; Peters, B.; Johnson, J. K.; Gates, B. C.; Scott, S. L. Beyond Ordered Materials: Understanding Catalytic Sites on Amorphous Solids. *ACS Catal.* **2017**, *7*, 7543–7557. https://doi.org/10.1021/acscatal.7b01767.

(13) Pereira-Hernández, X. I.; DeLaRiva, A.; Muravev, V.; Kunwar, D.; Xiong, H.; Sudduth, B.; Engelhard, M.; Kovarik, L.; Hensen, E. J. M.; Wang, Y.; et al. Tuning Pt-CeO_2 Interactions by High-Temperature Vapor-Phase Synthesis for Improved Reducibility of Lattice Oxygen. *Nat. Commun.* **2019**, *10*, 1358. https://doi.org/10.1038/s41467-019-09308-5.

(14) Seo, C.; Yi, E.; Nahata, M.; Laine, R. M.; Schwank, J. W. Facile, One-Pot Synthesis of Pd@CeO_2 Core@shell Nanoparticles in Aqueous Environment by Controlled Hydrolysis of Metalloorganic Cerium Precursor. *Mater. Lett.* **2017**, *206*, 105–108. https://doi.org/10.1016/j.matlet.2017.06.114.

(15) Hill, A. J.; Bhat, A.; Berquist, Z. J.; Fisher, G. B.; Lenert, A.; Schwank, J. W. Stabilizing Highly Dispersed Halo Sites in Thermally Restructured Palladium Core@Shell Nanoparticles for Improved Catalyst Activity and Durability. *ACS Appl. Nano Mater.* **2021**, *4* (10), 10985–10998. https://doi.org/10.1021/acsanm.1c02436.

(16) Huang, Y.; Pemberton, J. E. Synthesis of Uniform, Spherical Sub-100 Nm Silica Particles Using a Conceptual Modification of the Classic LaMer Model. *Colloids Surfaces A Physicochem. Eng. Asp.* **2010**, *360*, 175–183. https://doi.org/10.1016/j.colsurfa.2010.02.031.

(17) Cargnello, M.; Wieder, N. L.; Montini, T.; Gorte, R. J.; Fornasiero, P. Synthesis of Dispersible Pd@CeO_2 Core-Shell Nanostructures by Self-Assembly. *J. Am. Chem. Soc.* **2010**, *132*, 1402–1409. https://doi.org/10.1039/b916035c.(20).

(18) Duprat, F. Light-off Curve of Catalytic Reaction and Kinetics. *Chem. Eng. Sci.* **2002**, *57*, 901–911. https://doi.org/10.1016/S0009-2509(01)00409-2.

(19) Ye, J.; Cheng, D.; Chen, F.; Zhan, X. Controlled Synthesis of Sintering-Resistant Pd@CeO_2 Core–Shell Nanotube Catalysts for CO Oxidation. *Ind. Eng. Chem. Res.* **2019**, *58*, 21972–21982. https://doi.org/10.1021/acs.iecr.9b04697.

(20) Peterson, E. J.; DeLaRiva, A. T.; Lin, S.; Johnson, R. S.; Guo, H.; Miller, J. T.; Hun Kwak, J.; Peden, C. H. F.; Kiefer, B.; Allard, L. F.; et al. Low-Temperature Carbon Monoxide Oxidation Catalysed by Regenerable Atomically Dispersed Palladium on Alumina. *Nat. Commun.* **2014**, *5*, 4885.

https://doi.org/10.1038/ncomms5885.
(21) Li, P.; Chen, X.; Li, Y.; Schwank, J. W. A Review on Oxygen Storage Capacity of CeO_2-Based Materials: Influence Factors, Measurement Techniques, and Applications in Reactions Related to Catalytic Automotive Emissions Control. *Catal. Today* **2019**, *327* (February 2018), 90–115. https://doi.org/10.1016/j.cattod.2018.05.059.
(22) Alcala, R.; DeLaRiva, A.; Peterson, E. J.; Benavidez, A.; Garcia-Vargas, C. E.; Jiang, D.; Pereira-Hernández, X. I.; Brongersma, H. H.; Veen, R. ter; Staněk, J.; et al. Atomically Dispersed Dopants for Stabilizing Ceria Surface Area. *Appl. Catal. B Environ.* **2021**, *284*, 119722. https://doi.org/10.1016/j.apcatb.2020.119722.
(23) Su, Y.-Q.; Liu, J.-X.; Filot, I. A. W.; Hensen, E. J. M. Theoretical Study of Ripening Mechanisms of Pd Clusters on Ceria. *Chem. Mater.* **2017**, *29*, 9456–9462. https://doi.org/10.1021/acs.chemmater.7b03555.
(24) Jiang, D.; Wan, G.; García-Vargas, C. E.; Li, L.; Pereira-Hernández, X. I.; Wang, C.; Wang, Y. Elucidation of the Active Sites in Single-Atom Pd_1/CeO_2 Catalysts for Low-Temperature CO Oxidation. *ACS Catal.* **2020**, *10*, 11356–11364. https://doi.org/10.1021/acscatal.0c02480.
(25) Xiong, H.; Datye, A. K.; Wang, Y. Thermally Stable Single-Atom Heterogeneous Catalysts. *Adv. Mater.* **2021**, *2004319*. https://doi.org/10.1002/adma.202004319.
(26) Martin, T. E.; Mitchell, R. W.; Boyes, E. D.; Gai, P. L. Atom-by-Atom Analysis of Sintering Dynamics and Stability of Pt Nanoparticle Catalysts in Chemical Reactions. *Philos. Trans. R. Soc. A Math. Phys. Eng. Sci.* **2020**, *378*, 20190597. https://doi.org/10.1098/rsta.2019.0597.
(27) Goodman, E. D.; Carlson, E. Z.; Dietze, E. M.; Tahsini, N.; Johnson, A.; Aitbekova, A.; Nguyen Taylor, T.; Plessow, P. N.; Cargnello, M. Size-Controlled Nanocrystals Reveal Spatial Dependence and Severity of Nanoparticle Coalescence and Ostwald Ripening in Sintering Phenomena. *Nanoscale* **2021**, *13*, 930–938. https://doi.org/10.1039/D0NR07960J.
(28) Wan, Q.; Hu, S.; Dai, J.; Chen, C.; Li, W.-X. First-Principles Kinetic Study for Ostwald Ripening of Late Transition Metals on TiO_2 (110). *J. Phys. Chem. C* **2019**, *123*, 1160–1169. https://doi.org/10.1021/acs.jpcc.8b08530.
(29) Lieske, H.; Voelter, J. Palladium Redispersion by Spreading of Palladium(II) Oxide in Oxygen Treated Palladium/Alumina. *J. Phys. Chem.* **1985**, *89*, 1841–1842. https://doi.org/10.1021/j100256a001.
(30) Chen, X.; Schwank, J. W.; Fisher, G. B.; Cheng, Y.; Jagner, M.; McCabe, R. W.; Katz, M. B.; Graham, G. W.; Pan, X. Nature of the Two-Step Temperature-Programmed Decomposition of PdO Supported on Alumina. *Appl. Catal. A Gen.* **2014**, *475*, 420–426. https://doi.org/10.1016/j.apcata.2014.01.056.
(31) Lupescu, J. A.; Schwank, J. W.; Dahlberg, K. A.; Seo, C. Y.; Fisher, G. B.; Peczonczyk, S. L.; Rhodes, K.; Jagner, M. J.; Haack, L. P. Pd Model Catalysts: Effect of Aging Environment and Lean Redispersion. *Appl. Catal. B Environ.* **2016**, *183*, 343–360. https://doi.org/10.1016/j.apcatb.2015.10.018.
(32) Chin, Y. H. C.; García-Diéguez, M.; Iglesia, E. Dynamics and Thermodynamics of Pd-PdO Phase Transitions: Effects of Pd Cluster Size and Kinetic Implications for Catalytic Methane Combustion. *J. Phys. Chem. C* **2016**, *120*, 1446–1460. https://doi.org/10.1021/acs.jpcc.5b06677.
(33) Goodman, E. D.; Johnston-Peck, A. C.; Dietze, E. M.; Wrasman, C. J.; Hoffman, A. S.; Abild-Pedersen, F.; Bare, S. R.; Plessow, P. N.; Cargnello, M. Catalyst Deactivation via Decomposition into Single Atoms and the Role of Metal Loading. *Nat. Catal.* **2019**, *2*, 748–755. https://doi.org/10.1038/s41929-019-0328-1.
(34) Bonati, M. L. M.; Douglas, T. M.; Gaemers, S.; Guo, N. Synthesis, Characterization, and Catalytic Properties of Novel Single-Site and Nanosized Platinum Catalysts. *Organometallics* **2012**, *31*, 5243–5251. https://doi.org/10.1021/om200778r.
(35) Rimoldi, M.; Mezzetti, A. Site Isolated Complexes of Late Transition Metals Grafted on Silica: Challenges and Chances for Synthesis and Catalysis. *Catal. Sci. Technol.* **2014**, *4*, 2724–2740. https://doi.org/10.1039/C4CY00450G.
(36) Su, Y.-Q.; Filot, I. A. W.; Liu, J.-X.; Hensen, E. J. M. Stable Pd-Doped Ceria Structures for CH_4 Activation and CO Oxidation. *ACS Catal.* **2018**, *8* (1), 75–80. https://doi.org/10.1021/acscatal.7b03295.
(37) Hinokuma, S.; Fujii, H.; Okamoto, M.; Ikeue, K.; Machida, M. Metallic Pd Nanoparticles Formed by Pd−O−Ce Interaction: A Reason for Sintering-Induced Activation for CO Oxidation. *Chem. Mater.* **2010**, *22*, 6183–6190. https://doi.org/10.1021/cm102355x.
(38) Lashina, E. A.; Slavinskaya, E. M.; Boronin, A. I. Low-Temperature Activity of Pd/CeO_2 Catalysts:

Mechanism of CO Interaction and Mathematical Modelling of TPR-CO Kinetic Data. *Chem. Eng. Sci.* **2021**, *244*, 116812. https://doi.org/10.1016/j.ces.2021.116812.

(39) Lu, Y.; Thompson, C.; Kunwar, D.; Datye, A. K.; Karim, A. M. Origin of the High CO Oxidation Activity on CeO_2 Supported Pt Nanoparticles: Weaker Binding of CO or Facile Oxygen Transfer from the Support? *ChemCatChem* **2020**, *12*, 1726–1733. https://doi.org/10.1002/cctc.201901848.

(40) Wang, M.; Shen, M.; Jin, X.; Tian, J.; Li, M.; Zhou, Y.; Zhang, L.; Li, Y.; Shi, J. Oxygen Vacancy Generation and Stabilization in CeO 2– x by Cu Introduction with Improved CO 2 Photocatalytic Reduction Activity. *ACS Catal.* **2019**, *9* (5). https://doi.org/10.1021/acscatal.8b03975.

(41) Yu, X.; Li, J.; Wei, Y.; Zhao, Z.; Liu, J.; Jin, B.; Duan, A.; Jiang, G. Three-Dimensionally Ordered Macroporous Mn x Ce 1– x O δ and Pt/Mn 0.5 Ce 0.5 O δ Catalysts: Synthesis and Catalytic Performance for Soot Oxidation. *Ind. Eng. Chem. Res.* **2014**, *53* (23). https://doi.org/10.1021/ie500666m.

(42) Li, W. J.; Wey, M. Y. Design of a Thermally Resistant Core@shell/Halloysite Catalyst with Optimized Structure and Surface Properties for a Pd-Only Three-Way Catalyst. *Appl. Catal. A Gen.* **2020**, *602* (June), 117732. https://doi.org/10.1016/j.apcata.2020.117732.

(43) Barth, C.; Laffon, C.; Olbrich, R.; Ranguis, A.; Parent, P.; Reichling, M. A Perfectly Stoichiometric and Flat CeO_2(111) Surface on a Bulk-like Ceria Film. *Sci. Rep.* **2016**, *6* (1). https://doi.org/10.1038/srep21165.

(44) Wang, T.; Tao, X.; Li, X.; Zhang, K.; Liu, S.; Li, B. Synergistic Pd Single Atoms, Clusters, and Oxygen Vacancies on TiO_2 for Photocatalytic Hydrogen Evolution Coupled with Selective Organic Oxidation. *Small* **2021**, *17* (2). https://doi.org/10.1002/smll.202006255.

(45) Tana; Zhang, M.; Li, J.; Li, H.; Li, Y.; Shen, W. Morphology-Dependent Redox and Catalytic Properties of CeO_2 Nanostructures: Nanowires, Nanorods and Nanoparticles. *Catal. Today* **2009**, *148*, 179–183. https://doi.org/10.1016/j.cattod.2009.02.016.

(46) Lee, J.; Ryou, Y.; Chan, X.; Kim, T. J.; Kim, D. H. How Pt Interacts with CeO_2 under the Reducing and Oxidizing Environments at Elevated Temperature: The Origin of Improved Thermal Stability of Pt/CeO_2 Compared to CeO_2. *J. Phys. Chem. C* **2016**, *120*, 25870–25879. https://doi.org/10.1021/acs.jpcc.6b08656.

(47) Song, W.; Su, Y.; Hensen, E. J. M. A DFT Study of CO Oxidation at the Pd–CeO 2 (110) Interface. *J. Phys. Chem. C* **2015**, *119* (49), 27505–27511. https://doi.org/10.1021/acs.jpcc.5b09293.

(48) Neitzel, A.; Figueroba, A.; Lykhach, Y.; Skála, T.; Vorokhta, M.; Tsud, N.; Mehl, S.; Ševčíková, K.; Prince, K. C.; Neyman, K. M.; et al. Atomically Dispersed Pd, Ni, and Pt Species in Ceria-Based Catalysts: Principal Differences in Stability and Reactivity. *J. Phys. Chem. C* **2016**, *120* (18), 9852–9862. https://doi.org/10.1021/acs.jpcc.6b02264.

(49) Spezzati, G.; Su, Y.; Hofmann, J. P.; Benavidez, A. D.; DeLaRiva, A. T.; McCabe, J.; Datye, A. K.; Hensen, E. J. M. Atomically Dispersed Pd–O Species on CeO_2 (111) as Highly Active Sites for Low-Temperature CO Oxidation. *ACS Catal.* **2017**, *7*, 6887–6891. https://doi.org/10.1021/acscatal.7b02001.

(50) Stonkus, O. A.; Kardash, T. Y.; Slavinskaya, E. M.; Zaikovskii, V. I.; Boronin, A. I. Thermally Induced Structural Evolution of Palladium-Ceria Catalysts. Implication for CO Oxidation. *ChemCatChem* **2019**, *11*, 3505–3521. https://doi.org/10.1002/cctc.201900752.

(51) Hatanaka, M.; Takahashi, N.; Takahashi, N.; Tanabe, T.; Nagai, Y.; Suda, A.; Shinjoh, H. Reversible Changes in the Pt Oxidation State and Nanostructure on a Ceria-Based Supported Pt. *J. Catal.* **2009**, *266* (2), 182–190. https://doi.org/10.1016/j.jcat.2009.06.005.

(52) Colussi, S.; Gayen, A.; Farnesi Camellone, M.; Boaro, M.; Llorca, J.; Fabris, S.; Trovarelli, A. Nanofaceted Pd-O Sites in Pd-Ce Surface Superstructures: Enhanced Activity in Catalytic Combustion of Methane. *Angew. Chemie Int. Ed.* **2009**, *48* (45), 8481–8484. https://doi.org/10.1002/anie.200903581.

(53) Hatanaka, M.; Takahashi, N.; Tanabe, T.; Nagai, Y.; Dohmae, K.; Aoki, Y.; Yoshida, T.; Shinjoh, H. Ideal Pt Loading for a Pt/CeO2-Based Catalyst Stabilized by a Pt–O–Ce Bond. *Appl. Catal. B Environ.* **2010**, *99* (1–2), 336–342. https://doi.org/10.1016/j.apcatb.2010.07.003.

(54) Lardinois, T. M.; Bates, J. S.; Lippie, H. H.; Russell, C. K.; Miller, J. T.; Meyer, H. M.; Unocic, K. A.; Prikhodko, V.; Wei, X.; Lambert, C. K.; et al. Structural Interconversion between Agglomerated Palladium Domains and Mononuclear Pd(II) Cations in Chabazite Zeolites. *Chem. Mater.* **2021**, *33*, 1698–1713. https://doi.org/10.1021/acs.chemmater.0c04465.

(55) Wang, X.; Liu, D.; Li, J.; Zhen, J.; Wang, F.; Zhang, H. γ-Al 2 O 3 Supported Pd@CeO 2 Core@shell

Nanospheres: Salting-out Assisted Growth and Self-Assembly, and Their Catalytic Performance in CO Oxidation. *Chem. Sci.* **2015**, *6*, 2877–2884. https://doi.org/10.1039/C4SC03854A.

(56) Liu, Y.; Wang, Q.; Wu, L.; Long, Y.; Li, J.; Song, S.; Zhang, H. Tunable Bimetallic Au–Pd@CeO 2 for Semihydrogenation of Phenylacetylene by Ammonia Borane. *Nanoscale* **2019**, *11* (27), 12932–12937. https://doi.org/10.1039/C9NR02953B.

(57) Li, P.; Chen, X.; Ma, L.; Bhat, A.; Li, Y.; Schwank, J. W. Effect of Ce and La Dopants in Co_3O_4 Nanorods on the Catalytic Activity of CO and C_3H_6 Oxidation. *Catal. Sci. Technol.* **2019**, *9* (5), 1165–1177. https://doi.org/10.1039/C8CY02460J.

Chapter 4 : Regenerating Catalytic Performance and Dispersed Sites Through Favorable Restructuring

4.1 Motivation

The increased cost, scarcity, and demand of precious metals that comprise industrial catalysts has motivated interest in improving performance, lifetime, and consequently the utilization of catalytic material. Such goals are particularly relevant to automotive emissions control applications that must simultaneously manage wide windows of operating temperature, increasing costs of active metals (Pd, Pt and Rh), and regulations controlling emission quality.[1,2] Efforts in this field have focused on optimizing the number of active metal atoms that interact directly with reducible oxide supports such as CeO_2, as the participation of lattice oxygen at the metal–support interface can dramatically improve activity.[3,4] Despite advancements in catalyst design, the unfavorable active site restructuring caused by high-temperature sintering still remains a challenge.[5] Consequently, there has been significant interest in understanding catalyst restructuring at high temperatures to develop techniques that can improve or regenerate the abundance of active metal sites that interface with reducible supports.

To this end, the dynamics of active metals under high-temperature, oxidizing conditions have been of particular interest.[6–8] These conditions can cause active metal particles to shrink through the emission of adatom species that exhibit high mobility.[9–12] This process can improve the fraction of sites that interact with the reducible support in two ways. First, the shrinkage of metal particles improves the abundance of perimeter sites that interface with the support.[3] Second,

the mobile adatoms can be anchored or trapped on reducible oxides, such as CeO_2, on undercoordinated sites (e.g., Ce^{3+}).[9,13,14] Computational and experimental investigations show that the active metal sites formed from such trapping processes are highly dispersed as single atoms.[15,16] Recent work has demonstrated that if the density of trap sites exceeds the density of active metal atoms, particles completely disintegrate into highly dispersed single atom sites.[12] The coordination of these single atoms provides improved thermal stability and accessibility to reaction pathways mediated at the metal–support interface, through the formation of strong M–O–Ce interactions (where M is a metal).[17–19] Consequently, these favorable restructuring strategies show promise for improving material utilization. Other processes that improve the density of support-interfacing sites include wet chemistry methods such as strong electrostatic adsorption,[16] dispersing metals with short thermal pulses[20,21] and chemical treatments with halogenated compounds.[22] It is important to note that while catalysts with single atom dispersion exhibit good material utilization in well-controlled probe reactions such as CO oxidation, their efficacy in application-relevant conditions is still being investigated. One such example is managing competitively adsorbing reactants, which is necessary in emissions control. Recent work shows that single atom catalysts (SACs) perform poorly in such reaction mixtures, as there are no alternative sites available to adsorb competing reactants.[23,24]

Favorable thermal restructuring is often conducted at intermediate temperatures (≤800°C), which are below the thermal decomposition temperature of the active metal oxide subjected to redispersion (e.g., PdO, PtO_2).[25] As previously demonstrated however, conditions that disrupt metal oxide stability, such as reduction under mild temperature, can decompose M–O–Ce bonds and result in sintering of redispersed sites.[26,27] Consequently, the stability of restructured catalysts

at temperatures that favor metal oxide thermal decomposition (but are still relevant to application, e.g., 1000°C), remains to be addressed.

If sintering occurs, catalysts must be regenerated to recover the material. Techniques that can be deployed *in–operando* are particularly valuable as they avoid the cost associated with taking a deactivated catalyst off–stream for regeneration. Many of the strategies used to synthesize highly dispersed and interfacing sites, however, are not applicable for *in–operando* regeneration as they require wet chemistry, specialized equipment, or halogenated compounds, which can have environmental risks.[16,28] Alternatively, favorable restructuring appears as a promising regeneration method as it relies on parameters which are readily controllable in many catalytic settings such as temperature and oxygen composition.

Here we investigate favorable thermal restructuring through intermediate temperature (800°C) exposure as a simple method to regenerate 1000°C-sintered catalysts that could be deployed *in-operando*. This study is graphically summarized in Figure 4.1. We use a Pd-CeO_2 system due to its widespread use and high cost, which warrants material utilization. As our model catalyst, we encapsulate Pd nanoparticles with a porous CeO_2 shell that has a high density of undercoordinated Ce^{3+} trap sites.[27,29] Aging these core@shell catalysts at 800°C in air redisperses core Pd in into highly dispersed sites, which exhibit the characteristic dispersion and Pd–O–Ce bonding of single atoms in literature.[15,30] Although 1000°C aging sinters Pd in core@shell catalysts, exposure to the 800°C aging protocol partially redisperses Pd. Sintered Pd particles shrink as a result, and a partial recovery of single atom sites is observed. This increases the density of interfacial sites, which regenerates catalytic performance. The Pd particles do not completely disintegrate after 1000°C sintering as redispersion scales with the retention of Ce^{3+} trap sites. This is demonstrated by comparing the effects of regeneration on as–synthesized (control) and 800°C

pretreated Pd@CeO_2. Notably, the regenerative effect is larger if the catalyst is pretreated at 800°C prior to aggressive sintering at 1000ºC. We identify that pretreatment simultaneously impedes the formation of large Pd particles and stabilizes small, polycrystalline CeO_2 domains, which contain greater densities of trap sites. This increases the fraction of Pd that can be redispersed, which improves the shrinkage of sintered particles. The performance of the regenerated catalyst is examined through the co-oxidation of CO and C_3H_8, two reactants that competitively adsorb on single-atom-rich catalysts.[24] We find that the regenerated catalyst is the most effective for the complete co-oxidation of CO and C_3H_8. This is due to the presence of bulk and interfacial Pd sites, which can effectively oxidize C_3H_8 and CO, respectively.

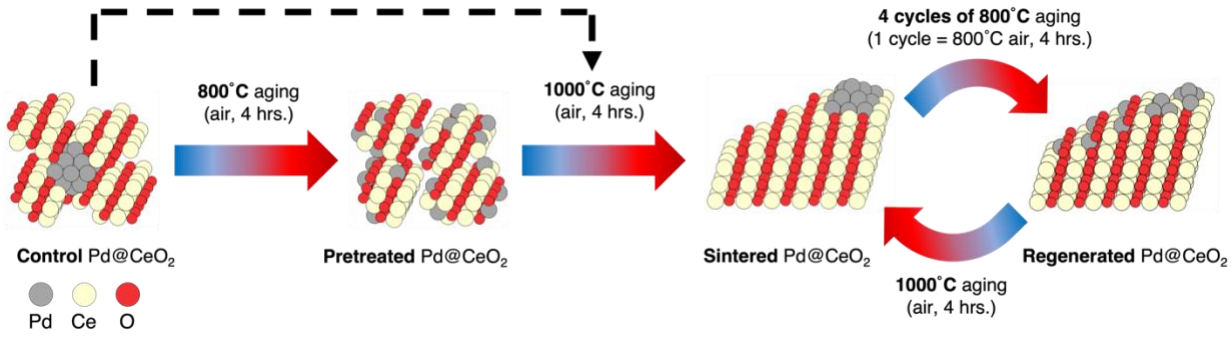

Figure 4.1. Graphical depiction of experimental approach used.

The sintering and redispersion phenomena observed here align with the thermodynamic stability limits of PdO, which is demonstrated by aging the Pd-CeO_2 catalysts over a range of temperatures around the PdO decomposition temperature. Altogether, this work provides a framework for understanding regeneration of Pd-CeO_2 catalysts, which can be applied to other material systems that use active metals with well-defined decomposition thermodynamics. Furthermore, it introduces a simple method to improve thermal stability and regenerate catalytic performance upon high-temperature sintering, thereby addressing material utilization challenges.

4.2 Results and Discussion

4.2.1 The role of 800°C pretreatment on catalyst stability at 1000°C

CO oxidation is an effective probe reaction to examine the effects of aging on catalyst stability. This is due to the well-established scaling of CO conversion with active metal dispersion, and accessibility to lattice oxygen provided by reducible oxide supports.[3,4,31] The temperature required for 90% conversion of a target reactant (T_{90}) is used here to define light-off and compare how aging conditions affect nanoscale structure and macroscale activity. Figure. 4.2 shows T_{90} values for Pretreated and Control Pd@CeO_2 samples after aging at 1000°C and regeneration by repeated aging at 800°C. These two as prepared states are labelled A1. Four repeated cycles of 800°C define the regeneration treatment. As such, the four cycles are indexed a–d. Aging cycles have been labelled as 'S' or 'R' to indicate sintering or regeneration, respectively. Catalyst samples that come from the Pretreated and Control batches are denoted as 'P' and 'C', respectively. As such, Pretreated and Control catalysts prior to sintering or regeneration are denoted as A1-P and A1-C, respectively. These catalysts would be denoted as S1-P and S1-C, respectively, after an initial cycle of 1000°C aging. Similarly, R1a-P would describe a Pretreated catalyst that is exposed to one cycle of 800°C aging as part of the regeneration treatment and R1d-P would describe that catalyst after four cycles of 800°C aging.

As previously indicated, the T_{90} for these catalysts varies due to highly dispersed sites in the Pretreated (A1-P) sample and Pd nanoparticles on the order of 3–5 nm in diameter in the Control (A1-C) sample.[29] T_{90} values for these samples are 95°C and 137°C, respectively. Arrhenius experiments corroborate the trends in T_{90}, as the Pretreated and Control catalysts exhibit apparent activation energies for CO oxidation of 23.5 and 47.2 kJ/mol, respectively (Table 4.1).

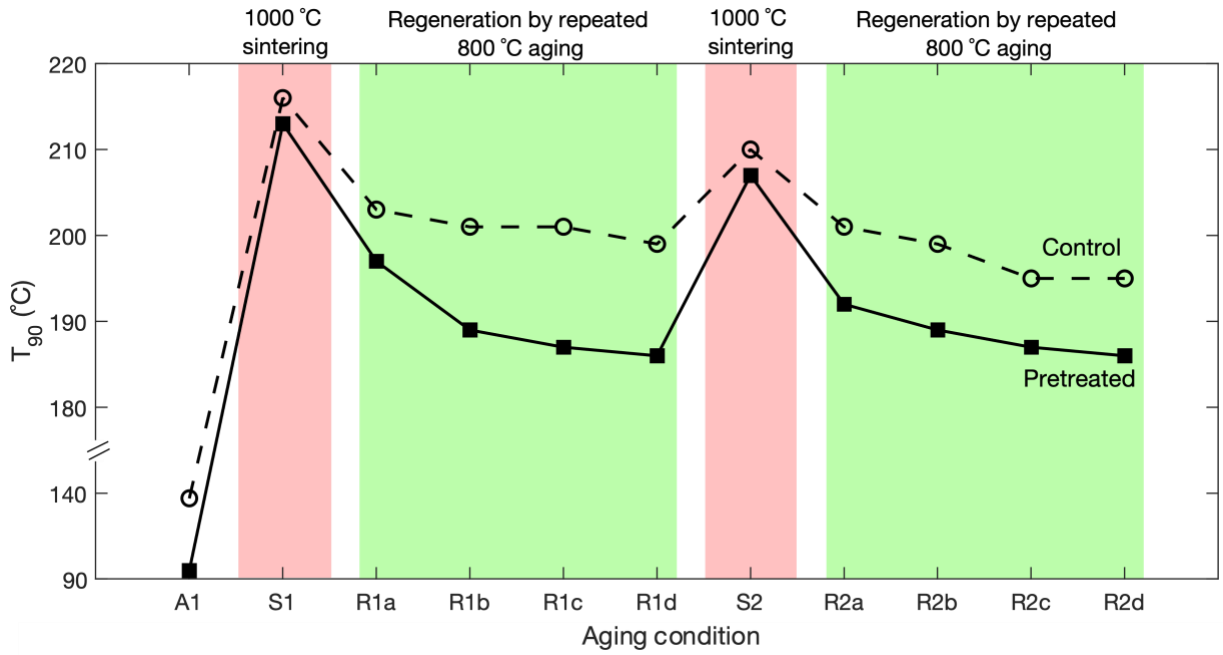

Figure 4.2. CO T_{90} (°C) for Control and Pretreated Pd@CeO_2 catalysts as a function of aging condition. As prepared samples are denoted as A1. Aging conditions have been abbreviated to signify the cycle of sintering (e.g., S1) or regeneration (e.g., R1d). A break in the Y-axis for T_{90} has been used to highlight the differences in T_{90} behavior during the 1000°C sintering and 800°C regeneration protocols. Test gas composition was as follows: 1% CO, 2.5% O_2 (N_2 gas balance). Total flow rate was maintained at 200 mL/min and the ramp used was 2°C/min.

After 1000°C aging in air for 4 hours, T_{90} increases to 213°C for the Pretreated sample. The increased T_{90} coincides with an increase in E_a for CO oxidation to 116.8 kJ/mol. This indicates sintering of the active Pd species as CO oxidation exhibits a strong structure sensitivity to the interface between active sites and reducible oxide supports.[3,15] Consistent with this observation, the S1-C catalyst exhibits a similar increase in T_{90} to 216°C after 1000°C aging. STEM characterization of the S1-P and S1-C catalysts (Figure 4.3a, b) show agglomerated CeO_2 crystallites that exceed 40 nm in diameter in addition to large Pd nanoparticles on the order of 20–50 nm in diameter. In addition, the EDS Pd signal indicative of highly dispersed species in the Pretreated sample has decreased and given way to larger, concentrated signals indicative of agglomerated particles.

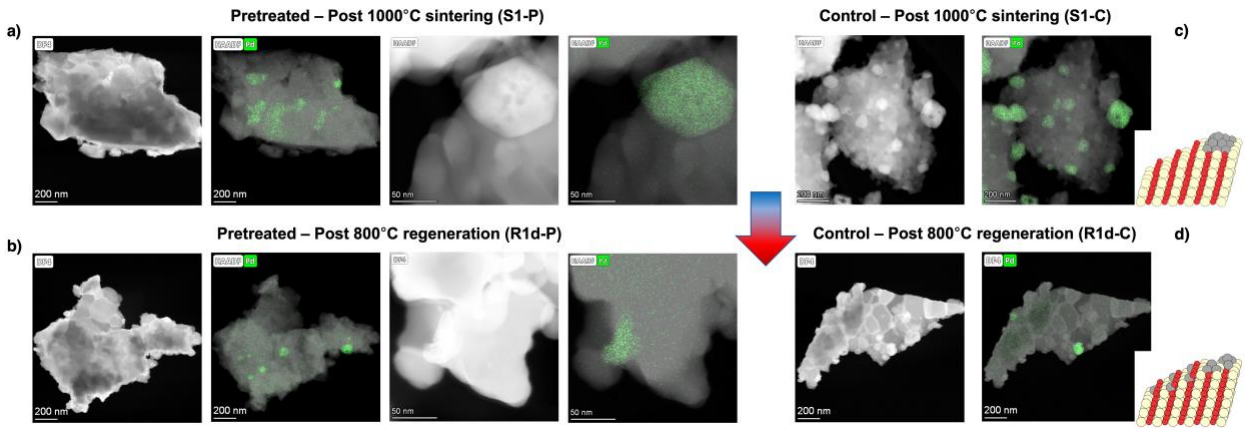

Figure 4.3. STEM and EDS characterization of Pretreated and Control Pd@CeO_2 after 1000°C sintering and 800°C regeneration.
Samples depicted correspond to the (a, b) Pretreated and (c, d) Control Pd@CeO_2 samples after 1000°C sintering (S1) and 800°C regeneration (R1d) stages of aging, respectively. EDS figures contain embedded legends to indicate the corresponding colors for the elemental maps (Pd: Green) and the detector used to collect the STEM image (HAADF: high angle annular dark-field).

Table 4.1. Apparent activation energy (E_a) for CO oxidation.

Sample	Activation energy (kJ/mol)
Control (A1-C)	47.2
Pretreated (A1-P)	23.5
Post 1000°C sintering (S1-P)	116.8
Post 800°C regeneration (R1d-P)	90.5

The sintering of Pd and CeO_2 was probed at the bulk scale by XRD. This analysis demonstrates that both Pretreated and Control catalysts exhibit sintering of active metal and support components upon 1000°C aging, and that pretreatment at 800°C appears to reduce the degree of adverse restructuring. It is important to note that XRD does not detect any remaining highly dispersed Pd atoms or clusters. Therefore, the XRD particle size for Pd reported here corresponds to just the sintered part of the Pd, not the total average particle size. As shown in Figure 4.4 and summarized in Table 4.2, 1000°C aging increases the average CeO_2 and Pd particle size of the Pretreated (S1-P) samples to 43 and 36 nm, respectively. The Control (S1-C) samples exhibit similar increases in CeO_2 and Pd particle size to 56 and 47 nm, respectively. These values

are markedly higher than those of the S1-P sample, which suggests that pretreatment has improved thermal stability during 1000°C aging. Thermal pretreatments at intermediate temperatures (≤800°C) have been shown to improve stability under elevated temperature aging in Pd/CeO_2 through the crystallization of support domains.[5,32,33] Furthermore, a critical difference between the Pretreated and Control samples is the presence of highly dispersed Pd species after 800°C pretreatment. As previous work shows, atomically dispersed metals can coordinate strongly with support domains and stabilize structure and high catalytic performance under elevated temperature aging.[27,34,35] Although these dispersed species cannot completely negate the effects of aging at 1000°C, our work demonstrates that pretreatments which form strongly coordinated metal-support interactions can improve stability during high temperature exposure. Such outcomes can be valuable to extend the lifetime and material utilization of catalysts on-stream.

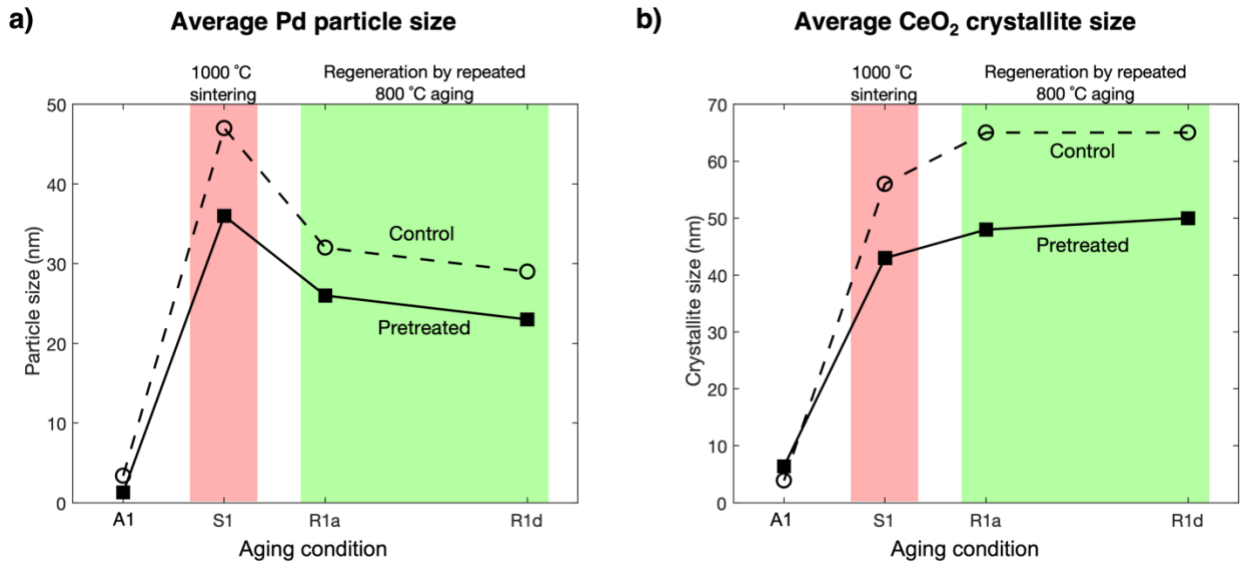

Figure 4.4. Average Pd nanoparticle and CeO_2 crystallite size for Pd@CeO_2 catalysts with aging condition. Aging conditions have been abbreviated to signify the cycle of sintering (e.g., S1) or regeneration (e.g., R1d).

4.2.2 Regenerating activity and dispersed sites through intermediate 800°C aging

The 1000°C-sintered catalysts were exposed to the 800°C aging conditions previously shown to produce favorable restructuring to recover catalytic performance. As shown in Figure 4.2, the T_{90} for the Pretreated catalyst decreased after an initial 800°C aging to 197°C (R1d-P). Coinciding with this partial performance regeneration was an average Pd particle size that decreased to 26 nm. This suggests that the sintered Pd particles have shrunk through partial disintegration and redispersion, which increases the fraction of interfacial sites that exhibit superior low-temperature oxidation activity. This is corroborated by the Arrhenius experiments, which show an E_a that decreases from 116.8 to 90.5 kJ/mol post-regeneration (Table 4.1).

Table 4.2. Summary of average CeO_2 crystallite and sintered Pd nanoparticle size.

Sample	Average CeO_2 crystallite size (nm)		Average bulk Pd particle size (nm)	
	Pretreated (P)	**Control (C)**	**Pretreated (P)**	**Control (C)**
As prepared (A1)	6.4	3.9	1.3*	3.4*
Post 1000°C sintering (S1)	43	56	36	47
Post one 800°C aging cycle (R1a)	48	65	26	32
Post 800°C regeneration (R1d)	50	65	23	29

*Denotes sizes were determined by CO chemisorption per previous work.[27] All other size values were calculated from XRD data via the Debye-Scherrer equation.

The activity continued to improve with 800°C aging, as evidenced by the decreasing T_{90}. The T_{90} continued to decrease for the Pretreated sample until an approximate plateau value of 186°C was reached after the fourth cycle of 800°C aging (R1d–P). This trend is reflected in the XRD analysis (Figure 4.4a), with the average sintered Pd particle size decreasing to 23 nm. STEM characterization of the catalysts shows partial redispersion of sintered Pd post-regeneration. As

seen in Figure. 4.3b, the average sintered Pd particle size has decreased, and the dispersed Pd signal indicative of highly dispersed sites on the surface of supporting CeO_2 crystallites has returned. As shown in Figure 4.5, Pd particles on the order of 5 nm can be observed post-regeneration. This characterization suggests that aging sintered catalysts at intermediate temperatures (800°C) facilitates partial disintegration and redispersion of agglomerated clusters, which decreases the bulk particle size and increases the abundance of sites that interface directly with the reducible oxide support.

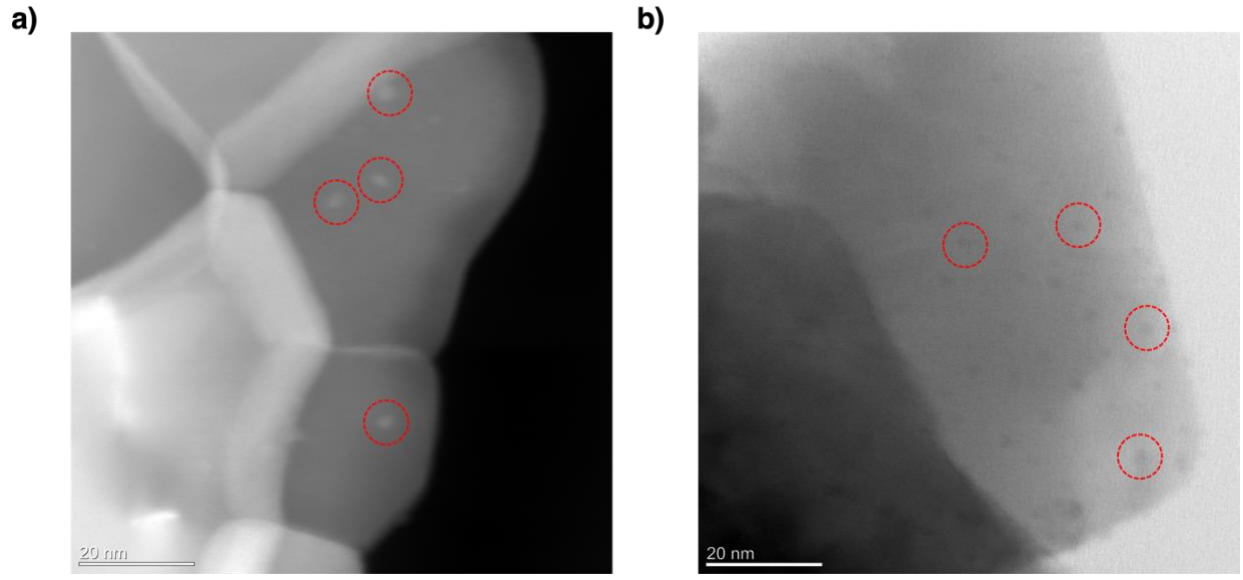

Figure 4.5. Additional electron microscopy characterization of Pretreated catalyst post regeneration (R1d-P). (a) Dark-field and (b) bright-field microscopy characterization is shown. Red circles highlight small Pd particles on the order of 5 nm in diameter.

The redispersion of agglomerated Pd and coinciding recovery of T_{90} performance post-regeneration was also observed for the Control Pd@CeO_2 (R1d-C), as T_{90} and average Pd size decreased to 199°C and 26 nm, respectively. It is important to note that the Pretreated Pd@CeO_2 exhibited a more significant regeneration of T_{90}, dispersed Pd species and bulk particle shrinkage during cycled 800°C aging than the Control. Thus, pretreatment at 800°C results in greater regeneration. This phenomenon is further discussed in *Section 4.2.3*.

To investigate whether the regeneration process is repeatable, the 1000°C sintering and 800°C regeneration steps were re-applied to the catalysts. The T_{90} increased to 207°C for the Pretreated sample (S2-P) and 210°C for the Control sample (S2-C). These T_{90} values are slightly lower than after the first 1000°C aging. This is likely due to partial sintering during the catalysts' prior exposure to 1000°C. As shown in previous works, high-temperature exposures can crystallize active metal and support domains, which can slow further sintering and improve oxygen mobility.[32,36] With respect to regeneration, the second round of cycled 800°C aging (R2a–d) produced a similar T_{90} recovery outcome as the first (Figure. 4.2). This suggests that this catalyst system can exist in a sintered state and a partially redispersed or regenerated state, depending on the aging or working conditions applied. These observations also demonstrate that the regeneration protocol can be repeatably deployed to catalysts that undergo deactivation due to high-temperature exposure. The importance of this result is that the procedure should be suitable for *in–operando* catalyst regeneration, which can significantly lower operational costs.[5] To this end, there have been significant advancements in controlling oxygen content and temperature for reactor systems in industrial applications.[37,38] Developments for emissions control catalysts, such as on-board air: fuel ratio control, are particularly relevant.[39]

4.2.3 Ce^{3+} trap site density influences regeneration efficacy

The intermediate temperature exposure, discussed above, has been proven to regenerate low temperature catalytic activity through the partial shrinkage and redispersion of sintered Pd particles. As mentioned in *Section 3.2*, the efficacy of regeneration improves if the catalyst is pretreated at 800°C prior to aging at 1000°C. The ability to recover highly dispersed active sites on CeO_2 is dependent on the density of Ce^{3+} trap sites,[12,40,41] with smaller CeO_2 crystals exhibiting greater trap site densities (Figure 4.6). Further, the highly dispersed metal species anchored to

these sites through M–O–Ce bonding exhibit electron-deficient ($M^{\delta+}$) characteristics, which can be readily examined through XPS analysis and spectra deconvolution.[26,42,43] These $M^{\delta+}$ characteristics are also observed at the perimeter sites on Pd nanoparticles,[44] which allows the $M^{\delta+}$ composition to effectively describe the Pd–CeO_2 interfacial site abundance. Consequently, XPS was conducted on the Pretreated and Control catalysts before and after 1000°C sintering (S1) and 800°C regeneration (R1d) protocols to investigate how changes in the distribution of dispersed and agglomerated Pd can be correlated to changes in the fraction of Ce^{3+}.

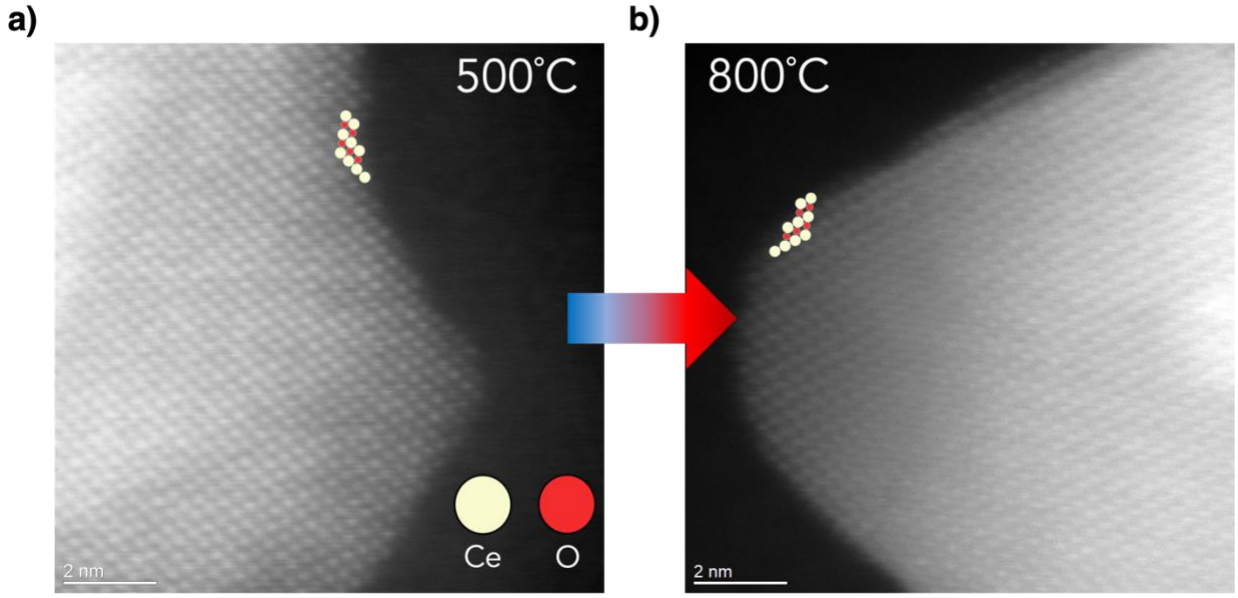

Figure 4.6. STEM characterization of changing Ce^{3+} trap site abundance with average crystallite size.

Table 4.3. Summary of Pd and Ce oxidation states for Pretreated and Control Pd@CeO_2 as a function of aging condition.

Sample	$Pd^{\delta+}$ / Pd^{2+} / Pd^0 composition (%)		Ce^{3+} composition (%)	
	Pretreated (P)	Control (C)	Pretreated (P)	Control (C)
As prepared	74.5 / 14.7 / 10.8	– / – / –	22.6	24.7
S1	34.2 / 25.1 / 40.7	23.2 / 30.9 / 45.9	18.0	13.3
R1d	40.5 / 29.1 / 30.4	26.1 / 35.5 / 38.4	17.5	12.6

– Denotes that the composition could not be accurately determined from XPS data

Figure 4.7 and Table 4.3 show the Pd and Ce oxidation states as a function of aging condition as determined by XPS (the Pd composition is not shown for the Control sample because the encapsulating CeO_2 shell attenuates the signal).[29] The Pretreated Pd@CeO_2 catalyst exhibits a large fraction (74.5%) of $Pd^{\delta+}$, which is associated with highly dispersed Pd–O–Ce sites.[27,29] During 1000°C aging, the fraction of electron deficient Pd decreases in favor of Pd^0, which is associated with sintered particles and consistent with activity and structure characterization presented above (Figure. 4.2). The Pretreated catalyst (S1-P) does contain a larger fraction of $Pd^{\delta+}$ (34.2%) than the Control (S1-C, 23.2%) after 1000°C aging. This outcome emphasizes the importance of intermediate temperature pretreatments for promoting thermal stability at elevated temperatures. The fraction of $Pd^{\delta+}$ for both the Pretreated and Control catalysts increases upon 800°C regeneration, which corroborates the increase in interfacial sites through the redispersion and subsequent shrinkage of agglomerated Pd^0 observed through STEM and XRD characterization. Notably, regeneration produces approximately 1.5 times more $Pd^{\delta+}$ in the Pretreated catalyst (R1d-P, 40.5%) than in the Control catalyst (R1d-C, 26.1%). As highly

dispersed and perimeter Pd sites exhibit superior performance in CO oxidation,[3,15] the differences in $Pd^{\delta+}$ fraction explain why the Pretreated catalyst has better T_{90} performance post-regeneration.

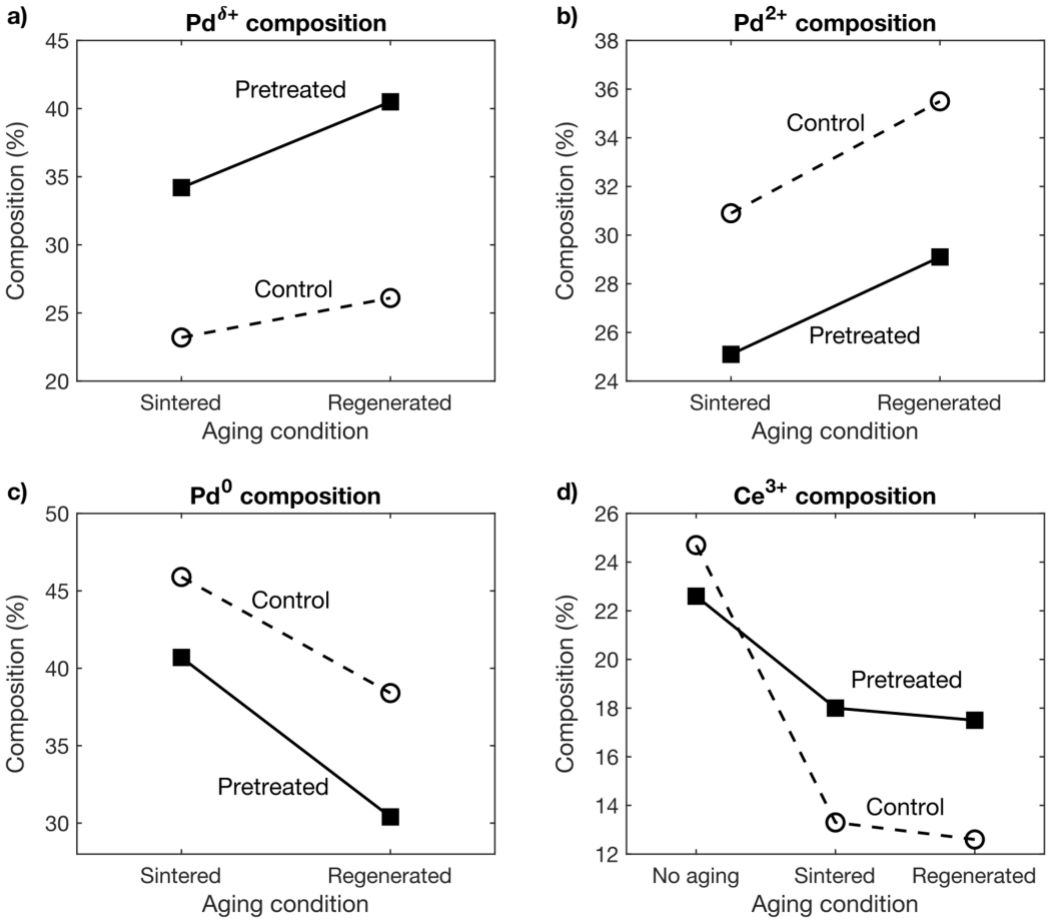

Figure 4.7. Changes in oxidation state distribution as a function of aging condition.
Distribution of (a) $Pd^{\delta+}$, (b) Pd^{2+}, (c) Pd^{0}, and (d) Ce^{3+} oxidation states as determined by deconvoluting XPS spectra obtained from Pretreated and Control Pd@CeO_2 after 1000°C sintering and 800°C regeneration aging protocols.

With respect to trap sites, the Control Pd@CeO_2 has a slightly higher density of Ce^{3+} (24.7%) compared to the Pretreated sample (22.6%) as prepared (Figure 4.7d). After 1000°C sintering, however, the Pretreated (S1-P) sample contains approximately 1.35 times more Ce^{3+} than the Control (S1-C) sample (18.0% compared to 13.3). This is likely due to the formation of dispersed Pd sites during 800°C pretreatment, which stabilize the supporting CeO_2 and slow sintering at 1000°C (Figure. 4.4b). These Ce^{3+} sites in turn facilitate regeneration by trapping Pd

during 800°C aging as highly dispersed $Pd^{\delta+}$. As the number of dispersible metal atoms exceeds the trap site density, bulk particles will be unable to completely redispersion and will remain, albeit at smaller sizes.[12] Such effects appear to mediate the shrinkage of sintered Pd and partial recovery of dispersed Pd sites here. The smaller bulk Pd size and greater Ce^{3+} density observed in the R1d-P sample is consistent with this framework. The lower fraction of Ce^{3+} species in the R1d-C sample correlate with a greater Pd^0 fraction and lower $Pd^{\delta+}$ fraction. Combined with XRD characterization and probe CO oxidation (Figure 4.2) data, these results show that the efficacy of the regeneration depends on the retention of undercoordinated Ce^{3+} trap sites. As CeO_2 undergoes adverse restructuring at temperatures approaching 1000°C, it is expected that re-exposure to sintering conditions will decrease the fraction of Ce^{3+} trap sites. This was probed by conducting XPS on the Pretreated Pd@CeO_2 after a second round of 1000°C aging (S2-P). The fraction of Ce^{3+} decreased from 17.5% to 15.9%. The loss in Ce^{3+} trap density explains why the second round of regeneration on the catalyst results in a higher T_{90} than the first round, as seen in Figure 4.2. This data suggests that improving support thermal stability will improve the efficacy of regeneration. To this end, recent work with solid solutions of metal oxides and high-entropy oxides show promise.[34,45–47]

4.2.4 General mechanism of agglomeration and regeneration

Several studies have investigated the process by which mobile species are generated, and have demonstrated the importance of oxidizing the active metal (e.g., PdO, PtO_2) for redispersion.[10,13,48,49] Even in the absence of gas phase oxygen, prior work has shown that lattice oxygen in CeO_2 can facilitate redispersion at 800°C.[29] An oxidized active metal is also necessary for trapping on CeO_2 surfaces, as it facilitates M–O–Ce bonding at undercoordinated Ce^{3+} sites. Although such bonds exhibit high thermal stability, conditions that destabilize the oxygen bond, such as aging in reducing environments,[26,27] can dislodge trapped metal species. Specifically, Pd–

O bonds are known to decompose at temperatures beyond 800°C in the partial pressure of O_2 contained in air (2.13×10^4 Pa), which can facilitate sintering as demonstrated by a number of computational and experimental works.[25,50,51] As such, we hypothesize that the decomposition thermodynamics of Pd–O bonding can describe the thermal restructuring outcomes observed in this study.

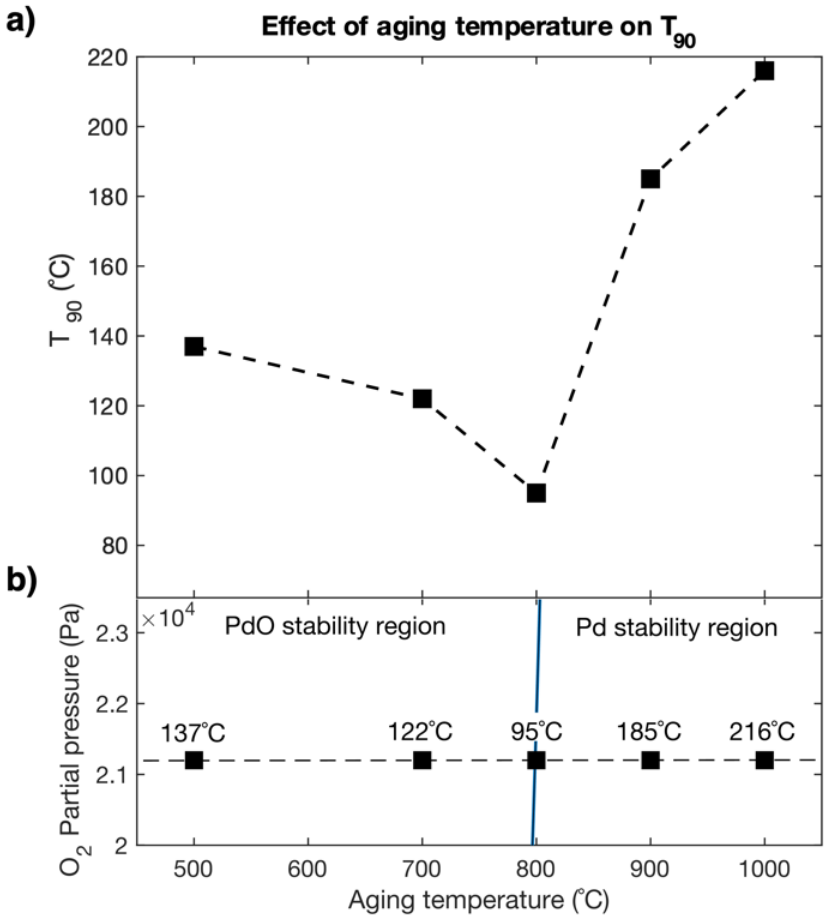

Figure 4.8. Effect of aging temperature on restructuring outcome.
(a) Summary of T_{90} values for fresh Pd@CeO_2 subjected to 4-hour aging at various temperatures outlined in the phase diagram depicted below. (b) PdO–Pd phase diagram, plotted from the relationship described in reference,[25] with inset points corresponding to aging temperatures used. Each point is labelled with its respective T_{90} for CO oxidation.

Figure 4.8 shows the CO oxidation T_{90} values for Pd@CeO_2 catalysts aged at a variety of temperatures alongside the PdO equilibrium decomposition line.[25] The T_{90} decreases as the aging temperature approaches 800°C, indicating favorable Pd redispersion. The decreasing T_{90} trend

with temperature is attributed to kinetic effects. Once the aging temperature surpasses 800°C, the trend reverses and T_{90} begins to increase with increasing temperature. This corresponds in Figure 4.8b to conditions that promote the thermal decomposition of the PdO phase, in favor of the Pd^0 phase. Under these conditions, Pd–O–Ce bonds appear to decompose, which facilitates the unfavorable sintering of bulk Pd^0 observed in our material characterization. While it is likely a simplification of the process, the thermodynamics of PdO decomposing into oxygen and metallic Pd is consistent with experimental data and, therefore a relevant indicator of the onset of sintering.

Based on these observations, we propose the following mechanism for sintering and regeneration in Pd-CeO_2 systems shown below. These insights should generalize to other catalyst systems containing reducible supports and active metal species with well-defined oxide decomposition thermodynamics.

(a) Below the PdO equilibrium decomposition temperature, Pd redisperses through the formation of mobile PdO, which interacts strongly with undercoordinated Ce^{3+} sites on supporting CeO_2 through Pd–O–Ce bonding.

(b) The extent of redispersion is governed by both the density of the Ce^{3+} trapping sites between the Pd domains and the aging temperatures applied, with higher temperatures improving the kinetics of metal disintegration, redispersion and trapping.

(c) Above the PdO equilibrium decomposition temperature (e.g., 1000°C), dispersed species become mobile and sinter.

(d) Returning to conditions that favor the PdO phase and provide sufficient kinetics (e.g., 800°C) redisperses a portion of the sintered Pd. This process is governed by the same factors outlined in (a).

(e) Retention of trap sites during elevated temperature exposure is integral to regeneration.

4.2.5 Catalyst performance in the co-oxidation of CO and C_3H_8

The above sections demonstrate that intermediate temperature exposure partially regenerates highly dispersed active sites in sintered catalysts, offering a simple and low-cost approach to improving material utilization on stream. Nonetheless, the performance under more application-relevant conditions has yet to be examined. As previously mentioned, automotive emissions control is a particularly relevant application.[2] The management of competitively adsorbing species, such as CO and uncombusted hydrocarbons (HCs), is a consistent challenge in this space.[23] Previous work has shown that CO oxidation occurs at interfacial sites due to the extraction of lattice oxygen from reducible supports.[3,4] HC oxidation, in contrast, is catalyzed by larger metal ensembles where facile scission of C–C and C–H bonds can occur.[1,24,52,53] The poor adsorption-desorption characteristics of single atom sites with respect to HCs such as C_3H_8, impedes catalytic performance[24,54] and the access of CO. This shifts light-off plots for CO oxidation to higher temperatures when HCs are co-fed.[1,24] Thus, catalysts that contain both site types, such as the 800°C Regenerated Pd@CeO_2, are expected to conduct the co-oxidation of CO and C_3H_8 more effectively. To this end, we investigate the activity of the Pretreated catalysts (A1-P) in the co-oxidation of CO + C_3H_8 after sintering (S1-P) and regeneration (R1d-P). The as synthesized Control catalyst (A1-C) was also studied for comparison. Figure 4.9 shows compiled light-off plots for CO and C_3H_8 oxidation in single and co-fed oxidation conditions for the four aforementioned catalysts. T_{90} data is summarized in Table 4.4. Meanwhile, *in situ* DRIFTS (shown in Figure 4.10) was conducted under CO single fed and CO + C_3H_8 co-fed conditions to further investigate how cofeeding affected adsorption.

Table 4.4. T_{90} summaries for CO and C_3H_8 oxidation in single and co-fed oxidation conditions.

Sample	Single fed oxidation		Co-fed oxidation	
	CO T_{90} (°C)	C_3H_8 T_{90} (°C)	CO T_{90} (°C)	C_3H_8 T_{90} (°C)
Control (A1-C)	137	–	136	–
Pretreated (A1-P)	95	–	210	–
Post 1000°C sintering (S1-P)	213	405	213	–
Post 800°C regeneration (R1d-P)	186	374	193	345

– Indicates catalyst did not reach T_{90} over the 50–450°C temperature range used in the light-off experiment.

The Control catalyst does not exhibit a change in CO oxidation T_{90} upon cofeeding C_3H_8. This effect may be due to the encapsulating CeO_2 shell restricting C_3H_8 transport to core active sites, which would be consistent with a number of other studies.[55–57] Further, the catalyst shows poor activity for C_3H_8 oxidation, particularly at low temperatures (Figure 4.9a), requiring temperatures above 300°C to begin oxidizing C_3H_8. The initial particle size in the Control Pd@CeO_2 (~3–5 nm) is unoptimized for C_3H_8 oxidation, for which larger Pd particles are better.[58] DRIFTS experiments indicate that adding C_3H_8 incurs no significant change in the bands of adsorbed CO on the Control catalysts, which shows peaks that can be assigned to (i) CO adsorbed on oxidized PdO, (ii) Pd that is interfacing strongly with the reducible CeO_2 support, and (iii) bulk Pd.[15,31,59]

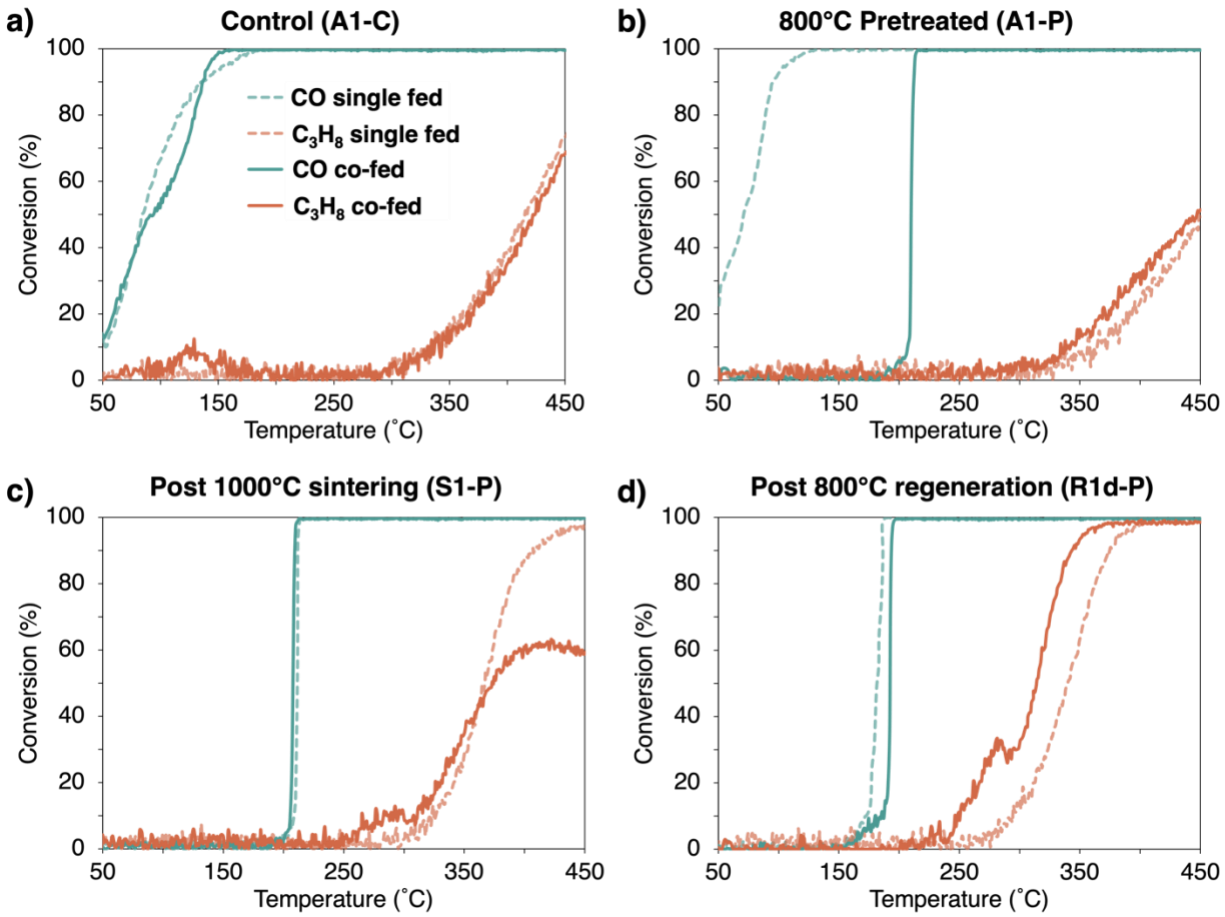

Figure 4.9. Light-off plots for CO and C_3H_8 oxidation in single and co-fed oxidation conditions. Catalysts tested are (a) Control, (b) Pretreated, (c) S1-P, and (d) R1-P catalysts. Test gas compositions were as follows: CO single fed oxidation – 1% CO, 2.5% O_2 (N_2 gas balance), C_3H_8 single fed oxidation – 0.1% C_3H_8, and 3% O_2 (N_2 gas balance), co-fed oxidation – 1% CO, 0.1% C_3H_8, and 3% O_2 (N_2 gas balance). Total flow rates were maintained at 200 mL/min and the ramp used was 2°C/min.

The Pretreated Pd@CeO_2 showed the lowest CO oxidation T_{90} and E_a among all catalysts (95°C and 23.5 kJ/mol, respectively), but the highest E_a for C_3H_8 decomposition (78.3 kJ/mol). This observation is consistent with the poor adsorption–desorption exhibited by SACs for HCs. Such effects are likely responsible for the unchanged C_3H_8 light-off profile when CO is co-fed (Figure 4.9b). In contrast, the light-off plot for CO oxidation shifts to higher temperatures (T_{90} increases from 95°C to 210°C). when C_3H_8 is present. These effects are consistent with C_3H_8 impeding the accessibility of CO to active sites, i.e., competitive adsorption.[24] CO-DRIFTS experiments show a single vibrational peak centered at 2099 cm^{-1} (Figure 4.10b). This peak is

indicative of CO adsorbed on Pd that is electron deficient due to strong interactions with the CeO_2 support.[59] The absence of other characteristic CO adsorption bands suggests that the sites are not at the edges of Pd nanoparticles, but more likely single-atom Pd sites.[31,60] The intensity of this peak decreases significantly upon the addition of C_3H_8, which is consistent with competitive adsorption impeding CO oxidation activity. The CO adsorption peak also shifts to lower wavenumbers in the presence of C_3H_8. Such phenomena have been attributed to decreased CO coverage.[61]

1000°C sintering of the Pretreated catalyst (S1-P) improved C_3H_8 oxidation activity, resulting in T_{90} and E_a values of 405°C and 56.7 kJ/mol, respectively. Sintering increases the fraction of bulk Pd (Table 4.3), which is known to be active in oxidizing hydrocarbons such as C_3H_8.[53] *In situ* DRIFTS corroborates that C_3H_8 preferentially adsorbs at these sites as the addition of C_3H_8 decreases the CO band intensity at ~1970 cm^{-1}, which corresponds to CO adsorbed on bulk Pd (Figure 4.10c). The decreased CO coverage causes these peaks to shift to lower wavenumbers. As seen in Figure 4.9c, there is no significant difference in the light-off characteristics for CO when C_3H_8 is added to the reaction mixture. This is likely because CO still adsorbs to oxidized and interfacial Pd sites.

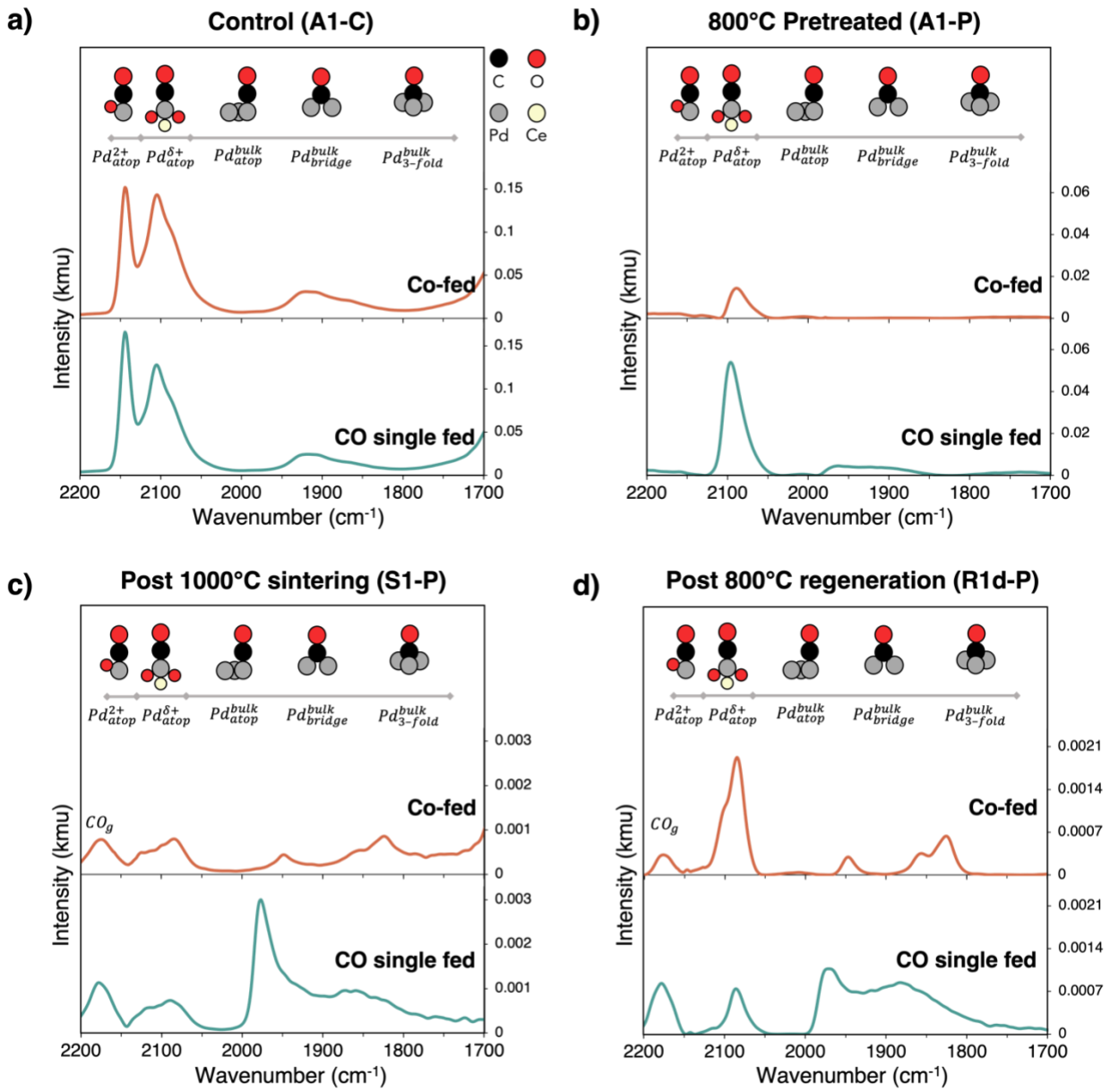

Figure 4.10. In situ DRIFTS conducted under CO single fed and CO + C_3H_8 co-fed conditions. Catalysts tested are (a) Control, (b) 800°C Pretreated, (c) 1000°C Sintered, and (d) 800°C Regenerated catalysts. Gas compositions were as follows: CO single fed – 1% CO, 2.5% O_2 (N_2 gas balance), CO + C_3H_8 co-fed– 1% CO, 0.1% C_3H_8, and 3% O_2 (N_2 gas balance). Total flow rates were maintained at 100 mL/min and the temperature used was 50°C.

After the Pretreated catalyst is regenerated (R1d-P), the abundance of Pd–CeO_2 interfacial sites increases through the partial redispersion of Pd, and coinciding decrease in average sintered particle size (Figure 4.3–4.5). As demonstrated in Figure 4.10b these sites can be susceptible to poisoning by C_3H_8, which impedes CO light-off. When CO and C_3H_8 are cofed to the R1d-P

catalyst, the intensity of peaks in the 1970–1800 cm^{-1} range decreases (Figure 4.10d). This suggests that C_3H_8 is adsorbing on the bulk Pd sites that remain in the R1d-P sample and not on the interfacial sites. As C_3H_8 is co-fed, the intensity of the peak at ~2080 cm^{-1} increases. Such growth may indicate that CO displaced from bulk Pd sites by C_3H_8 can adsorb on interfacial sites, which are now more abundant due to regeneration. These adsorption dynamics result in two outcomes observed in light-off experiments for the regenerated catalyst (Figure 4.9d). First, the CO oxidation activity is unaffected by the presence of C_3H_8. Second, the R1d-P catalyst retains its C_3H_8 oxidation activity when CO is co-fed, unlike the S1-P catalyst. In fact, the C_3H_8 T_{90} decreases by approximately 30°C to 345°C in the presence of CO. This makes the R1d-P catalyst the most effective for achieving the complete co-oxidation of CO and C_3H_8. Given the exothermic nature of CO oxidation,[62,63] conversion at interfacial sites at temperatures ≤200°C may provide excess heat to accelerate C_3H_8 oxidation on nearby bulk sites, which decreases the thermal requirements for T_{90}. This may close the gap between CO T_{90} and the onset of C_3H_8 conversion during co-fed conditions.

4.3 Conclusions

This work demonstrates that intermediate temperature exposure, when applied in combination with a suitable pretreatment, effectively regenerates the abundance of metal–support interface sites and catalytic performance in sintered Pd-CeO_2 catalysts. We find that the combination of bulk and interfacial sites achieved through this regeneration produces a catalyst with superior activity in applied conditions that contain competitively adsorbing reactants. The catalyst facilitates the co-oxidation of CO and C_3H_8, two species which are known to competitively adsorb.

Using a Pd@CeO_2 model catalyst system, we show that the boundary between favorable and unfavorable restructuring is well described by the thermodynamic decomposition of the PdO phase. Aging temperatures that approach the thermodynamic limit of PdO stability were shown to facilitate redispersion of metal into dispersed sites that are anchored to the surface of reducible CeO_2 through oxygen-mediated bonding. When this limit is surpassed, e.g., high temperature aging at 1000°C, Pd–O–Ce bonds decompose and the active metal sinters. Returning to aging conditions that favor the PdO phase, shown here through 800°C aging, can recover catalytic performance through the partial redispersion of sintered Pd. Pretreating the catalyst at 800°C creates a larger fraction of dispersed metal sites, which help stabilize small polycrystalline CeO_2 domains during 1000°C aging. This preserves the Ce^{3+} sites that can trap mobile metal upon returning to 800°C conditions, which increases the efficacy of the regeneration protocol. We show the applicability of this regeneration mechanism through its successful reuse when catalysts are repeatedly sintered at 1000°C.

Our findings provide a framework that informs how controlling temperature can be used to regenerate catalyst performance. Such protocols are simple and require little intervention, which makes them attractive for *in-operando* regeneration strategies, given the control over temperature and aging environment that can be achieved in many modern reactor systems including those in automotive emissions control. The development of such simple, yet effective strategies help improve lifetime, which addresses growing concerns over the sustainability and utilization of costly materials in industrial catalysis.

4.4 Experimental Details

4.4.1 Synthesis of model core@shell catalysts

Pd@CeO_2 catalysts were synthesized according to the methods outlined in *Section 2.4.1* and *Section 3.4.1*.

4.4.2 Catalyst aging

Fresh Pd@CeO_2 catalysts were divided into two batches: a Control batch (C) that was directly aged at 1000°C and a Pretreated batch (P), that was aged at 800°C in air for 4 hours, to produce highly dispersed halo sites.[27] Each batch of catalysts was subjected to a 4 hour *in situ* aging at 1000°C, for catalytic activity measurements, and *ex situ* aging, for structural characterization. For this study, *in situ* aging denotes aging done in the catalytic testbed described below, and *ex situ* aging denotes aging conducted in a temperature programmable furnace. One aging cycle is defined by ramping at 5°C/min to a target temperature in dry air, holding said temperature for 4 hours, then cooling back down to ambient conditions. Catalysts exposed to aging at 1000°C are referred to as 'Sintered'. Upon completion of the respective characterization, the catalysts were subjected to four repeated cycles of 800°C aging. These four cycles, which were indexed a–d, define the catalytic performance and structure regeneration protocol. Catalysts exposed to these four cycles were referred to as 'Regenerated'. The CO light-off capability of each batch of catalysts was examined after each cycle of 800°C aging. After completing the four 800°C aging cycles that define the regeneration protocol, samples were once again exposed to 1000°C sintering conditions (S2) and probed for CO oxidation activity. Following this, samples were again subjected to four 800°C aging cycles (R2a–d). This was done to investigate the repeatability of the regeneration protocol.

4.4.3 Catalytic testing parameters

Light-off experiments to evaluated catalyst performance: Light-off experiments were split into three categories: CO oxidation, C_3H_8 oxidation and CO + C_3H_8 co-oxidation. Before catalytic tests, 50 mg of catalyst was sieved between 60 – 80 mesh and diluted with 80 mg of SiO_2 (which was also sieved between 60 – 80 mesh). Once sieved and mixed, the catalyst samples were loaded into a 4.00 mm (internal diameter) quartz reactor tube, placed inside a temperature programmable furnace, and subjected to continuous gas flow. Samples were cleaned by heating to 500°C for 2 hours under the flow of dry air, achieved with a ramp rate of 5°C/min. All total flow rates were set to 200 mL/min. In addition, all light-off experiments used a temperature range of 50–450°C achieved with a ramp rate of 2°C/min to ensure appropriate linear control of temperature and heat transfer within the catalyst bed. A downstream FTIR analyzer was used to provide real-time quantification of effluent gas components. CO oxidation light-off experiments used a test gas made of 1% CO and 2.5% O_2 with N_2 gas balance (CO single fed). C_3H_8 light-off experiments used a test gas made of 0.1% C_3H_8, and 3% O_2 with N_2 gas balance (C_3H_8 single fed). Co-oxidation experiments used a test gas made of 1% CO, 0.1% C_3H_8, and 3% O_2 with N_2 gas balance (co-fed).

The conversion of the target reactant (CO or C_3H_8) was used to identify T_{90} values and to plot light-off curves. The conversion of a target reactant at a given temperature, X_R, was calculated as follows:

$$X_R[\%] = \left(1 - \frac{[R]_{out}}{[R]_{in}}\right) \times 100[\%]$$

where $[R]_{in}$ is the inlet concentration of the target reactant and $[R]_{out}$ is the outlet concentration of the target reactant at a given temperature.

Arrhenius experiments to identify activation energy: Arrhenius experiments were conducted using the reactor setup and CO and C_3H_8 oxidation experiment test gas compositions outlined above. The temperature was increased in a stepwise method to ensure that conversion was under 20%. Each temperature point was stabilized for 30 minutes, with constant effluent gas analysis by a downstream FTIR. The rate of conversion of a target reactant, r_R, was calculated as follows:

$$r_R \left[\frac{mol}{g\ cat\ \cdot sec}\right] = \frac{X_R\ \cdot\ [R]_{in}\ \cdot\ \dot{V}_f}{m_{cat}}$$

where $\dot{V}_f$ is the total test gas flow rate and m_{cat} is the mass of the catalyst.

4.4.4 Material characterization

Catalysts were characterized using five techniques: STEM, EDS, XPS, XRD and *in situ* diffuse reflectance infrared Fourier transform spectroscopy (DRIFTS). Refer to *Section 3.4.5* for STEM and EDS characterization details and *Section 2.4.5* for XRD and XPS characterization details as acquisition parameters were identical.

A Bruker Tensor 27 spectrometer equipped with a Harrick Praying Mantis high-temperature reaction chamber and an MCT detector cooled by liquid nitrogen was used to collect *in situ* diffuse reflectance infrared spectra (DRIFTs). Approximately 50 mg of sample was diluted with KBr (99+% Fisher Scientific) to increase IR reflectance prior to loading into the Praying Mantis sample cup. The samples were then pumped down to vacuum (~10^{-6} torr), to clean the catalyst surface prior to pretreatment and 315°C for 2 hours under 20% O_2 with an N_2 gas balance flowing at 100 mL/min. Once pretreatment had been completed, the sample was cooled to 50°C.

Background signals for *in situ* DRIFTS experiments were collected under the flow of 3% O_2 with a N_2 balance flowing at 100 mL/min. *in situ* DRIFTS spectra were collected for catalysts

under two flow conditions, which were similar to light-off experiment conditions: 1% CO with 3% O_2 (CO single fed) and 1% CO with 0.1% C_3H_8 and 3% O_2 (co-fed). The total flow rate was maintained at 100 mL/min for all experiments. Gases were left to flow over the catalyst after for 30 minutes prior to data collection, to ensure steady–state transport. The peak area in regions corresponding to the adsorption of CO (2200–1700 cm^{-1})[15,31,59] were monitored to probe competitive adsorption dynamics. It should be noted that the same catalyst sample was used for single and cofed experiments. Catalysts were heated to 500°C for 2 hours under 20% O_2 with an N_2 gas balance flowing at 100 mL/min to remove any adsorbates remaining from the single fed experiments. Catalysts were then exposed to the vacuum and pretreatment steps discussed above.

4.5 References

(1) Jeong, H.; Kwon, O.; Kim, B.-S.; Bae, J.; Shin, S.; Kim, H.-E.; Kim, J.; Lee, H. Highly Durable Metal Ensemble Catalysts with Full Dispersion for Automotive Applications beyond Single-Atom Catalysts. *Nat. Catal.* **2020**, *3* (4), 368–375. https://doi.org/10.1038/s41929-020-0427-z.

(2) Datye, A. K.; Votsmeier, M. Opportunities and Challenges in the Development of Advanced Materials for Emission Control Catalysts. *Nat. Mater.* **2020**. https://doi.org/10.1038/s41563-020-00805-3.

(3) Cargnello, M.; Doan-Nguyen, V. V. T.; Gordon, T. R.; Diaz, R. E.; Stach, E. A.; Gorte, R. J.; Fornasiero, P.; Murray, C. B. Control of Metal Nanocrystal Size Reveals Metal-Support Interface Role for Ceria Catalysts. *Science.* **2013**, *341*, 771–773. https://doi.org/10.1126/science.1240148.

(4) Puigdollers, A. R.; Schlexer, P.; Tosoni, S.; Pacchioni, G. Increasing Oxide Reducibility: The Role of Metal/Oxide Interfaces in the Formation of Oxygen Vacancies. *ACS Catal.* **2017**, *7*, 6493–6513. https://doi.org/10.1021/acscatal.7b01913.

(5) Argyle, M. D.; Bartholomew, C. H. Heterogeneous Catalyst Deactivation and Regeneration: A Review. *Catalysts* **2015**, *5*, 145–269. https://doi.org/10.3390/catal5010145.

(6) Hansen, T. W.; DeLaRiva, A. T.; Challa, S. R.; Datye, A. K. Sintering of Catalytic Nanoparticles: Particle Migration or Ostwald Ripening? *Acc. Chem. Res.* **2013**, *46*, 1720–1730. https://doi.org/10.1021/ar3002427.

(7) Johns, T. R.; Goeke, R. S.; Ashbacher, V.; Thüne, P. C.; Niemantsverdriet, J. W.; Kiefer, B.; Kim, C. H.; Balogh, M. P.; Datye, A. K. Relating Adatom Emission to Improved Durability of Pt–Pd Diesel Oxidation Catalysts. *J. Catal.* **2015**, *328*, 151–164. https://doi.org/10.1016/j.jcat.2015.03.016.

(8) Su, Y.-Q.; Liu, J.-X.; Filot, I. A. W.; Hensen, E. J. M. Theoretical Study of Ripening Mechanisms of Pd Clusters on Ceria. *Chem. Mater.* **2017**, *29*, 9456–9462. https://doi.org/10.1021/acs.chemmater.7b03555.

(9) Jones, J.; Xiong, H.; DeLaRiva, A. T.; Peterson, E. J.; Pham, H.; Challa, S. R.; Qi, G.; Oh, S.; Wiebenga, M. H.; Hernández, X. I. P.; et al. Thermally Stable Single-Atom Platinum-on-Ceria Catalysts via Atom Trapping. *Science.* **2016**, *353* (6295), 150–154. https://doi.org/10.1126/science.aaf8800.

(10) Chin, Y. H. C.; García-Diéguez, M.; Iglesia, E. Dynamics and Thermodynamics of Pd-PdO Phase Transitions: Effects of Pd Cluster Size and Kinetic Implications for Catalytic Methane Combustion. *J. Phys. Chem. C* **2016**, *120*, 1446–1460. https://doi.org/10.1021/acs.jpcc.5b06677.

(11) Wan, Q.; Wei, F.; Wang, Y.; Wang, F.; Zhou, L.; Lin, S.; Xie, D.; Guo, H. Single Atom Detachment from Cu Clusters, and Diffusion and Trapping on CeO_2(111): Implications in Ostwald Ripening and

Atomic Redispersion. *Nanoscale* **2018**, *10* (37), 17893–17901. https://doi.org/10.1039/C8NR06232C.
(12) Farnesi Camellone, M.; Dvořák, F.; Vorokhta, M.; Tovt, A.; Khalakhan, I.; Johánek, V.; Skála, T.; Matolínová, I.; Fabris, S.; Mysliveček, J. Adatom and Nanoparticle Dynamics on Single-Atom Catalyst Substrates. *ACS Catal.* **2022**, 4859–4871. https://doi.org/10.1021/acscatal.2c00291.
(13) Kunwar, D.; Zhou, S.; Delariva, A.; Peterson, E. J.; Xiong, H.; Pereira-Hernández, X. I.; Purdy, S. C.; Ter Veen, R.; Brongersma, H. H.; Miller, J. T.; et al. Stabilizing High Metal Loadings of Thermally Stable Platinum Single Atoms on an Industrial Catalyst Support. *ACS Catal.* **2019**, *9*, 3978–3990. https://doi.org/10.1021/acscatal.8b04885.
(14) Su, Y. Q.; Liu, J. X.; Filot, I. A. W.; Hensen, E. J. M. Theoretical Study of Ripening Mechanisms of Pd Clusters on Ceria. *Chem. Mater.* **2017**, *29*, 9456–9462. https://doi.org/10.1021/acs.chemmater.7b03555.
(15) Jiang, D.; Wan, G.; García-Vargas, C. E.; Li, L.; Pereira-Hernández, X. I.; Wang, C.; Wang, Y. Elucidation of the Active Sites in Single-Atom Pd_1/CeO_2 Catalysts for Low-Temperature CO Oxidation. *ACS Catal.* **2020**, *10*, 11356–11364. https://doi.org/10.1021/acscatal.0c02480.
(16) Xiong, H.; Datye, A. K.; Wang, Y. Thermally Stable Single-Atom Heterogeneous Catalysts. *Adv. Mater.* **2021**, *2004319*. https://doi.org/10.1002/adma.202004319.
(17) Dvořák, F.; Camellone, M. F.; Tovt, A.; Tran, N. D.; Negreiros, F. R.; Vorokhta, M.; Skála, T.; Matolínová, I.; Mysliveček, J.; Matolín, V.; et al. Creating Single-Atom Pt-Ceria Catalysts by Surface Step Decoration. *Nat. Commun.* **2016**, *7*. https://doi.org/10.1038/ncomms10801.
(18) Wu, Z.; Hwang, I.; Cha, G.; Qin, S.; Tomanec, O.; Badura, Z.; Kment, S.; Zboril, R.; Schmuki, P. Optimized Pt Single Atom Harvesting on TiO_2 Nanotubes—Towards a Most Efficient Photocatalyst. *Small* **2022**, *18* (2), 2104892. https://doi.org/10.1002/smll.202104892.
(19) Figueroba, A.; Kovács, G.; Bruix, A.; Neyman, K. M. Towards Stable Single-Atom Catalysts: Strong Binding of Atomically Dispersed Transition Metals on the Surface of Nanostructured Ceria. *Catal. Sci. Technol.* **2016**, *6* (18), 6806–6813. https://doi.org/10.1039/C6CY00294C.
(20) Yao, Y.; Huang, Z.; Xie, P.; Wu, L.; Ma, L.; Li, T.; Pang, Z.; Jiao, M.; Liang, Z.; Gao, J.; et al. High Temperature Shockwave Stabilized Single Atoms. *Nat. Nanotechnol.* **2019**, *14*, 851–857. https://doi.org/10.1038/s41565-019-0518-7.
(21) Xie, H.; Hong, M.; Hitz, E. M.; Wang, X.; Cui, M.; Kline, D. J.; Zachariah, M. R.; Hu, L. High-Temperature Pulse Method for Nanoparticle Redispersion. *J. Am. Chem. Soc.* **2020**, *142*, 17364–17371. https://doi.org/10.1021/jacs.0c04887.
(22) Giulimondi, V.; Kaiser, S. K.; Agrachev, M.; Krumeich, F.; Clark, A. H.; Mitchell, S.; Jeschke, G.; Pérez-Ramírez, J. Redispersion Strategy for High-Loading Carbon-Supported Metal Catalysts with Controlled Nuclearity. *J. Mater. Chem. A* **2022**, No. ii. https://doi.org/10.1039/d1ta09238c.
(23) AL-Harbi, M.; Hayes, R.; Votsmeier, M.; Epling, W. S. Competitive No, Co and Hydrocarbon Oxidation Reactions over a Diesel Oxidation Catalyst. *Can. J. Chem. Eng.* **2012**, *90* (6), 1527–1538. https://doi.org/10.1002/cjce.20659.
(24) Jeong, H.; Lee, G.; Kim, B.-S.; Bae, J.; Han, J. W.; Lee, H. Fully Dispersed Rh Ensemble Catalyst To Enhance Low-Temperature Activity. *J. Am. Chem. Soc.* **2018**, *140*, 9558–9565. https://doi.org/10.1021/jacs.8b04613.
(25) Peuckert, M. XPS Study on Surface and Bulk Palladium Oxide, Its Thermal Stability, and a Comparison with Other Noble Metal Oxides. *J. Phys. Chem.* **1985**, *89* (12), 2481–2486. https://doi.org/10.1021/j100258a012.
(26) Lee, J.; Ryou, Y.; Chan, X.; Kim, T. J.; Kim, D. H. How Pt Interacts with CeO_2 under the Reducing and Oxidizing Environments at Elevated Temperature: The Origin of Improved Thermal Stability of Pt/CeO_2 Compared to CeO_2. *J. Phys. Chem. C* **2016**, *120*, 25870–25879. https://doi.org/10.1021/acs.jpcc.6b08656.
(27) Hill, A. J.; Bhat, A.; Berquist, Z. J.; Fisher, G. B.; Lenert, A.; Schwank, J. W. Stabilizing Highly Dispersed Halo Sites in Thermally Restructured Palladium Core@Shell Nanoparticles for Improved Catalyst Activity and Durability. *ACS Appl. Nano Mater.* **2021**, *4* (10), 10985–10998. https://doi.org/10.1021/acsanm.1c02436.
(28) Zhou, X.; Zhang, Y.; Wang, J. DFT Study on the Regeneration of $Pt/\gamma\text{-}Al_2O_3$ Catalyst: The Effect of Chlorine on the Redispersion of Metal Species. *Appl. Surf. Sci.* **2021**, *545*, 148988. https://doi.org/10.1016/j.apsusc.2021.148988.

(29) Hill, A. J.; Seo, C. Y.; Chen, X.; Bhat, A.; Fisher, G. B.; Lenert, A.; Schwank, J. W. Thermally Induced Restructuring of Pd@CeO_2 and Pd@SiO_2 Nanoparticles as a Strategy for Enhancing Low-Temperature Catalytic Activity. *ACS Catal.* **2020**, *10*, 1731 – 1741. https://doi.org/10.1021/acscatal.9b05224.

(30) Pereira-Hernández, X. I.; DeLaRiva, A.; Muravev, V.; Kunwar, D.; Xiong, H.; Sudduth, B.; Engelhard, M.; Kovarik, L.; Hensen, E. J. M.; Wang, Y.; et al. Tuning Pt-CeO_2 Interactions by High-Temperature Vapor-Phase Synthesis for Improved Reducibility of Lattice Oxygen. *Nat. Commun.* **2019**, *10*, 1358. https://doi.org/10.1038/s41467-019-09308-5.

(31) Muravev, V.; Spezzati, G.; Su, Y.-Q.; Parastaev, A.; Chiang, F.-K.; Longo, A.; Escudero, C.; Kosinov, N.; Hensen, E. J. M. Interface Dynamics of Pd–CeO_2 Single-Atom Catalysts during CO Oxidation. *Nat. Catal.* **2021**, *4*, 469–478. https://doi.org/10.1038/s41929-021-00621-1.

(32) Huang, M.; Wang, S.; Li, L.; Zhang, H.; Shi, Z.; Chen, Y. Effect of High Temperature Pretreatment on the Thermal Resistance Properties of Pd/CeO_2/Al_2O_3 Close-Coupled Catalysts. *J. Rare Earths* **2017**, *35* (2), 149–157. https://doi.org/10.1016/S1002-0721(17)60893-7.

(33) Xu, H.; Lin, C.; Lin, Q.; Feng, X.; Zhang, Z.; Wang, Y.; Chen, Y. Grain Size Effect on the High-Temperature Hydrothermal Stability of Cu/SAPO-34 Catalysts for NH_3-SCR. *J. Environ. Chem. Eng.* **2020**, *13* (61), 104559. https://doi.org/10.1016/j.jece.2020.104559.

(34) Xie, S.; Wang, Z.; Tan, W.; Zhu, Y.; Collier, S.; Ma, L.; Ehrlich, S. N.; Xu, P.; Yan, Y.; Xu, T.; et al. Highly Active and Stable Palladium Catalysts on Novel Ceria–Alumina Supports for Efficient Oxidation of Carbon Monoxide and Hydrocarbons. *Environ. Sci. Technol.* **2021**, *55* (11), 7624–7633. https://doi.org/10.1021/acs.est.1c00077.

(35) Alcala, R.; DeLaRiva, A.; Peterson, E. J.; Benavidez, A.; Garcia-Vargas, C. E.; Jiang, D.; Pereira-Hernández, X. I.; Brongersma, H. H.; Veen, R. ter; Staněk, J.; et al. Atomically Dispersed Dopants for Stabilizing Ceria Surface Area. *Appl. Catal. B Environ.* **2021**, *284*, 119722. https://doi.org/10.1016/j.apcatb.2020.119722.

(36) Kang, S. B.; Lim, J. Bin; Jo, D.; Nam, I.-S.; Cho, B. K.; Hong, S. B.; Kim, C. H.; Oh, S. H. Ostwald-Ripening Sintering Kinetics of Pd-Based Three-Way Catalyst: Importance of Initial Particle Size of Pd. *Chem. Eng. J.* **2017**, *316*, 631–644. https://doi.org/10.1016/j.cej.2017.01.136.

(37) Julbe, A.; Farrusseng, D.; Guizard, C. Porous Ceramic Membranes for Catalytic Reactors — Overview and New Ideas. *J. Memb. Sci.* **2001**, *181* (1), 3–20. https://doi.org/10.1016/S0376-7388(00)00375-6.

(38) Metcalfe, I. S.; Ray, B.; Dejoie, C.; Hu, W.; de Leeuwe, C.; Dueso, C.; García-García, F. R.; Mak, C.-M.; Papaioannou, E. I.; Thompson, C. R.; et al. Overcoming Chemical Equilibrium Limitations Using a Thermodynamically Reversible Chemical Reactor. *Nat. Chem.* **2019**. https://doi.org/10.1038/s41557-019-0273-2.

(39) Munahar, S.; Purnomo, B. C.; Setiyo, M.; Triwiyatno, A.; Setiawan, J. D. Design and Application of Air to Fuel Ratio Controller for LPG Fueled Vehicles at Typical Down-Way. *SN Appl. Sci.* **2020**, *2* (1), 37. https://doi.org/10.1007/s42452-019-1839-8.

(40) Chen, J.; Wanyan, Y.; Zeng, J.; Fang, H.; Li, Z.; Dong, Y.; Qin, R.; Wu, C.; Liu, D.; Wang, M.; et al. Surface Engineering Protocol To Obtain an Atomically Dispersed Pt/CeO 2 Catalyst with High Activity and Stability for CO Oxidation. *ACS Sustain. Chem. Eng.* **2018**, *6* (11), 14054–14062. https://doi.org/10.1021/acssuschemeng.8b02613.

(41) Hu, B.; Sun, K.; Zhuang, Z.; Chen, Z.; Liu, S.; Cheong, W.; Chen, C.; Hu, M.; Cao, X.; Ma, J.; et al. Distinct Crystal-Facet-Dependent Behaviors for Single-Atom Palladium-on-Ceria Catalysts: Enhanced Stabilization and Catalytic Properties. *Adv. Mater.* **2022**, 2107721. https://doi.org/10.1002/adma.202107721.

(42) Slavinskaya, E. M.; Gulyaev, R. V.; Zadesenets, A. V.; Stonkus, O. A.; Zaikovskii, V. I.; Shubin, Y. V.; Korenev, S. V.; Boronin, A. I. Low-Temperature CO Oxidation by Pd/CeO_2 Catalysts Synthesized Using the Coprecipitation Method. *Appl. Catal. B Environ.* **2015**, *166–167*, 91–103. https://doi.org/10.1016/j.apcatb.2014.11.015.

(43) Slavinskaya, E. M.; Kardash, T. Y.; Stonkus, O. A.; Gulyaev, R. V.; Lapin, I. N.; Svetlichnyi, V. A.; Boronin, A. I. Metal-Support Interaction in Pd/CeO_2 Model Catalysts for CO Oxidation: From Pulsed Laser-Ablated Nanoparticles to Highly Active State of the Catalyst. *Catal. Sci. Technol.* **2016**, *6* (17), 6650–6666. https://doi.org/10.1039/c6cy00319b.

(44) Hinokuma, S.; Fujii, H.; Okamoto, M.; Ikeue, K.; Machida, M. Metallic Pd Nanoparticles Formed by

Pd−O−Ce Interaction: A Reason for Sintering-Induced Activation for CO Oxidation. *Chem. Mater.* **2010**, *22*, 6183–6190. https://doi.org/10.1021/cm102355x.

(45) Tan, W.; Xie, S.; Cai, Y.; Wang, M.; Yu, S.; Low, K.-B.; Li, Y.; Ma, L.; Ehrlich, S. N.; Gao, F.; et al. Transformation of Highly Stable Pt Single Sites on Defect Engineered Ceria into Robust Pt Clusters for Vehicle Emission Control. *Environ. Sci. Technol.* **2021**, *55* (18), 12607–12618. https://doi.org/10.1021/acs.est.1c02853.

(46) Xu, H.; Zhang, Z.; Liu, J.; Do-Thanh, C.-L.; Chen, H.; Xu, S.; Lin, Q.; Jiao, Y.; Wang, J.; Wang, Y.; et al. Entropy-Stabilized Single-Atom Pd Catalysts via High-Entropy Fluorite Oxide Supports. *Nat. Commun.* **2020**, *11* (1), 3908. https://doi.org/10.1038/s41467-020-17738-9.

(47) Shu, Y.; Bao, J.; Yang, S.; Duan, X.; Zhang, P. Entropy-stabilized Metal-CeO_x Solid Solutions for Catalytic Combustion of Volatile Organic Compounds. *AIChE J.* **2020**, No. February. https://doi.org/10.1002/aic.17046.

(48) Lieske, H.; Voelter, J. Palladium Redispersion by Spreading of Palladium(II) Oxide in Oxygen Treated Palladium/Alumina. *J. Phys. Chem.* **1985**, *89*, 1841–1842. https://doi.org/10.1021/j100256a001.

(49) Lupescu, J. A.; Schwank, J. W.; Dahlberg, K. A.; Seo, C. Y.; Fisher, G. B.; Peczonczyk, S. L.; Rhodes, K.; Jagner, M. J.; Haack, L. P. Pd Model Catalysts: Effect of Aging Environment and Lean Redispersion. *Appl. Catal. B Environ.* **2016**, *183*, 343–360. https://doi.org/10.1016/j.apcatb.2015.10.018.

(50) Lupescu, J. A.; Schwank, J. W.; Fisher, G. B.; Chen, X.; Peczonczyk, S. L.; Drews, A. R. Pd Model Catalysts: Effect of Aging Duration on Lean Redispersion. *Appl. Catal. B Environ.* **2016**, *185*, 189–202. https://doi.org/10.1016/j.apcatb.2015.12.012.

(51) Goodman, E. D.; Carlson, E. Z.; Dietze, E. M.; Tahsini, N.; Johnson, A.; Aitbekova, A.; Nguyen Taylor, T.; Plessow, P. N.; Cargnello, M. Size-Controlled Nanocrystals Reveal Spatial Dependence and Severity of Nanoparticle Coalescence and Ostwald Ripening in Sintering Phenomena. *Nanoscale* **2021**, *13*, 930–938. https://doi.org/10.1039/D0NR07960J.

(52) Luo, J.-Y.; Meng, M.; Zha, Y.-Q.; Guo, L.-H. Identification of the Active Sites for CO and C_3H_8 Total Oxidation over Nanostructured CuO−CeO_2 and Co_3O_4−CeO_2 Catalysts. *J. Phys. Chem. C* **2008**, *112* (23), 8694–8701. https://doi.org/10.1021/jp800651k.

(53) Liu, Y.; Yang, J.; Yang, J.; Wang, L.; Wang, Y.; Zhan, W.; Guo, Y.; Zhao, Y.; Guo, Y. Understanding the Three-Way Catalytic Reaction on Pd/CeO_2 by Tuning the Chemical State of Pd. *Appl. Surf. Sci.* **2021**, *556*, 149766. https://doi.org/10.1016/j.apsusc.2021.149766.

(54) Jeong, H.; Shin, S.; Lee, H. Heterogeneous Atomic Catalysts Overcoming the Limitations of Single-Atom Catalysts. *ACS Nano* **2020**, *14* (11), 14355–14374. https://doi.org/10.1021/acsnano.0c06610.

(55) Zhang, Q.; Lee, I.; Joo, J. B.; Zaera, F.; Yin, Y. Core-Shell Nanostructured Catalysts. *Acc. Chem. Res.* **2013**, *46* (8), 1816–1824. https://doi.org/10.1021/ar300230s.

(56) Zhang, J.; Wang, B.; Nikolla, E.; Medlin, J. W. Directing Reaction Pathways through Controlled Reactant Binding at Pd–TiO_2 Interfaces. *Angew. Chem. Int. Ed* **2017**, *56* (23), 6594–6598. https://doi.org/10.1002/anie.201703669.

(57) Wang, G.-H.; Chen, K.; Engelhardt, J.; Tüysüz, H.; Bongard, H.-J.; Schmidt, W.; Schüth, F. Scalable One-Pot Synthesis of Yolk–Shell Carbon Nanospheres with Yolk-Supported Pd Nanoparticles for Size-Selective Catalysis. *Chem. Mater.* **2018**, *30* (8), 2483–2487. https://doi.org/10.1021/acs.chemmater.8b00456.

(58) Zhou, R.; Xing, F.; Wang, S.; Lu, J.; Jin, L.; Luo, M. CO and C_3H_8 Total Oxidation over Pd/La-Al_2O_3 Catalysts: Effect of Calcination Temperature and Hydrothermal Treatment. *J. Rare Earths* **2014**, *32* (7), 621–627. https://doi.org/10.1016/S1002-0721(14)60117-4.

(59) Spezzati, G.; Su, Y.; Hofmann, J. P.; Benavidez, A. D.; DeLaRiva, A. T.; McCabe, J.; Datye, A. K.; Hensen, E. J. M. Atomically Dispersed Pd–O Species on CeO_2 (111) as Highly Active Sites for Low-Temperature CO Oxidation. *ACS Catal.* **2017**, *7*, 6887–6891. https://doi.org/10.1021/acscatal.7b02001.

(60) Spezzati, G.; Benavidez, A. D.; DeLaRiva, A. T.; Su, Y.; Hofmann, J. P.; Asahina, S.; Olivier, E. J.; Neethling, J. H.; Miller, J. T.; Datye, A. K.; et al. CO Oxidation by Pd Supported on CeO_2 (100) and CeO_2 (111) Facets. *Appl. Catal. B Environ.* **2019**, *243*, 36–46. https://doi.org/10.1016/j.apcatb.2018.10.015.

(61) Ortega, A.; Huffman, F. M.; Bradshaw, A. M. The Adsorption of CO on Pd(100) Studied by IR Reflection Absorption Spectroscopy. *Surf. Sci.* **1982**, *119* (1), 79–94. https://doi.org/10.1016/0039-

6028(82)90189-3.
(62) Al Soubaihi, R.; Saoud, K.; Dutta, J. Critical Review of Low-Temperature CO Oxidation and Hysteresis Phenomenon on Heterogeneous Catalysts. *Catalysts* **2018**, *8*, 660. https://doi.org/10.3390/catal8120660.
(63) Dann, E. K.; Gibson, E. K.; Catlow, C. R. A.; Celorrio, V.; Collier, P.; Eralp, T.; Amboage, M.; Hardacre, C.; Stere, C.; Kroner, A.; et al. Combined Spatially Resolved Operando Spectroscopy: New Insights into Kinetic Oscillations of CO Oxidation on Pd/γ-Al_2O_3. *J. Catal.* **2019**, *373*, 201–208. https://doi.org/10.1016/j.jcat.2019.03.037.

Chapter 5 : Favorable Restructuring in Monometallic Au@CeO_2 and Bimetallic AuPd@CeO_2 core@shell catalysts

5.1 Motivation

The favorable restructuring of core@shell nanoparticles is a simple and effective strategy to redisperse active metal into highly dispersed sites with improved stability and activity. Highly dispersed sites are valuable to a variety of catalytic processes beyond oxidation.[1–3] In addition, these high atomic efficiency arrangements have garnered attention for a number of other applications such as biosensing,[4] and energy storage and conversion.[5] As demonstrated during the aging of Pd@SiO_2 and Pd@CeO_2 catalysts, core@shell architectures can effectively promote the redispersion of active metal species that would otherwise agglomerate in conventional morphologies.[6,7] The ability to generalize this favorable restructuring strategy to redisperse metals other than Pd, however, has yet to be observed.

The previous chapters of this thesis have demonstrated how oxidation plays a significant role in the ability to redisperse an active metal at elevated temperature. The stability of the redispersed phase is also effectively described by the thermodynamics of metal–oxygen interactions. These observations suggests that if a metal can be oxidized in elevated temperature, oxygen–rich conditions, it should redisperse in the encapsulating environment of a core@shell architecture. This chapter probes this hypothesis by investigating the restructuring of Au in a Au@CeO_2 core@shell system, as Au exhibits much poorer oxidation thermodynamics when compared to Pd. As shown in Figure 5.1, Au does not form a stable oxide at oxygen partial

pressures below 10^{15} Pa. Consequently, it is a good model system to probe the importance of oxidation thermodynamics for mediating favorable restructuring in core@shell architectures.

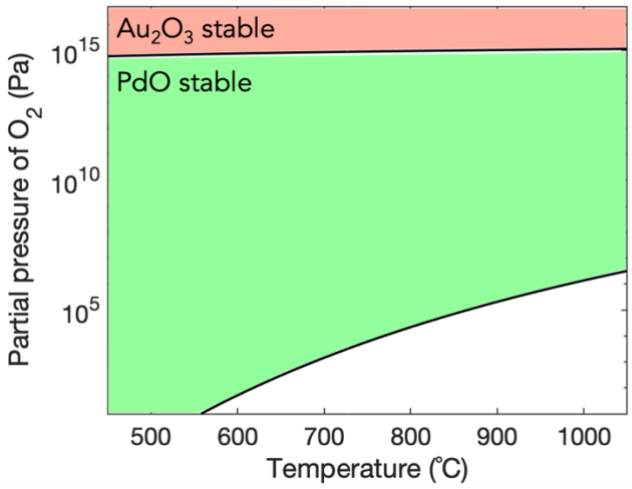

Figure 5.1. Thermodynamics of oxidation for Au and Pd.
Au–Au_2O_3 and Pd–PdO gas phase equilibrium diagrams plotted from the relationships described in reference.[8]

Au is found to not redisperse in Au@CeO_2 systems using the same aging conditions that redisperse Pd in Pd@SiO_2 and Pd@CeO_2 (800°C in air for 4 hours). This suggests that oxidation thermodynamics can effectively describe the propensity for metal redispersion. Consequently, in instances where core metals exhibit unstable oxides, the role of encapsulation changes from a restructuring template to a physical barrier that promotes thermal stability.

As previously described in Chapter 1, alloying active metal species together can alter local electronic structure, which can improve catalytic performance.[9,10] Au can be readily alloyed with Pd, which results in a high performing catalyst for applications such as the production of commodity chemicals and the remediation of volatile organic compounds.[11–14] The synergy between Au and Pd has also been investigated for use in emissions control catalysts.[15,16] In addition to their catalytic relevance, Au–Pd bimetallic systems have been shown to dynamically restructure under catalytic working conditions.[17–19] As such, this work investigates whether a metal with a

very stable oxide such as Pd, through alloying, can facilitate the favorable restructuring of a metal with an unstable oxide such as Au.

Au cores are synthesized with overlayers of Pd in AuPd@CeO_2 nanoparticles due to the superior reduction potential of the Au precursor, $AuBr_4^-$, in solution when compared to the Pd precursor, $PdBr_4^{2-}$.[20] In contrast to the monometallic Au@CeO_2 system, Au appears to redisperse in bimetallic AuPd@CeO_2. As demonstrated by scanning transmission electron microscopy (STEM) and energy dispersive spectroscopy (EDS) elemental mapping, bimetallic cores break up and form smaller particles in addition to regions of highly dispersed Au and Pd. The redispersion of bimetallic cores at 800°C is tracked in real time using *in situ* STEM. X-ray diffraction (XRD) characterization identifies that average metal particles have shrunk and reconstructed to form intermixed alloys of Au and Pd, instead of Pd overlaid on Au. Consequently, this work shows that alloying can facilitate favorable restructuring for Au in a core@shell architecture, which demonstrates a promising method to both redisperse active metals with poor thermodynamics of oxidation and produce dispersed bimetallic sites for catalysis.

5.2 Results and Discussion

5.2.1 Defining model nanoparticle systems

Au@CeO_2 and AuPd@CeO_2 catalysts were synthesized using methods similar to those previously described by Zhang *et. al*, where pH conditions and metal precursor redox potentials are controlled in a one-pot procedure.[21] The synthesis proceeds as an autoredox reaction between brominated core metal precursors and a CeO_2 precursor, cerium hydroxide ($Ce(OH)_3$), which form through reactions as outlined in Figure 5.2. The autoredox behavior of the core and shell precursors makes for a straightforward synthesis that can be volumetrically scaled to improve batch yield. Cerium acetylacetonate ($Ce(acac)_3$) is converted to $Ce(OH)_3$ through a reaction with NH_3 in-

solution. $Ce(OH)_3$ is used as a shell precursor as it can readily reduce brominated metal precursors through the formation of –Ce–O–Ce– linkages (i.e., CeO_2 nanoparticles) and HBr, which dissociates in the aqueous synthesis environment. Addition of a surfactant such as polyvinylpyrrolidone (PVP) helps control metal nanoparticle size, minimize particle aggregation, and facilitates the growth of CeO_2 around metal particles in a core@shell morphology. As the formation of the core and shell simultaneously occur through reactions with $Ce(OH)_3$, the rate of producing $Ce(OH)_3$ can be used to control core and shell thickness. This is done by tuning the solution alkalinity introduced through NH_3 addition. When greater amounts of NH_3 are added, core sizes are smaller and active metal species are highly distributed throughout the shell. Adding lower concentrations of NH_3 allows $Ce(OH)_3$ to form more slowly, which allows active metal ions to coalesce in solution before reacting to zero-valent states. This results in larger core sizes.

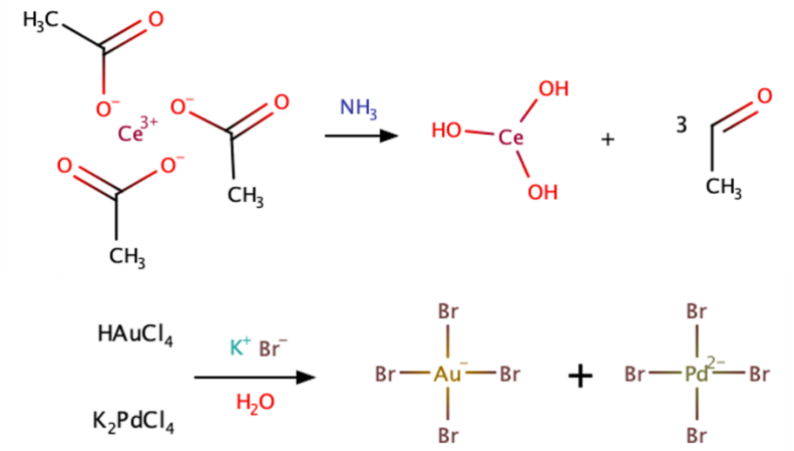

Figure 5.2. Mechanism of core and shell precursor formation.

$AuBr_4^-$ is preferentially reduced by $Ce(OH)_3$ when compared to $PdBr_4^{2-}$.[20] As such, Au ions aggregate and form particles, which act as seeds for Pd ions to adsorb upon. This results in bimetallic AuPd@CeO_2, which exist as cores of Au with overlayers of Pd. These cores are then encapsulated by CeO_2 shells that form through the stacking of smaller CeO_2 particles, similar to

those described in Chapters 2–4. In the absence of Pd precursors, monometallic Au@CeO_2 particles are a formed, as shown in Figure 5.3.

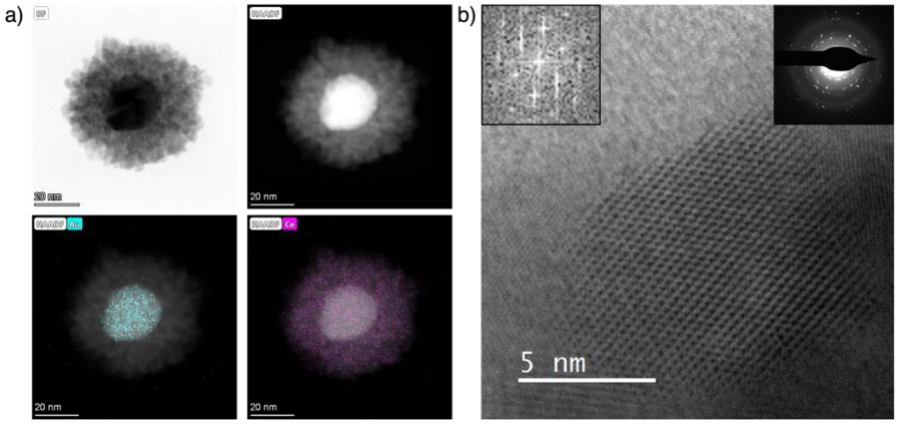

Figure 5.3. STEM, EDS and high-resolution TEM characterization of fresh Au@CeO_2.
(a) STEM characterization and EDS elemental mapping. EDS figures contain embedded legends to indicate the corresponding colors for the elemental maps (Au: Blue, Ce: Pink) and the detector used to collect the STEM image (BF: bright-field, HAADF: high angle annular dark-field). (b) High-resolution TEM characterization of an individual CeO_2 crystallite on a Au@CeO_2 particle. Fast Fourier transform (FFT) of the CeO_2 crystallite has been inset (left) in addition to a selected area electron diffraction pattern of a whole Au@CeO_2 nanoparticle (right).

As seen in Figure 5.3, Au cores are approximately 20 – 30 nm in diameter and CeO_2 shells are on the order of 10 nm thick. This results in fresh Au@CeO_2 nanoparticles that are approximately 50 nm in diameter. XRD characterization in Figure 5.4 identifies that Au cores are 27.3 nm in diameter and CeO_2 crystallites are 6.8 nm in diameter on average. Figure 5.3b confirms that these crystallites are small, randomly oriented, and polycrystalline. These structural features allow for a high density of steps, edges and consequently, undercoordinated Ce^{3+} sites, which are effective for trapping metal species during elevated temperature mobility.[22–24]

Figure 5.5 shows successfully synthesized bimetallic AuPd@CeO_2 particles prepared with an equimolar concentration of Au and Pd. As can be seen, the cores are comparable in size to the monometallic Au cores in Au@CeO_2, with an average diameter of 23.03 nm, as determined by the Debye-Scherrer equation. The peak locations of the (111) and (200) Au reflections directly overlap that of monometallic Au@CeO_2. In addition, no discernable reflection for bulk Pd can be observed.

These observations are consistent with a Au core that has an overlayer of Pd instead of being atomically mixed.[25] CeO_2 crystallites have a comparable average size of 5.91 nm (Figure 5.4,b), and stack together to form shells of similar thickness to their monometallic counterparts. EDS characterization shows that Pd overlayers have formed atop the Au cores.

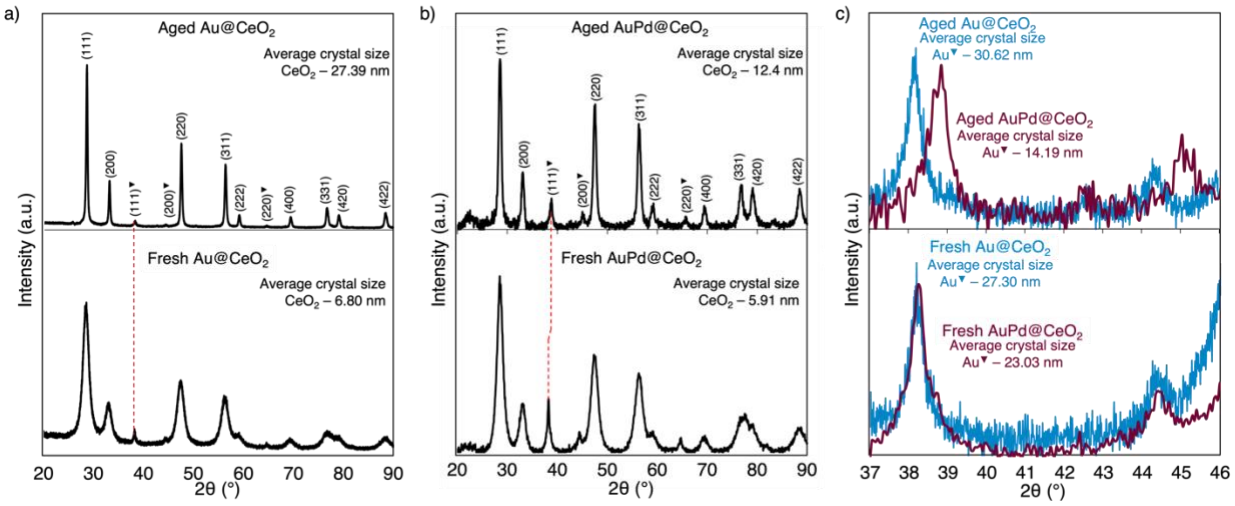

Figure 5.4. X-ray diffraction characterization of fresh and aged $Au@CeO_2$ and $AuPd@CeO_2$.
XRD characterization of fresh and aged (a) $Au@CeO_2$ and (b) $AuPd@CeO_2$ catalysts. Peaks corresponding to Au reflections have been highlighted with ▼. All other peaks are attributed to reflections of the CeO_2 shell. (c) XRD characterization in the region corresponding to Au (111) and (200) reflections for fresh and aged $Au@CeO_2$ and $AuPd@CeO_2$. Average CeO_2 and Au crystals sizes has been inset.

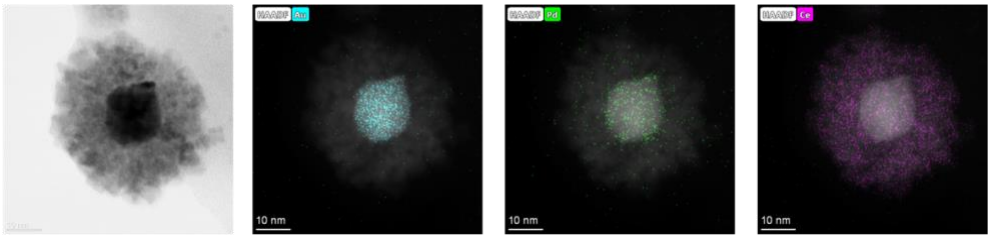

Figure 5.5. STEM and EDS characterization of fresh $AuPd@CeO_2$.
EDS elemental mapping figures contain embedded legends to indicate the corresponding colors for the elemental maps (Au: Blue, Pd: Green, Ce: Pink) and the detector used to collect the STEM image (BF: bright-field, HAADF: high angle annular dark-field).

5.2.2 Absence of redispersion in $Au@CeO_2$ nanoparticles

$Au@CeO_2$ catalysts were aged at 800°C in air for 4 hours to examine whether the favorable restructuring observed in $Pd@CeO_2$ systems would occur.[6,7] As seen in Figure 5.6, Au cores are still intact after high-temperature aging. The concentrated Au signal at the core, as shown by EDS

elemental mapping, suggests that partial redispersion of Au did not occur. This outcome is expected due to the poor oxidation thermodynamics exhibited by Au nanoparticles,[8] which decreases the likelihood of cluster disintegration and redispersion without the use of an adsorbate such as a halogenated compound.[26,27] The lack of core disintegration and redispersion is corroborated by XRD, which shows that the average Au core size remains relatively consistent (30.62 nm) after aging. The cores appear to have reshaped during the elevated temperature aging. This may have been caused by the restructuring of CeO_2 shell crystallites, which have agglomerated into larger particles, with an average size of 27.39 nm, around the Au core.

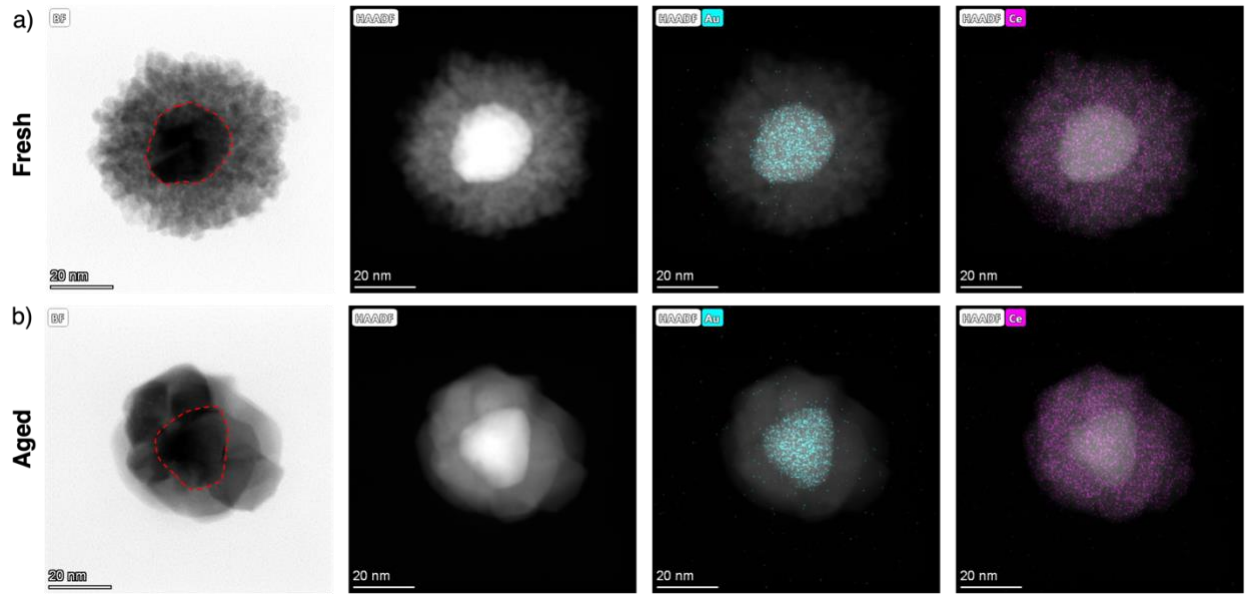

Figure 5.6. STEM and EDS characterization of Au@CeO_2 before and after ex situ aging. Au@CeO_2 catalyst (a) as fresh and (b) after aging at 800°C in air for 4 hours. EDS elemental mapping figures contain embedded legends to indicate the corresponding colors for the elemental maps (Au: Blue, Ce: Pink) and the detector used to collect the STEM image (BF: bright-field, HAADF: high angle annular dark-field). Red outlines of the cores have been included to identify their shape prior to and post 800°C aging.

Additional characterization of Au@CeO_2 shows that CeO_2 crystallites from neighboring particles have grown together after aging at 800°C (Figure 5.7). This emphasizes the importance of dispersible active metal species for stabilizing support morphology during high temperature exposure.[7,22] Despite the interparticle coalescence of supporting CeO_2 crystallites, Au cores in neighboring particles have not sintered. This suggests that when an active metal with poor

oxidation thermodynamics is used, the core@shell morphology does not act as a template to direct restructuring behaviors. Encapsulation instead acts to impede active metal accessibility and consequently slow the effects of high temperature sintering, as shown in a number of other works.[28–30] When the aging temperature is increased to 1000°C, CeO_2 crystallite sintering continues, forming particles over 200 nm in diameter (Figure 5.7c). In addition, a large Au particle on the order of 100 nm in diameter, over four times the size of an as-synthesized Au core, can be found with no dispersed Au signal throughout the sintered CeO_2 crystals. This, combined with the observations in Figure 5.7b, suggests that CeO_2 crystallites continue to sinter between neighboring particles as aging temperatures increase. As these crystallites continue to grow and the core@shell morphology begins to deteriorate, Au cores can access one another and sinter together.

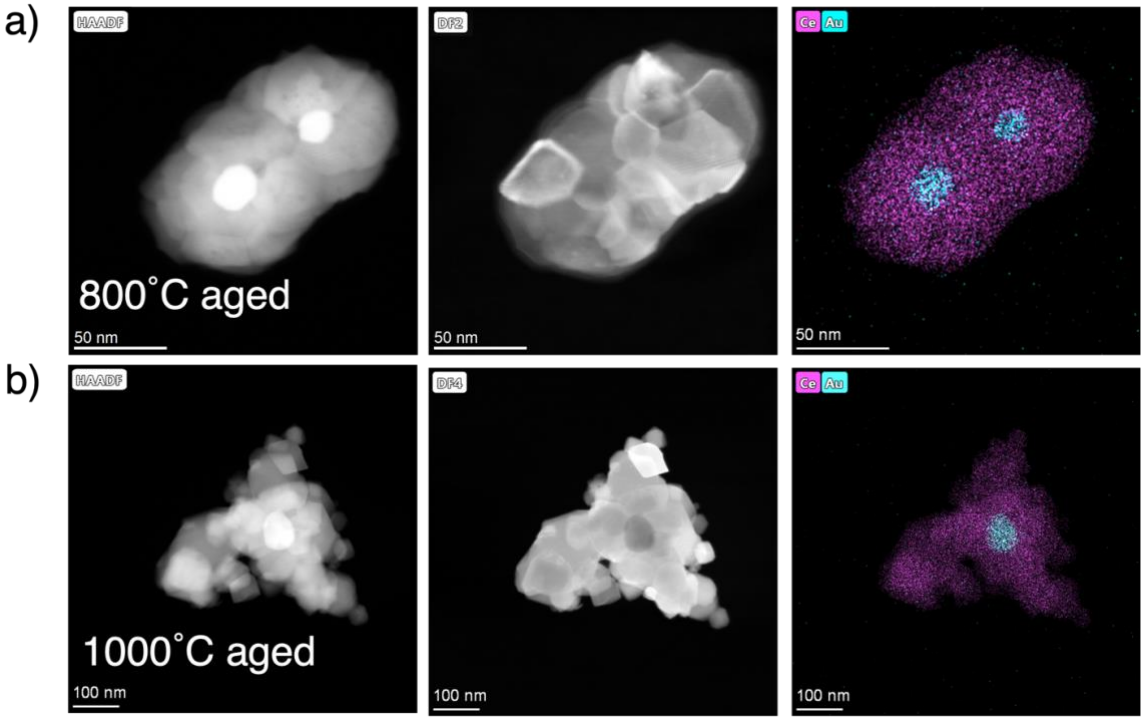

Figure 5.7. STEM and EDS characterization of monometallic Au@CeO_2 aged at 800°C and 1000°C. EDS elemental mapping figures contain embedded legends to indicate the corresponding colors for the elemental maps (Au: Blue, Ce: Pink) and the detector used to collect the STEM image (DF: dark-field, HAADF: high angle annular dark-field).

In situ STEM was conducted to observe the restructuring of Au@CeO_2 in real time (Figure 5.8). The Protochips Fusion Select *in situ* electrothermal holder used in these experiments was not gas-flow compatible. Therefore, the *in situ* heating experiments were conducted under vacuum. Favorable restructuring was previously observed for a Pd@CeO_2 catalyst aged at 800°C under an inert N_2 atmosphere,[6] however, which shows that reducible oxides such as CeO_2 can provide the oxygen necessary to facilitate adsorbate-induced disintegration and redispersion, albeit to a lesser extent compared to samples aged in air. Consequently, it is expected that conducting these experiments in vacuum would not readily confound results and Au would redisperse from its core location during these experiments if it were capable of being oxidized at the temperatures used.

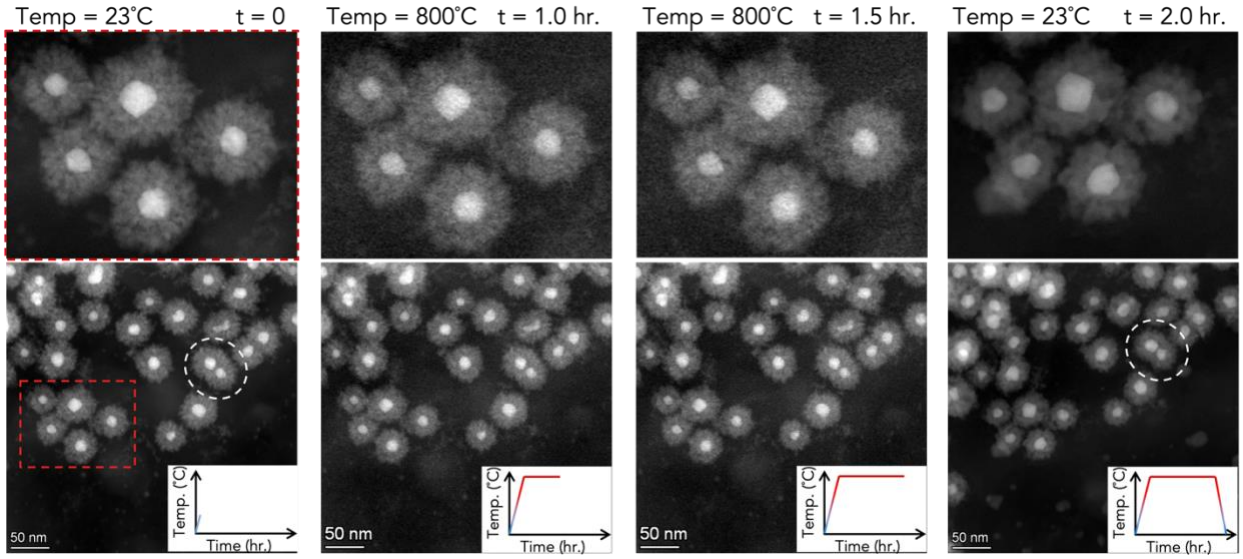

Figure 5.8. Characterization of Au@CeO_2 during in situ aging in the STEM.
Subfigures have been labelled with their respective time points and temperatures. A collection of five particles, boxed in red, has been magnified. A serendipitous finding of a Au@CeO_2 particle with two Au cores has been circled in white.

The stability of Au in the core@shell particles is corroborated by *in situ* STEM, as Au cores do not agglomerate over two hours of exposure to 800°C. In a serendipitous instance of a Au@CeO_2 particle containing two cores, agglomeration of Au is still not observed. This demonstrates the value of encapsulation for inhibiting metal particle mobility and agglomeration, even over distances smaller than the particles themselves. The reshaping of Au cores and sintering

of CeO_2 domains during the elevated temperature observed during *ex situ* aging is corroborated in these *in situ* experiments.

5.2.3 Co–redispersion of Au and Pd in bimetallic AuPd@CeO_2 nanoparticles

PdO forms readily upon exposure to 800°C in the partial pressure of oxygen contained in air (2.13×10^4 Pa).[8] The high temperatures, coupled with the strain to Pd–Pd bonds caused by the dissociative chemisorption of oxygen can drive adsorbate-induced disintegration of Pd clusters.[31–33] These adatoms can readily redisperse throughout a core@shell structure, as the porous encapsulation separates active metal domains during periods of thermally induced mobility.[6,7] As shown in previous work by Lee *et. al.*,[34] hydrothermal aging (10% H_2O at 750°C) bimetallic Pd–Fe, Pd–Ni and Pd–Co systems redispersed both metal species and increased their coordination to one another. As Au and Pd readily form alloys, bimetallic AuPd@CeO_2 nanoparticles were synthesized to investigate if Au and Pd could be redispersed together during elevated temperature aging in air.

Figure 5.9 shows AuPd@CeO_2 catalysts before and after 800°C *ex situ* aging in air for 4 hours. While CeO_2 crystallites appear to have agglomerated during the elevated temperature exposure, EDS elemental mapping shows a highly dispersed signal of both Au and Pd. This observation is starkly different from the Au@CeO_2 system, which suggests that alloying the Au core with a readily dispersible metal such as Pd has indeed facilitated a co–redispersion of both metals. As shown in Figure 5.10, many small CeO_2 crystallites (≤20 nm in diameter) can still be found after 800°C aging. XRD characterization shows these crystallites are 12.4 nm in diameter on average, approximately 15 nm smaller than the average crystallites found in Au@CeO_2 (27.39 nm) aged in identical conditions. This is consistent with past work that shows atomically

dispersed active metals can stabilize small polycrystalline support domains and slow their sintering during high-temperature annealing.[7,22]

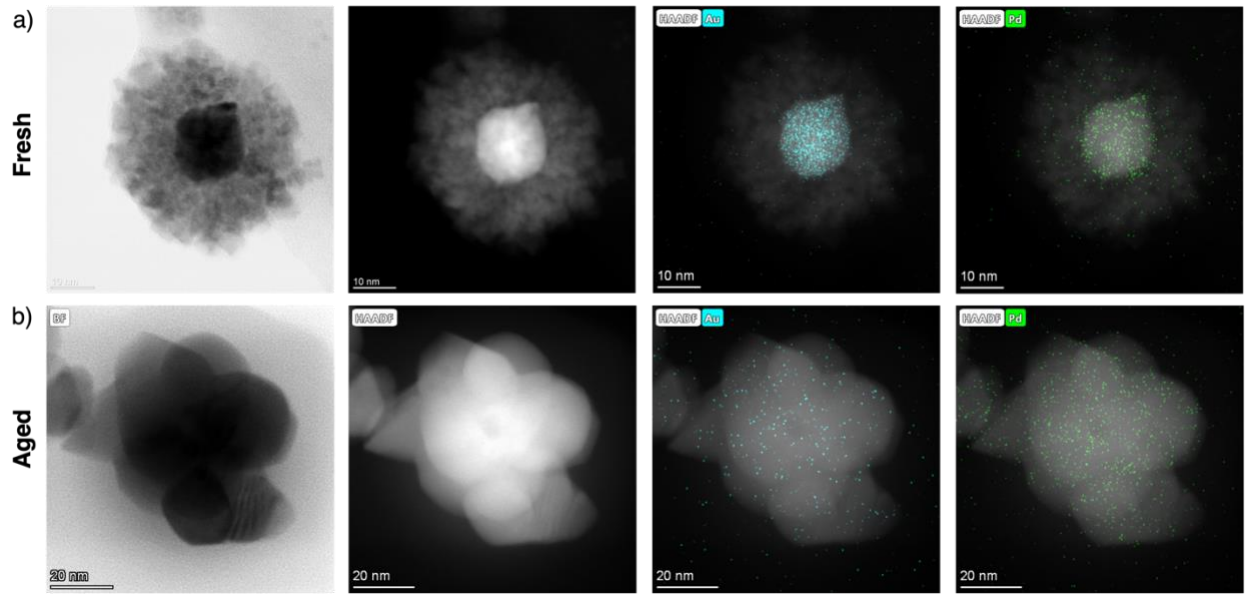

Figure 5.9. STEM and EDS characterization of Au@CeO_2 before and after ex situ aging.
EDS elemental mapping figures contain embedded legends to indicate the corresponding colors for the elemental maps (Au: Blue, Pd: Green) and the detector used to collect the STEM image (BF: bright-field, HAADF: high angle annular dark-field).

The redispersion observed in microscopy characterization is corroborated by XRD analysis, which shows peak broadening in the (111) and (200) reflections of Au particles and an average particle size that has decreased to 14.19 nm. This does contrast with other works that show a disappearance of bulk metal reflections in XRD when particles redisperse completely into single atoms.[35] Consequently, it appears that Au particles do not completely disintegrate and redisperse. EDS analysis of individual crystallites of CeO_2 after aging show highly dispersed signals of Au and Pd (Figure 5.10). This combined with the retention of smaller crystallites after aging suggests that some near-atomically dispersed species exist within the restructured AuPd@CeO_2.

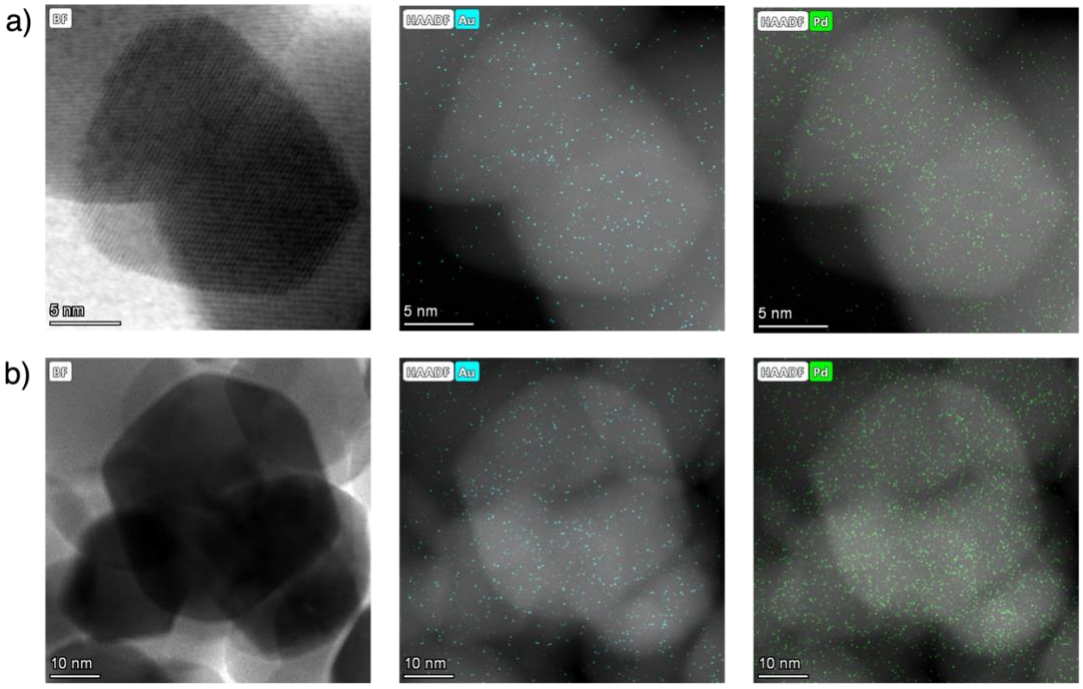

Figure 5.10. Additional STEM and EDS characterization of Au@CeO_2 after ex situ aging.
EDS elemental mapping figures contain embedded legends to indicate the corresponding colors for the elemental maps (Au: Blue, Pd: Green) and the detector used to collect the STEM image (BF: bright-field, HAADF: high angle annular dark-field).

The (111) and (200) reflections for Au in the aged AuPd@CeO_2 have shifted by approximately 0.7° towards the (111) and (200) reflections of bulk Pd (Figure 5.4c). This contrasts with the peaks in monometallic Au@CeO_2, which do not shift or change in width after aging. Shifts in XRD peaks are indicative of alloying between metals.[16,36,37] The continued absence of a bulk Pd reflection suggests that Pd has not segregated from the Au phase during annealing. As such, it is unlikely that Pd segregated from the Au cores is responsible for the decreased particle size found in XRD analysis. Instead, it appears as though the presence of Pd species has facilitated the disintegration and redispersion of Au clusters into smaller bimetallic particles that exhibit interatomic mixing. It is possible that the small size of the AuPd nanoparticles enables mixing that deviates from the modeled thermodynamic behaviors of bulk AuPd systems.[38]

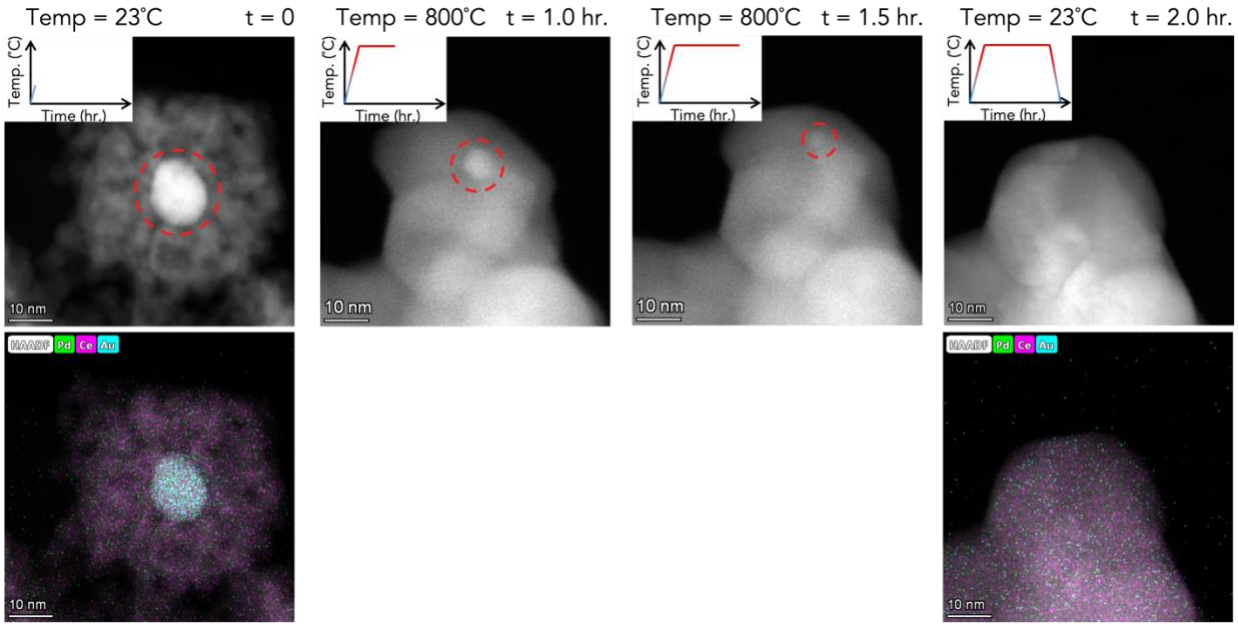

Figure 5.11. Characterization of AuPd@CeO_2 during in situ aging in the STEM.
EDS elemental mapping figures conducted before and after the heating experiment have been placed below their respective figures. EDS figures contain embedded legends to indicate the corresponding colors for the elemental maps (Au: Blue, Pd: Green, Ce: Pink) and the detector used to collect the STEM image (BF: bright-field, HAADF: high angle annular dark-field). Red circles highlight the bimetallic core during the heating experiment.

In situ STEM was conducted on AuPd@CeO_2 to corroborate the redispersion of Au and Pd observed after *ex situ* aging. As seen in Figure 5.11, the bimetallic core begins to decrease in size and eventually disappear over two hours of annealing at 800°C. EDS elemental mapping before and after the annealing experiment confirm that the disappearance of the core is associated with the redispersion of both Au and Pd. This observation corroborates that Au can be redispersed through elevated temperature aging when it is alloyed with an easily oxidized metal such as Pd. This approach provides an alternative to conventional strategies that use thermal treatment alongside halogenated chemicals that can exhibit adverse environmental properties.[26] As these *in situ* TEM experiments are conducted under vacuum, these data also demonstrate that successful redispersion can occur in the absence of gas phase oxygen. In such cases, it is likely that lattice oxygen is provided from the reducible CeO_2 as shown in previous work.[7] It should be noted that the CeO_2 shell crystallites appear to rapidly sinter into larger particles in the *in situ* microscopy

experiments, when compared to CeO_2 crystallites of AuPd@CeO_2 after *ex situ* aging. The sintering of support crystallites at elevated temperatures can be impeded by atomically dispersed metal species.[22] We have demonstrated this in past work using a Pd@CeO_2 system.[6,7] The absence of gas phase oxygen may have impeded redispersion during the *in situ* aging experiments, which would allow the CeO_2 to sinter more rapidly.

5.2.4 Proposing a mechanism for bimetallic restructuring

Owing to the thermodynamic favorability of their oxide phase, platinum group metals can be readily oxidized at elevated temperature, and subsequently redispersed throughout reducible CeO_2 domains through the formation of M–O–Ce interactions (where M is a metal).[39,40] It is clear from aging monometallic Au@CeO_2, that the thermodynamics of oxidation can describe the propensity to undergo redispersion in an oxygen-rich environment.

Au nanoparticles can undergo adsorbate–mediated disintegration and redispersion through the use of highly electrophilic halogenated compounds such as CH_3I.[27] For example, Yuan *et. al.* demonstrated that treating sintered Au particles with average diameter >30 nm with CH_3I at 40°C for 72 hours resulted in Au particles with an average diameter of 0.73 nm.[26] It was proposed that the iodohydrocarbons oxidized Au species through the formation of Au–I interactions, which facilitated their fragmentation and redispersion on carbon supports. XPS was used to track the degree of Au oxidation. Fresh Au/C catalysts displayed similar fractions of Au^0 (41.9%) and oxidized $Au^{\delta+}$ (42.6%). The oxidation state distribution changed to favor $Au^{\delta+}$ (72.3%) over Au^0 (27.7%) after CH_3I treatment, which supported successful oxidation and redispersion of bulk Au. As shown in Figure 5.12 and Table 5.1, the changes in $Au^{\delta+}$ and Au^0 distributions in AuPd@CeO_2 after 800°C aging are consistent with the trends observed in the Au/C system. This suggests that a similar oxidation and redispersion process has taken place. The driving force for diffusing Au_xI_y

complexes, once fragmentation has occurred, was proposed to be the difference in reduction potential for Au_xI_y and the oxidation potential for the carbon surface. This redox behavior is similar to redispersion on reducible CeO_2 supports, as the oxidation of undercoordinated Ce^{3+} sites is a driving force for the deposition of highly dispersed metal species.[41–43]

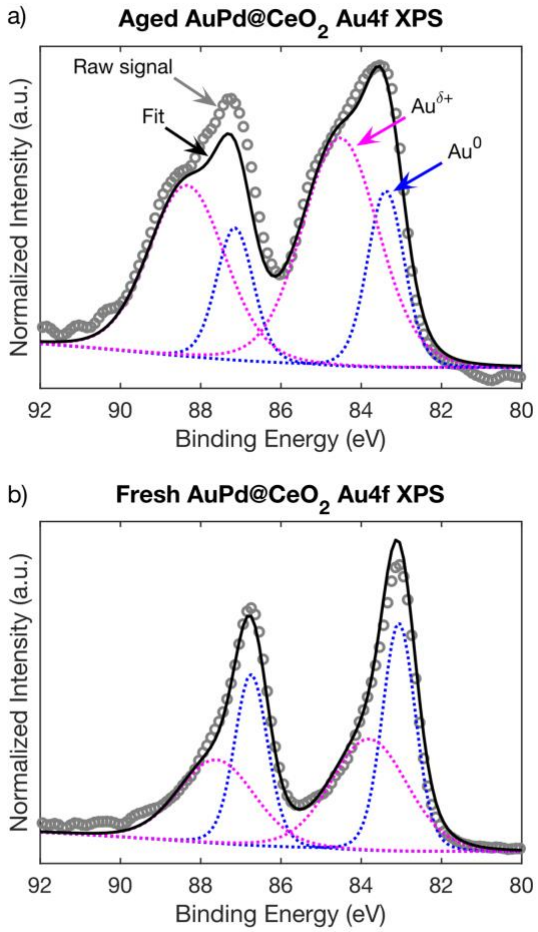

Figure 5.12. XPS characterization of fresh and aged $AuPd@CeO_2$ nanoparticles in the Au4f core scan region.

The degree of Au redispersion can be modulated by the iodohydrocarbon chosen, with smaller compounds resulting in greater redispersion. Yuan *et. al.* demonstrated this by treating sintered Au particles with CH_3I, C_3H_7I and C_6H_5I at 40°C for 72 hours.[26] The resulting nanoparticles exhibited average diameters of 0.73, 2.94 and 7.21 nm, respectively. It was proposed that the strength of the C–I bond influenced degree of redispersion. Compounds with C–I bond

dissociation energies (BDEs) lower than the BDE of Au–I (270 kJ/mol) facilitated Au redispersion. The greater the difference in C–I and Au–I BDE, the greater the redispersion and the smaller the resulting Au nanoparticles.[26,44] Several studies have demonstrated Au redispersion during elevated temperature (300–400°C) exposure in oxidizing environments.[45,46] While such studies do not quantify the degree of redispersion or particle size decrease with the rigor as in the aforementioned studies,[26] they demonstrate that it is possible to redisperse Au using oxygen. Given that the ease of abstracting iodine from iodohydrocarbons influences the degree of Au redispersion, it stands to reason that improving the ease of abstracting oxygen would increase the likelihood and degree of particle disintegration and redispersion.

Table 5.1. Oxidation state distribution of Au in fresh and aged AuPd@CeO_2 nanoparticles.

Sample	$Au^{\delta+}$ composition (%)	Au^0 composition (%)
Fresh AuPd@CeO_2	52.9	47.1
Aged AuPd@CeO_2	72.7	27.3

Several computational research efforts describe that alloying Au with Pd decreases the energetic requirements for oxidation and increases the thermodynamic stability of the alloyed oxide phase.[47,48] O–O bond breakage is found to be thermodynamically favorable, with negative energies of reaction, when Au is alloyed with Pd. DFT analysis shows that diatomic oxygen can dissociate on neighboring Pd atoms and transport to the interface sites between Pd and Au atoms. Consequently, theory supports that an alloyed structure is more readily oxidized than monometallic Au. This provides a possible basis for the redispersion observed here, given the high kinetic impetus for mobility provided by the 800°C aging environment. The participation of lattice oxygen in the reducible CeO_2 provides a low energy pathway for oxidation, as has been demonstrated for

the oxidation of reactants such as CO.[49,50] It is possible this phenomenon also contributes to the improved ease of Au oxidation and subsequent redispersion.

5.3 Conclusions

This work sought to investigate the generalizability of favorable restructuring in core@shell morphologies with a Au@CeO_2 nanoparticle system. The absence of Au redispersion upon 800°C aging confirmed that the thermodynamics of metal oxidation can effectively describe whether favorable restructuring can occur. While metals with unstable oxides (Au) do not redisperse, alloying such elements with readily dispersible metals (Pd) can promote redispersion. The favorable restructuring of a bimetallic AuPd@CeO_2 system was confirmed using a combination of *ex situ* and *in situ* STEM, EDS, XRD and XPS. The improvement in oxygen abstraction and stabilization on an alloyed Au–Pd surface was proposed to incite the redispersion of Au from core particles. Consequently, this work demonstrates a method to achieve the favorable restructuring of active metal species that exhibit poor thermodynamics of oxidation using a simple thermal treatment in air.

5.4 Experimental details

5.4.1 Synthesis of monometallic Au@CeO_2 and bimetallic AuPd@CeO_2 nanoparticles

Au@CeO_2 and AuPd@CeO_2 nanoparticles were synthesized similar to previous work, methods where pH conditions and metal precursor redox potentials are controlled in a one-pot procedure to tune core size, bimetallic composition and shell thickness.[21]

A deionized water (DI) solution was made with mM polyvinyl pyrrolidone (PVP) and 84.0 mM potassium bromide (KBr). The solution was left to stir at 60°C for 30 minutes. During this time, separate 20 mM aqueous solutions of chloroauric acid ($HAuCl_4$) and potassium

tetrachloropalladate (K_2PdCl_4) were prepared. A 50 mM solution of cerium acetate hydrate ($Ce(ac)_3$) was also prepared during this time. The three solutions were added in sequence to the PVP/ KBr solution (in the case of synthesizing monometallic $Au@CeO_2$, the K_2PdCl_4 solution was not prepared). A 2.8 mM aqueous solution of ammonia (NH_3) was then added to the solution to facilitate the autoredox reaction between the CeO_2 and core precursors. The solution was left to stir at 60°C for an hour prior to collection by centrifugation and washing (three times with water and three times with ethanol). All samples were treated in a muffle furnace at 500°C in air for 2 hours. At this stage, samples were considered 'fresh'. All fresh samples were subjected to STEM, EDS, XRD and XPS characterization (see Section 5.4.3).

5.4.2 Aging parameters

For the purposes of this study, *in situ* aging refers to aging using an electrothermal STEM holder to monitor the restructuring of $Au@CeO_2$ and $AuPd@CeO_2$ in real time. *Ex situ* aging refers to aging in a tube-furnace system for morphology characterization as a function of aging.

Ex situ aging was conducted in a tube-furnace at 800°C in air for 4 hours, achieved with a temperature ramp of 5°C/min. The gas flow rate was set to 200 mL/min total. Upon aging, samples were characterized by STEM, EDS, XRD and XPS characterization (see Section 5.4.3).

In situ aging was conducted with a Protochips Fusion Select *in situ* electrothermal holder and compatible E-chips (product number E-FHDC-VO-10). Samples were heating to 800°C using a ramp of 1000°C/sec. Samples were held at 800°C for 2 hours to observe restructuring.

5.4.3 Material characterization

Characterization of samples was done using four techniques: scanning transmission electron microscopy (STEM), x-ray energy dispersive spectroscopy (EDS), x-ray photoelectron spectroscopy (XPS) and x-ray powder diffraction (XRD).

Refer to *Section 3.4.5* for STEM and EDS characterization details and *Section 2.4.5* as acquisition parameters were identical. XPS was conducted in the same instrument as described in previous chapters (refer to *Section 2.4.5*). Deconvolution also used the CasaXPS software, however the parameters differed. Deconvolution was done in the Au4f core scan region using two, each with a spin-doublet at +3.7 eV: zero-valent Au^0 (83.0 – 83.5 eV) and oxidized $Au^{\delta+}$ (84.0 – 84.6 eV).[26,51] XRD characterization was conducted using the same instrument as described in previous chapters (refer to *Section 2.4.5*). Application of the Debye–Scherrer equation for average particle size was conducted similar to that described in *Section 2.4.5*, albeit at the peak corresponding to the (111) reflection of Au, which was located between 38.2°and 38.9°.

5.5 References

(1) Zhang, Z.; Li, H.; Wu, D.; Zhang, L.; Li, J.; Xu, J.; Lin, S.; Datye, A. K.; Xiong, H. Coordination Structure at Work: Atomically Dispersed Heterogeneous Catalysts. *Coord. Chem. Rev.* **2022**, *460*, 214469. https://doi.org/10.1016/j.ccr.2022.214469.

(2) Jeong, H.; Shin, S.; Lee, H. Heterogeneous Atomic Catalysts Overcoming the Limitations of Single-Atom Catalysts. *ACS Nano* **2020**, *14* (11), 14355–14374. https://doi.org/10.1021/acsnano.0c06610.

(3) Xiong, H.; Datye, A. K.; Wang, Y. Thermally Stable Single-Atom Heterogeneous Catalysts. *Adv. Mater.* **2021**, *2004319*. https://doi.org/10.1002/adma.202004319.

(4) Jiao, L.; Xu, W.; Wu, Y.; Yan, H.; Gu, W.; Du, D.; Lin, Y.; Zhu, C. Single-Atom Catalysts Boost Signal Amplification for Biosensing. *Chem. Soc. Rev.* **2021**, *50* (2), 750–765. https://doi.org/10.1039/D0CS00367K.

(5) Zhang, L.; Wang, Y.; Niu, Z.; Chen, J. Single Atoms on Graphene for Energy Storage and Conversion. *Small Methods* **2019**, *3* (9), 1800443. https://doi.org/10.1002/smtd.201800443.

(6) Hill, A. J.; Seo, C. Y.; Chen, X.; Bhat, A.; Fisher, G. B.; Lenert, A.; Schwank, J. W. Thermally Induced Restructuring of Pd@CeO_2 and Pd@SiO_2 Nanoparticles as a Strategy for Enhancing Low-Temperature Catalytic Activity. *ACS Catal.* **2020**, *10*, 1731 – 1741. https://doi.org/10.1021/acscatal.9b05224.

(7) Hill, A. J.; Bhat, A.; Berquist, Z. J.; Fisher, G. B.; Lenert, A.; Schwank, J. W. Stabilizing Highly Dispersed Halo Sites in Thermally Restructured Palladium Core@Shell Nanoparticles for Improved Catalyst Activity and Durability. *ACS Appl. Nano Mater.* **2021**, *4* (10), 10985–10998. https://doi.org/10.1021/acsanm.1c02436.

(8) Peuckert, M. XPS Study on Surface and Bulk Palladium Oxide, Its Thermal Stability, and a Comparison with Other Noble Metal Oxides. *J. Phys. Chem.* **1985**, *89* (12), 2481–2486. https://doi.org/10.1021/j100258a012.

(9) Schumann, J.; Bao, Y.; Hannagan, R. T.; Sykes, E. C. H.; Stamatakis, M. Periodic Trends in Adsorption Energies Around Single-Atom Alloy Active Sites. 1–25.

(10) Chen, Z.; Zhang, P. Electronic Structure of Single-Atom Alloys and Its Impact on The Catalytic Activities. *ACS Omega* **2022**, acsomega.1c06067. https://doi.org/10.1021/acsomega.1c06067.

(11) Wang, X.; Maeda, N.; Meier, D. M.; Baiker, A. Bimetallic AuPd@CeO2 Nanoparticles Supported on Potassium Titanate Nanobelts: A Highly Efficient Catalyst for the Reduction of NO with CO. *Catal. Letters* **2021**, No. 0123456789. https://doi.org/10.1007/s10562-020-03502-7.

(12) Liu, Y.; Wang, Q.; Wu, L.; Long, Y.; Li, J.; Song, S.; Zhang, H. Tunable Bimetallic Au–Pd@CeO 2 for Semihydrogenation of Phenylacetylene by Ammonia Borane. *Nanoscale* **2019**, *11* (27), 12932–12937. https://doi.org/10.1039/C9NR02953B.

(13) Olmos, C. M.; Chinchilla, L. E.; Villa, A.; Delgado, J. J.; Hungría, A. B.; Blanco, G.; Prati, L.; Calvino, J. J.; Chen, X. Size, Nanostructure, and Composition Dependence of Bimetallic Au–Pd Supported on Ceria–Zirconia Mixed Oxide Catalysts for Selective Oxidation of Benzyl Alcohol. *J. Catal.* **2019**, *375*, 44–55. https://doi.org/10.1016/j.jcat.2019.05.002.

(14) Carter, J. H.; Althahban, S.; Nowicka, E.; Freakley, S. J.; Morgan, D. J.; Shah, P. M.; Golunski, S.; Kiely, C. J.; Hutchings, G. J. Synergy and Anti-Synergy between Palladium and Gold in Nanoparticles Dispersed on a Reducible Support. *ACS Catal.* **2016**, *6* (10), 6623–6633. https://doi.org/10.1021/acscatal.6b01275.

(15) Wang, X.; Maeda, N.; Meier, D. Synergistic Effects of Bimetallic AuPd and La_2O_3 in the Catalytic Reduction of NO with CO. *Catalysts* **2021**, *11* (8), 916. https://doi.org/10.3390/catal11080916.

(16) Ulrich, V.; Moroz, B.; Pyrjaev, P.; Sinev, I.; Bukhtiyarov, A.; Gerasimov, E.; Bukhtiyarov, V.; Cuenya, B. R.; Grünert, W. Three-Way Catalysis with Bimetallic Supported Pd-Au Catalysts: Gold as a Poison and as a Promotor. *Appl. Catal. B Environ.* **2021**, *282* (July 2020), 119614. https://doi.org/10.1016/j.apcatb.2020.119614.

(17) Gibson, E. K.; Beale, A. M.; Catlow, C. R. A.; Chutia, A.; Gianolio, D.; Gould, A.; Kroner, A.; Mohammed, K. M. H.; Perdjon, M.; Rogers, S. M.; et al. Restructuring of AuPd Nanoparticles Studied by a Combined XAFS/DRIFTS Approach. *Chem. Mater.* **2015**, *27* (10), 3714–3720. https://doi.org/10.1021/acs.chemmater.5b00866.

(18) Ouyang, M.; Papanikolaou, K. G.; Boubnov, A.; Hoffman, A. S.; Giannakakis, G.; Bare, S. R.; Stamatakis, M.; Flytzani-Stephanopoulos, M.; Sykes, E. C. H. Directing Reaction Pathways via in Situ Control of Active Site Geometries in PdAu Single-Atom Alloy Catalysts. *Nat. Commun.* **2021**, *12* (1), 1549. https://doi.org/10.1038/s41467-021-21555-z.

(19) Silva, T. A. G.; Ferraz, C. P.; Gonçalves, R. V.; Teixeira-Neto, E.; Wojcieszak, R.; Rossi, L. M. Restructuring of Gold-Palladium Alloyed Nanoparticles: A Step towards More Active Catalysts for Oxidation of Alcohols. *ChemCatChem* **2019**, *11* (16), 4021–4027. https://doi.org/10.1002/cctc.201900553.

(20) Hsu, S.-C.; Chuang, Y.-C.; Sneed, B. T.; Cullen, D. A.; Chiu, T.-W.; Kuo, C.-H. Turning the Halide Switch in the Synthesis of Au–Pd Alloy and Core–Shell Nanoicosahedra with Terraced Shells: Performance in Electrochemical and Plasmon-Enhanced Catalysis. *Nano Lett.* **2016**, *16* (9), 5514–5520. https://doi.org/10.1021/acs.nanolett.6b02005.

(21) Liu, Y.; Wang, Q.; Wu, L.; Long, Y.; Li, J.; Song, S.; Zhang, H. Tunable Bimetallic Au–Pd@CeO_2 for Semihydrogenation of Phenylacetylene by Ammonia Borane. *Nanoscale* **2019**, *11* (27), 12932–12937. https://doi.org/10.1039/C9NR02953B.

(22) Alcala, R.; DeLaRiva, A.; Peterson, E. J.; Benavidez, A.; Garcia-Vargas, C. E.; Jiang, D.; Pereira-Hernández, X. I.; Brongersma, H. H.; Veen, R. ter; Staněk, J.; et al. Atomically Dispersed Dopants for Stabilizing Ceria Surface Area. *Appl. Catal. B Environ.* **2021**, *284*, 119722. https://doi.org/10.1016/j.apcatb.2020.119722.

(23) Aitbekova, A.; Wrasman, C. J.; Riscoe, A. R.; Kunz, L. Y.; Cargnello, M. Determining Number of Sites on Ceria Stabilizing Single Atoms via Metal Nanoparticle Redispersion. *Chinese J. Catal.* **2020**, *41* (6), 998–1005. https://doi.org/10.1016/S1872-2067(19)63504-7.

(24) Chen, J.; Wanyan, Y.; Zeng, J.; Fang, H.; Li, Z.; Dong, Y.; Qin, R.; Wu, C.; Liu, D.; Wang, M.; et al. Surface Engineering Protocol To Obtain an Atomically Dispersed Pt/CeO 2 Catalyst with High Activity and Stability for CO Oxidation. *ACS Sustain. Chem. Eng.* **2018**, *6* (11), 14054–14062. https://doi.org/10.1021/acssuschemeng.8b02613.

(25) Lee, Y. W.; Kim, N. H.; Lee, K. Y.; Kwon, K.; Kim, M.; Han, S. W. Synthesis and Characterization of Flower-Shaped Porous Au−Pd Alloy Nanoparticles. *J. Phys. Chem. C* **2008**, *112* (17), 6717–6722. https://doi.org/10.1021/jp710933d.

(26) Duan, X.; Tian, X.; Ke, J.; Yin, Y.; Zheng, J.; Chen, J.; Cao, Z.; Xie, Z.; Yuan, Y. Size Controllable Redispersion of Sintered Au Nanoparticles by Using Iodohydrocarbon and Its Implications. *Chem. Sci.* **2016**, *7*, 3181–3187. https://doi.org/10.1039/C5SC04283F.

(27) Sá, J.; Taylor, S. F. R.; Daly, H.; Goguet, A.; Tiruvalam, R.; He, Q.; Kiely, C. J.; Hutchings, G. J.; Hardacre, C. Redispersion of Gold Supported on Oxides. *ACS Catal.* **2012**, *2*, 552–560. https://doi.org/10.1021/cs300074g.

(28) Gawande, M. B.; Goswami, A.; Asefa, T.; Guo, H.; Biradar, A. V; Peng, D.-L.; Zboril, R.; Varma, R. S. Core-Shell Nanoparticles: Synthesis and Applications in Catalysis and Electrocatalysis. *Chem. Soc. Rev.* **2015**, *44*, 7540–7590. https://doi.org/10.1039/c5cs00343a.

(29) Zhang, Q.; Lee, I.; Joo, J. B.; Zaera, F.; Yin, Y. Core-Shell Nanostructured Catalysts. *Acc. Chem. Res.* **2013**, *46* (8), 1816–1824. https://doi.org/10.1021/ar300230s.

(30) Gao, C.; Lyu, F.; Yin, Y. Encapsulated Metal Nanoparticles for Catalysis. *Chem. Rev.* **2021**, *121*, 834–881. https://doi.org/10.1021/acs.chemrev.0c00237.

(31) Lieske, H.; Voelter, J. Palladium Redispersion by Spreading of Palladium(II) Oxide in Oxygen Treated Palladium/Alumina. *J. Phys. Chem.* **1985**, *89*, 1841–1842. https://doi.org/10.1021/j100256a001.

(32) Morgan, K.; Goguet, A.; Hardacre, C. Metal Redispersion Strategies for Recycling of Supported Metal Catalysts: A Perspective. *ACS Catal.* **2015**, *5* (6), 3430–3445. https://doi.org/10.1021/acscatal.5b00535.

(33) Lupescu, J. A.; Schwank, J. W.; Fisher, G. B.; Chen, X.; Peczonczyk, S. L.; Drews, A. R. Pd Model Catalysts: Effect of Aging Duration on Lean Redispersion. *Appl. Catal. B Environ.* **2016**, *185*, 189–202. https://doi.org/10.1016/j.apcatb.2015.12.012.

(34) Choi, M. S.; Jeong, H.; Lee, H. Re-Dispersion of Pd-Based Bimetallic Catalysts by Hydrothermal Treatment for CO Oxidation. *RSC Adv.* **2021**, *11*, 3104–3109. https://doi.org/10.1039/D0RA09912K.

(35) Jones, J.; Xiong, H.; DeLaRiva, A. T.; Peterson, E. J.; Pham, H.; Challa, S. R.; Qi, G.; Oh, S.; Wiebenga, M. H.; Hernández, X. I. P.; et al. Thermally Stable Single-Atom Platinum-on-Ceria Catalysts via Atom Trapping. *Science (80-.).* **2016**, *353* (6295), 150–154. https://doi.org/10.1126/science.aaf8800.

(36) Venezia, A. M.; La Parola, V.; Liotta, L. F. Structural and Surface Properties of Heterogeneous Catalysts: Nature of the Oxide Carrier and Supported Particle Size Effects. *Catal. Today* **2017**, *285*, 114–124. https://doi.org/10.1016/j.cattod.2016.11.004.

(37) Qian, K.; Huang, W. Au–Pd Alloying-Promoted Thermal Decomposition of PdO Supported on SiO2 and Its Effect on the Catalytic Performance in CO Oxidation. *Catal. Today* **2011**, *164* (1), 320–324. https://doi.org/10.1016/j.cattod.2010.10.018.

(38) Sluiter, M. H. F.; Colinet, C.; Pasturel, A. Ab Initio Calculation of the Phase Stability in Au-Pd and Ag-Pt Alloys. *Phys. Rev. B* **2006**, *73* (17), 174204. https://doi.org/10.1103/PhysRevB.73.174204.

(39) Kunwar, D.; Zhou, S.; Delariva, A.; Peterson, E. J.; Xiong, H.; Pereira-Hernández, X. I.; Purdy, S. C.; Ter Veen, R.; Brongersma, H. H.; Miller, J. T.; et al. Stabilizing High Metal Loadings of Thermally Stable Platinum Single Atoms on an Industrial Catalyst Support. *ACS Catal.* **2019**, *9*, 3978–3990. https://doi.org/10.1021/acscatal.8b04885.

(40) Wei, S.; Li, A.; Liu, J.-C.; Li, Z.; Chen, W.; Gong, Y.; Zhang, Q.; Cheong, W.-C.; Wang, Y.; Zheng, L.; et al. Direct Observation of Noble Metal Nanoparticles Transforming to Thermally Stable Single Atoms. *Nat. Nanotechnol.* **2018**, *13* (9), 856–861. https://doi.org/10.1038/s41565-018-0197-9.

(41) Figueroba, A.; Kovács, G.; Bruix, A.; Neyman, K. M. Towards Stable Single-Atom Catalysts: Strong Binding of Atomically Dispersed Transition Metals on the Surface of Nanostructured Ceria. *Catal. Sci. Technol.* **2016**, *6* (18), 6806–6813. https://doi.org/10.1039/C6CY00294C.

(42) Neitzel, A.; Figueroba, A.; Lykhach, Y.; Skála, T.; Vorokhta, M.; Tsud, N.; Mehl, S.; Ševčíková, K.; Prince, K. C.; Neyman, K. M.; et al. Atomically Dispersed Pd, Ni, and Pt Species in Ceria-Based Catalysts: Principal Differences in Stability and Reactivity. *J. Phys. Chem. C* **2016**, *120* (18), 9852–9862. https://doi.org/10.1021/acs.jpcc.6b02264.

(43) Pereira-Hernández, X. I.; DeLaRiva, A.; Muravev, V.; Kunwar, D.; Xiong, H.; Sudduth, B.; Engelhard, M.; Kovarik, L.; Hensen, E. J. M.; Wang, Y.; et al. Tuning Pt-CeO_2 Interactions by High-Temperature Vapor-Phase Synthesis for Improved Reducibility of Lattice Oxygen. *Nat. Commun.* **2019**, *10*, 1358. https://doi.org/10.1038/s41467-019-09308-5.

(44) Luo, Y.-R. *Comprehensive Handbook of Chemical Bond Energies*, 1st ed.; CRC Press, 2007. https://doi.org/10.1201/9781420007282.

(45) Deng, W.; Frenkel, A. I.; Si, R.; Flytzani-Stephanopoulos, M. Reaction-Relevant Gold Structures in the Low Temperature Water-Gas Shift Reaction on Au-CeO_2. *J. Phys. Chem. C* **2008**, *112* (33), 12834–12840. https://doi.org/10.1021/jp800075y.

(46) Bezkrovnyi, O.; Kraszkiewicz, P.; Krivtsov, I.; Quesada, J.; Ordóñez, S.; Kepinski, L. Thermally Induced Sintering and Redispersion of Au Nanoparticles Supported on $Ce_{1-x}Eu_xO_2$ Nanocubes and Their Influence on Catalytic CO Oxidation. *Catal. Commun.* **2019**, *131* (April), 105798. https://doi.org/10.1016/j.catcom.2019.105798.

(47) Dar, M. A.; Krishnamurty, S. Molecular and Dissociative Adsorption of Oxygen on Au–Pd Bimetallic Clusters: Role of Composition and Spin State of the Cluster. *ACS Omega* **2019**, *4* (7), 12687–12695.

https://doi.org/10.1021/acsomega.9b01581.
(48) Oğuz, I.-C.; Mineva, T.; Guesmi, H. The Effect of Pd Ensemble Structure on the O 2 Dissociation and CO Oxidation Mechanisms on Au—Pd(100) Surface Alloys. *J. Chem. Phys.* **2018**, *148* (2), 024701. https://doi.org/10.1063/1.5007247.
(49) Puigdollers, A. R.; Schlexer, P.; Tosoni, S.; Pacchioni, G. Increasing Oxide Reducibility: The Role of Metal/Oxide Interfaces in the Formation of Oxygen Vacancies. *ACS Catal.* **2017**, *7*, 6493–6513. https://doi.org/10.1021/acscatal.7b01913.
(50) Mullins, D. R. The Surface Chemistry of Cerium Oxide. *Surf. Sci. Rep.* **2015**, *70* (1), 42–85. https://doi.org/10.1016/j.surfrep.2014.12.001.
(51) Kruse, N.; Chenakin, S. XPS Characterization of Au/TiO_2 Catalysts: Binding Energy Assessment and Irradiation Effects. *Appl. Catal. A Gen.* **2011**, *391* (1–2), 367–376. https://doi.org/10.1016/j.apcata.2010.05.039.

Chapter 6 : Conclusions and Future Work

6.1 Conclusions

Industrial catalysts are integral technologies for chemical and fuel production, energy generation and storage and environmental remediation. As society continues to rely on catalytic processes, the cost, scarcity, and demand for the metals that comprise industrial catalysts will continue to increase. Combined with growing interests in material and environmental sustainability, it is paramount to develop methods that can improve the utilization of costly metal resources in industrial catalysts.

Thermally induced deactivation through the sintering of active metal species presents a consistent challenge to improving material utilization in catalytic systems. This thesis demonstrates that nanoscale restructuring can be controlled to produce favorable outcomes that improve dispersion, activity, and thermal stability. Building upon a substantial review of nanoscale restructuring dynamics, this thesis proposes that the emission and mobility of atomic-scale species that is part of sintering mechanisms can be used to redisperse active metal species into highly dispersed sites. The ability to redisperse these adatoms is limited however, as they readily interact and agglomerate during periods of thermally induced mobility. Consequently, this thesis investigated how nanoscale catalyst morphology can be used to segregate active metal species such that they redisperse upon high temperature exposure.

This thesis demonstrates that encapsulating active metal domains in a core@shell morphology can effectively promote favorable restructuring. Encapsulation changes the dominant

restructuring pathway to particle disintegration and adatom emission, instead of whole particle migration. This encapsulation, coupled with the porous, tortuous nature of the metal oxide shell separates mobile adatoms to increase the likelihood of metal redispersion. Using Pd@SiO_2 and Pd@CeO_2 catalysts, this work shows that core@shell architectures can effectively promote the redispersion of active metal species that would otherwise agglomerate in conventional morphologies. Thus, core@shell architectures provide a simple and effective strategy for improving material utilization in catalytic systems. Using core@shell catalysts, this thesis identifies that the thermodynamics of metal oxide formation and decomposition can describe the ease of forming and stabilizing highly dispersed metal species. This thesis demonstrates that these interactions can be leveraged to promote dispersed site stability (as shown through the formation of stable M–O–Ce interactions on reducible CeO_2), recover dispersed sites after sintering at high temperature, and extend favorable restructuring to metals other than Pd, such as Au.

This closing chapter proposes some future directions that can build upon the findings of this thesis to improve activity, stability, and material utilization in catalytic systems.

6.2 Developing a predictive redispersion model

This thesis demonstrates that thermally induced restructuring is a simple and effective strategy for creating high dispersions of stable and active catalytic sites. Chapter 4 demonstrates however, that the density of trap sites impacts the degree of metal redispersion on reducible CeO_2 during high temperature aging. Consistent with other literature, if the density of trap sites exceeds the amount of dispersible metal, near complete redispersion will occur.[1,2] Should the trap site density be exceeded by the amount of metal, particles will decrease in size through the emission and trapping of adatoms, but will still persist. Although there are many industrial catalytic applications that benefit from highly dispersed single atom active sites, the relationship between

trapping site density and optimum metal loading for total redispersion through thermally induced restructuring has yet to be developed. Developing a relationship that informs the optimum loading of metals for maximizing redispersion can be a valuable tool for industrial-scale catalyst design that seeks to improve utilization of costly active metal resources. This is depicted in Figure 6.1.

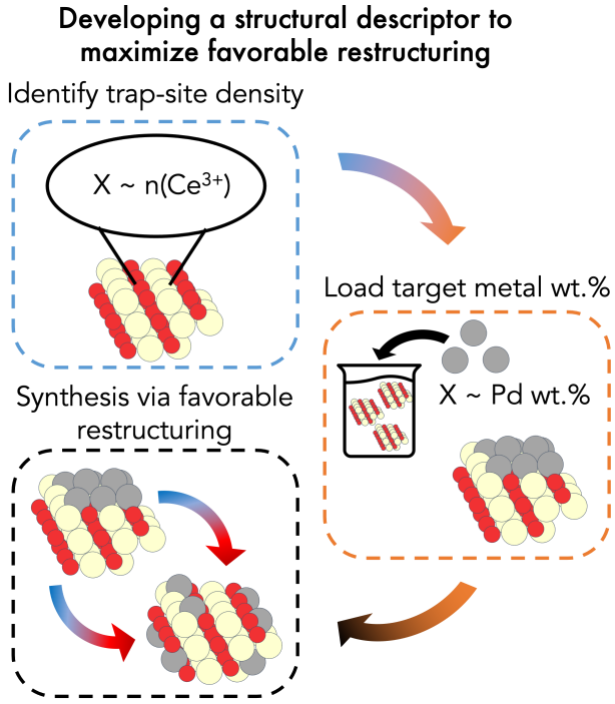

Figure 6.1. Vision for applying a general descriptor to maximize the redispersion of active metal using thermally induced restructuring.
A structural parameter X would be correlated to trap site density, $n(Ce^{3+})$. Once identified, this parameter would then inform the optimum weight% (wt.%) loading of active metal such that maximum redispersion into single atom sites would be obtained upon exposure to high temperatures.

To this end, recommended future work would be to first identify a structural parameter that can be easily analyzed, which acts as a proxy for Ce^{3+} trap site density. While XPS can be effectively used, it is a costly and low-throughput technique and thus not ideal for industrial analysis of support densities. CeO_2 crystallite size and by extension, surface area, are bulk parameters that are known to scale with the density of trap sites. Trap site density is expected to scale proportionately with the surface area and scale inversely with average crystallite size.

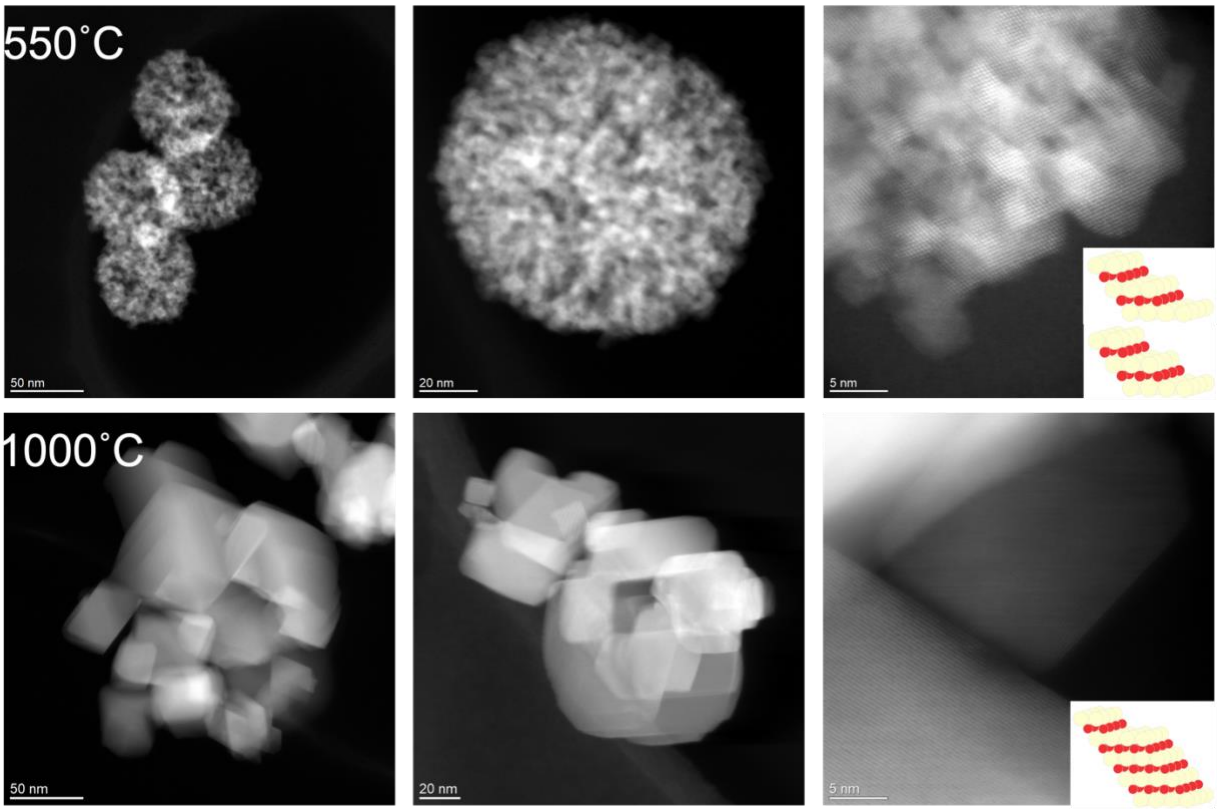

Figure 6.2. CeO_2 nanospheres aged at 550°C and 1000°C in air for 2 hours.
As can be seen, the average particle size increases substantially with aging temperature, which decreases Ce^{3+} density.

As a preliminary test, CeO_2 nanospheres, synthesized according to the protocol outlined in *Section 2.4.1*, were aged at a variety of temperatures for 2 hours in air, to sinter crystallites and subsequently change the density of Ce^{3+} trap sites. As shown in Figure 6.2, treating the bare nanospheres at elevated temperature increases average crystallite size, which decreases both the specific surface area (m^2/g) and Ce^{3+} abundance. As BET is a high throughput and bulk analytical technique; specific surface area (m^2/g) is a promising structural proxy for trap site density. Figure 6.3 shows the specific surface area for CeO_2 nanospheres aged from 550°C – 800°C plotted against Ce^{3+} composition (which was obtained through XPS according to *Section 2.4.5*). Ce^{3+} abundance appears to scale according to the square of nanosphere surface area. Given this relationship, future work could load varying weight percent (wt.%) amounts of Pd through conventional wet impregnation on this library of CeO_2 nanospheres. The dispersion before and after 800°C can then

be determined using CO chemisorption to discern the relationship between surface area and optimum loading of active metal to ensure 100% dispersion upon thermally induced restructuring.

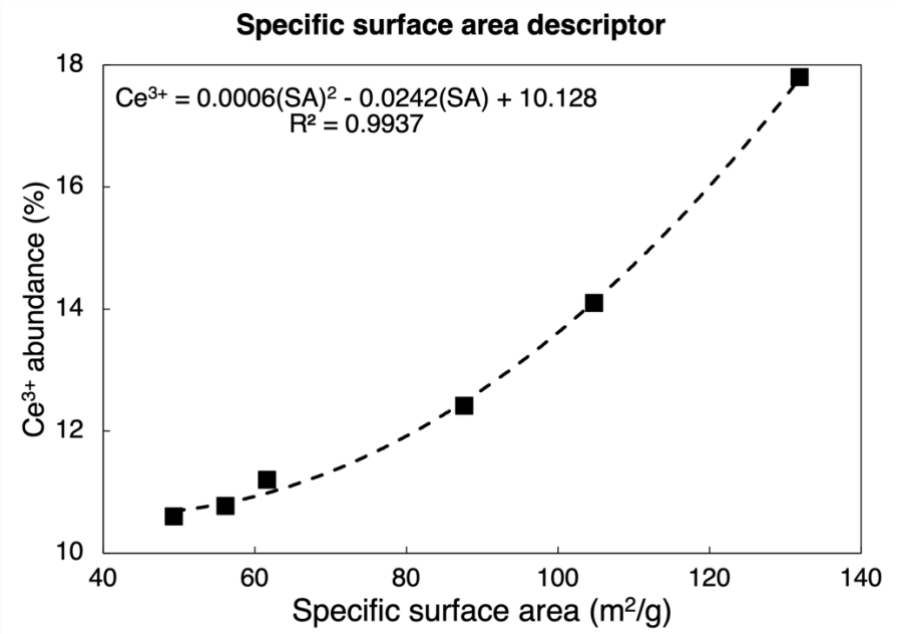

Figure 6.3. Ce^{3+} abundance as a function of specific surface area.

Table 6.1. Ce^{3+} abundance and specific surface area for CeO_2 nanospheres aged at a variety of temperatures.

Aging temperature (°C)	Specific surface area (m^2/g)	Ce^{3+} abundance (%)
550	131.9	17.8
600	104.8	14.1
650	87.7	12.4
700	61.6	11.2
750	56.2	10.8
800	49.3	10.6

A predictive model would be a valuable means of generalizing favorable restructuring phenomena, particularly when informed by an empirically derived approach such as the one outlined above. As summarized in Figure 6.4, a predictive model would benefit from two distinct modeling segments: a thermodynamic model and a kinetic model. As described in Chapter 3 and 4, the thermodynamics of the formation and decomposition of active metal oxides, which can effectively describe whether redispersion or sintering, respectively, is more likely. A

thermodynamic model would compile these thermodynamic equilibria for catalytically relevant active metals to inform what temperature and oxygen partial pressure ranges would be necessary to produce mobile metal oxide adatoms. The proposed thermodynamic segment of this model would also provide the energy of adsorption of the metal adatom to the undercoordinated trap sites of a chosen support, and the likelihood that stable trapping is maintained at an aging temperature of interest. CeO_2 is a good metal oxide to begin with as the adsorption energy to a Ce^{3+} trap site has been computed for a variety of metals.[3] Other metal oxides such as TiO_2, which has demonstrated some atom-trapping potential, may also be of interest.[4]

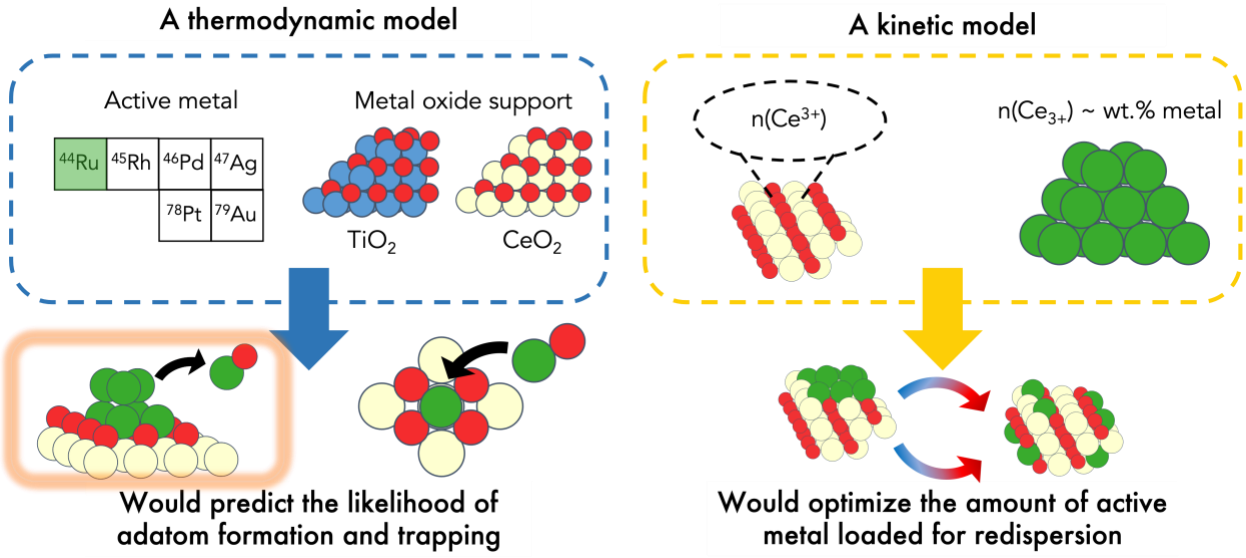

Figure 6.4. Proposed overview of predictive model.

A kinetic model would take the aging conditions outlined in the thermodynamic model and would be able to identify, per a given density of trap sites and amount of active metal, the likely redispersion outcome. Given the high temperatures used to drive favorable restructuring, the mobility of emitted adatoms is unlikely to be rate limiting. This has been demonstrated in recent work by Cargnello *et. al.*, who developed a model that treated the emission of mobile species as the rate-limiting step.[5] Similarly, the kinetic model proposed here could use the rate of mobile adatom emission as a rate limiting step. The model could then use an input of temperature, mean

free path length and trap site concentration, to determine the ratio of sintered vs. trapped metal. This could be experimentally corroborated using the approach outlined above.

6.3 Stabilizing the CeO_2 support to retain trap site density

As demonstrated in Chapter 4, the loss of Ce^{3+} trap sites during the 1000°C aging of Pd@CeO_2 inhibited the complete regeneration of halo sites. Future work could look to address this by investigating methods to stabilize the CeO_2 support or otherwise retain the trap sites at high temperatures. Treatment with reductive chemicals can increase the abundance of surface Ce^{3+} sites. This was demonstrated by Zheng *et. al.* who used an ascorbic acid treatment to increase the fraction of Ce^{3+} sites to disperse up to 1.0 wt.% Pt on porous CeO_2 nanorods.[6] These treatments were conducted prior to the addition of Pt to the system. As such it would be important to investigate whether such treatments would still be effective if sintered active metal species were already loaded onto the support, as is would be the case in a regeneration application.

Combining the CeO_2 with other thermally robust materials can also improve stability. This was demonstrated by Liu *et. al.* who showed thermally treating CeO_2, which was synthesized and impregnated onto a commercial γ-Al_2O_3 support, resulted in small, stable CeO_2 domains that could effectively trap Pd species through Pd–O–Ce interactions and persist up to 800°C.[7] Other methods of stabilizing CeO_2, such as forming CeO_2–ZrO_2 solid solutions, could improve Ce^{3+} density. As described in Chapter 1, high entropy structures containing Ce have shown promise as supports with thermal stability and atom-trapping affinity. It is important to note however, that reducing the content of CeO_2 may effectively decrease the Ce^{3+} trap site abundance. This may also occur if the CeO_2 surface is doped on the surface to improve stability, as dopants may compete with active metal species for atom-trapping sites. As such, a tradeoff between improving thermal stability of CeO_2 and trapping active metal atoms is likely to occur. Future work may investigate this tradeoff

by identifying how the dopant percent, or molar ratio of Ce to other metals in a solid solution or high entropy oxide would affect the degree of redispersion.

6.4 Elucidating the mechanisms of bimetallic redispersion

As described in Chapter 5, Au appears to redisperse when alloyed with Pd in a bimetallic AuPd@CeO_2 structure. It was proposed that nearby Pd increases the ease that Au atoms can abstract and stabilize oxygen. This is analogous to iodohydrocarbons, which promote the ease of iodine abstraction and stabilization onto Au surfaces.[8] This adsorption destabilizes Au–Au bonds, which promotes fragmentation and redispersion, akin to adsorbate–mediated disintegration. While this dissertation has established the role of oxygen for promoting redispersion in a monometallic (e.g. Pd) system, the role of oxygen is less clear in a bimetallic structure. As such, future work could conduct an experiment like that described in *Section 2.2.5*, where a Pd@SiO_2 catalyst was aged in pure N_2. Similarly, a AuPd@SiO_2 catalyst could be synthesized and aged in the *in situ* TEM at 800°C. As there is no gas phase oxygen present and the SiO_2 cannot donate lattice oxygen, the role of oxygen in bimetallic restructuring could be elucidated.

It is possible that mobile PdO adatoms can facilitate the disintegration and redispersion of Au clusters. Under this proposed mechanism, Pd, owing to its favorable thermodynamics of oxidation, readily forms PdO. Au atoms, through their strong interactions with PdO, are subsequently emitted from larger clusters during high temperature exposure as a Au/Pd/O complex. This mechanism is difficult to experimentally verify, however. Consequently, future work that seeks to understand the origins of bimetallic redispersion in the AuPd@CeO_2 system could pursue a computational investigation. A small Au nanoparticle can be built as a test system and the Au–Au bond strength can be calculated using density functional theory (DFT). The Au–Au and Au–Pd bond strength can then be examined when an overlayer of Pd, resembling the

bimetallic AuPd cores, is added. This modeling would identify whether alloying helps weaking metal–metal bonds in bulk nanoparticles and whether it is feasible that a Au atom remains attached to a Pd atom at elevated temperatures. The strength of these bonds can be calculated when the Pd overlayer is subsequently oxidized, in order to see if the oxidation of surface Pd can sufficiently weaken Au–Au interactions to permit the emission of a Au/Pd/O complex. Similar studies have been conducted by Goldsmith *et. al.* and Liu *et. al.* who examined the adsorbate-induced disintegration and redispersion of active metals relevant to emissions control.[9,10] In addition, it may be valuable to model a potential energy diagram for the oxidation of a bimetallic AuPd particle. This would help inform the most stable structure of a Au/Pd/O complex.

Building a theoretical understanding of this bimetallic restructuring process can help inform compatible metals that, when combined, can effectively redisperse in a core@shell morphology during high temperature exposure. This would provide the basis for a generalizable strategy that can produce highly dispersed bimetallic sites for catalysis using well–controlled nanoscale architectures and simple heating protocols.

6.5 Generalizing and scaling the synthesis of core@shell catalysts

Morphology–directed restructuring in core@shell nanoparticle systems demonstrates a strategy to obtain high dispersions of active metal species that may not readily redisperse in conventionally–synthesized architectures. To realize this potential, it would be valuable to develop a core@shell synthesis strategy that can be generalized for a variety of core and shell combinations and scaled to the large batch quantities necessary in industrial catalyst manufacturing.

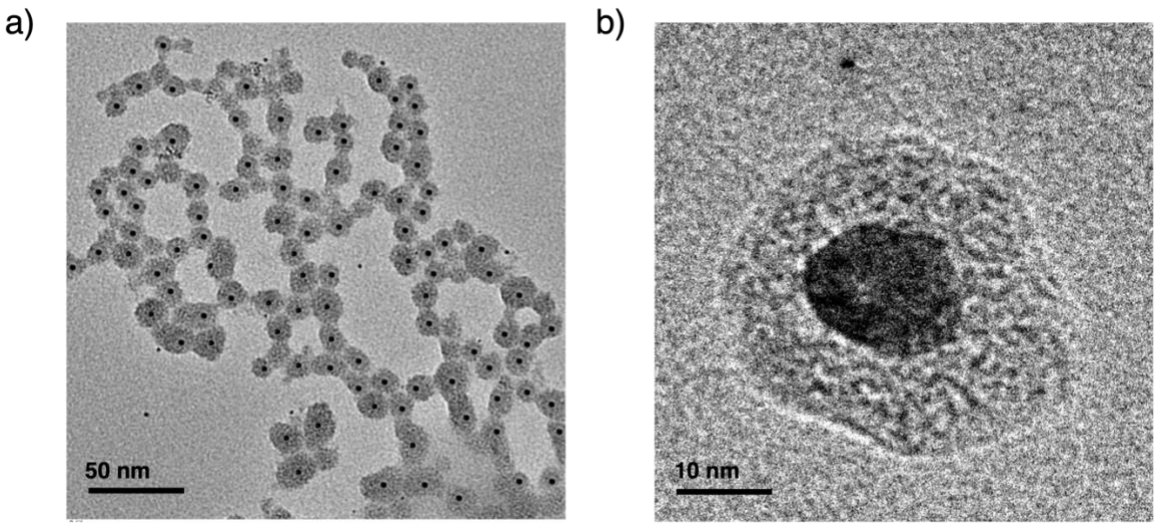

Figure 6.5. Synthesized $Ag@TiO_2$ core@shell nanoparticles done in collaboration with Dr. Adarsh Bhat.

The two-step core@shell synthesis strategy used in Chapters 2–4 relies on the base-catalyzed hydrolysis of a shell precursor around nanoparticle core seeds, which have been formed through reduction via hydrazine hydrate and are stabilized using a surfactant (trimethyl tetradecyl ammonium bromide, TTAB).[11,12] The ability to form $Pd@SiO_2$ and $Pd@CeO_2$ nanoparticles from this synthesis method demonstrates potential for generalizability. This is further shown in Figure 6.5, through the recent synthesis of $Ag@TiO_2$ core@shell particles, which used the ionic dissolution and hydrazine–induced reduction of a Ag precursor ($AgNO_3$) and subsequent hydrolysis of a TiO_2 precursor (titanium isopropoxide). In this instance, hexadecyltrimethylammonium bromide (CTAB) was used as the surfactant. This suggests that any core precursor that ionically dissociates in aqueous solution is compatible with this synthesis technique.

Many synthesis techniques exhibit difficulty scaling due to changes in mass and thermal transport, which can affect nucleation and growth rates.[13] Core@shell particles are particularly susceptible as precise tuning of surfactant concentrations is required to ensure appropriate interactions between core and shell precursors. Too little of an interaction (low surfactant), and

cores can agglomerate to become larger than intended. Too great of an interaction (excess surfactant) and metal particles become encapsulated in a contiguous envelop of metal oxide as opposed to individual shells. It should be noted that such arrangements may still result in the same favorable restructuring outcomes at elevated temperature as found in particles with one core per shell. In these cases, it is expected that the critical distance between active metal particles, as described in Chapter 1, is the determining factor for whether active metal particles can successfully redisperse during elevated temperature exposure. Determining this critical distance, by tuning properties such as the active metal loading, porosity, and shell thickness, could be the focus of future work.

Returning to the volumetric scaling of the core@shell synthesis, examining how the concentration of surfactant necessary for successful encapsulation scales volumetrically would build this protocol's industrial relevance. In addition, synthesis methods that use alternative strategies to obtain encapsulating morphologies may also be valuable to investigate. Protocols that leverage autoredox reactions between core and shell precursors, such as those used in Chapter 5,[14] facilitate encapsulation. As shown in Figure 6.6, the synthesis of Au@CeO_2 nanoparticles produced from this synthesis method was scaled volumetrically by a factor of five, with only slight changes to core size or shell thickness distribution. It should be noted however, that the generalizability of such autoredox methods have yet to be investigated. This could be the focus of future work, given this promising preliminary result in volumetric scaling.

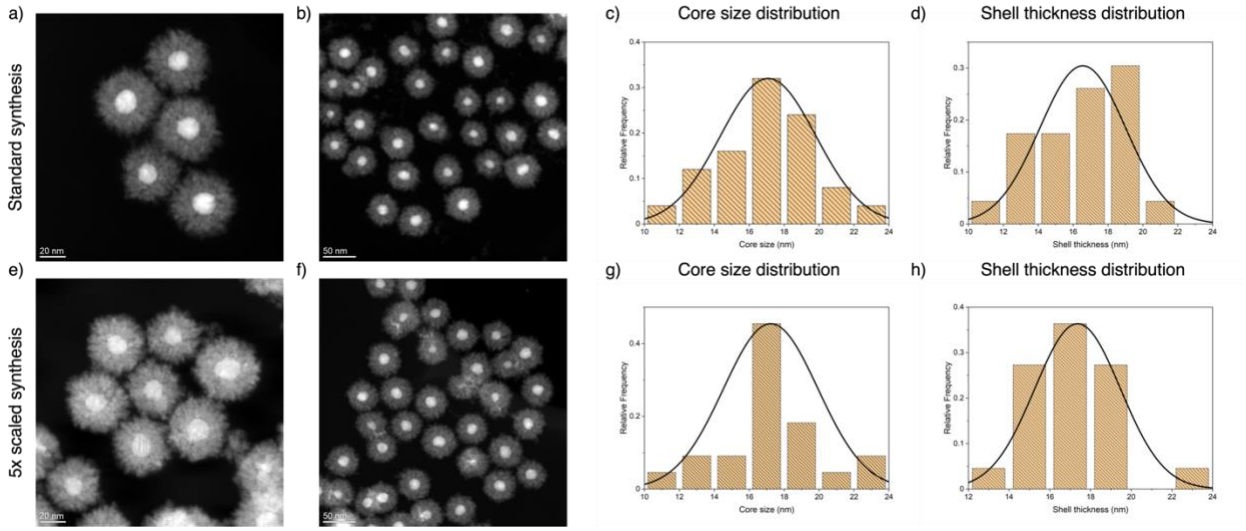

Figure 6.6. Au@CeO_2 synthesized according to a standard and 5x volumetrically scaled protocol. STEM characterization, core size and shell thickness distributions for Au@CeO_2 synthesized from the protocol described in *Section 5.4.1* (a–d) exactly as described (i.e., standard) and (e–h) when volumetrically scaled by a factor of five.

Transitioning conventional one-pot aqueous synthesis methods to continuously flowing systems can be an effective means of achieving high product yields while simultaneously avoiding the altered nucleation and growth rates that can occur in traditional volumetric scaling of synthesis solutions. Ruddy *et. al.* demonstrated this using a heated millifluidic system for the synthesis of transition metal carbide catalysts.[13,15] It is possible that such flow-based systems could be an effective means of scaling the production of core@shell nanoparticles synthesized from two-step methods.

6.6 Applying encapsulation to other catalytic systems

Encapsulation is an effective method to facilitate the morphology–directed restructuring of catalytic systems for improved material utilization. Similar to Chapter 5, future efforts could attempt to generalize this behavior for novel core and shell combinations, should a generalizable synthesis strategy be developed as discussed in *Section 6.4*. Rh and Ir are candidate core metals, as their oxidation thermodynamics have been well-defined, they are relevant in many catalytic applications and exhibit high cost.[16–18] TiO_2 is a promising candidate shell material due to its high

UV absorption, which makes it highly application for photocatalytic processes.[19,20] Encapsulating morphologies, however, can benefit many other catalytic applications.

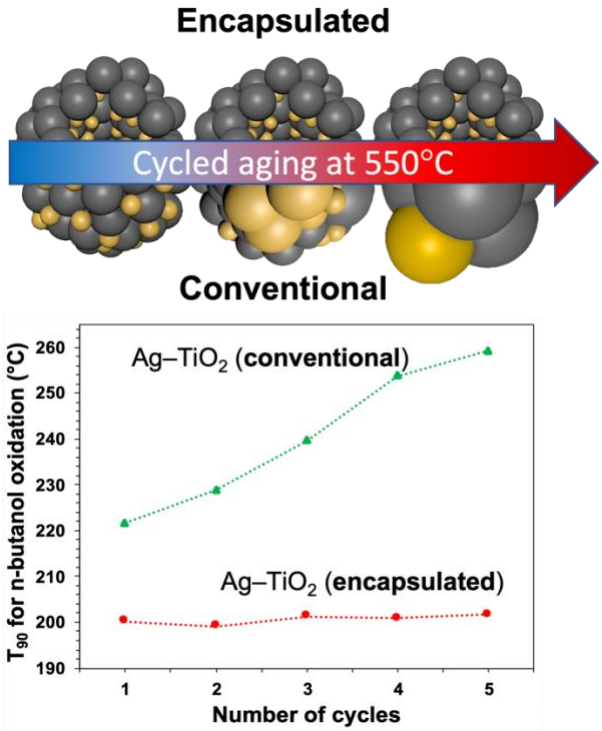

Figure 6.7. Summary of Ag–TiO_2 catalyst restructuring.
Conventional Ag–TiO_2 catalysts undergo sintering and lose T_{90} performance for n-butanol oxidation during repeated aging at 550°C in air for 10 hours. In contrast, encapsulated Ag–TiO_2 catalysts exhibit appreciable structural and catalytic stability when exposed to the same aging conditions.

One such example is using encapsulation to improve thermal stability, when operation temperatures are not high enough to make adatom emission and mobility the dominant restructuring mechanism. This was demonstrated in a recent collaborative work with Dr. Adarsh Bhat, whereby Ag nanoparticles were encapsulated by a porous TiO_2 envelope in order to improve their thermal stability during 550°C aging, which is typically used to remove carbonaceous deposits, also referred to as 'coke', from catalysts remediating volatile organic compound concentration in industrial settings.[21] It was found that encapsulation hindered sintering over five 10 hour 550°C aging cycles when compared to Ag–TiO_2 catalysts prepared by conventional wet impregnation (Figure 6.7). Similar to the Pd@CeO_2 catalysts described in Chapter 2, encapsulation

also lowered T_{90} temperatures for the oxidation of a probe VOC, n-butanol, due to improved metal–support interactions, which increased the participation of TiO_2 lattice oxygen as part of MvK oxidation mechanisms. The encapsulating morphology has been found to impede Ag nanoparticle sintering at temperatures as high as 800°C as determined by preliminary aging studies, despite the adverse sintering of the TiO_2 support (Figure 6.8). The mechanisms for this improved stability have yet to be fully understood and could be the subject of future work.

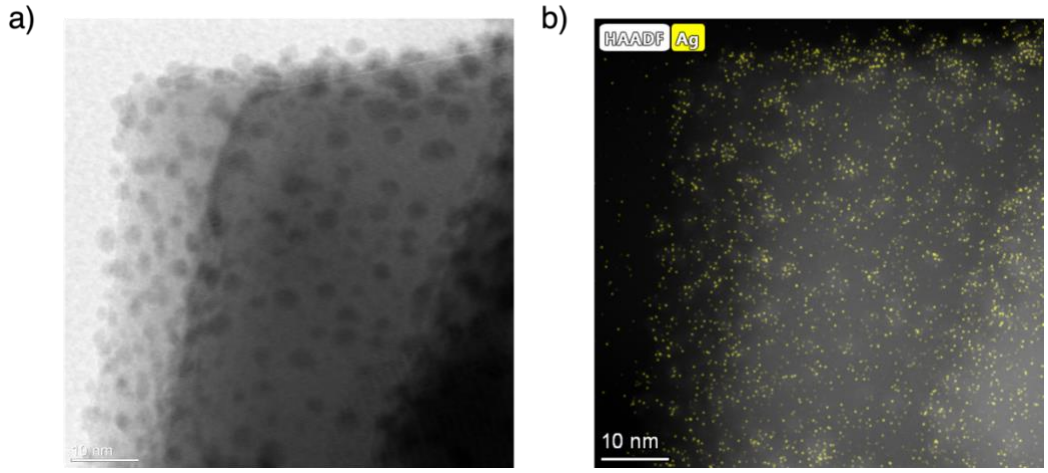

Figure 6.8. Encapsulation promotes Ag stability at 800°C.
(a) TEM and (b) EDS elemental mapping characterization of encapsulated Ag–TiO_2 after aging in air at 800°C for 4 hours. As can be seen, small, highly dispersed clusters of Ag persist, despite the sintering of the underlying TiO_2 support.

The spatial separation of active metal species conferred by encapsulation is an attractive platform for designing novel catalysts. Photocatalysts use semiconductor materials that use incident photons with equal or higher energy than its to move electrons in from its valence band (highest occupied molecular orbital) to its conduction bad (lowest unoccupied molecular orbital).[22,23] These photoexcitation events produce a mobile electron, which can be used to drive reduction and a hole that remains in the valence band, which can conduct oxidation. The efficiency of such processes are typically low, due to the recombination of electrons and holes (charge carriers). A semiconductor can be doped or decorated with active metal particles, which can adsorb target reactants and act as electron reservoirs to increase the charge carrier lifetime. As charge

carrier stabilization relates to the ease of electron transport and acceptance by active metal centers, encapsulating morphologies may be a promising architecture for photocatalyst design as they improve the degree of metal–support interaction.[24,25] Plasmonic photocatalysis relies on the absorption of photos with energy that resonates with the frequency of electron oscillation in an active metal.[26,27] This results in substantial enhancements in electric field. The energy stored in these plasmonic resonant oscillations can be used to drive catalytic processes in a manner similar to traditional photocatalysts. There are few metals, such as Ag, Au and Cu that exhibit plasmonic resonance in practical wavelength regions. Such metals however, are useful as catalysts for a limited number of reactions. In contrast, metals such as Pd, Pt and Rh, which have high catalytic performance for a variety of reactions, do not support plasmonic resonance. Combining the plasmonic and catalytic properties of these two metal types could be a path towards high performing photocatalysts. The high interfacial contact conferred by core@shell morphologies can be beneficial for designing cocatalysts that contain both a plasmonic and catalytically active metal component in close contact. This has been demonstrated in recent work by Halas *et. al.* using a Al@Cu_2O catalyst for enhanced CO_2 reduction,[28] and by Linic *et. al.* using a Ag@Pt catalyst.[29,30] Building upon the preliminary results described in *Section 6.4*, future work could decorate Ag@TiO_2 nanoparticles with a catalytically active metal such as Ru, which has been shown to be highly active for NH_3 synthesis and CO_2 reduction.[31,32] In these arrangements, the Ag core would act as the plasmonic metal, the Ru would be the catalytically active center and the TiO_2 would provide high surface area and a medium to transfer charge.

6.7 References

(1) Farnesi Camellone, M.; Dvořák, F.; Vorokhta, M.; Tovt, A.; Khalakhan, I.; Johánek, V.; Skála, T.; Matolínová, I.; Fabris, S.; Mysliveček, J. Adatom and Nanoparticle Dynamics on Single-Atom Catalyst Substrates. *ACS Catal.* **2022**, 4859–4871. https://doi.org/10.1021/acscatal.2c00291.

(2) Aitbekova, A.; Wrasman, C. J.; Riscoe, A. R.; Kunz, L. Y.; Cargnello, M. Determining Number of Sites on Ceria Stabilizing Single Atoms via Metal Nanoparticle Redispersion. *Chinese J. Catal.* **2020**, *41* (6), 998–1005. https://doi.org/10.1016/S1872-2067(19)63504-7.

(3) Figueroba, A.; Kovács, G.; Bruix, A.; Neyman, K. M. Towards Stable Single-Atom Catalysts: Strong Binding of Atomically Dispersed Transition Metals on the Surface of Nanostructured Ceria. *Catal. Sci. Technol.* **2016**, *6* (18), 6806–6813. https://doi.org/10.1039/C6CY00294C.

(4) Wu, Z.; Hwang, I.; Cha, G.; Qin, S.; Tomanec, O.; Badura, Z.; Kment, S.; Zboril, R.; Schmuki, P. Optimized Pt Single Atom Harvesting on TiO_2 Nanotubes—Towards a Most Efficient Photocatalyst. *Small* **2022**, *18* (2), 2104892. https://doi.org/10.1002/smll.202104892.

(5) Goodman, E. D.; Carlson, E. Z.; Dietze, E. M.; Tahsini, N.; Johnson, A.; Aitbekova, A.; Nguyen Taylor, T.; Plessow, P. N.; Cargnello, M. Size-Controlled Nanocrystals Reveal Spatial Dependence and Severity of Nanoparticle Coalescence and Ostwald Ripening in Sintering Phenomena. *Nanoscale* **2021**, *13*, 930–938. https://doi.org/10.1039/D0NR07960J.

(6) Chen, J.; Wanyan, Y.; Zeng, J.; Fang, H.; Li, Z.; Dong, Y.; Qin, R.; Wu, C.; Liu, D.; Wang, M.; et al. Surface Engineering Protocol To Obtain an Atomically Dispersed Pt/CeO_2 Catalyst with High Activity and Stability for CO Oxidation. *ACS Sustain. Chem. Eng.* **2018**, *6* (11), 14054–14062. https://doi.org/10.1021/acssuschemeng.8b02613.

(7) Xie, S.; Wang, Z.; Tan, W.; Zhu, Y.; Collier, S.; Ma, L.; Ehrlich, S. N.; Xu, P.; Yan, Y.; Xu, T.; et al. Highly Active and Stable Palladium Catalysts on Novel Ceria–Alumina Supports for Efficient Oxidation of Carbon Monoxide and Hydrocarbons. *Environ. Sci. Technol.* **2021**, acs.est.1c00077. https://doi.org/10.1021/acs.est.1c00077.

(8) Duan, X.; Tian, X.; Ke, J.; Yin, Y.; Zheng, J.; Chen, J.; Cao, Z.; Xie, Z.; Yuan, Y. Size Controllable Redispersion of Sintered Au Nanoparticles by Using Iodohydrocarbon and Its Implications. *Chem. Sci.* **2016**, *7*, 3181–3187. https://doi.org/10.1039/C5SC04283F.

(9) Goldsmith, B. R.; Sanderson, E. D.; Ouyang, R.; Li, W. X. CO- and NO-Induced Disintegration and Redispersion of Three-Way Catalysts Rhodium, Palladium, and Platinum: An Ab Initio Thermodynamics Study. *J. Phys. Chem. C* **2014**, *118*, 9588–9597. https://doi.org/10.1021/jp502201f.

(10) Su, Y. Q.; Liu, J. X.; Filot, I. A. W.; Hensen, E. J. M. Theoretical Study of Ripening Mechanisms of Pd Clusters on Ceria. *Chem. Mater.* **2017**, *29*, 9456–9462. https://doi.org/10.1021/acs.chemmater.7b03555.

(11) Hill, A. J.; Bhat, A.; Berquist, Z. J.; Fisher, G. B.; Lenert, A.; Schwank, J. W. Stabilizing Highly Dispersed Halo Sites in Thermally Restructured Palladium Core@Shell Nanoparticles for Improved Catalyst Activity and Durability. *ACS Appl. Nano Mater.* **2021**, *4* (10), 10985–10998. https://doi.org/10.1021/acsanm.1c02436.

(12) Hill, A. J.; Seo, C. Y.; Chen, X.; Bhat, A.; Fisher, G. B.; Lenert, A.; Schwank, J. W. Thermally Induced Restructuring of $Pd@CeO_2$ and $Pd@SiO_2$ Nanoparticles as a Strategy for Enhancing Low-Temperature Catalytic Activity. *ACS Catal.* **2020**, *10*, 1731 – 1741. https://doi.org/10.1021/acscatal.9b05224.

(13) Baddour, F. G.; Roberts, E. J.; To, A. T.; Wang, L.; Habas, S. E.; Ruddy, D. A.; Bedford, N. M.; Wright, J.; Nash, C. P.; Schaidle, J. A.; et al. An Exceptionally Mild and Scalable Solution-Phase Synthesis of Molybdenum Carbide Nanoparticles for Thermocatalytic CO2 Hydrogenation. *J. Am. Chem. Soc.* **2020**, *142* (2), 1010–1019. https://doi.org/10.1021/jacs.9b11238.

(14) Liu, Y.; Wang, Q.; Wu, L.; Long, Y.; Li, J.; Song, S.; Zhang, H. Tunable Bimetallic Au–Pd@CeO 2 for Semihydrogenation of Phenylacetylene by Ammonia Borane. *Nanoscale* **2019**, *11* (27), 12932–12937. https://doi.org/10.1039/C9NR02953B.

(15) Karadaghi, L. R.; Madani, M. S.; Williamson, E. M.; To, A. T.; Habas, S. E.; Baddour, F. G.; Schaidle, J. A.; Ruddy, D. A.; Brutchey, R. L.; Malmstadt, N. Throughput Optimization of Molybdenum Carbide Nanoparticle Catalysts in a Continuous Flow Reactor Using Design of Experiments. *ACS Appl. Nano Mater.* **2022**, *5* (2), 1966–1975. https://doi.org/10.1021/acsanm.1c02916.

(16) Gandhi, H. S.; Graham, G. W.; McCabe, R. W. Automotive Exhaust Catalysis. *J. Catal.* **2003**, *216* (1–2), 433–442. https://doi.org/10.1016/S0021-9517(02)00067-2.

(17) Khivantsev, K.; Vargas, C. G.; Tian, J.; Kovarik, L.; Jaegers, N. R.; Szanyi, J.; Wang, Y. Economizing on Precious Metals in Three-Way Catalysts: Thermally Stable and Highly Active Single-Atom Rhodium on Ceria

for NO Abatement under Dry and Industrially Relevant Conditions. *Angew. Chemie Int. Ed.* **2021**, *60*, 391–398. https://doi.org/10.1002/anie.202010815.

(18) Alcock, C. B.; Hooper, G. W. Thermodynamics of the Gaseous Oxides of the Platinum-Group Metals. *Proc. R. Soc. London. Ser. A. Math. Phys. Sci.* **1960**, *254* (1279), 551–561. https://doi.org/10.1098/rspa.1960.0040.

(19) Zhang, Q.; Lee, I.; Joo, J. B.; Zaera, F.; Yin, Y. Core-Shell Nanostructured Catalysts. *Acc. Chem. Res.* **2013**, *46* (8), 1816–1824. https://doi.org/10.1021/ar300230s.

(20) Pelaez, M.; Nolan, N. T.; Pillai, S. C.; Seery, M. K.; Falaras, P.; Kontos, A. G.; Dunlop, P. S. M.; Hamilton, J. W. J.; Byrne, J. A.; O'Shea, K.; et al. A Review on the Visible Light Active Titanium Dioxide Photocatalysts for Environmental Applications. *Appl. Catal. B Environ.* **2012**, *125*, 331–349. https://doi.org/10.1016/j.apcatb.2012.05.036.

(21) Bhat, A.; Hill, A. J.; Fisher, G. B.; Schwank, J. W. Improving the Thermal Stability and N-Butanol Oxidation Activity of Ag-TiO_2 Catalysts by Controlling the Catalyst Architecture and Reaction Conditions. *Appl. Catal. B Environ.* **2021**, *297*, 120476. https://doi.org/10.1016/j.apcatb.2021.120476.

(22) Karamian, E.; Sharifnia, S. On the General Mechanism of Photocatalytic Reduction of CO2. *J. CO2 Util.* **2016**, *16*, 194–203. https://doi.org/10.1016/j.jcou.2016.07.004.

(23) Mondal, K.; Sharma, A. Recent Advances in the Synthesis and Application of Photocatalytic Metal–Metal Oxide Core–Shell Nanoparticles for Environmental Remediation and Their Recycling Process. *RSC Adv.* **2016**, *6*, 83589–83612. https://doi.org/10.1039/C6RA18102C.

(24) Hirakawa, T.; Kamat, P. V. Charge Separation and Catalytic Activity of Ag@TiO 2 Core−Shell Composite Clusters under UV−Irradiation. *J. Am. Chem. Soc.* **2005**, *127* (11), 3928–3934. https://doi.org/10.1021/ja042925a.

(25) Wang, D.; Hisatomi, T.; Takata, T.; Pan, C.; Katayama, M.; Kubota, J.; Domen, K. Core/Shell Photocatalyst with Spatially Separated Co-Catalysts for Efficient Reduction and Oxidation of Water. *Angew. Chemie Int. Ed.* **2013**, *52* (43), 11252–11256. https://doi.org/10.1002/anie.201303693.

(26) Zhou, L.; Zhuang, S.; He, C.; Tan, Y.; Wang, Z.; Zhu, J. Self-Assembled Spectrum Selective Plasmonic Absorbers with Tunable Bandwidth for Solar Energy Conversion. *Nano Energy* **2017**, *32* (December 2016), 195–200. https://doi.org/10.1016/j.nanoen.2016.12.031.

(27) Johns, R. W.; Bechtel, H. A.; Runnerstrom, E. L.; Agrawal, A.; Lounis, S. D.; Milliron, D. J. Direct Observation of Narrow Mid-Infrared Plasmon Linewidths of Single Metal Oxide Nanocrystals. *Nat. Commun.* **2016**, *7* (May), 1–6. https://doi.org/10.1038/ncomms11583.

(28) Robatjazi, H.; Zhao, H.; Swearer, D. F.; Hogan, N. J.; Zhou, L.; Alabastri, A.; McClain, M. J.; Nordlander, P.; Halas, N. J. Plasmon-Induced Selective Carbon Dioxide Conversion on Earth-Abundant Aluminum-Cuprous Oxide Antenna-Reactor Nanoparticles. *Nat. Commun.* **2017**, *8* (1), 27. https://doi.org/10.1038/s41467-017-00055-z.

(29) Aslam, U.; Chavez, S.; Linic, S. Controlling Energy Flow in Multimetallic Nanostructures for Plasmonic Catalysis. *Nat. Nanotechnol.* **2017**, *12* (10), 1000–1005. https://doi.org/10.1038/nnano.2017.131.

(30) Aslam, U.; Rao, V. G.; Chavez, S.; Linic, S. Catalytic Conversion of Solar to Chemical Energy on Plasmonic Metal Nanostructures. *Nat. Catal.* **2018**, *1* (9), 656–665. https://doi.org/10.1038/s41929-018-0138-x.

(31) Jacobsen, C. J. H.; Dahl, S.; Hansen, P. L.; Törnqvist, E.; Jensen, L.; Topsøe, H.; Prip, D. V.; Møenshaug, P. B.; Chorkendorff, I. Structure Sensitivity of Supported Ruthenium Catalysts for Ammonia Synthesis. *J. Mol. Catal. A Chem.* **2000**, *163* (1–2), 19–26. https://doi.org/10.1016/S1381-1169(00)00396-4.

(32) Panagiotopoulou, P. Methanation of CO2 over Alkali-Promoted Ru/TiO2 Catalysts: II. Effect of Alkali Additives on the Reaction Pathway. *Appl. Catal. B Environ.* **2018**, *236* (March), 162–170. https://doi.org/10.1016/j.apcatb.2018.05.028.